DE FE0004542

Final Report

PROOF-OF-FEASIBILITY OF USING WELL BORE DEFORMATION AS A DIAGNOSTIC TOOL TO IMPROVE CO_2 SEQUESTRATION

Larry Murdoch, Principal Investigator, Clemson University
Stephen Moysey, Co-Investigator, Clemson University
Leonid Germanovich, Co-Investigator, Georgia Tech
Industry Collaborator: Baker Hughes

Award to

Clemson University
Office for Sponsored Programs
300 Brackett Hall
Clemson, SC 29634-5702

13 January 2016

DISCLAIMER

This work was funded by the Department of Energy National Energy Technology Laboratory under contract DE FE0004542.

ABSTRACT

Injecting CO_2 raises pore pressure and this causes subsurface formations to deform. The pattern and amount of deformation will reflect the distribution of pressure and formation properties in the subsurface, two quantities of interest during CO_2 storage. The hypothesis underlying this research is that the small deformation accompanying CO_2 storage can be measured and interpreted to improve the storage process. To address this hypothesis we sought answers to three key questions:

1. How much deformation should occur in the vicinity of injection wells used for CO_2 storage?
2. How can deformation of the expected magnitudes be measured?
3. How can the resulting measurement be interpreted?

We answered the first question by reviewing properties and specifications of previous CO_2 storage operations, and then we set up numerical simulations using these characteristics. The results of the models indicated that strains in the vicinity of the wellbore would be 1 to several tens of microstrain (for reference, 1 microstrain of deformation would occur when a bar 1 km long was stretched by 1 mm). The strain level drops to 0.1 microstrain within 1 km and 0.01 with several km of the injection well. The next question was answered by reviewing the literature describing high-resolution displacement instruments, and by building and testing our own prototype instruments. We concluded that it should be possible to measure the expected strains using instruments based on available technology. The last question was answered by developing new computer algorithms for matching simulations of the deformation process with field data obtained from the instruments. The results show that deformation data can be interpreted to improve estimates of key formation properties, like permeability and Young's modulus, that are important for forecasting CO_2 storage performance. The methods also show potential for characterizing heterogeneities in formation properties and anticipating problems associated with leaks.

The primary result of this project is to demonstrate that it should be feasible to measure and interpret in situ deformation during CO_2 storage. This will improve the ability to design safe and CO_2 secure storage systems, and it contributes directly to the DOE program goals to a.) predict CO_2 storage capacity, and b.) demonstrate that CO_2 remains in the zones where it was injected. Improving the ability to measure and interpret small deformations also has potential beneficial applications in improving hydrocarbon production, natural gas storage, geothermal energy production, hydraulic fracturing, ground water recovery and aquifer management, and other operations important to energy and the environment.

Table of Contents

Chapter One: Introduction and Summary of Findings

Chapter Two: Simulations

Chapter Three: Optimization and Parameter Estimation

Chapter Four: Instrumentation

Chapter Five: Summary and Conclusions

PROOF-OF-FEASIBILITY OF USING WELL BORE DEFORMATION AS A DIAGNOSTIC TOOL TO IMPROVE CO_2 STORAGE

EXECUTIVE SUMMARY

Geologic storage of carbon dioxide is a promising way to limit the increase of greenhouse gases in the atmosphere. The objectives of the project described here were to advance the ability to a.) predict CO_2 storage capacity, and b.) demonstrate that CO_2 remains in the zones where it was injected, two goals of the program at the Department of Energy that funded this research. We hypothesized that these objectives could be met by measuring and interpreting the deformation of wellbores used to inject CO_2 or for monitoring. The underlying principle is that injection raises fluid pressure, which deforms the porous material of the reservoir and cap rock. The pattern and extent of deformation is a result of the distributions of fluid pressure and mechanical properties in the reservoir.

The project consisted of three tasks, and the first one was to estimate the magnitude and extent of deformation in the vicinity of injection wells. We did this using fully coupled, poroelastic simulations of idealized scenarios resembling CO_2 well testing and storage. We found that injection into a reservoir layer causes the layer to move radially outward and increase in thickness, or extend vertically. The displacement of the reservoir drags the caprock outward and both compresses it vertically and lifts it upward to form a dome. The injection well itself bulges outward and stretches axially adjacent to the reservoir and it compresses axially in the cap rock. The transition from extension to compression in the casing moves upward as the pressure in the reservoir moves into the caprock, and tracking the casing deformation appears to be a way to track the changes in pressure on the outside of the casing. We assumed fluid was injected into the well at a constant pressure of 1 MPa and this resulted in a flow that decreased with time, but was approximately 100 gpm after 100 days of injection. This simulation was based on a detailed compilation of poroelastic parameters, which we made available as a database. The axial strain along the injection well was approximately 10^{-5} of stretching in the reservoir, and several microstrain (10^{-6}) of compression in the cap rock. Horizontal and vertical strains were greater than 10^{-8} within several km of the injection well. Tilts greater than 10^{-8} rad also occurred within several km of the injection well. Strain rates were approximately 10^{-12} 1/s or larger in the vicinity of the well early in the injection period, but they decreased with time and distance. The magnitude of strain increases in proportion to the well injection pressure, and the strain rate increases in proportion to the well injection rate. CO_2 storage operations will likely use injection pressures and rates that are larger than the benchmark conditions we analyzed, so the strain magnitudes and rates are expected to be larger as a result. The patterns of strain and tilt were controlled by deformation of the reservoir and interactions with the ground surface, and variations in the deformation field occurred when heterogeneities were introduced. This is important because it suggests that deformation data could be used to improve understanding of heterogeneities.

Another task investigated methods for measuring deformation and it found that there were three main classes of instruments that could be used for this application. The highest spatial density, but lowest resolution measurements were from the WIRE system from Baker Hughes. It uses specialized optical fiber attached to the outside of casing to measure multiple components of strain at many hundreds of locations with resolution of approximately 10^{-6}.

WIRE is cemented in the annulus of new wells, and it has been demonstrated on several commercial projects. Another class consists of portable extensometers or tiltmeters that are temporarily anchored to a borehole wall. They only measure one location at a time, so they lack the spatial density of WIRE, but they use longer sensors to sharpen the strain resolution to 10^{-8}. We developed and demonstrated in a field setting a portable strainmeter that uses optical fiber strain gauges to measure multiple components of strain in a borehole during this investigation. Grouted strainmeters provide the highest resolution of any borehole meter, with the ability to measure strains approaching 10^{-10}. This comes at a cost, however, because these instruments are sealed in a borehole with grout, so the bottom of a borehole and the instrument must be dedicated. Taken together, we find it should be possible to measure the magnitude of strain expected to occur in the vicinity of injection wells using instruments that are either already available or that are developed based on existing techniques. Moreover, we expect that it should be feasible to measure strains in caprock at relatively shallow depth that result from pressurization of the underlying reservoir. This is important because measuring strains at shallow depths in caprock will be less expensive than measurements at the depth of reservoirs. How instruments are coupled to subsurface materials will affect strain-measuring performance, particularly when strain rates are slow.

The other component of the project involved evaluating methods for interpreting deformation data. The challenge is that simulations of deformation are computationally expensive, and objective functions may contain many local minima, so readily available optimization methods perform poorly. We developed an approach that integrates several different sampling and optimization schemes (genetic algorithms, MCMC, naïve Monte Carlo, and Voronoi polygons) to balance algorithmic speed versus the evaluation of parameter uncertainty and tradeoffs in the data. Applying our optimization model to various case studies, we clearly demonstrated that geomechanical data have substantial value for improving estimates of reservoir properties. We also found that there is flexibility in where these measurements are made (i.e., at the injection point, in the reservoir, or in the caprock), but that using multiple measurements is likely to be the most effective strategy as the complimentary information in the data set is likely to aid in identification and filtering of random and systematic noise. This work also showed that geomechanical data have substantial potential for detecting and identifying heterogeneities within formations.

The results of this project suggest that in situ deformation during CO_2 storage will be large enough to measure in the general vicinity of an injection well and caprock, and it should be feasible to interpret these data using high performance optimization methods. It appears feasible that this approach will improve the ability to estimate formation properties, characterize heterogeneities and estimate the distribution of subsurface pressure, which will contribute to the program goals of predicting CO_2 storage capacity, and demonstrating that CO_2 remains in the zones where it was injected.

CHAPTER ONE
INTRODUCTION AND SUMMARY OF FINDINGS

Geologic storage of carbon dioxide is a promising way to limit the increase of greenhouse gases in the atmosphere [*IPCC*, 2005], and monitoring the injection process is important to ensure the security of CO_2 storage. A wide range of techniques are being considered for monitoring the injection process [*IPCC*, 2005; *Liu*, 2012], and one of them involves assessing deformation of the formation caused by changes in fluid pressure [*Davis*, 2011; *Verdon et al.*, 2013].

Deformation during injection can range in magnitude, extent and rate, causing both opportunities and problems. Deformation at the ground surface may damage infrastructure [*Mayuga and Allen*, 1969], but modest surface deformation forms a pattern that can be interpreted to estimate the distribution of volume change in the reservoir [*Vasco et al.*, 2001; *Vasco et al.*, 2010]. Surface deformation is typically slow, with rates measured in mm/yr [*Vasco et al.*, 2010]. Radar interferometry (InSAR) and Global Positioning System (GPS) are available for measuring this process [*Phillips et al.*, 2003]. At the other end of the time scale, seismicity can also cause problems if magnitudes are excessive [*Zoback and Gorelick*, 2012; *Ellsworth*, 2013], while microseismicity provides a signal useful for monitoring changes in fluid pressure [*Maxwell et al.*, 2008; *Gutierrez et al.*, 2012].

Deformation also occurs at scales intermediate between the small and rapid events detected by geophones and the large and slow surface displacement detected by InSAR and GPS. Shear strains accompany injection, and shear on a horizontal plane can be monitored using tiltmeters mounted in boreholes [*Meertens et al.*, 1989]. Shear may also occur on a vertical plane due to differences between horizontal stresses. This can deform casing into an oval cross-section [*Markley et al.*, 2002] that has been characterized using an ultrasonic logging tool with resolutions of several centimeters [*Morris et al.*, 2007]. Much smaller deformations can be monitored with borehole strainmeters that are grouted in place instead of deployed temporarily as a logging tool [*Sacks et al.*, 1971; *Gladwin*, 1984; *Gladwin and Hart*, 1985; *Agnew*, 1986]. Borehole strainmeters are designed to characterize strains caused by tectonic processes, and they can measure strains of 10^{-9} or less. This increase in resolution comes at a cost, however, as borehole strainmeters are grouted in place, effectively sealing the bottom of the borehole.

Straddling the middle ground between the resolution of the ultrasonic logging tool and the borehole strainmeter is the borehole extensometer. Early instruments were permanently built into boreholes [*Davis et al.*, 1969], but portable instruments have been in use for several decades [*Gale*, 1975; *Hesler et al.*, 1990; *Martin et al.*, 1990; *Thompson and Kozak*, 1991], and recent applications have improved resolution of axial deformation to better than 10^{-8} m [*Hisz et al.*, 2013].

The general benefits of deformation monitoring are either to provide an early warning of an impending large strain that could be damaging, or to provide a data stream that can be inverted to improve understanding of either properties, like permeability, or processes, like changes in pressure or fluid volume (see Figure 1.0-1 for other examples). Well casings are known to fail catastrophically when sheared by a slipping fault [*Dusseault et al.*, 2001], and more subtle deformation processes may affect the seal between the casing and the formation, leading to a degradation of wellbore integrity [*Crow et* al., 2010]. Elevated pore pressure resulting from injection may reduce effective stress and potentially lead to fracturing in the

annular space, for example. Maintaining wellbore integrity is important to the security of CO_2 sequestration operations [*Chiaramonte et al*., 2007; *Benge*, 2009], so it is important to be able to characterize and monitor for localized deformation processes that could affect wellbore integrity. Recent innovations have shown that optical fiber strain gauges can be embedded in casing to anticipate possible failure of casing [*Childers et al*., 2007].

Transient hydraulic wells tests, where pressures are recorded at wells while fluid is produced or injected for a short period of time, are widely used to forecast long-term well performance in reservoirs or aquifers. Similar tests have been used to anticipate the response of wells to CO_2 injection, and hydraulic well tests will undoubtedly be a mainstay in the initial assessment of wells used for CO_2 injection in the future. Despite their importance, hydraulic well tests are vulnerable to problems that could cause serious errors when their results are used in simulations. For example, well tests on isolated wells are notorious for producing poor estimates of specific storage or formation compressibility [*Krusemann and deRitter*, 1980; *Horne*, 1995]. Errors in this parameter will result in either over-estimating the pressure rise in the formation when the estimated compressibility is too stiff, or under-estimating it when the estimated compressibility is too soft. In the first case, the capacity of the well will be under-utilized and the value of the unrecognized capacity will be lost, whereas in the second one the well could create excessive injection pressures that required expensive remediation.

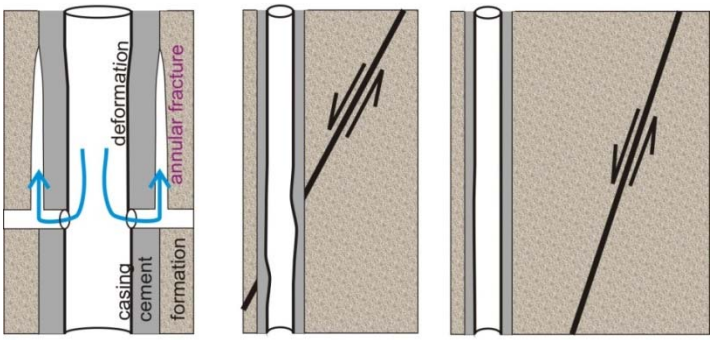

Figure 1.0-1. Potential problems during CO_2 storage that could be detected by monitoring well bore deformation. a.) annular hydraulic fracture. b.) fault intersecting casing. c.) fault separated from casing—increase in strain rate preceding fault slip is detected at casing.

Measuring and interpreting both pressure and deformation is done during a hydromechanical well test [*Schweisinger et al.* 2009]. Techniques for conducting and interpreting hydromechanical well tests are available for shallow water wells [*Murdoch and Germanovich,* 2006; *Svenson et al.* 2007; 2008; *Schweisinger et al.* 2009]. The field technique involves using a portable downhole tool [*Murdoch et al*. 2007] that is anchored at multiple points along the borehole wall (Figure 1.0-2). Displacements are measured between the anchored points while the well is stressed by pumping or injection.

Interpretation of displacement and pressure signals is a key component of hydromechanical well tests. The approach to interpretation has been to first develop a heuristic understanding of the hydromechanical response through analytical solutions and simulations of idealized cases [*Murdoch and Germanovich*, 2006; *Schweisinger*, 2007; *Svenson et al*, 2007]. This type of evaluation showed, for example, that displacements are a hysteretic function of the injection pressure, so displacements early in a test when pressure (or hydraulic head) change is increasing are always less than they are later when pressure change is decreasing. This occurs because displacement depends on the distribution of pressure throughout the aquifer or reservoir, not just on the local pressure at the wellbore.

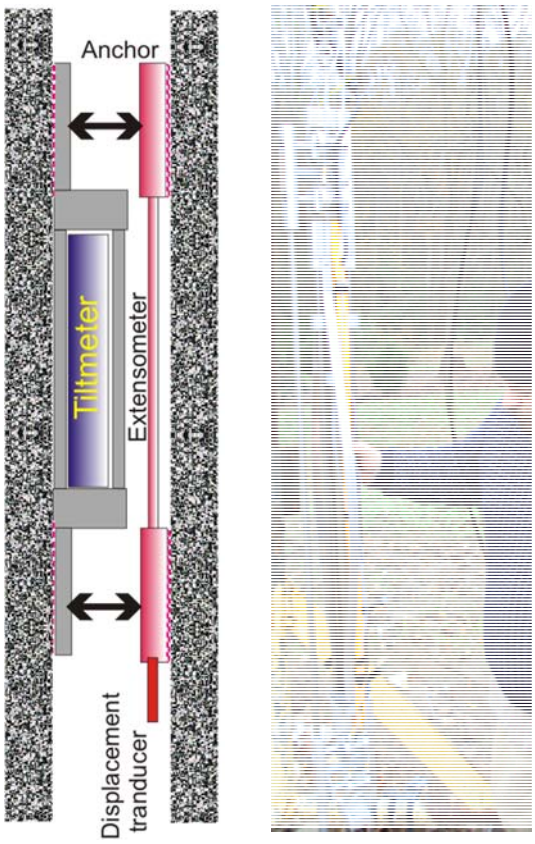

Figure 1.0-2. Extensometer and tiltmeter device capable of simultaneously measuring high resolution axial displacements with an extensometer and rotation with a tiltmeter.

Analysis of data from hydromechanical tests has also shown that the response is affected by several factors, so interpretation is best done using parameter estimation schemes [*Vasco et al.*, 1998; *Vasco et al.*, 2000; *Vasco et al.*, 2001; *Vasco*, 2004]. Gradient-based optimization methods have been used to minimize an objective function based on displacements and heads [*Svenson et al.*, 2009; *Schweisinger*, 2007; *Murdoch et al.*, 2009]. This work demonstrated the feasibility of using hydromechanical data to constrain formation parameters, but they were time consuming and prone to non-uniqueness and problems with local minima in the objective function.

1.1 Motivation for the Project

Hydromechanical well tests and other applications for wellbore deformation measurements appear to have significant potential applications to improving CO_2 storage. In order to achieve this potential, it must be feasible to measure subsurface deformation caused by CO_2 storage, and then interpret the resulting data. Several methods are available for measuring subsurface deformation, but the magnitude and distribution of the deformation that would occur in the vicinity of a CO_2 injection well is unclear and this blocks an evaluation of the suitability of available instrumentation. Some instruments are already used to measure wellbores during well testing, but the highest resolution instrumentation for measuring strain has been developed for applications to geodesy and its suitability for applications related to well testing has, to our knowledge, never been considered. As a result, the magnitudes and distribution of deformation to expect, and the capabilities of measurement methods were unclear at the start of this project. Moreover, even if it was possible to measure the deformation, methods for interpreting those data were unavailable.

1.2 Project Objectives

The ultimate objective of the proposed project is to evaluate the feasibility of using measurements of well bore deformation to improve CO_2 sequestration, and to develop the theoretical and instrumentation background to plan a field demonstration. Three important sub-objectives include:

1.) characterize wellbore deformation under conditions anticipated for use in geologic CO_2 storage;

2.) identify and evaluate techniques for interpreting the results of simultaneous measurements of displacement and pressures during well testing or operation;

3.) evaluate capabilities and requirements for instruments used to measure deformation in a bore hole.

This project was originally motivated by opportunities to monitor deformation in boreholes used for injection or monitoring. We envisioned using the wellbores to deploy sensors to measure deformation of the casing, and then retrieving the sensors after the measurements were no longer useful. During the course of the project, we have expanded the scope to include strain gauges that are deployed on the outside of casing, along with instruments that are grouted in a borehole.

1.3 Overview of the Project

The project was conducted with three tasks, each focused on one of the objectives. One task focused on simulating the deformation caused by injection into a well, and this was called Task Two. Task Three involved evaluating and developing inversion methods for interpreting deformation measurements. Task Four evaluated methods for measuring small deformation in the subsurface.

1.4 Participants

The project was a collaboration between Clemson University, Georgia Tech and Baker Hughes. Larry Murdoch at Clemson was the Principal Investigator and he led Task 4. Stephen Moysey from Clemson led Task Three, and Leonid Germanovich from Georgia Tech led Task Two. Cem Ozan was the representative from Baker Hughes. Later in the project, Roger Duncan at Baker Hughes provided us with details of the WIRE technology for measuring casing deformation.

Much of the important work on the project was done by talented students and a post-doctoral researcher at Clemson and Georgia Tech. Sihyun Kim contributed to the simulations in Chapter Two, and Josh Smith put together the database on poroelastic properties in Chapter Two. Johnathan Ebenhack and Glenn Skawski designed and built the 3DX and 5DX instruments, and Dave Hisz designed and built the Tilt-X instrument described in Chapter Four. Scott DeWolf was another contributor to Chapter Four. He characterized the DVRT and Eddy Current sensors, and described the Borehole Optical Fiber Strainmeter that he developed prior to the project. Alex Hanna played a leading role in innovating and evaluating the inverse methods described in Chapter Three.

Brian Dressel managed this project at the National Energy Technology Office of the DOE. Brian provided input on technical and administrative topics throughout the course of the investigation.

1.5 Organization of the Report

The following report consists of three chapters, each describing one of the major tasks in the project. The chapters outline the major methods and results from the task, and the organization of the chapter follows from the tasks outlined in the Statement of Project Objectives. We have revised the organization of the chapters for clarity, however, so their structure departs from that of the SOPO.

1.6 SUMMARY OF MAJOR FINDINGS

The major findings are described in detail in the following report. To facilitate access to this information, the findings are summarized below.

1.6.1 CHAPTER TWO: SIMULATION

The objective of this chapter was to estimate the magnitude and pattern of deformation associated with injecting fluid into reservoir. To meet this objective, we conducted a series of theoretical analyses using analytical and numerical models that solved problems in poroelasticity. We found that readily available computer codes (ABAQUS and COMSOL) can solve problems related to deformation in the vicinity of injection wells using finite element methods. We tested these codes in a variety of relevant example problems, and we developed a poroelastic benchmark model intended to be used by other investigators interested in validating other codes. The run times for fully coupled finite element codes can be time consuming and may be prohibitive for some inverse methods. To address this constraint, we developed two analytical asymptotic solutions that can be used to calculate deformation very quickly.

The magnitude and pattern of deformation were calculated using an idealized simulation that was based on properties typical of CO_2 storage operations. The analysis assumed an injection pressure of 1 MPa, which resulted in an injection rate of approximately 100 gpm, and the injection lasted for 100 days. This is a lower pressure and shorter duration than full scale operations, but it may be a higher pressure and longer than an injection test conducted for formation evaluation.

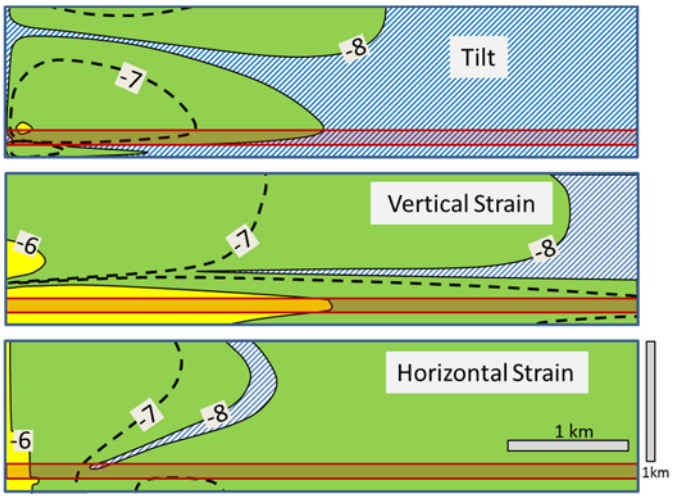

Figure 1.6-1. Summary strain magnitudes (as log of absolute value) in cross section after injecting for 100 days at 1MPa according to baseline example. Colors show three categories (yellow: $\varepsilon > 10^{-6}$; green: $10^{-8} < \varepsilon < 10^{-6}$; hatched: $\varepsilon < 10^{-8}$). Aquifer/reservoir as red. Well on the lower left.

The results indicate that the axial strain will be tensile and approximately 10 με adjacent to the pressurized interval. It will decrease and change sign upward with axial compression of several με in the casing adjacent to the confining unit. Radial displacements of several microns are largely due to pressurizing the wellbore, but smaller changes in radial displacements occur with time as the formation pressure changes.

The pattern of strain in the casing is sensitive to the pressure in the annular space and in the confining unit. It may be feasible to estimate changes in pressure on the outside of solid casing by measuring casing deformation, and this could be used to characterize well bore integrity or the permeability of confining units.

Strain rates of 10^{-12} 1/s or greater are expected in the vicinity of the wellbore early in the injection. The strain rate will decrease with time to 10^{-13} 1/s or less in the first 100 days of injection. Strain rates of 10^{-13} 1/s occur in the confining unit and they also decrease with time.

The magnitude of strain at the well and in the formation increases roughly in proportion to the injection pressure (the results above are for 1 MPa)

The magnitude of the strain rate at the well and in the formation increases roughly in proportion to the injection rate (the results above are for approximately 100 gpm).

Formation properties will affect the magnitude of expected deformation, but the overall effect is generally less than a factor of two when using ranges of properties associated with a particular type of reservoir.

The distributions of strain components in the formation create varied patterns that evolve with time. An example of three components of the strain tensor after injecting for 100 days is summarized in Figure 1.6-1. The strain patterns depend on the magnitude and distribution of formation properties, so they are sensitive to heterogeneities in the aquifer and overlying confining unit. Patterns of horizontal and vertical strains, as well as displacement gradients (tilts) occur in the overlying confining unit in response to pressure changes in the underlying reservoir. The patterns result from both a.) radially outward and upward displacement of the reservoir, and b.) upward bending of the ground surface.

The strains predicted to occur in the vicinity of an injection well are in the range of available instrumentation. Strain in excess of 1 με ($>10^{-6}$) will likely occur in the vicinity of the injection well, according to the analysis. Strains of this magnitude can be measured by common strain gauges, and a system called WIRE, which consists of many strain gauges on a fiber optic cable, is available for downhole deployment along wellbores. Strains in excess of 10^{-8} can be measured by portable extensometers and tiltmeters, according to tests conducted in shallow aquifers. Vertical and horizontal strains and tilts of this magnitude occur within a few km of the injection well within 100 days of injection (Figure 1.6-1), according to the simulations. It appears that the strains that are expected to occur in the vicinity of injection wells are within the resolution of instruments that could be temporarily anchored in monitoring wells. Horizontal and vertical strains greater than 10^{-10} can be resolved by instruments that are grouted into boreholes. Strains of these low magnitudes occur up to many km from injection wells, although distinguishing these small strains from background noise may be challenging.

1.6.2 CHAPTER THREE: PARAMETER ESTIMATION

The goal of this task is to evaluate the potential of geomechanical data collected during injection operations as a constraint on reservoir model parameters. A major enabling contribution of this work was, therefore, the development of advanced optimization algorithms that leverage high performance computing to calibrate reservoir parameters. The approach developed here integrates several different sampling and optimization schemes (genetic algorithms, MCMC, naïve Monte Carlo, and Voronoi polygons) to balance algorithmic speed versus the evaluation of parameter uncertainty and tradeoffs in the data. This method was then used to study the ability of different types of data to constrain reservoir parameters and evaluate how this translates to predictions of long-term operational behavior. The key outcomes of the research are summarized in the three sections below that relate directly to the three goals outlined in the original project proposal. The rest of this report, however, is structured in a format that provides a clearer explanation of the results given substantial overlaps between the sections.

Parameter Uncertainty and Uniqueness We demonstrated that different combinations of geomechanical measurements such as pressure, tilt and strain can be used to estimate poroelastic parameter values and their uncertainties. Notably, the most accurate parameter estimates with the lowest uncertainties are obtained when pressure data are used in conjunction with measurements sensitive to all three components of reservoir strain. We have also investigated how measurement location impacts our ability to estimate parameters and found that measurements within cap rock theoretically provide sufficient information for calibrating the model parameters, thus suggesting that field studies may not require penetration of the target formation, thus reducing risk.

Prediction Sensitivity Evaluating the sensitivity of predictions to uncertainty and error in model estimates was considered within the scope of this work. Using Monte Carlo simulations, we were able to produce forecasts of reservoir performance for different data constraint cases, i.e., where parameter uncertainty depended on the type of data used in the optimization. We found that the degree of uncertainty in the forecasts scaled with the degree of uncertainty in the parameter estimates. A second type of study we performed evaluated the effect of model errors on predictions, i.e., the case where a model does not capture key information about the underlying reservoir system, such as a preferential flow path through a fracture or along the borehole. We found that in these scenarios, significant errors in parameter estimates could occur, but model predictions were well outside reasonable uncertainties in the data thus providing a mechanism to identify and correct these model errors when geomechanical data are used as a constraint.

Large-scale Optimization We investigated stochastic and deterministic optimization methods, and evaluated their viability for large-scale optimization of poroelastic forward models. We have observed that while some deterministic methods, e.g., gradient descent, converge quickly in ideal circumstances, they perform poorly in the presence of non-unique problems or non-convex error structures. By integrating these methods with stochastic techniques like genetic algorithms, Markov chain Monte Carlo, and naïve Monte Carlo with a novel sampling technique based on Voronoi polygons, we have developed a new hybrid algorithm that balances fast convergence with an improved exploration of the parameter space. As these stochastic methods require many simulation runs in order to perform adequately, we have used high-performance computing methods to distribute simulation runs over many computational nodes on a cluster computer. To support the analysis of these data, we implemented a statistical method for combining non-unique pieces of information into superior parameter estimates.

1.6.3 CHAPTER FOUR: INSTRUMENTATION

Three classes of in situ instruments have been evaluated for measuring deformation of wellbores associated with pressure changes in aquifers or reservoirs. The classes trade logistics of deployment and well use, for resolution in strain magnitude, and spatial resolution in the distribution of strain that can be measured. This results in causes the different classes of instruments to be suitable for different applications.

Annular strain sensors ($\varepsilon > 10^{-6}$) provide the most flexible logistics because they are mounted on the outside of casing so the wellbore is open and use of the wellbore is unaffected. Moreover, the sensors are isolated by casing and cement from the harsh conditions inside the wellbore.

The WIRE system developed by Baker Hughes is currently the only available system for making this measurement, to our knowledge. WIRE is currently designed to be deployed on the outside of casing, so deployment must be done during well completion. The deployment process is relatively straightforward, but the use of this system currently requires deployment on a new well—a capability to retrofit existing wells is currently unavailable.

The WIRE system uses FBGs configured using a proprietary interferometric interrogator system. The strain resolution of each sensor appears to be in the range of 10^{-7} to 10^{-6}, which is the lowest resolution of the systems we evaluated. Strain signals of ~1 με (1000 nε) could likely be characterized with the system in its current form. Even though this is lower resolution than other system, it is feasible to deploy hundreds of sensors along a borehole using WIRE, and this is by far the highest spatial resolution of the systems we considered here. Moreover, the system is design to measure multiple degrees of freedom, so both axial and bending strains can be measured.

The WIRE system is particularly well suited to monitoring complicated strain patterns in casing under conditions where strains are particularly large. Strains during brief well tests may be too small to be resolved, but it seems highly likely that strains during CO_2 storage operations could be resolved by this technique. The WIRE system appears to be well suited to monitoring for large strains in injection casings that could lead to problems with wellbore integrity.

Portable strain instruments ($\boldsymbol{\varepsilon > 10^{-8}}$), including extensometers, tiltmeters and strainmeters, are temporarily anchored to the inside of a wellbore. The instruments are several meters long and occupy a significant fraction of the cross-section of the wellbore. This will affect the logistics of well operation, but injection operations could likely continue during deployment. Water wells can be pumped or used for injected while these instruments are in place, for example. The instrument could be removed when testing was completed, or for maintenance. This would reduce the cost and improve the reliability compared to instruments that are grouted in place. The instruments could be deployed in existing wells, which would reduce costs and increase versatility compared to instruments that must be installed during completion.

The portable instruments can measure smaller deformations than the embedded annular sensors, with axial and tilt strain resolutions in the range of 10^{-9} to 10^{-8}. Strains signals of 10s of $n\epsilon$ or nrad could be characterized by these instruments. This improved resolution in the magnitude of strain comes at the expense of the spatial resolution because portable strain instruments are designed to only measure one location at a time.

Electromagnetic and fiber sensors are available that have characteristics suitable for use in portable strain instruments. DVRTs, eddy current sensors, fiber Bragg gratings, fiber interferometers, electrolytic tilt sensors and pendulum sensors all appear suitable for some downhole applications, and they each have constraints on deployment that must be considered in the design of a downhole instrument.

Portable strain instruments appear to be suited to applications in injection wells during short-term testing. This would include injection tests to characterize the formation prior to full scale operations, for example. These types of instruments also appear to be suited to applications in monitoring wells in the vicinity of the injection interval where strains are expected to be greater than approximately 10^{-8}.

Grouted Strainmeters $\varepsilon > 10^{-10}$) are the most sensitive strain meters available, but they are also have the most logistical constraints. They can resolve strains on the order of 10^{-11}, so strain signals of less than 1 nε could likely be characterized with these instruments.

They are designed to be grouted in place, so the bottom of the bore cannot be used for injection or monitoring. The completion can include a well screen for access to the formation and fluid pressure monitoring above the grouted instrument, however. As a result, it seems feasible to include a grouted strainmeter in the bottom of wells that are used to monitor fluid pressure or water composition in a CO_2 storage project. Grouting in place increases costs because instruments must be dedicated to a particular location, and maintenance is difficult.

Grouted strainmeters are the most cumbersome and expensive to deploy, but they can provide multiple components of the highest resolution strain data. This is the most likely instrument to be able to detect strains associated with injection, so it would have applications a larger lateral distances, or further above the injection formation than the portable instruments.

Application The three classes of instruments that are currently available have their own application niche, and a full complement of monitoring could include all of them. The WIRE system is the best suited to monitoring deformation of the injection well itself, although it currently requires installation during completion of the well. Portable strainmeters are best suited to preliminary testing of the injection well, and to applications in monitoring wells in the vicinity of the injection well. Grouted strainmeters are best suited to deployment further away from the injection well where strains will be small.

An opportunity to advance the application is to combine the strengths of the different classes of instruments. For example, it could be feasible to increase the resolution of the portable instruments so they rival that of grouted strainmeters. Alternatively, it could be feasible to reduce the cost and complexity of the grouted strainmeters so they could be included as a routine component of monitoring wells.

1.7 PRODUCTS

1.7.1 THESES

Glenn Skawski (MS) 2012. *Hydromechanical Well Testing Using a 3D Optical Fiber Extensometer*, Clemson University.

Alex Hanna (MS) 2015. *Stochastic optimization as a site assessment and monitoring tool during carbon storage projects*, Clemson University.

1.7.2 PAPERS

Kim, S., L.C. Murdoch, and L.N. Germanovich, (2015). Feasibility of using in situ deformation measurements during CO_2 storage. *International Journal of Greenhouse Gas Control*, in preparation.

Murdoch, L.C., G. Skawski, J. Ebenhack, and D. Hisz, (2015). A 3D fiber optic borehole extensometer for in situ well testing. *International Journal of Rock Mechanics*, in preparation.

Murdoch, L.C., S. Kim, and L.N. Germanovich. (2015). Deformation in the vicinity of an injection well. *Journal of Hydrology*, in preparation.

Hanna, A.C., S.M.J. Moysey and L.C. Murdoch, (2015). Development of a parallelized framework for multiobjective optimization of geologic systems, *Computers and Geosciences*, in preparation.

Hanna, A.C., S.M.J. Moysey and L.C. Murdoch, (2015). Numerical proof-of-feasibility of using geomechanical measurements to estimate poroelastic parameters, *Geomechanics for Energy and the Environment*, in preparation.

1.7.3 CONFERENCE PRESENTATIONS AND ABSTRACTS

Baldwin, J. and L.C. Murdoch, (2013). Quantifying radial borehole deformation during well tests. 21st Clemson Hydrogeology Symposium, Clemson, SC, April 4, 2013.

Freeman, C. and L.C. Murdoch. (2012). Estimating changes in water content from displacement measurements. 20th Clemson Hydrogeology Symposium, Clemson, SC, April 12, 2012.

Hanna, A.C., S.M.J. Moysey and L.C. Murdoch, (2014). Evaluation of the potential for geomechanical monitoring and stochastic calibration methods to improve characterization during geologic carbon storage, Abstract H23O-04. 2014 Fall Meeting of the American Geophysical Union, San Francisco, CA, Dec. 15-19, 2014.

Hanna, A.C., S.M.J. Moysey and L.C. Murdoch, (2015). Using geomechanical measurements for subsurface characterization, 23rd Clemson Hydrogeology Symposium, Clemson, SC, March 28, 2015.

Hanna, A.C., S. Moysey, and L.C. Murdoch, (2014). Stochastic parameter optimization of poroelastic systems. 22nd Clemson Hydrogeology Symposium, Clemson, SC, April 3, 2014.

Hisz, D., J. Ebenhack, L.N. Germanovich, and L.C. Murdoch, (2010). Characterization of Fractured Rock during Well Tests using Tilt-X, a Portable Tiltmeter and Extensometer for Multi-Component Deformation measurements. 2010 Fall Meeting of the American Geophysical Union, San Francisco, CA, Dec. 13-17, 2010.

Hisz, D. and L.C. Murdoch, (2012). Characterizing the hydromechanical response of a fracture under pumping and ambient stresses. 20th Clemson Hydrogeology Symposium, Clemson, SC, April 12, 2012.

Hisz, D. and L.C. Murdoch, (2013). Ambient Deformation of Permeable Fractures. 21st Clemson Hydrogeology Symposium, Clemson, SC, April 4, 2013.

Kim, S., L.C. Murdoch, L.N. Germanovich, S.M. Moysey, G.M. Skawski, J. Ebenhack, J. Smith, and C. Ozan, (2012). Using wellbore deformation as a diagnostic tool during CO2 sequestration. 2012 Fall Meeting of the American Geophysical Union, San Francisco, CA, Dec. 3-7, 2012.

Murdoch, L.C., (2012). Proof-of-Feasibility of Using Well bore Deformation as a Diagnostic Tool to Improve CO2 Sequestration, Project Status. DOE Carbon Storage R&D Project Review Meeting, Pittsburg, PA.

Murdoch, L.C., (2013). Proof-of-Feasibility of Using Well bore Deformation as a Diagnostic Tool to Improve CO2 Sequestration, Project Status. DOE Carbon Storage R&D Project Review Meeting, Pittsburg, PA.

Murdoch, L.C., (2011). Feasibility of Using Casing Deformation as a Diagnostic Tool During Injection of CO2. 19th Clemson Hydrogeology Symposium, Clemson, SC, April 7, 2011.

Murdoch, L.C., S. Kim, S.M. Moysey, J. Ebenhack, G. Skawski, D. Hisz, and L.N. Germanovich, (2012). Wellbore deformation as a monitoring and assessment tool during CO2 sequestration. Geological Society of America Annual Meeting, Charlotte, NC, Nov. 4-7, 2012.

Skawski, G. and L.C. Murdoch, (2012). Hydromechanical well testing using a 3D fiber optic extensometer. 20th Clemson Hydrogeology Symposium, Clemson, SC, April 12, 2012.

Skawski, G., M.T. Tokunaga, Y. Ito, K. Mogi, A. Cho, L.N. Germanovich, D. Hisz, J. Ebenhack, H.F. Wang, and L.C. Murdoch, (2011). Development of a 3D FBG extensometer for hydromechanical well testing. 2011 Fall Meeting of the American Geophysical Union, San Francisco, CA, Dec. 2011.

1.7.4 OTHER PRODUCTS

Poroelastic Properties Database. This is to our knowledge the most comprehensive compilation of poroealastic properties publically available. A copy the database is included in Chapter Two. We plan to make this database available on line.

Stochastic Optimization Database: Uses a relational database architecture to interface with our object-oriented optimization code, and efficiently store complex data structures including large numbers of poroelastic function evaluations.

Downhole Instruments, 3DX and 5DX. These are state of the art downhole tools for measuring

in situ deformation. They use optical fiber strain gauges arranged around a flexure to characterize displacements in 3D. The ability to measure 3D displacements with a compact tool using optical fibers has many potential applications. These instruments were developed and tested as part of this project.

Stochastic Optimization Engine (SOE) – a software package for integrating multiple stochastic optimization algorithms within a powerful and generalized sampling framework. The software uses gradient descent, Markov chain Monte Carlo, and multiple Genetic Algorithms, in a manner that allows for information sharing between algorithms. The result is a hybrid optimization tool that is capable of leveraging the strengths from many different techniques to perform well under many different problem settings. We used it to invert hydromechanical problems, but it is applicable to general optimization applications. Versions of the code have been developed in MATLAB and Python, and are available on request. We plan to publish the code after additional testing and refinement.

Simulation Files. The COMSOL and ABAQUS model files developed for this project are available by request to the PI. Many of the files were made available at http://www.clemson.edu/ces/ hydromodelgallery/, but this site is under revision and currently unavailable.

1.8 REFERENCES

Bai, M. and D. Elsworth, (2000). Coupled Processes in Subsurface Deformation, Flow and Transport. Reston, Va, ASCE.

Baker Hughes, (2009). Shell and Baker Hughes pioneer real-time compaction imaging system. http://www.epmag.com/WebOnly2009/item45985.php; also http://www.oilonline.com /News/NewsArticles/UnconventionalResources/articleType/ArticleView/articleId/22162/Monitoring-stress-levels.aspx

Birkholzer, J.T. and Q. Zhou, (2009). Basin-scale hydrogeologic impacts of CO2 storage: Capacity and regulatory implications. *International Journal of Greenhouse Gas Control* 3(6): 745-756.

Birkholzer, J.T., Q. Zhou, and C.-F. Tsang (2009). Large-scale impact of CO2 storage in deep saline aquifers: A sensitivity study on pressure response in stratified systems. *International Journal of Greenhouse Gas Control* 3(2): 181-194.

Bruno, M.S., (1990). Subsidence-induced well failure, Ventura, CA, USA, Published by the Society of Petroleum Engineers of AIME.

Cappa, F., Y. Guglielmi, P. Fenart, V. Merrien-Soukatchoff, and A. Thoraval, (2005). Hydromechanical interactions in a fractured carbonate reservoir inferred from hydraulic and mechanical measurements. *International Journal of Rock Mechanics and Mining Sciences* 42(2): 287-306.

Cappa, F., Y. Guglielmi, S. Gaffet, H. Lancon, and I. Lamarque, (2006). Use of in situ fiber optic sensors to characterize highly heterogeneous elastic displacement fields in fractured rocks. International *Journal of Rock Mechanics and Mining Sciences* 43(4): 647-654.

Cappa, F., Y. Guglielmi, J. Rutqvist, C.-F. Tsang, and A. Thoraval, (2008). Estimation of fracture flow parameters through numerical analysis of hydromechanical pressure pulses. *Water Resources Research* 44(11).

Cappa, F., Y. Guglielmi, J. Rutqvist, C. F. Tsang, and A. Thoraval, (2006). Hydromechanical modelling of pulse tests that measure fluid pressure and fracture normal displacement at the Coaraze Laboratory site, France. *International Journal of Rock Mechanics and Mining Sciences* 43(7): 1062-1082.

Cheung, S.H., and J.L. Beck, (2009). Bayesian model updating using Hybrid Monte Carlo simulation with application to structural dynamic models with many uncertain parameters, *Journal of Engineering Mechanics-ASCE*, 135(4): 243-255.

Dusseault, M.B., M.S. Bruno and J. Barrera, (1998). Casing shear: Causes, cases, cures, Beijing, China, Soc Pet Eng (SPE).

Dusseault, M.B., H. Han, B. Xu, and B. Peng, (2006). Simulation on tectonic deformation and large area casing shear mechanisms - Part A: Operations (SPE100360), Vienna, Austria, Society of Petroleum Engineers.

Hisz, D., J. Ebenhack, G. Alapatt, and L.C. Murdoch, (2009). Hydromechanical well tests in dipping fractured clastic rock, Newark Basin, New Jersey. 17th Clemson Hydrogeology Symposium, Clemson, SC, April 2, 2009.

Hisz, D., J. Ebenhack, T.J. Burbey, L.N. Germanovich, and L.C. Murdoch, (2009). Multi-Component Deformation of a Dipping Fracture Zone during a Well Test. *Eos Trans. AGU*, 90(52), Fall Meet. Suppl., Abstract N: H21C-0851.

Gamerman, D., and H.F. Lopes, (2006). *Markov Chain Monte Carlo: Stochastic Simulation for Bayesian Inference*, Chapman & Hall/CRC, Boca Raton, FL, pp.329.

Guglielmi, Y., F. Cappa, J. Virieux, J. Rutqvist, C.-F. Tsang and A. Thoraval, (2008). *A new in-situ approach for hydromechanical characterization of mesoscale fractures: The High-pulse poroelasticity protocol (HPPP)*. Omnipress, San Francisco, CA.

Horne, R, (1995). *Modern Well Test Analysis: A Computer-Aided Approach*. PetroWay, 257 p.

Mosegaard, K., and A. Tarantola, (1995). Monte Carlo sampling of solutions to inverse problems. *Journal of Geophysical Research*, 100(12): 431-12,447.

Murdoch, L.C. and L.N. Germanovich, (2006). Analysis of a deformable fracture in a permeable material. *International Journal of Numerical and Analytical Methods in Geomechanics*, 30:529-561.

Murdoch, L.C. (2010). Emerging Applications for Hydromechanics. 18th Clemson Hydrogeology Symposium, Clemson, SC, April 1, 2010.

Murdoch, L.C., D.B. Hisz, J.F. Ebenhack, D.E. Fowler, C. R. Tiedeman, L. N. Germanovich, (2009). Analysis of Hydromechanical Well Tests in Fractured Sedimentary Rock at the NAWC Site, New Jersey. Asheville 2009, the 43rd US Rock Mechanics Symposium and 4th U.S.-Canada Rock Mechanics Symposium, held in Asheville, NC June 28th – July 1, 2009, 8 p.

Murdoch, L.C., T. Schweisinger, and C.O. Huey Jr., (2005). Device to measure axial displacement in a borehole, US Patent Application 20050120576, filed June 9, 2005

Rutqvist, J., D. Barr, R. Datta, A. Gens, A. Millard, S. Olivella, C.F. Tsang, and Y. Tsang, (2005). Coupled thermal-hydrological-mechanical analyses of the Yucca Mountain Drift Scale Test - Comparison of field measurements to predictions of four different numerical models. *International Journal of Rock Mechanics and Mining Sciences* 42(5-6 SPEC. ISS.): 680-697.

Rutqvist, J., J. Birkholzer, F. Cappa, and C.F. Tsang, (2007). Estimating maximum sustainable injection pressure during geological sequestration of CO_2 using coupled fluid flow and geomechanical fault-slip analysis. *Energy Conversion and Management* 48(6): 1798-1807.

Rutqvist, J., J. Birkholzer, F. Cappa, and C.F. Tsang, (2007). Estimating maximum sustainable injection pressure during geological sequestration of CO_2 using coupled fluid flow and geomechanical fault-slip analysis. *Energy Conversion and Management* 48(6): 1798-807.

Rutqvist, J., J.T. Birkholzer, and C.-F. Tsang, (2008). Coupled reservoir-geomechanical analysis of the potential for tensile and shear failure associated with CO_2 injection in multilayered reservoir-caprock systems. *International Journal of Rock Mechanics and Mining Sciences* 45(2): 132-143.

Rutqvist, J. and O. Stephansson, (2003). The role of hydromechanical coupling in fractured rock engineering. *Hydrogeology Journal* 11(1): 7-40

Schweisinger, T., L.C. Murdoch, and C.O. Huey, (2007). Design of a removeable borehole extensometer. *Journal of Geotechnical Measurement* 30(3): 202-211.

Schweisinger,T., E. Svenson, and L.C. Murdoch, (2005). Transient changes in fracture aperture during hydraulic well tests in fractured gneiss. *Proceedings Georgia Water Resources Conference*, ed. K.J. Hatcher. April 25-27, 2005. University of Georgia. 4 pages.

Schweisinger, T., E.J. Svenson, and L.C. Murdoch, (2009). Introduction to hydromechanical well tests in fractured rock aquifers. *Ground Water* 47(1): 69-79.

Schiozer, D.J., E.L. Ligero, C. Maschio, and F.V.A. Risso, (2008). Risk assessment of petroleum fields - Use of numerical simulation and proxy models, *Petroleum Science and Technology*, 26: 1247-1266.

Subbey, S., M. Christie, and M. Sambridge, 2004. Prediction under uncertainty in reservoir modeling, *Journal of Petroleum Science and Engineering*, 44, 143-153.

Svenson, E. T. Schweisinger, L.C. Murdoch, 2008. Field evaluation of the hydromechanical behavior of flat-lying fractures during slug tests. *Journal of Hydrology* 359(1-2): 30-45.

Svenson, E., T. Schweisinger, and L.C. Murdoch, 2007. Analysis of the hydromechanical response of a flat-lying fracture to a slug test. *Journal of Hydrology* 347: 35-47

Tsang, C.-F., J. Birkholzer, and J. Rutqvist, 2008. A comparative review of hydrologic issues involved in geologic storage of CO2 and injection disposal of liquid waste. *Environmental Geology* 54(8): 1723-1737.

Vasco, D. W., 2004. Estimation of flow properties using surface deformation and head data: A trajectory-based approach. *Water Resources Research* 40(10): W10104-1-W10104-14.

Vasco, D.W., K. Karasaki, and C. Doughty, 2000. Using surface deformation to image reservoir dynamics. *Geophysics* 65(1): 132-147.

Vasco, D.W., K. Karasaki, and K. Kishida, 2001. A coupled inversion of pressure and surface displacement. *Water Resources Research* 37(12): 3071-3089.

Vasco, D.W., K. Karasaki, and L. Myer, 1998. Monitoring of fluid injection and soil consolidation using surface tilt measurements. *Journal of Geotechnical and Geoenvironmental Engineering* 124(1): 29-37.

Vrugt, J.A., C.J.F. ter Braak, M.P. Clark, J.M. Hyman, and B.A. Robinson, 2008. Treatment of input uncertainty in hydrologic modeling: Doing hydrology backward with Markov chain Monte Carlo simulation, *Water Resources Research* 44: W00B09, doi:10.1029/2007WR006720.

Vrugt, J.A., C.J.F. ter Braak, C.G.H. Diks, D. Higdon, B.A. Robinson, and J.M. Hyman, 2009. Accelerating Markov chain Monte Carlo simulation by differential evolution with self-adaptive randomized subspace sampling, *International Journal of Nonlinear Sciences and Numerical Simulation*, 10(3), 273-290.

Wang, H.F, 2000. *Theory of Linear Poroelasticity with Applications to Geomechanics and Hydrogeology*. Princeton University Press, 285 p.

CHAPTER TWO
SIMULATIONS

CONTENTS

CHAPTER TWO
SIMULATIONS

The objective of this chapter is to estimate the magnitude and pattern of deformation associated with injecting fluid into reservoir. These estimates will be a cornerstone in the evaluation of the feasibility of measuring deformation in situ using instrumentation described in Chapter Four. This chapter also includes an evaluation of methods for calculating deformation using analytical and numerical methods. These exercises validate the estimates of magnitude and pattern, but they also will be the basis of forward models used in the inverse analyses described in Chapter Three.

This main content of this chapter is broken into six subsections. Section 2.1 describes scaling analyses applied to deformation during well testing or reservoir depletion. Section 2.2 evaluates numerical codes and uses the results of those codes to characterize the deformation in several idealized example problems. Section 2.3 examines deformation in the vicinity of an injection well, and Section 2.4 looks at the impact of varying material properties of the reservoir. Section 2.5 evaluates effects of aquifer heterogeneities, and Section 2.6 focuses on evaluating deformation of the wellbore.

2.1 SCALING ANALYSES

Conventional analyses of well tests assume fluid pressures evolve as a diffusive process, which give rise to scalings of length and time that provide important fundamental insights into how well tests behave and how they should be interpreted. Full coupling between fluid flow and deformation may invalidate the conventional scaling, so poroelastic analyses of well tests currently must be performed on a case-by-case basis. The objective of this task is to use scaling analyses to identify the appropriate length and time scales control near- and far-field poroelastic deformation during well tests. It is important to evaluate the feasibility of obtaining analytical solutions to critical problems, such as constant-rate or pulse injections. Solutions derived using asymptotic methods, integral transforms, or other appropriate mathematical techniques are used to identify fundamental processes related to the poroelastic process and borehole deformation.

2.1.1 APPROACH

The approach we have taken is to first evaluate the deformation of a thin reservoir of finite or infinite extend during pumping or injection. The analysis focused on deriving an expression for compressibility, as well as displacement and stresses as functions of time and space. The reservoir is modeled as a poroelastic inclusion in elastic body (bounded or unbounded) or as an interface between two elastic half-spaces. In the latter case, the constitutive relationship for the reservoir is approximated by the Winkler's hypothesis, which is asymptotically accurate for a relatively soft layer material (compared to the half-spaces). Based on this, the problem is reduced to an integral equation for the normal displacement of the half-space surface (or the reservoir boundary) as a result of injection and deformation. The cases of radial symmetry and plain strain are considered to simulate CO_2 injection in the horizontal reservoir via a vertical or horizontal boreholes, respectively.

2.1.2 RESULTS: POROELASTIC HALF SPACE

Considering local half-thickness change being equal to the non-local displacement response of the half-space surface (Figure 2.1-1) gives:

$$C(\rho,\tau)\frac{\partial P(\rho,\tau)}{\partial \tau}=\varepsilon\int_0^1[1+C(\eta,\tau)]K_1(\rho,\eta)\frac{\partial P(\eta,\tau)}{\partial \tau}d\eta\,,\ K_1(\rho,\eta)=\frac{\eta}{\eta+\rho}K\left(\frac{2\sqrt{\eta\rho}}{\eta+\rho}\right) \quad (2.1\text{-}1)$$

where $C_f = dv/dp$ is the apparent hydraulic compliance, v is displacement normal to the layer, $\rho = r/a$ is the dimensionless radial coordinate, $\tau = tD/a^2$ is the dimensionless time with D the hydraulic diffusivity of the layer, $\partial P/\partial\tau$ is the (arbitrary) rate of pressure change in the layer, $\varepsilon = 4(1-\upsilon^2)a/(C_n\pi E)$ is the small parameter, υ is the Poisson's ratio, E is the Young's modulus, a is the radial dimension of the permeable layer, $C = C_f/(C_n\varphi)$, C_n is the layer normal compressibility, φ is the layer porosity, and $K(x)$ is the complete elliptic integral of the first kind. Here pressure p has been normalized as $P = p/p_1$ with $p_1 = q/(\pi D c_r \rho_r)$ and q being the volume of liquid injected per unit length of the line source (borehole) per unit time.

Equation (2.1-1) is a non-homogeneous Fredholm integral equation of the second kind with respect to the unknown function $A_n(\rho,\tau) = C\partial P/\partial\tau$. The kernel of this equation is square integrable, and therefore, the equation has a solution. When parameter ε is sufficiently small, we further used the Banah fixed point theorem and obtained a closed-form (and unique) solution in the form of rapidly converging Neumann series of the powers of ε. Because the terms in this converging series alternate their sign, the error of the truncated series does not exceed the first omitted term. We, therefore, kept only the first term, but controlled the error with an acceptable accuracy for scaling considerations.

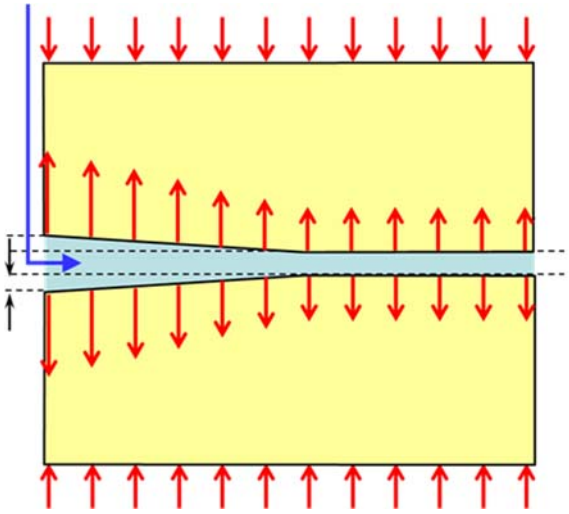

Figure 2.1-1. Geometry of the problem under consideration.

The compressibility is the derivative of volumetric strain as a function of pressure. The analysis gives a remarkably compact expression for transient compressibility as:

$$C \approx \alpha_n(\rho,\tau) = \varepsilon A_1(\rho,\tau)[\partial P(\rho,\tau)/\partial\tau]^{-1} \quad (2.1\text{-}2)$$

The scaling function A_1 on the right hand side is defined by:

$$A_1(\rho,\tau) = E(\rho) + \int_0^1 K_1(\rho,\eta)\partial P(\eta,\tau)/\partial\tau d\eta \quad (2.1\text{-}3)$$

where $E(\rho)$ is the complete elliptic integral of the second kind. For the pressure distribution $p(r, t)$ caused by a constant line source along the axis of a disk of radius a, expression:

$$\partial P / \partial \tau = 1 + \sum_{n=1}^{\infty} \exp(-\tau x_n^2) J_0(\rho x_n) J_0(x_n)^{-2} \qquad (2.1\text{-}4)$$

is obtained by differentiating the analytical expression given by Carslaw and Jaeger (1959), where $J_0(x)$ is the Bessel function of the first kind, and x_n is the n^{th} positive root of the Bessel function $J_1(x)$. In this case, the Neumann series converges for $\varepsilon < 0.572$.

Computing Eq. 2.1-2 as function of dimensionless time τ and radial distance ρ shows that compressibility changes with both time and location (Figures 2.1-2a and 2.1-2b). It increases sharply with radial distance at early times, and this effect diminishes with increasing time (Figure 2.1-2a). Compressibility increases with time early in the test and the rate of change diminishes at later times (Figure 2.1-2b).

The analysis developed thus far shows how compressibility changes with time and space, and we have extended this result to include displacement and strain. We have also obtained initial results for the case of the relatively rigid layer, which represents another asymptotic case compared to that of the soft layer. This is a new analysis that serves as an important benchmark for codes that seek to analyze deformation caused by injection into layers.

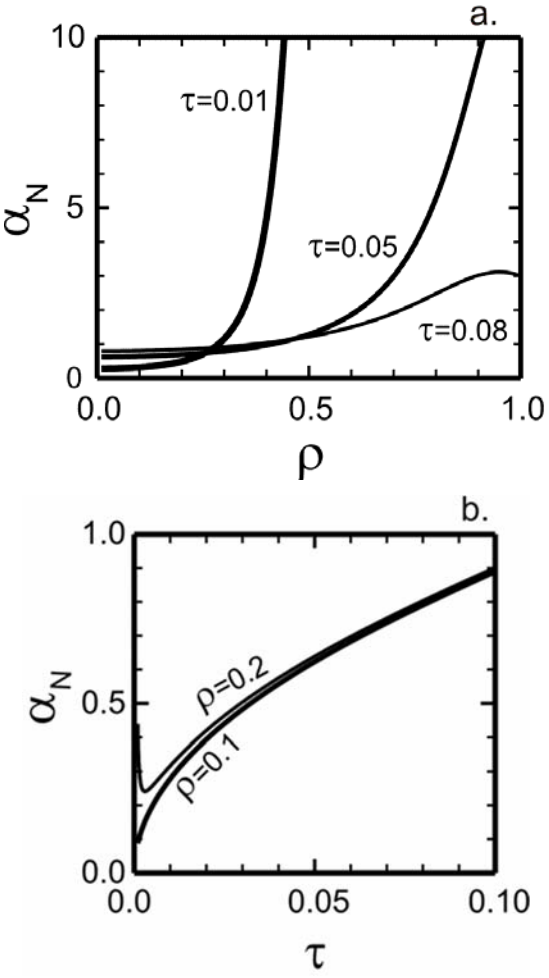

Figure 2.1-2. Dimensionless effective compressibility as (a.) a function of dimensionless radial distance (ρ =r/a) from well at three dimensionless times, and (b.) as function of dimensionless time at two dimensionless radial distances.

2.1.3 RESULTS: POROELASTIC RESERVOIR

The analysis described above considers an infinite space with the infinite layer, where the pressure distribution changes in a finite domain. In other words, the layer is mechanically infinite but hydraulically finite. We also considered a truly finite poroelastic reservoir (i.e., finite poroelastic mechanically and hydraulically) in an infinite space.

In many cases, a reservoir undergoing CO_2 injection is modeled as a thin poroelastic reservoir in an undrained poroelastic host rock (Figure 2.1-2a). The closed-form solutions for these types of problems are only available for a very few reservoir shapes (such as elliptical) and for homogeneous pressure distributions [e.g., *Berryman*, 1995; *Mura*, 1982]. If the reservoir shape is not elliptical and the pore pressure distribution is not uniform, a numerical method needs to be used. Modeling bodies with great difference in dimensions is often computationally difficult and time consuming, which often creates a challenge for inverse analysis (Task 3). Fortunately, instead of attempting to overcome this difficulty, one can take advantage of the

thinness of the reservoir and model a *thin* reservoir based on suitable asymptotic techniques [e.g., *Kanaun*, 1984a and 1984b; *Klarbring*, 1991; *Vil'chevskaya and Kanaun*, 1992; *Movchan and Movchan*, 1995; *Klarbring and Movchan*, 1998].

Let ε be a small parameter such that the top and bottom of the reservoir sides can be represented by $y = \pm h_{\pm}(x) = \pm \varepsilon H_{\pm}(x)$ $(0 < \varepsilon << 1)$, where the given functions, $H_{\pm}(x)$, characterize the reservoir *shape*. The reservoir thickness $h(x) = h_{+}(x) + h_{-}(x) = \varepsilon H(x)$, where $H(x) = H_{+}(x) + H_{-}(x)$ is the (known) thickness of the reference reservoir ($\varepsilon = 1$). For example, $\varepsilon = \max[h(x)/(2c)]$. Then, the domain occupied by the reservoir is $\Omega_{\varepsilon}^{1} = \{|x| < c, -h_{-}(x) < y < h_{+}(x)\}$. The reservoir, Ω_{ε}^{1}, and host rock, Ω_{ε}^{2}, domains have the common boundary, $\partial\Omega_{\varepsilon}^{1} = \{|x| < c, y = \pm h_{\pm}(x)\}$ (Figure 2.1-3a). The body, $\Omega_{\varepsilon} = \Omega_{\varepsilon}^{1} \cup \Omega_{\varepsilon}^{2}$, under consideration can be infinite, semi-infinite, or finite.

In the spirit of perturbation analysis, the solution inside and outside the reservoir domain is represented as a series of powers of the small parameter ε. The asymptotic representations of displacements can be chosen in the form of [*Movchan and Nazarov*, 1987]

$$u_i(\varepsilon, x, y) = v_i^{(0)} + \varepsilon v_i^{(1)} + \varepsilon^2 v_i^{(2)} + \ldots \quad (i = x, y) \tag{2.1-5}$$

where $v_i^{(k)} = v_i^{(k)}(x, y)$ $(k = 0, 1, 2, \ldots)$ outside the reservoir and $v_i^{(k)} = v_i^{(k)}(x, z)$ $(k = 0, 1, 2, \ldots)$ inside. Here

$$z(x, y) = \frac{2y + h_{-}(x) - h_{+}(x)}{2h(x)} \qquad (x, y) \in \Omega_{\varepsilon}^{1} \tag{2.1-6}$$

is a scaled (stretched), local coordinate (Figure 2.1-3c). The advantage of using Eq. 2.1-5 is that unknown functions, $v_i^{(k)}(x, y)$ $(k = 0, 1, 2, \ldots)$, outside the reservoir are defined in the plane with a mathematical cut (discontinuity), $L = L_{+} \cup L_{-} = \{|x| < c, y = \pm 0\}$ (Figure 2.1-3b) while inside the reservoir, functions $v_i^{(k)}(x, z)$ $(k = 0, 1, 2, \ldots)$, are defined in a rectangular region, $\Omega_z^{1} = \{x < |c|, |z| < ½\}$, which is independent of ε (Figure 2.1-3c).

The asymptotic procedure consists in substituting the expansion shown in Eq. 2.1-5, and a similar expansion for pore pressure, into the boundary value problem of interest (Figure 2.1-3a), collecting terms of the same orders with respect to ε, and formulating and solving in each order the corresponding auxiliary boundary problem. The external and internal problems for $v_i^{(k)}(x, y)$ are connected through the continuity boundary conditions for displacements and tractions generated on the reservoir boundary, $\partial\Omega_{\varepsilon}^{1}$, from the sides of reservoir and host rock, respectively. The solution in each order is defined by the solution in the previous order, with zero order being the solution for a continuous host rock body without the reservoir present. This establishes the asymptotic recurrence sequence. After functions $v_i^{(k)}(x, y)$ are determined, the sought displacements can be computed directly from Eqs. 2.1-5 and 2.1-6. Then, calculating the respective stresses represents no difficulty [e.g., *Muskhelishvili*, 1953].

In the case of CO_2 injection in a finite reservoir, we are interested in displacement and stress changes (increments) caused by the pressure change p in the reservoir. For simplicity and because the reservoir is thin we assume that p(x) is a function of x only. The outer boundary conditions (e.g., on remote boundaries) do not change, so that the zero order terms in Eq. 2.1-5

nullify outside the reservoir. In the first order with respect to ε, the conditions on L in the external problem can then be written as:

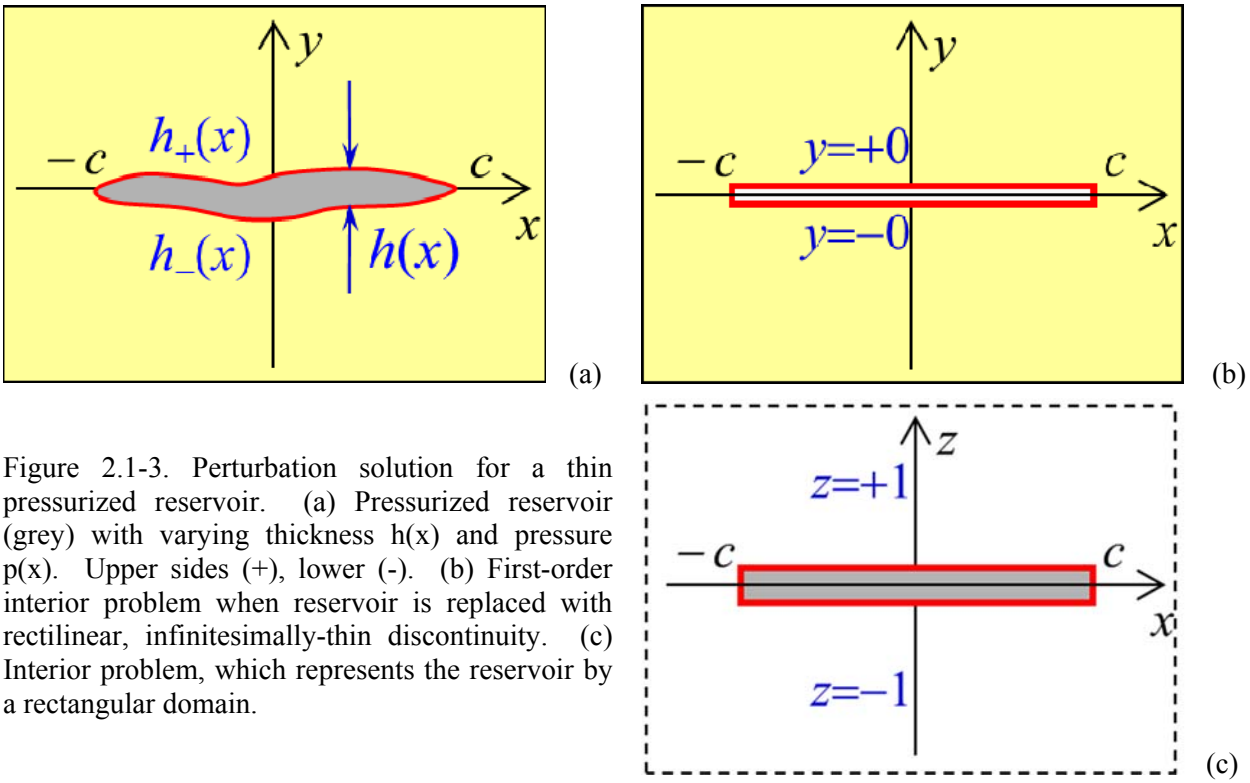

Figure 2.1-3. Perturbation solution for a thin pressurized reservoir. (a) Pressurized reservoir (grey) with varying thickness h(x) and pressure p(x). Upper sides (+), lower (-). (b) First-order interior problem when reservoir is replaced with rectilinear, infinitesimally-thin discontinuity. (c) Interior problem, which represents the reservoir by a rectangular domain.

$$u_x^+(x) - u_x^-(x) = 0, \qquad u_y^+(x) - u_y^-(x) = \frac{h(x)}{\lambda + 2\mu}\alpha p(x) \tag{2.1-7}$$

for displacements and:

$$\sigma_{yy}^+(x) - \sigma_{yy}^-(x) = 0, \qquad \tau_{yy}^+(x) - \tau_{yy}^-(x) = \frac{2\mu\alpha}{\lambda + 2\mu}\frac{\partial}{\partial x}[h(x)p(x)] \tag{2.1-8}$$

for stresses, where λ and μ are the Lame constants of the reservoir material, α is the Biot poroelastic coefficient of the reservoir material, and indices "+" and "-" mark the values of the corresponding functions on L for $y = +0$ and $y = -0$, respectively (Figure 2.1-3c).

As can be seen from Eq. 2.1-7, the normal component of displacement field is discontinuous on L and, therefore, L can be visualized as a 'crack' loaded by normal, σ_{yy}, and shear, τ_{xy}, tractions. According to Eq. 2.1-8, the normal tractions are continuous on L while the shear tractions are discontinuous. The external first-order problem, therefore, is completely defined by conditions Eqs. 2.1-7 and 2.1-8 on L and zero values at infinity [e.g., *Muskhelishvili*, 1953].

Solutions for 'cracks' are generally much simpler than for 'inclusions', and powerful mathematical techniques are available. Some conclusions can be derived, however, even without

explicitly solving the problem. For example, for thin reservoirs, the stress increments inside the reservoir (caused by the pressure increment p due to the CO_2 injection) are given by:

$$\tau_{xy} = 0, \quad \sigma_{yy} = 0, \quad \sigma_{xx} = -\frac{1-2\upsilon}{1-\upsilon}\alpha p(x) \tag{2.1-9}$$

in the zeroth order and by:

$$\begin{cases} \sigma_{xx}(x,z) = \dfrac{\lambda}{\lambda+2\mu}[\sigma_{yy}(x,0) - \alpha p(x)] + 4\mu\dfrac{\lambda+\mu}{\lambda+2\mu}\dfrac{\partial u_x(x,0)}{\partial x} = O(1) \\ \sigma_{yy}(x,z) = \sigma_{yy}^{+}(x,0) = \sigma_{yy}^{-}(x,0) = O(\varepsilon) \\ \tau_{xy}(x,z) = \dfrac{\mu\alpha}{\lambda+2\mu}\left\{2zh(x)\dfrac{\partial p(x)}{\partial x} - \dfrac{\partial[h_+(x) - h_+(x)]}{\partial x}p(x)\right\} = O(\varepsilon) \end{cases} \tag{2.1-10}$$

when the first order terms are also kept. Similarly, keeping the first order terms and using Eqs. 2.1-7 and 2.1-8, results in displacement increments:

$$\begin{cases} u_y(x,z) = u_y(x,0) + z\dfrac{h(x)}{\lambda+2\mu}\alpha p(x) \\ u_x(x,z) = u_x^{+}(x,0) = u_x^{-}(x,0) \end{cases} \tag{2.1-11}$$

inside the reservoir, which are caused by the same pressure change, p.

2.1.4 SIGNIFICANCE

Significance of Eqs. 2.1-8 through 2.1-11 is in their remarkably simple form, which allows fast analysis and benchmarking. For example, although Eq. 2.1-9 agrees with the Eshelby solution [e.g., *Segall and Fitzgerald*, 1998; *Rudnicki*, 1999], the important difference is that now p is not necessarily constant in the reservoir and the reservoir is not necessarily elliptical but can be of general shape.

Another example is given by a horizontal reservoir in a half space. Because the external problem is formulated on an infinitesimally this discontinuity (crack), its solution (including closed form) is readily available [e.g., *Dyskin et al*., 2000, and references therein] and provides displacements and stresses outside the reservoir. Eqs. 2.1-8 through 2.1-11 then immediately give displacement and stresses inside the reservoir.

In the previous analysis (Figure 2.1-1), we found $C_f = dv/dp$ by solving Eq. 2.1-1. Taking into account that in Eq. 2.1-1, $v = [u_y^{+} - u_y^{-}]/2$ with $u_y^{+} - u_y^{-}$ defined by Eq. 2.1-7, we immediately obtain that:

$$C_f = \frac{1}{2}\frac{h(x)}{\lambda + 2\mu}\alpha p(x) \qquad (2.1\text{-}12)$$

Hence, in a finite reservoir, the hydraulic compliance mimics the product of reservoir thickness and pore pressure distribution (at least not too close to the reservoir end).

Finally, it is also important that the analysis resulted in Eqs. 2.1-8 through 2.1-11 is applicable to both coupled and uncoupled poroelasticity. In fact an originally coupled problem becomes uncoupled in the first order. Furthermore, the external problem is purely elastic, so that the solution of the original poroelastic problem is reduced to the solution of elastic problem (at least, in the first order).

The analysis outlined above required considerable effort and the solution was developed only at the end of the project term, so we were unable to explore applications in this report. We envision that an important application of the solution described here will be in providing a fast preliminary analysis during inversion problems. This analysis will be several to many orders of magnitude faster than the numerical solution of fully coupled poroelastic problems, described in subsequent sections in this chapter. As a result, parameter space can be explored very quickly with analytical solution outlined above, which will trim the number of the more detailed, time consuming numerical analyses that will be required.

2.2 CODE EVALUATION AND EXAMPLE ANALYSES

The objective of this task was to evaluate and compare the capabilities and performance of numerical codes that can meet the needs of the project. This was accomplished by setting up several benchmark problems, solving the problems with several suitable codes and then comparing the results. The analysis required solving problems involving fully coupled poroelasticity. We selected COMSOL Multiphysics, ABAQUS, and FLAC as for evaluation because they are readily available codes that can solve problems in fully coupled poroelasticity.

Four benchmark problems were formulated with different degrees of complexity and designed to focus on different aspects of the project (Figure 2.2-1). All the problems consider fluid pressure and mechanical deformation. Example problem 1 is axisymmetric with a well injecting into a uniform aquifer at constant rate. The aquifer and well casing are the same material, so this problem would resemble injection into an open hole. Example problem 2 focused on the casing itself and evaluated how to characterize deformation of a cylindrical tube. Example problem 3 covered the close proximity of the well, including casing, cement and the enveloping formation. Problem 3 was a cylindrical region, but it was analyzed in 3D in order to evaluate effects of local perturbations, like perforations. Problem 4 was the most comprehensive benchmark, evaluating a casing in a formation extending out a radial distance of 30 km. This problem includes interaction at several important scales ranging from perforation (casing) to the entire formation and earth surface.

Example 1: Open borehole in regional aquifer

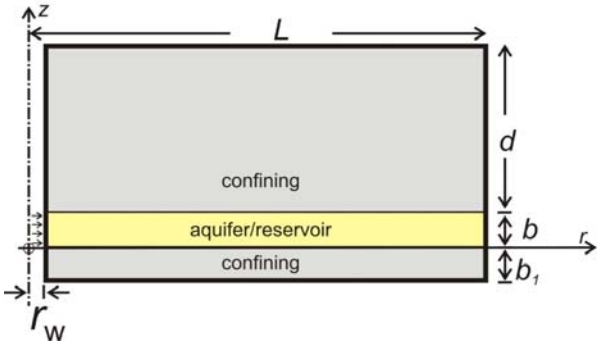

This problems considers flow and deformation of an idealized sand reservoir subjected to injection at constant rate. The borehole is represented as a quasi-open hole where the total stress equals the fluid pressure.

Example 2: Casing

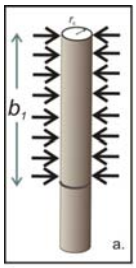

This problem considers the deformation of uniform cylindrical casing subjected to a uniform distributed load. Uniformly distributed compression is applied on the outside of the casing to represent the load on the casing during cementation.

Example 3: Well and Proximal Formation

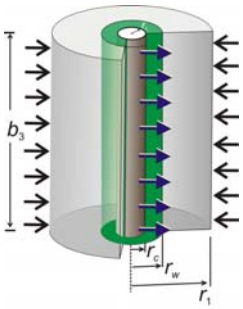

This problem considers steel casing or screen embedded in a porous medium representing the vicinity of the well. The porous medium includes a thin layer around the casing enveloped by uniform sand. Water is injected into the casing at a constant rate and there is negligible head loss along the casing itself over the length of the model. The outer boundary of the porous media is held at constant head.

Example 4: Cased well in uniform formation

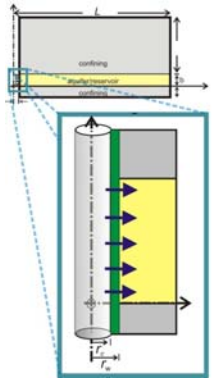

This problem considers deformation of a cased well in a uniform formation. The formation is characterized as in Example 1, and the casing is characterized as in Example 3.

Figure 2.2-1. Example problems related to deformation of wellbores.

Table 2.2-1. Variables and parameters used in the example analyses.

Parameter	Value
Well bore pressure	10^6 [Pa] (r = 0.1 m, 0 m < z < 100 m)
Bulk modulus of sandstone	10^{10} [Pa]
Bulk modulus of shale	10^9 [Pa]
Poisson's ratio of sandstone	0.25
Poisson's ratio of shale	0.25
Porosity of sandstone	0.2
Porosity of shale	0.2
Hydraulic conductivity of sandstone	10^{-6} [m/s]
Hydraulic conductivity of shale	10^{-12} [m/s]
Biot-Willis coefficient of sandstone	1
Biot-Willis coefficient of shale	1
Density of water	1000 [kg/m^3]
Viscosity of water	10^{-3} [Pa·s]
Bulk modulus of water	2.2x10^9 [Pa]

Table 2.2-2. Boundary conditions of example problem 1

Boundary		Fluid Flow	Elasticity
top (z = 1,100 m)		pore pressure = 0 (p = 0)	free (σ_{zz} = 0, τ_{rz} = 0)
bottom (z = -100 m)		impermeable	roller (u_z = 0, τ_{rz} = 0)
outer (r = 30,000 m)		pore pressure = 0 (p = 0)	roller (u_r = 0, τ_{rz} = 0)
inner (r = 0.1 m)	lower confinement (-100 m < z < 0 m)	impermeable	roller (u_r = 0, τ_{rz} = 0)
	sand aquifer (0 m < z < 100 m)	pore pressure = 1 MPa (p = 1 MPa)	Applied pressure = 1 MPa (σ_{rr} = p = 1 MPa, τ_{rz} = 0)
	upper confinement (100 m < z < 1,100 m)	impermeable	free (σ_{rr} = 0, τ_{rz} = 0)

2.2.1 EXAMPLE PROBLEM 1

This problem considers flow and deformation in the vicinity of a well in a circular aquifer bounded by no-flow conditions with a well at the center injecting at a specified hydraulic head (Figure 2.2-2).

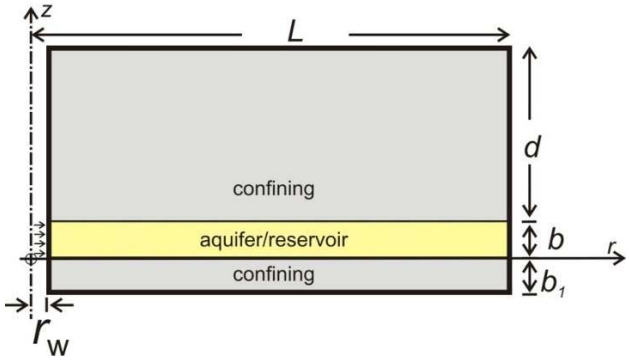

Figure 2.2-2. Geometric configuration of Example 1 in a cross-section view. Sand layer between $0 < z < 100$. $L = 30$ km, $d = 1$ km, $b = 100$ m, $b_1 = 100$ m.

Configuration

The aquifer is a layer of uniform thickness and properties. It is overlain by a uniform confining layer (1,000 m thick), and underlain by a 100 thick confining layer resting on impermeable basement rock. The well is a quasi-open hole (in that no flow is allowed in the confining layer, but it is allowed to deform) with uniform hydraulic head. Borehole radius is 0.1 m and the model boundary is at a radius of 30 km. The water is injected at constant head for 10^6 seconds and monitored for another 10^6 seconds during recovery (Table 2.2-2). Parameters used in the problem are given in Table 2.2-1.

Results: Pore Pressure

Pore pressure at the mid-height ($z = 50$ m) of the sand layer is close to a log-linear function of distance, according to both ABAQUS and COMSOL codes at $t = 10^6$ sec (Figure 2.2-3). The slope and intercept of the line varies slightly between the codes for $r < 100$ m, however, ranging from -104 kPa/m for COMSOL to 108 kPa/m for ABAQUS, a relative error of approximately 4%.

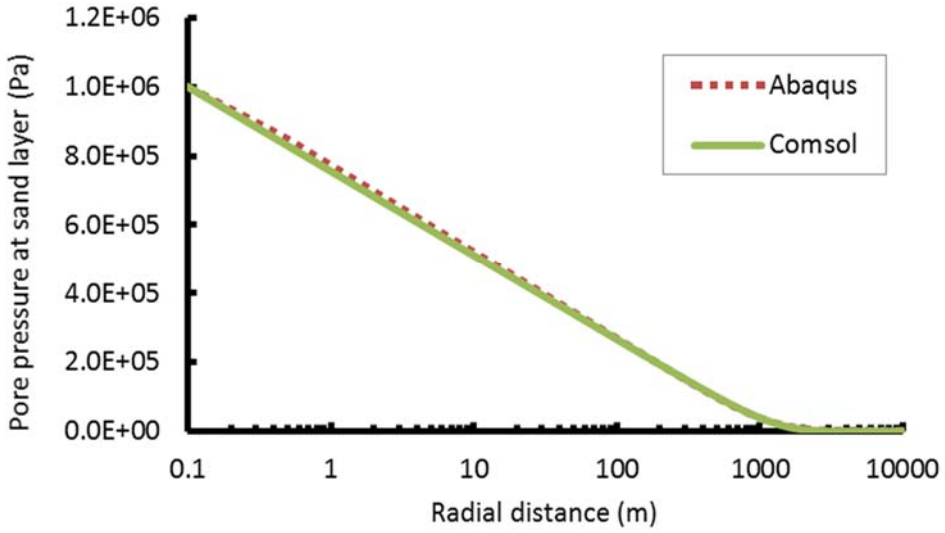

Figure 2.2-3. Pore pressure at time of 10^6 sec. Number of elements and run times are ABAQUS: 99,000 (3 hrs) and COMSOL: 153,336 (5 hrs).

This is a classic problem in well hydraulics where changes in fluid content are analyzed using compressibility, instead of using fully coupled poroelasticity as in this case. The distribution of pressure in the well hydraulics problem is a function of the log of the radius, which is consistent with Figure 2.2-3.

Results: Deformation

Radial and vertical displacements were used to evaluate deformation. Radial displacements were measured along horizontal, radial lines from the wellbore face outward. One line was at the center of the aquifer and the other was at the ground surface. At the end of the injection period ($t = 10^6$ sec), the radial displacement increased from the wellbore to a maximum of 1.1×10^{-3} m at $r \approx 1$ km. It decreased to approximately 2×10^{-4} m at $r = 10$ km (Figure 2.2-4a). The pattern of radial displacements along a parallel line at the ground surface is similar to the one through the aquifer, except the maximum displacement is less (3×10^{-4} m). Results from COMSOL and ABAQUS are within 1 percent of each other. The difference in two displacements diminishes with radial distance and both codes give similar results for $r > 5{,}000$ m.

Radial displacements along a vertical line on the wellbore face indicate magnitudes of approximately 1×10^{-5} m where the well intersects the aquifer and smaller displacements above and below the aquifer (Figure 2.2-4b). Displacements increases slightly from the middle of the aquifer to the upper or lower contact, with the maximum radial displacements occurring on the aquifer side of the contact in all cases. There are significant variations in the displacements at the upper contact, with oscillations predicted by all codes. The magnitude of the oscillation is greatest, but the extent of the oscillation is the least in the results from COMSOL. The COMSOL results predict displacements of -20 micron within less than 1m of the contact. The magnitude of the ABAQUS results are smaller but the extent is larger than the COMSOL results. Interestingly, displacements along the lower contact are relatively smooth compared to the upper contact.

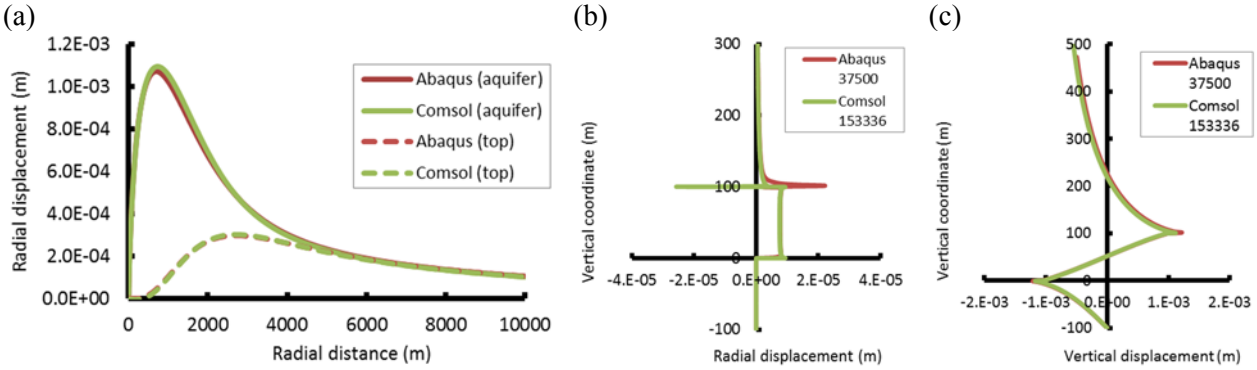

Figure 2.2-4. Displacements in the vicinity of the wellbore at $t = 10^6$ sec. (a) Radial displacement as a function of radial distance at $z = 50$ m (solid line) and $z = 1{,}100$ m (dashed and labeled "top" to indicate the line is at the ground surface. (b) Radial displacement as a function of vertical distance at $r = r_w$. (c) Vertical displacements as a function of vertical distance at $r = r_w$.

Vertical displacement along a vertical line on the wellbore face is shown in Figure 2.2-4c. Approximately in the middle of the aquifer ($z = 50$ m), the vertical displacement is zero and it increases to 1.2×10^{-3} at the top ($z = 100$ m), and decreases to -1.2×10^{-3} at the bottom of the aquifer ($z = 0$). In the upper confining layer, the vertical displacement decreases from the contact and reaches zero around $z = 220$ m, while in the lower confining layer the vertical displacement

increases from the contact and reaches to zero at the bottom of the simulation domain (z = -100 m). No significant error between two codes are observed in this profile.

The radial displacement changes sharply across the upper contact of the aquifer, z = 100 m, and the two codes give different results at this location (Figure 2.2-4b). This sharp change in displacement is a result of the abrupt change in material properties at the interface. This simulation assumes that the material properties are uniform in each layer, and the mesh is uniform across the boundary. In simulations not shown here we used a smoothed step function to change the material properties over a narrow band, and we used mesh elements that were smaller than the width of this band. This approach smoothed the change in displacement across the contact and decreased the difference between the codes. This type of tuning of the model will be needed to evaluate displacement across a contact when using the finite element codes we evaluated.

The ground surface moved down at $t = 10^6$ s by a maximum of approximately 8×10^{-4} m (Figure 2.2-5). The magnitude diminished with distance and it was approximately 10^{-6} m at r = 3000 m. Results from COMSOL and ABAQUS are within a few percent of each other.

The negative vertical displacements at the ground surface contrast with positive displacements along a radial line at the top of the aquifer—the aquifer is expanding vertically. This is effect is shown in Figure 2.2-4c, for example, where positive vertical displacements occur at the top of the aquifer, but the displacement goes to zero and it is negative above z = 220 m.

The difference in sign of displacements along the top and bottom of the upper confining layer was initially surprising. Upward displacement of the top of aquifer during injection was expected, but downward movement of the ground surface was unexpected. Nevertheless, this result was predicted by all codes. The explanation follows from radial displacements, which are positive within 1 km of the well at $t = 10^6$ s. Increasing radial displacement over r < 1 km causes a positive radial strain, or stretching. The Poisson ratio effect in elasticity causes displacements in one direction that are opposite in sign to displacements in a normal direction. Radial stretching shown in Figure 2.2-4a results in thinning of the confining unit through the Poisson ratio effect. It is worth pointing out that this effect is transient and continued injection causes upward displacement throughout the confining unit, including uplift at the ground surface. It may be possible to use this effect for a fast, robust, first-order evaluation of the sequestered CO_2 domain geometry during real field injections.

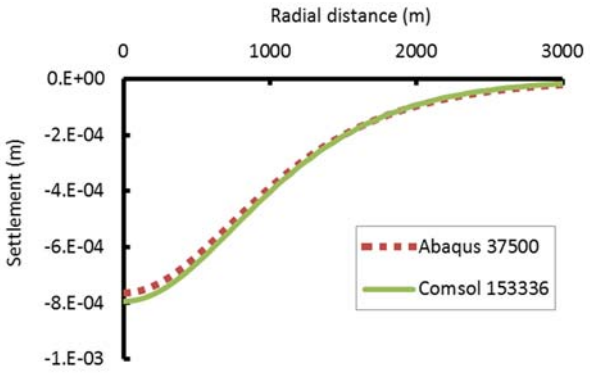

Figure 2.2-5. Vertical displacement at the ground surface after pumping for $t = 10^6$ sec.

2.2.2 EXAMPLE PROBLEM 2

This problem considers the deformation of uniform cylindrical casing subjected to distributed loads (Figure 2.2-6).

Configuration

We assume a uniformly distributed compression to represent the load on the outside of the casing. The load is distributed over a length b_1 of 8 m and the total length of the casing is 10 m (Figure 2.2-6). The bottom end of the casing is fixed and the top of it is unsupported. Compression on the outside of a casing could occur as a result of cementation. Parameters used in the analysis are in Table 2.2-1 and 2.2-3 and the boundary conditions are specified in Table 2.2-4. The radial displacements are summarized in Table 2.2-5.

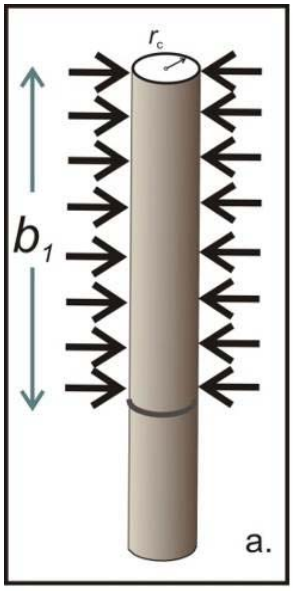

Figure 2.2-6. Uniformly loaded casing with a supported end.

Table 2.2-3. Fundamental elastic parameters for the casings (steel)

Parameter	Value
Inner radius of casing	0.1 [m]
Outer radius of casing	0.10813 [m]
Bulk modulus of casing material	6.67×10^{10} [Pa]
Poisson's ratio of casing material	0.25

Table 2.2-4. Boundary conditions of benchmark problem 2

Boundary		Condition
Top (z = 10 m)		free ($\sigma_{zz} = 0$, $\tau_{rz} = 0$)
Bottom (z = 0 m)		fixed ($u_r = 0$, $u_z = 0$)
outer (r = 0.10813 m)	lower support (0 m < z < 2 m)	fixed ($u_r = 0$, $u_z = 0$)
	upper pipe (2 m < z < 10 m)	applied pressure=10 MPa (σ_{rr} = 10 MPa, $\tau_{rz} = 0$)
inner (r = 0.1 m)	lower support (0 m < z < 2 m)	fixed ($u_r = 0$, $u_z = 0$)
	upper pipe (2 m < z < 10 m)	free ($\sigma_{rr} = 0$, $\tau_{rz} = 0$)

Table 2.2-5. Summary of radial displacement in various stress conditions. The negative sign denotes the contraction of pipe due to compressive loading.

	FLAC2D	ABAQUS	analytical solution
axisymmetry	-67.8 μm	-67.5 μm	N/A
plane stress	-67.7 μm	-67.5 μm	-67.5 μm
plane strain	-59.5 μm	-59.4 μm	-59.4 μm
3D	N/A	-67.4 μm	N/A

The analytical solution for radial displacement of an infinite thick-walled cylinder in a plane strain condition is [*Timoshenko and Goodier,* 1970]:

$$u_r(r) = -\frac{p}{2G}\left[\frac{1}{r_c^2} - \frac{1}{(r_c+w)^2}\right]^{-1}\left[(1-2\nu)\frac{r}{(r_c+w)^2} + \frac{1}{r}\right] \qquad (2.2\text{-}1)$$

where p is the applied pressure outside the cylinder (on the outer boundary $r = r_c + w$), r_c is the inside radius of the cylinder, w is the wall thickness of the cylinder, G is the shear modulus of steel and ν is the Poison's ratio of the steel. When we consider $r = r_c + w$, and the parameters in Tables 2.2-2 and 2.2-3, the radial displacement at the boundary is $u_r(r_c + w)$ = -59.4 μm, where the negative sign indicates radially inward displacement.

Radial displacement in plane stress is

$$u_r(r) = -\frac{p}{2G}\left[\frac{1}{r_c^2} - \frac{1}{(r_c+w)^2}\right]^{-1}\left(\frac{1-\nu}{1+\nu}\frac{r}{r_c^2} + \frac{1}{r}\right) \qquad (2.2\text{-}2)$$

The radial displacement for this problem is $u_r(r = r_c + w)$ = -67.5 μm for plane strain, according to Eq. 2.2-2 and the data in Tables 2.2-2 and 2.2-3.

The analytical solutions in Eqs. 2.2-1 and 2.2-2 were used to estimate the radial compliance of tubes for different geometries (Figure 2.2-7). The radial compliance is the displacement per unit pressure, which is the slope of the line in Figures 2.2-7a and 2.2-7b. We considered dimensions for 4-inch, 6-inch and 8-inch pipes in both schedule 40 and 80.

Results

In general, the compliance was smallest for the 4-inch pipe and it increased with diameter. The compliance of Schedule 40 pipes is greater than the thicker walled Schedule 80, although this difference is smaller than that caused by changing the diameter. Plane stress gives slightly larger compliance values than plane strain. In general, the compliance values for all pipes and conditions ranges from 3 to 14 microns/MPa (Figure 2.2-7).

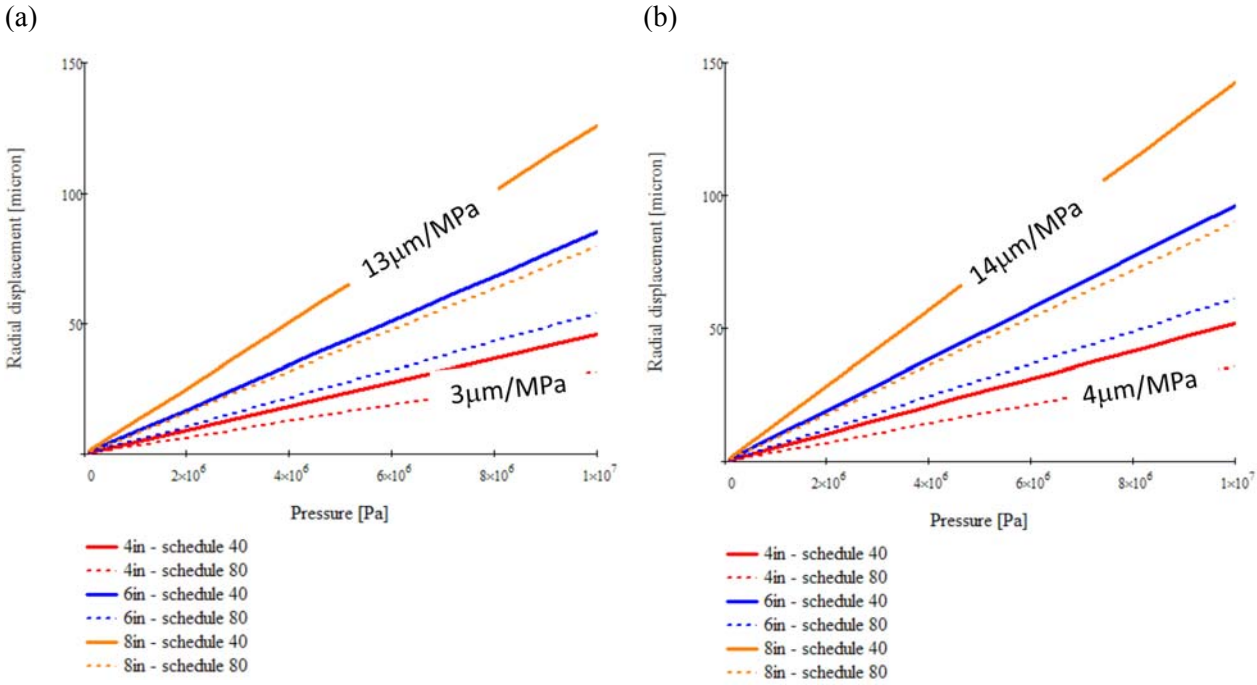

Figure 2.2-7. Radial displacement as a function of pressure for different sizes and schedules of pipe in (a) plane strain and (b) plane stress conditions.

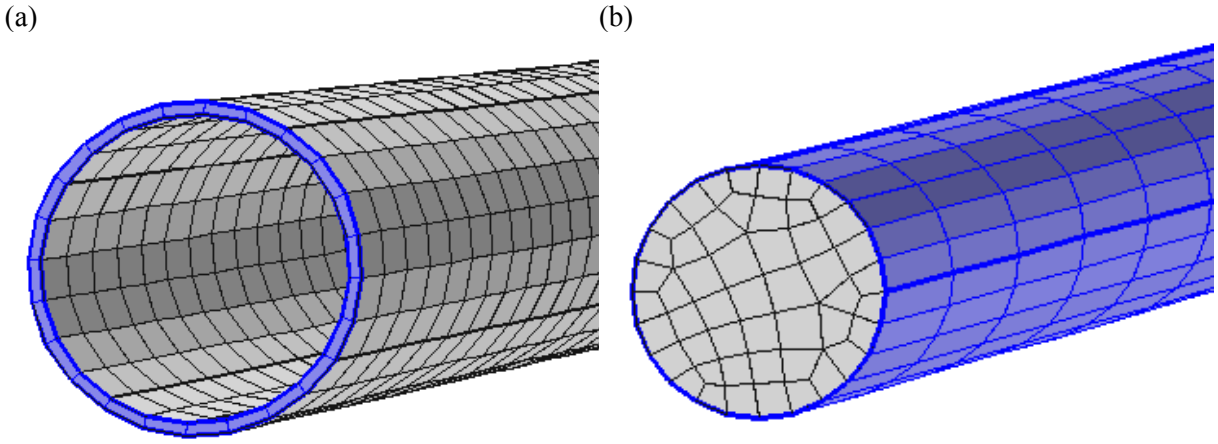

Figure 2.2-8. (a) Casing represented as cylinder of finite wall thickness with 6 elements per quadrant. (b) Casing represented as a shell on the boundary of a solid cylinder.

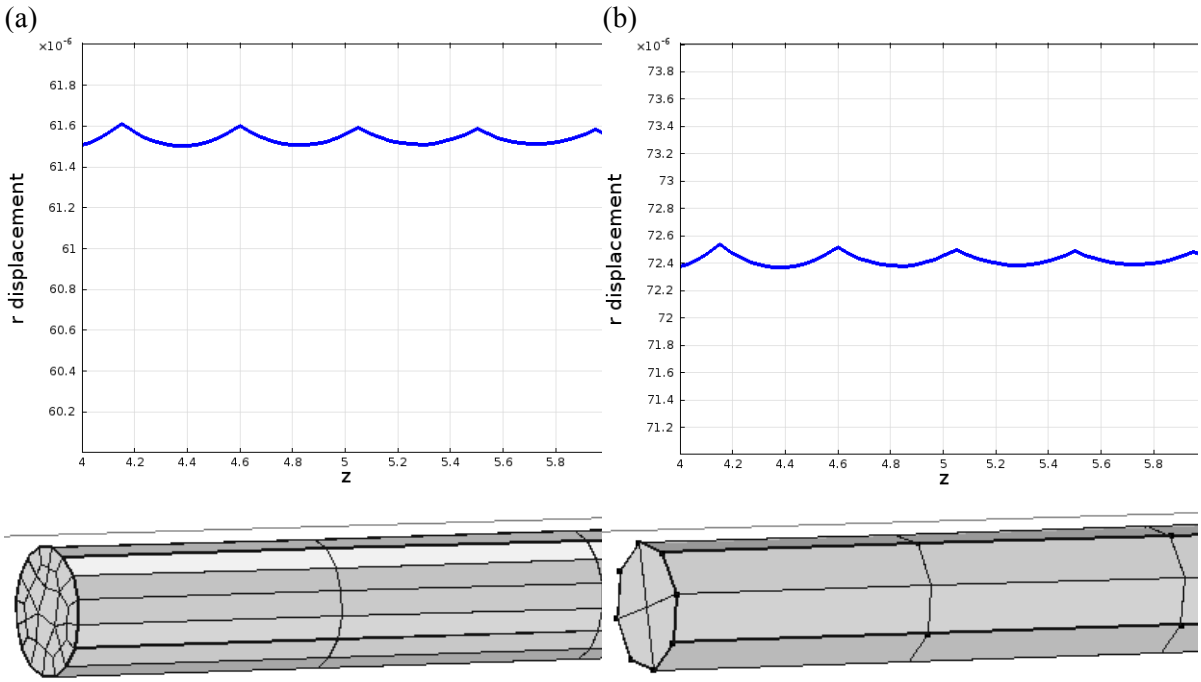

Figure 2.2-9. Radial displacement along uniformly loaded cylinder with mesh swept axially. Casing represented as a shell on a subdomain. (a) 4 elements/quadrant around circumference. Mean displacement is 61.55 microns. (b) 2 elements/quadrant, mean displacement 72.45 microns.

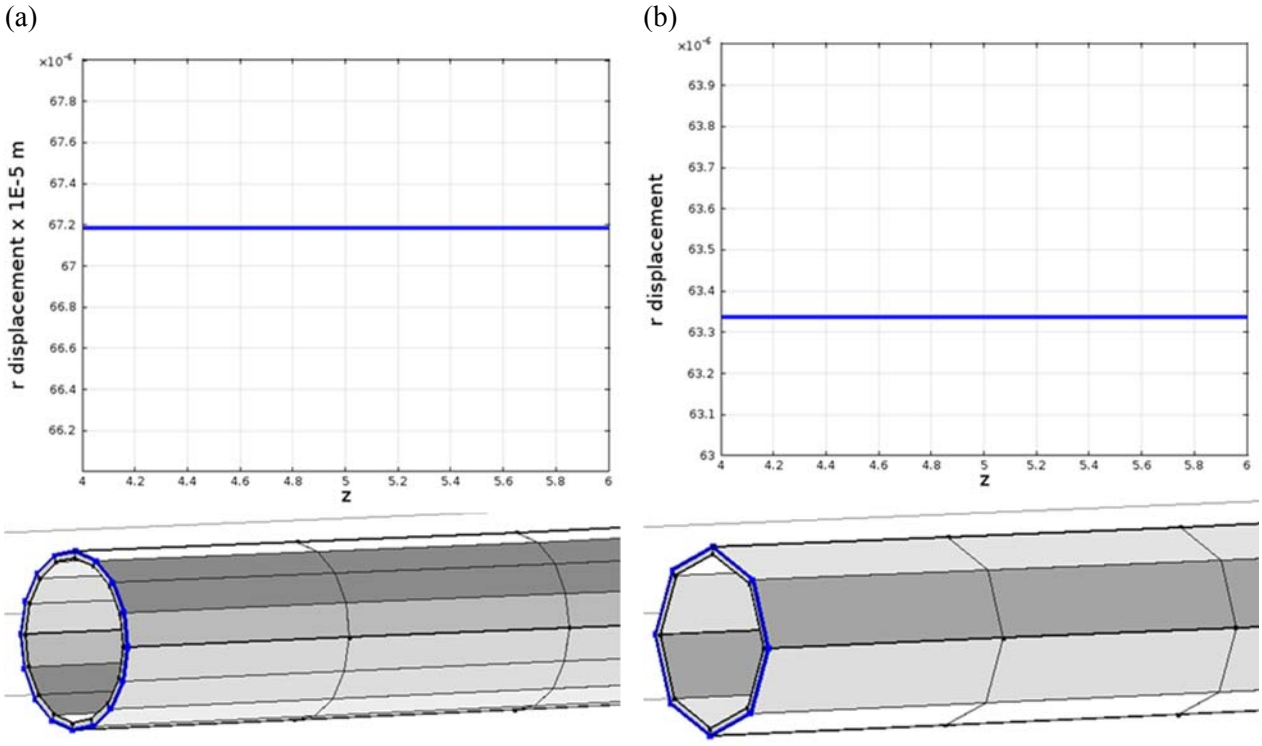

Figure 2.2-10. Radial displacement along uniformly loaded cylinder with meshed wall thickness. (a) 4 elements/quadrant around circumference. Mean displacement is 67.19 microns. (b) 2 elements/quadrant, mean displacement 63.35 microns.

Numerical Solution in COMSOL

The numerical solutions were conducted using two approaches, one that considers the casing as a shell on the boundary of a subdomain, and another that considers the casing explicitly (Figure 2.2-8). Considering the casing as a shell has the advantage of avoiding the need for a thin element representing the casing. Instead, the casing was represented as an elastic shell of specified thickness and properties bonded to the boundary of the subdomain. This approach is likely to be more numerically efficient than representing the wall thickness explicitly. However, some problems may require the casing to be explicitly considered; for example, when the analysis evaluates the separation of the casing and cement. Two general types of mesh were evaluated, one that uses a mesh swept axially along the casing and another that uses tetrahedral elements. The swept mesh generates long thin elements that conform to the casing and maintain axial symmetry. Tetrahedral elements are roughly equi-dimensional, so there are many more of them than occur in a swept mesh with elements of the same minimum dimension.

Simulations were conducted by varying the number of elements around the circumference in the swept mesh. The number of elements along the length of the model was held constant at 23, and this was sufficient to create a uniform displacement field along the mid-length of the casing. The cylinder was automatically divided by the software into 4 circumferential sections extending along the axis of the cylinder. Each section was divided into the same number of points around the edge of the casing. This number was specified in the mesh generator and used to create the mesh. Accordingly, a mesh with 4 elements/quadrant has a total of 16 elements around the circumference. After points were assigned around the circumference, a quadrilateral mesh was created at the end boundary of the casing. The quad mesh was then swept along the length of the casing (Figures 2.2-9 and 2.2-10).

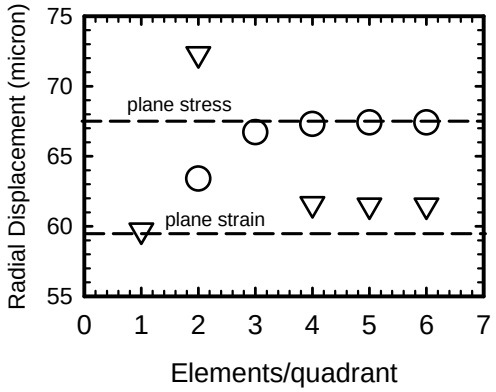

Figure 2.2-11. Radial displacement as a function of the number of elements per quadrant around the radius of the casing. Casing is represented as a shell on a cylinder (triangles) or as a cylinder with meshed wall (circles). Displacement from analytical solutions for reference (dashed line).

The results show that the displacement is mesh dependent for both shell and the meshed wall thickness when the number of elements/quadrant is 3 or less (Figure 2.2-11). Furthermore, the displacement is relatively independent of the mesh size when the elements/quadrant is 4 or more (Figure 2.2-11). The case where the casing is represented as a cylinder of explicit thickness matches the plane strain analytical solution to within 1 percent, whereas the case that represents the casing as a shell is closer to the plane stress analytical solution (Figure 2.2-11). Both numerical cases are 3D.

Profiles of displacement along the length of the casing vary slightly as values are interpolated within elements where the casing is represented as a shell (Figure 2.2-9). In this case, the variation is scalloped shaped with amplitudes of a few tenths of a percent for the cases

evaluated (Figure 2.2-9). This amount of variation is small and will likely be acceptable for expected applications.

The variation in displacement in simulations where casing has a finite wall thickness is even less than for the shell analyses (Figure 2.2-10). In these examples, the variability is at least one tenth that of the results from the shell analyses.

The encouraging results obtained from the swept-mesh analyses are contrasted sharply by results using tetrahedral elements (Figure 2.2-12). This application requires remarkably small elements (roughly 0.08 m or smaller) to obtain results that are symmetric and uniform, conforming to the applied load and material properties. However, the small meshes give displacement results that vary erratically along the length of the casing (Figure 2.2-13). Larger elements cause the casing to warp, flare or otherwise become erratically distorted. Not only do the tetrahedral meshes require considerably more elements than the swept mesh, but they also yield results that vary erratically as a result of numerical problems (Figure 2.2-13). Further reduction of the element sizes to mesh throughout the casing wall thickness may improve the accuracy of the calculations, but the required large number of elements is likely to make the analysis impractical.

Summary

The results of Benchmark 2 indicate that 3D numerical results should be similar to the plane stress analyses with a uniform displacement of approximately 67.7 microns. This result is best achieved by using a mesh that is swept along the length of the casing with a minimum of 4 elements/quadrant (Figure 2.2-14). Results from an analysis that meshes the wall of the casing were most accurate, but results from analyses where the casing was represented as a shell were only slightly (a few percent) less. Both approaches seem viable for further applications.

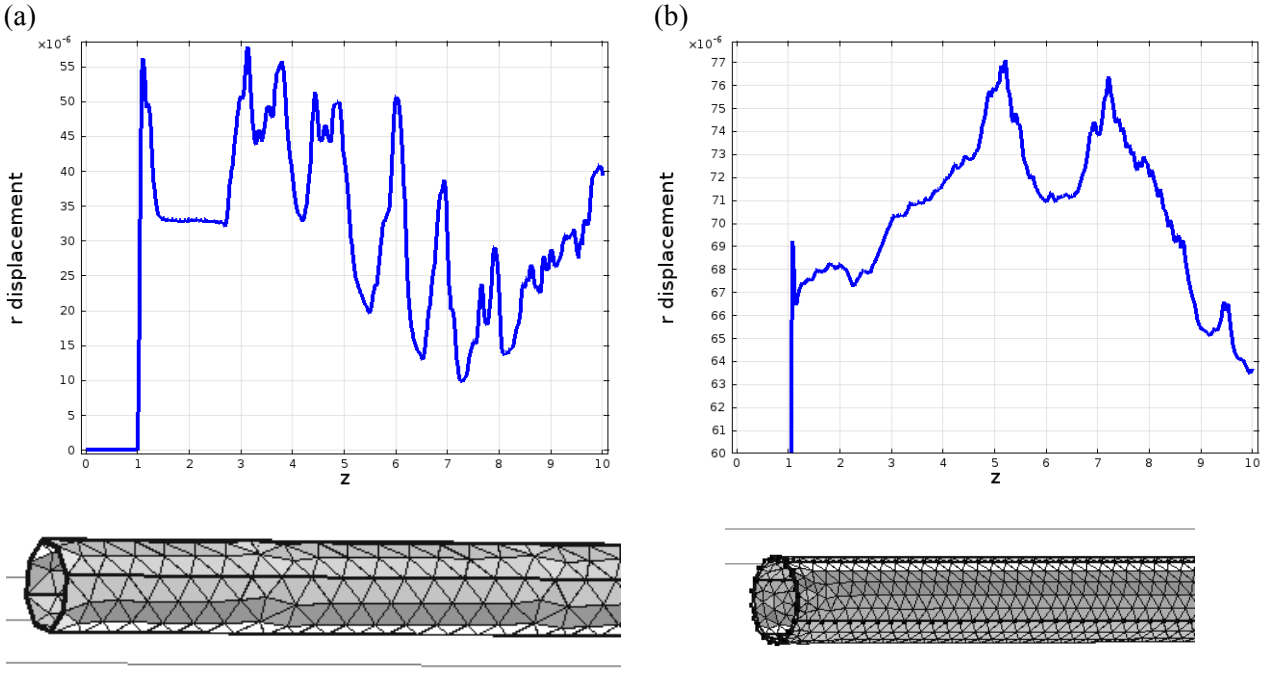

Figure 2.2-12. Radial displacement along uniformly loaded cylinder with wall thickness represented explicitly be a tetrahedral mesh. Minimum element size (a) 0.08 m, and (b) 0.04 m.

Mesh with 0.8 m minimum element size and resulting non-axial deformation (warping). Color is total radial displacement.

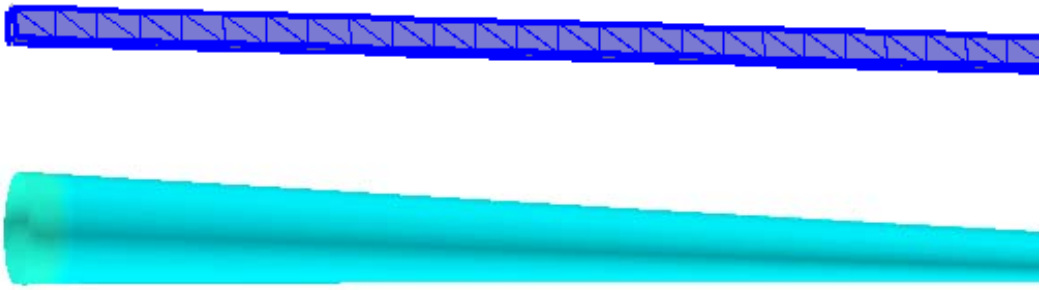

Mesh with 0.2 m minimum element size and resulting deformation. Color is total radial displacement. Tapered deformation is a mesh effect.

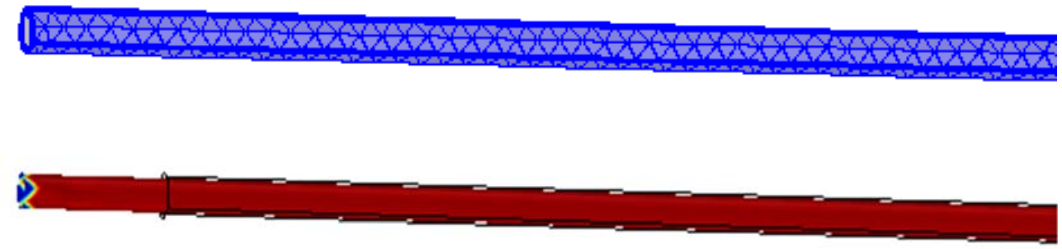

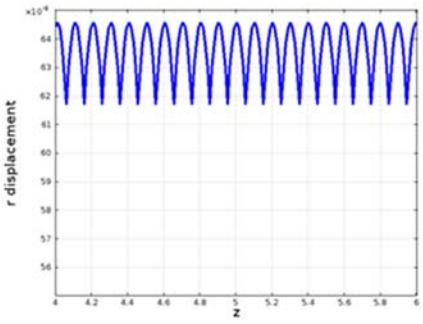

Mesh with minimum element size of 0.1 m and resulting deformation. Displacements are symmetric and oscillate between approximately 62 and 64 microns.

Figure 2.2-13. Effects of mesh density on deformation of casing represented as a shell on a solid cylinder. Tetrahedral mesh generator in COMSOL.

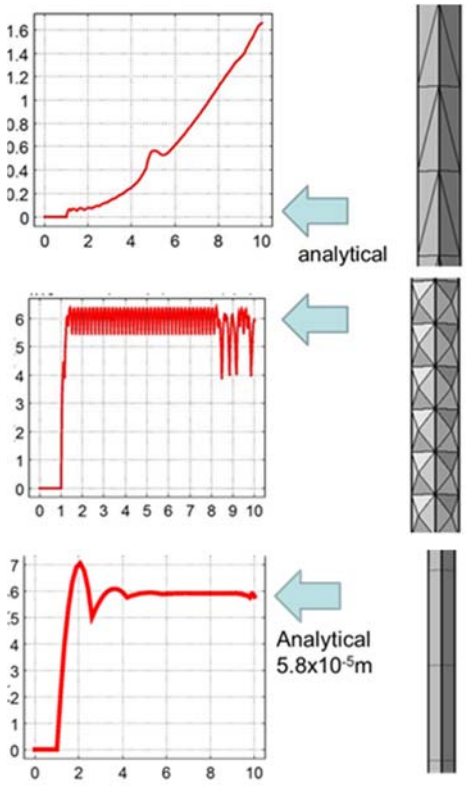

Triangular
256 elements

Poor accuracy, causes bending as artifact

Triangular
912 elements

Good average accuracy
Displacements rippled

Swept Mesh
15 cylindrical elements

Good accuracy
Need to bisect to use with tetrahedral elements

Figure 2.2-14. Summary of displacement as function of distance along the casing for example problem 2 for different sizes and styles of FEM mesh.

Numerical Solution in ABAQUS

Example problem 2 was solved using ABAQUS with both axisymmetric and 3D analyses. A quadratic, swept mesh was used for the 3-D problem (Figure 2.2-15). The casing thickness is much smaller than the radius or length, so only 1 element is assigned for the thickness, however, the several different number of elements in axial or circumferential direction were tested. In the shown mesh, no oscillation behavior is observed along the vertical axis. In the axisymmetric model, the radial displacement at z = 10 m is calculated for 24 to 180 elements. The results show that the displacement is essentially unaffected (within 0.1 micron of -67.5 microns) when the total number of elements is greater than 50. The displacement varies by several microns when the number of elements is less than 50 (Figure 2.2-16). It appears that mesh effects can be ignored when more than 50 elements are used in the axisymmetric model.

(a) (b)

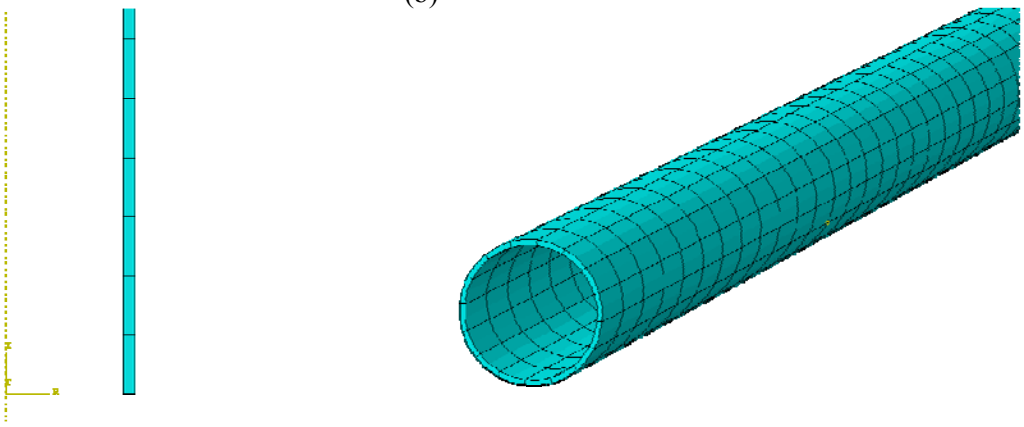

Figure 2.2-15. 3-D model. a) Casing represented in axial symmetry. b) Casing represented as cylinder of finite wall thickness with 4 elements/quadrant.

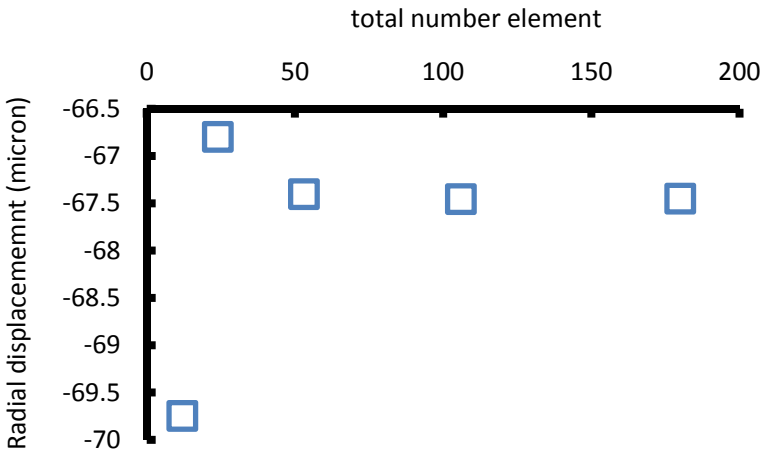

Figure 2.2-16. Radial displacement at z = 10 m as a function of the number of elements using ABAQUS in an axisymmetric simulation of example problem 2.

Similar results were observed in 3D. The mesh consisted of 2, 4, or 8 elements per quadrant around the circumference, and the number of elements along the axis varied from 24 to 250. The radial displacement at the top end (z = 10 m) was monitored (Figure 2.2-17).

Displacements in 3D converged to the same value of -67.5 microns as observed in the axially symmetric model. Variations of a few tenths of a micron occur when fewer than 100 elements were used (Figure 2.2-17). The stabilized value, 67.4 microns, is very close to axisymmetric model (67.5 microns).

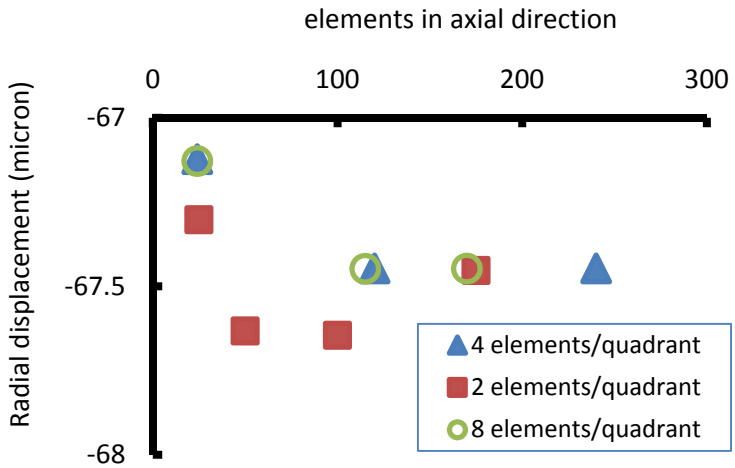

Figure 2.2-17. Radial displacement at z = 10 m for different meshes using ABAQUS in 3D for example problem 2.

2.2.3 EXAMPLE PROBLEM 3

This problem considers steel casing and cement embedded in a porous medium representing the vicinity of the well.

Configuration

The porous medium includes a thin layer around the casing enveloped by uniform sand or cement (Figure 2.2-18). Water is injected into the casing at a constant rate and there is negligible head loss along the casing over the length of the model. The outer boundary of the porous medium is held at constant head.

An axially symmetric version of this problem was analyzed with ABAQUS and COMSOL in 2D and 3D to evaluate performance of the codes. The problem was then modified to include the effects of 3D distributions, like a perforation. The size of the problem allowed 3D features, like perforations, to be included while still retaining a mesh that was small enough to solve the problem with reasonable execution times.

Boundary Conditions

The top (z = 10 m) and bottom (z = 0 m) boundaries are impermeable and roller conditions. Fluid pressure is fixed at the inner (r = 0.1 m) and outer boundaries (r = 10 m). The time for the analysis is 10^2 seconds, which is sufficient to reach steady state. A complete set of boundary conditions is presented in Table 2.2-6

The material properies for formation is same as Table 2.2-1, and for steel casing same as Table 2.2-3.

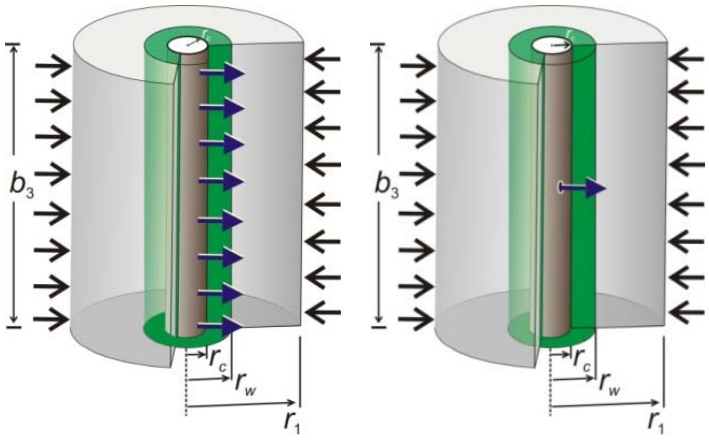

Figure 2.2-18. Cemented casing embedded in a uniform porous material (left) or in casing with perforation.

Table 2.2-6. Boundary conditions of benchmark problem 3.

Boundary	Fluid Flow	Elasticity
top (z = 10 m)	impermeable	roller ($u_z = 0$, $\tau_{rz} = 0$)
bottom (z = 0 m)	impermeable	roller ($u_z = 0$, $\tau_{rz} = 0$)
outer (r = 10 m)	pore pressure = 0 ($p = 0$)	roller ($u_r = 0$, $\tau_{rz} = 0$)
inner (r = 0.1 m)	pore pressure = 1 MPa (p = 1 MPa)	applied pressure = 1MPa ($\sigma_{rr} = p$ = 1 MPa, $\tau_{rz} = 0$)

Mesh

Mesh is designed similar to benchmark problem 1. Three simulation methods (ABAQUS axisymmetry, ABAQUS 3D and COMSOL axisymmetry) are tested and compared. In ABAQUS, quadratic or hexagonal elements are adopted while COMSOL has triangular shaped elements (Figures 2.2-19 and 2.2-20). Size of elements are relatively uniform in vertical direction since the considered domain is relatively small (10 m height), however, in a radial direction, the size of element gradually increases towards the outer boundary (r = 10 m). 3D model elements are also built similar to the axisymmetry case.

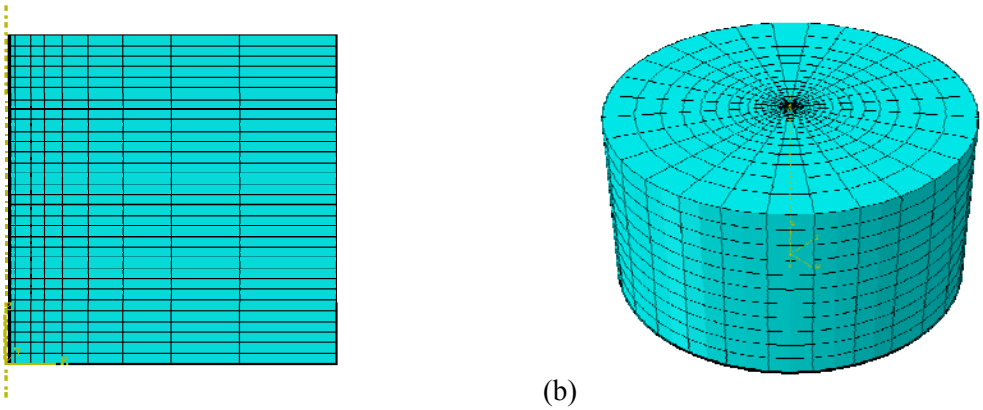

(a) (b)

Figure 2.2-19. (a) Axisymmetry mesh for benchmark problem 3 in ABAQUS. (b) 3 dimensional mesh for benchmark problem 3 in ABAQUS.

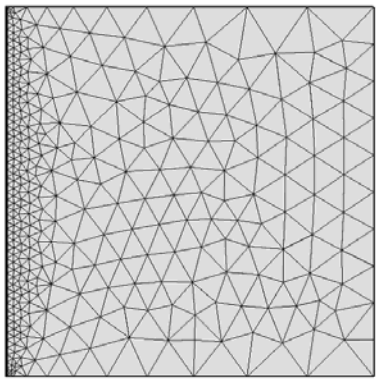

Figure 2.2-20. Axisymmetry mesh for cemented casing and screen in COMSOL.

Results

For three simulation methods (ABAQUS axisymmetry, ABAQUS 3D and COMSOL axisymmetry) pore pressure, radial displacement, radial and tangential effective stresses are assessed along the middle line of model (z = 5 m) in the radial direction. In general, all of the variables from the three simulations are similar.

Pore pressure is reduced from the borehole (r = 0.1 m) to outer boundary (10 m) and similar to benchmark problem 1, as it drops log-linearly (Figure 2.2-21). The slope is uniform because the permeability is uniform in this problem.

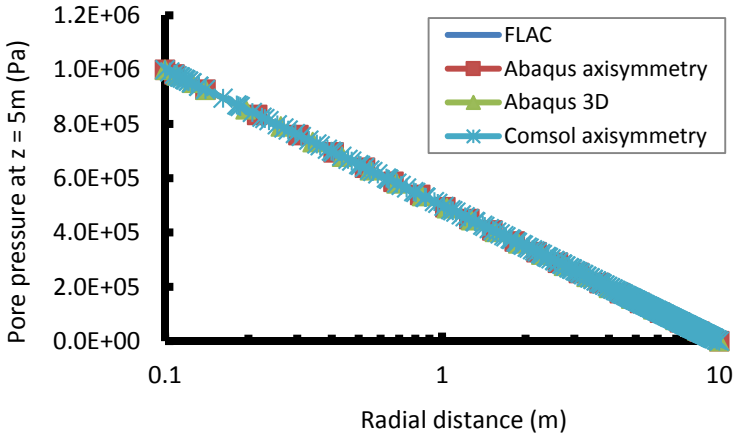

Figure 2.2-21. Pore pressure at time of 10^2 sec.

Radial displacement at the borehole is approximately 3.7×10^{-6}m and is roughly uniform over the casing (Figure 2.2-22). A peak displacment of roughly 2.2×10^{-5}m at $r = 3.7$ m, then the radial displacement reduces to zero at $r = 10$ m because of the boundary condition.

Radial effective stress, plotted in Figure 2.2-23, also changes linearly in log-scale similar to pore pressure. However, it increases over the casing and cement and then it decreases and turns negative at approximately $r = 4.7$ m. Therefore, this plot indicates that the formation is under tensile stress up to 4.7 m and for the outer part ($4.7 \text{ m} < r < 10 \text{ m}$) it is under compressive loading. This is consistent with the radial displacement where the peak value occurred at 4.7 m (Figure 2.2-22). It should be noted that in real applications, the total radial stress will probably be compressive due to the preexisting in-situ stress component caused by gravity.

Similar to radial stress, tangential effective stress also decreases from the borehole to the outer boundary and turns to negative value at $r = 7.8$ m (Figure 2.2-24).

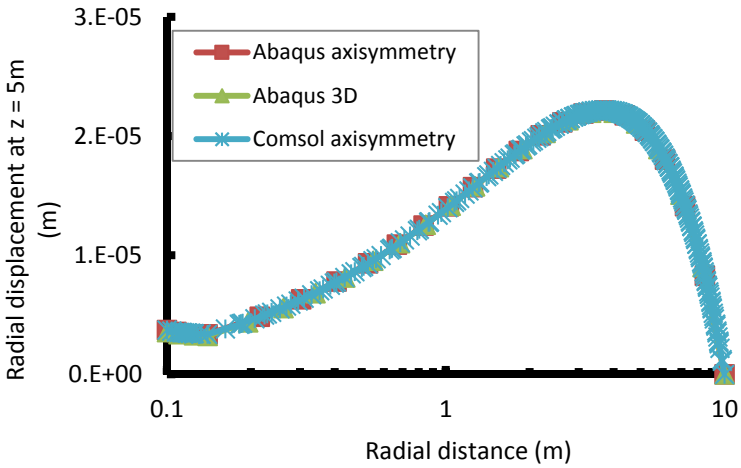

Figure 2.2-22. Radial displacement at time of 10^2 sec.

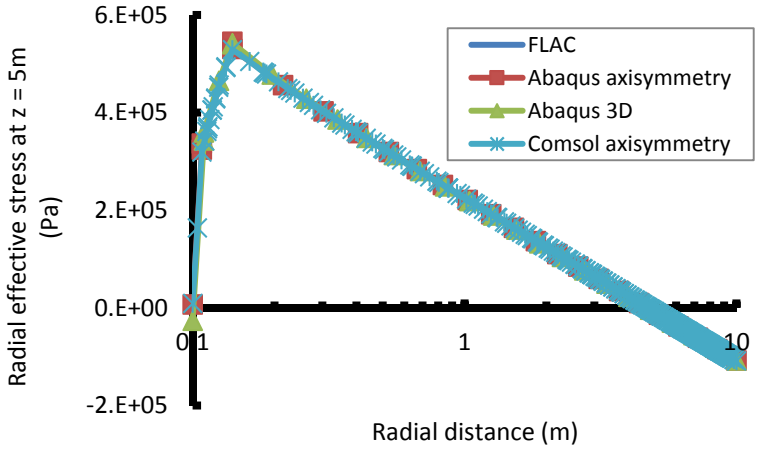

Figure 2.2-23. Radial effective stress at time of 10^2 sec.

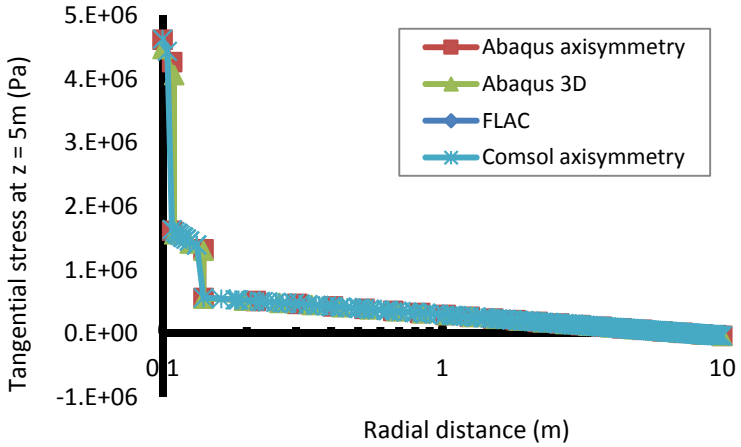

Figure 2.2-24. Tangential effective stress at time of 10^2 sec.

2.2.4 Example Problem 4

This problem involves demonstrating the ability to conduct an analysis at reservoir scale with a cased borehole. It is essentially a combination of the casing in Example 3 and reservoir in Example 1. This has been solved using all three codes, although the run times currently span a wide range. Excessive run times (more than 2 days) may eliminate FLAC from practical use for this type of problem. This problem is used later in the Chapter 3.

2.2.5 Benchmark Analysis

Analyses of deformation as described in the previous examples are important to the proposed application, as well as a variety of other applications related to CO_2 storage or resource production. The literature includes a wide range of problems describing well performance using analytical solutions, which are useful as benchmarks because of their inherent accuracy. Analytical solutions to poroelastic problems related to well performance are scarce, and this is a shortcoming when verifying the performance of numerical models.

Based on the example problem 1, we developed a benchmark solution to a problem involving deformation in the vicinity of an injection well, which cannot be solved in closed form to our knowledge. The approach was to solve the same problem with different codes and

different meshes compare the results along selected lines and points. The assumption was that mesh errors would be reduced by decreasing the size of the elements, and the result would converge on the correct value. We also assumed that differences caused by numerical methods would be small, and could be identified by comparing results from different codes.

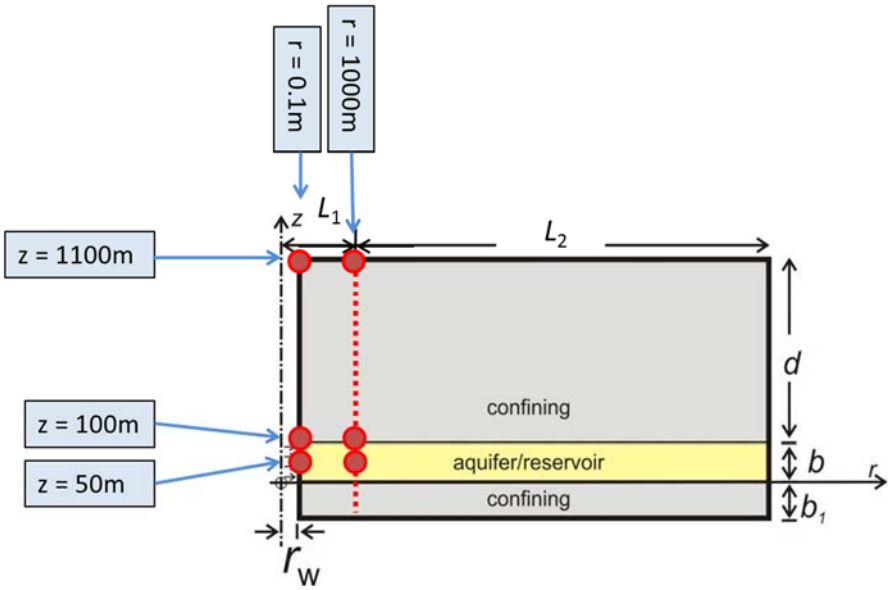

Figure 2.2-25. Cross section of reservoir and confining units with six observation points used in the code comparison.

Model

The reservoir is a circular, horizontal layer of uniform thickness. The well is at the center of the reservoir, so axial symmetry will be assumed. The model resembles idealized field conditions with a 100-m-thick reservoir overlain by a uniform confining layer (1,000 m thick), and underlain by a 100-m-thick confining layer resting on impermeable, rigid basement rock (Figure 2.2-25). The radial extent is 30 km. The well is represented as a cylindrical open hole in the formation. This application uses the example model 1 described above.

The analyses were solved using three different codes (ABAQUS, COMSOL, and FLAC) designed to solve problems of coupled poroelasticity. These codes are widely used and readily available. Boundary conditions can be modified as needed to properly represent a particular problem.

Benchmark values

Values of radial and vertical displacements were measured at a few key locations as a function of the number of elements or grid blocks used in the simulation (Figure 2.2-24). The number of mesh elements was varied within practical limits for the three codes. We used a maximum execution time of approximately 30 minutes to limit the size of the ABAQUS and COMSOL meshes. This time was selected because we expect that many runs will be needed to use parameter estimation methods, so run times longer than 30 minutes would make parameter estimation applications impractical. The maximum execution time used for the FLAC models was approximately 24 hrs. This long run time effectively eliminated parameter estimate applications for FLAC, but it was necessary to use this long run time in order to use several grids with different sizes with FLAC. The smallest grid (980 elements) used in for the FLAC

simulation required a run time of 7.5 hours. The execution speed varied markedly between the codes, so the maximum number of elements that was practical to use also varied. The maximum numbers of elements are 75,840 for ABAQUS, 19,305 for COMSOL, and 3,300 for FLAC, respectively.

Displacement values for meshes with infinite density were estimated by extrapolating calculated results. Regression function was used to characterize effect of the number of elements on the displacement at each of the selected points. Several functions were evaluated to extrapolate the data to a large number of mesh elements, and:

$$u_r = \frac{a_1}{N + a_2} + a_3 \tag{2.2-3}$$

was selected because it characterizes the data well, has a small number of parameters, and converges to a value, a_3, when the number of mesh elements, N, approaches infinity. The analysis consisted of estimating the parameters a_1, a_2, and a_3 by minimizing a sum-of-squared-error objective function. Parameters a_1 and a_2 were discarded, and a_3 was used as an estimate of the value that would be predicted by the code at infinite mesh density.

As an example, the radial displacement at the injection point (r = 0.1 m, z = 50 m) was calculated with meshes of different sizes and Eq. 2.2-3 was fit to them to obtain $a_3 = 6.50\text{x}10^{-6}$ m for ABAQUS, $a_3 = 6.59\text{x}10^{-6}$ m for COMSOL, and $a_3 = 5.78\text{x}10^{-6}$ m for FLAC (additional data are in Figure 2.2-22 and Table 2.2-7). Values of a_3 from the different codes generally differ by less than 2%. The results were averaged to obtain an estimate of the true value at that point, assuming the error from the codes was equal.

The data were then recast by plotting the error relative to the estimated true value for each simulation as a function of the run time for that simulation. This result provides an estimate of the tradeoff between error and run time for the different codes and meshes.

In addition to the measurements at points, vertical and radial displacements were calculated along radial profiles at two elevations at t = 100 days. Data at z = 100 m were along the upper contact between the reservoir and overlying confining unit, whereas the profile at z = 1100 m is at the ground surface. The profiles were also used to compare the results from the different codes.

Mesh Description

The numerical models all used rectangular elements. Preliminary analyses using COMSOL and ABAQUS indicated that rectangular elements were more effective than the triangular or quadrilateral elements. However, we did not explore meshes with those element shapes in detail. The size of the mesh elements is smallest at the boundary representing the injection well, and it gradually increases from the boundary (0 m < z < 100 m and r = 0.1 m) to the outer (r = 30 km) and upper (z = 1,100 m) boundaries (Figure 2.2-26). The number of elements along each segment in the geometry was specified by determining a baseline number multiplied by a coefficient. The coefficient was used to systematically change the size of the mesh. ABAQUS analyses used two mesh designs, where A1 (ABAQUS1) used columns widths that increased faster than A2 (ABAQUS2). As a result, the elements in A1 are more elongate in the vicinity of the monitoring well than the ones used in the A2 mesh (Figure 2.2-26). The size of elements along a

boundary was varied systematically by adjusting the mesh generator. A typical approach is to vary the size of the mesh using a geometric sequence where the ratio of adjacent elements is equal to a constant. However, details of how the mesh generators increment the size of adjacent elements differs between the codes, so we experimented with the mesh generation factors to create meshes that were similar. Baseline meshes were created using the values in Table 2.2-1. Meshes of different size but a similar style were then created by multiplying the numbers of elements along each boundary segment in the baseline mesh by a constant value.

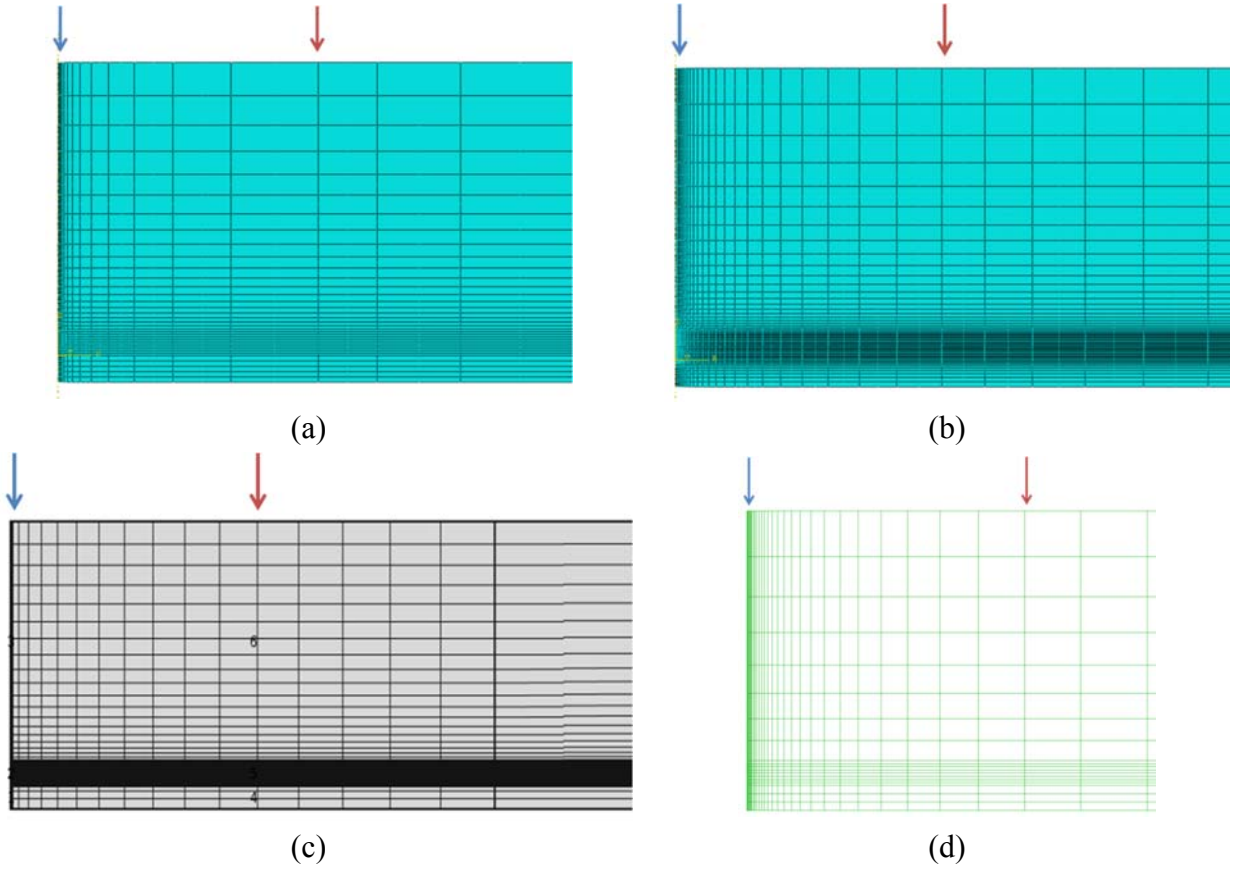

Figure 2.2-26. Mesh used in numerical codes (a) ABAQUS mesh 1, (b) ABAQUS mesh 2, (c) COMSOL mesh, and (d) FLAC mesh. Blue arrows indicate the location of injection well (r = 0.1 m) and red arrows of monitoring well (r = 1 km).

Table 2.2-7. The number of elements for each boundary segment (identified in Figure 2.2-24) used to create baseline meshes for each code. The values inside the parenthesis are mesh generation factors.

Simulations	b_1	B	d	L_1	L_2
Comsol	10 (10)	25 (1)	50 (12)	35 (8)	30 (10)
Abaqus 1 (A1)	10 (5)	50 (1)	20 (30)	15 (80)	25 (20)
Abaqus 2 (A2)	10 (20)	30 (1)	25 (100)	25 (200)	25 (20)
FLAC	10 (1)	30 (1)	25 (1.125)	30 (1.2)	20 (1.2)

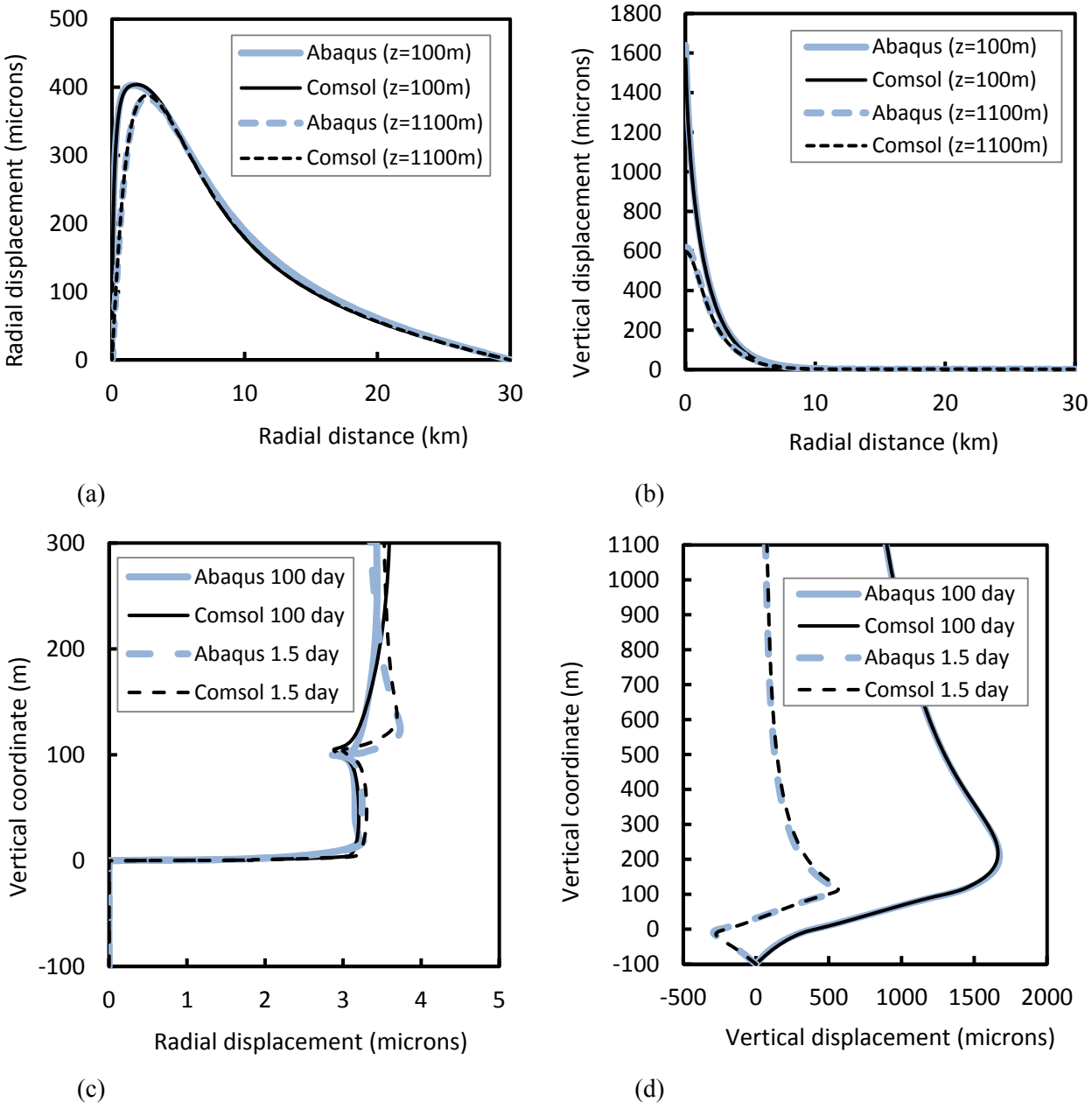

Figure 2.2-27. Displacements at t = 100 days in (a) radial displacement as a function of radial distance at z = 100 m (solid line) and z = 1,100 m (dashed and labeled "surface" to indicate the line is at the ground surface, (b) vertical displacement as a function of radial distance at z = 100 m (solid line) and z = 1,100m (dashed), (c) radial displacement profile , and (d) vertical displacement profile at r = 0.1 m (wellbore).

Results

The radial displacement increased to a maximum of roughly 400 microns at a distance of approximately 1 km, and it decreased to zero at the outer boundary, according to results from

both COMSOL and ABAQUS (Figure 2.2-27). The maximum vertical displacement was 500 to 1500 microns at the borehole (r = 0.1 m) and decreased to negligible values at r > 7 km.

COMSOL and ABAQUS generate similar results (Figure 2.2-27), but the relative error between the two codes increases when a sparser mesh is used. For example, vertical displacement of a point at the center of the injection interval decreases with the number of elements and stabilizes at approximately 50,000 elements for ABAQUS and 10,000 elements for COMSOL (Figure 2.2-27b). The radial displacement at the same point increases with the number of elements and COMSOL and ABAQUS converge to similar values for meshes with more than approximately 30,000 elements.

The results for the converged values of a_3 for the simulations are typically within a few percent for all three codes at the different measurement points (Figure 2.2-28 and Table 2.2-8). This indicates that all three codes converge on generally the same results. An exception is in Figure 2.2-28a, where the results from FLAC are approximately 10% smaller than the other results. In general, whereas the results from FLAC are similar to those from the other codes, the FLAC results are generally an outlier compared to the similarity between the results from the other two codes. This is probably because the FLAC results were extrapolated much further than the others. The densest mesh run with FLAC was 3,300 elements and required 24 hrs of run time. Even with this long run time the FLAC mesh was much smaller than those used by COMSOL (19,305 elements) and ABAQUS (75,840 elements). This is why extrapolation was required to compare the FLAC results to those from COMSOL and ABAQUS.

In order to infer a "correct" value of displacement, we assumed that the results from COMSOL and ABAQUS were more reliable than those from FLAC. This is because the results from COMSOL and ABAQUS were similar to each other and FLAC was noticeably different in most cases. Moreover, we assumed that the numerical error in the COMSOL and ABAQUS codes was random so an average of the a_3 value provided a best estimate of the exact value at each point and time (Table 2.2-8). The range of the two ABAQUS meshes and one COMSOL value used to estimate the uncertainty in the best estimate (Table 2.2-8). In general, the uncertainty is less than 1.5% for the COMSOL and ABAQUS results, and it is less than 1% in most cases. The uncertainty from FLAC is less than 2% for all but two cases, and it is approximately 10% at those points (Table 2.2-8).

Results from the simulations are also expressed as error as a function of run time. In general, the error decreased with run time (Figure 2.2-29). FLAC calculations are omitted here because the execution times were 7.5 to 24 hrs and showing them would have required significantly altering the plots. For many of cases, the errors are less than 5%, and the error is less than 2% in all the codes for simulations of 30 minutes. The uncertainty from simulations by COMSOL is within approximately 1% for simulation times greater than 5 minutes, whereas longer execution times are required for ABAQUS to achieve a similar level of uncertainty. This occurs for both meshes used in ABAQUS.

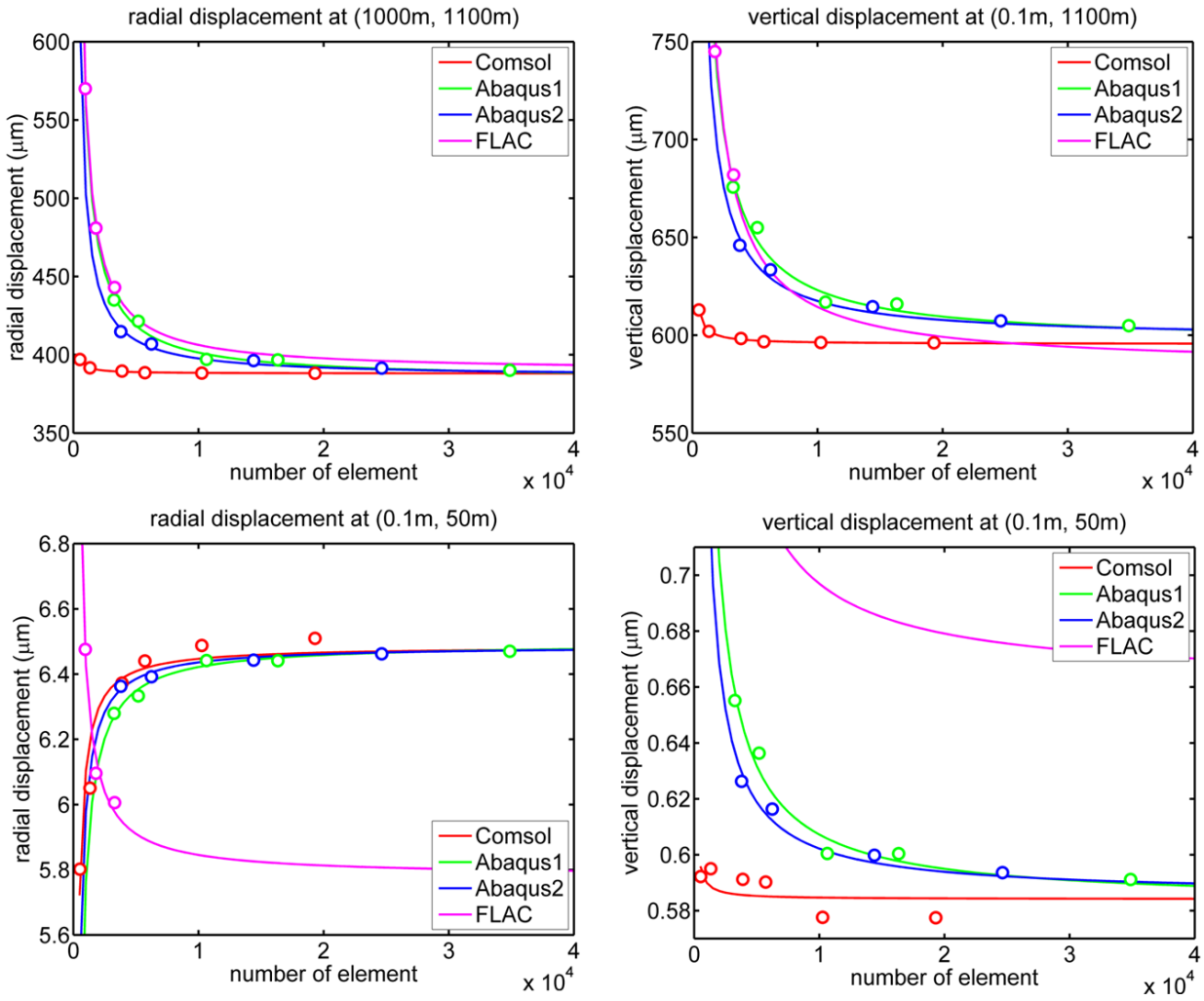

Figure 2.2-28. Displacements from ABAQUS (A1: triangles; A2: squares), COMSOL (diamonds) and FLAC (circles) at t = 100 days as a function of mesh density at different locations. (a) Radial displacement at r = 0.1 m, z = 50 m; (b) vertical displacement at r = 0.1 m, z = 50 m; (c) radial displacement at r = 1 km, z = 1,100 m; (d) vertical displacement at r = 0.1 m, z = 1,100 m. The points are data, the lines are from fitting Eq. 2.2-1 to the data.

Table 2.2-8. Summary of inferred displacement using an infinitely dense mesh determined as the a_3 values from Eq. 2.2-3 for the different codes. UR is the radial displacement, UV is vertical displacement. The values in the parenthesis are error relative to the average value. Units are microns.

Simulations	COMSOL	ABAQUS2 (A2)	ABAQUS1 (A1)	FLAC	Average
UR (0.1 m, 50 m)	6.59 (0.68%)	6.50 (0.68%)	6.52 (0.39%)	5.78 (11.6%)	6.54
UR (1 km, 50 m)	411.8 (0.02%)	411.6 (0.02%)	407.3 (1.07%)	406.5 (1.26%)	411.7
UR (1 km, 100 m)	403.6 (0.41%)	400.3 (0.41%)	397.8 (1.03%)	394.3 (1.91%)	402.0
UR (1 km, 1,100 m)	388.0 (0.75%)	382.2 (0.75%)	379.7 (1.41%)	389.2 (1.07%)	385.1
UV (0.1 m, 50 m)	576.6 (0.28%)	579.8 (0.28%)	576.4 (0.30%)	589.4 (1.95%)	578.2
UV (0.1 m, 100 m)	1,568.7 (0.48%)	1,584.0 (0.48%)	1,573.7 (0.17%)	1,740 (10.40%)	1,576
UV (0.1 m, 1,100 m)	595.5 (0.23%)	592.7 (0.23%)	587.5 (1.11%)	583.9 (1.71%)	574.1

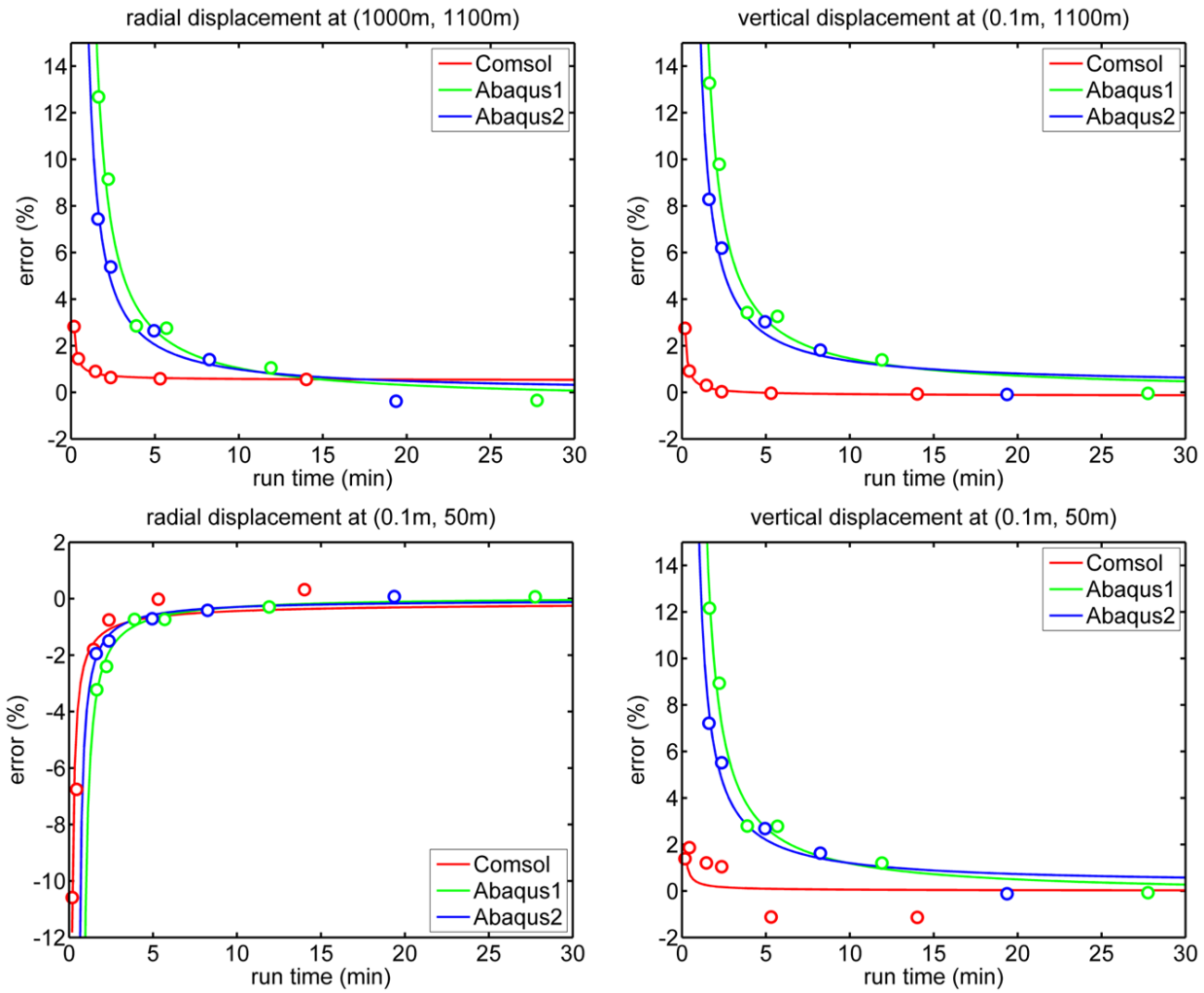

Figure 2.2-29. Error determined at different locations from ABAQUS (A1: triangles; A2: squares) and COMSOL (diamonds) at t = 100 days as a function of computation time. (a) Radial displacement at r = 0.1 m, z = 50 m; (b) vertical displacement at r = 0.1 m, z = 50 m; (c) radial displacement at r = 1 km, z = 1,100 m; (d) vertical displacement at r = 0.1 m, z = 1,100 m. The points are data, the lines are from fitting Eq. 2.2-1 fit to the data.

2.3 DEFORMATION IN THE VICINITY OF AN INJECTION WELL

The objective of this section is to use the methods outlined in the previous section to characterize the deformation of the vicinity of an injection well under conditions typical of CO_2 storage. These conditions can span a broad range, so we select a suite of representative values for this analysis. A sensitivity analysis that includes the ranges of conditions is presented in the next section.

The conceptual model for this study will assume the well is in a reservoir that resembles actual conditions, but it will be idealized to facilitate calculations. Localized heterogeneities may play a role in the details of the deformation, but they will be ignored for now in favor of characterizing the general response, and an idealized geometry will suffice for this purpose.

The reservoir assumed to be a circular, horizontal layer of uniform thickness. The well is at the center of the reservoir, so axial symmetry is assumed. Injection occurs into a 100-m-thick

layer overlain by a uniform confining layer (1,000 m thick), and underlain by a 100-m-thick confining layer resting on impermeable and rigid basement rock (Figure 2.3-1). The radial extent is 30 km. This analysis builds on example problem 4 in the previous section.

The well is represented as a cylindrical hole lined with a steel tube that represents casing and screen. The properties of cement are assumed to be identical to that of the formation. The steel casing is assumed to resemble steel pipe with a radius of 0.1 m and a wall thickness of 8 mm.

The model is based on geologic scenarios considered for CO_2 storage. These scenarios are quite variable, and we have tried to select geometries and dimensions that are typical. For example, the thickness of formations used for CO_2 storage demonstrations ranges from 8 m for the Sleipner project, Utsira Formation, Norway Snøhvit LNG field [*Chadwick et al.*, 2004], to 200 m for the Berlin natural gas storage facility [*Riddiford et al.*, 2003], so the 100-m thickness used here seems to be reasonable. The lateral extent of formations range from 1 km in the Powder River Basin, Wyoming [*Chiaramonte et al.*, 2007] to 200 km in the Williston basin, North Dakota [*Gibson et al.* 1995]. The minimum depth required to create the pressure needed for supercritical CO_2 is 800 m [*Lin and Ray*, 1994; *Shafeen et al.*, 2004; *Svenson et al.*, 2007], so the depth used in this analysis is on the shallow side of formations that will be considered for CO_2 injection. Nevertheless, some sites, such as the saline aquifer of the Triasssic Stuttgart Formation in the northeast Germany Basin, Ketzin, Germany [*Foerster et al.*, 2006], are at depths shallower than 1 km.

Injection wells may operate at constant rate early in their life, but the formation pressure will increase and later they would probably operate at constant pressure in order to avoid exceeding pore pressures that could damage the formation [*Senel and Chugunov*, 2013]. We have evaluated both constant rate and constant pressure injections, but the following analysis will be limited to the case of constant injection pressure in order to reduce the number of variables in this initial assessment.

The fluid pressure at the wellbore will be assumed to be fixed at 1 MPa with injection periods up to several hundred days. These conditions were selected to be between those used for well testing, which could use lower pressures and shorter durations, and those used for sustained operation, which would likely occur at higher pressure during longer periods [*Ghomian et al.*, 2008]. For example, injection pressures during CO_2 storage demonstrations were 8 MPa at Ketzin, Germany [*Liebschera et al.*, 2013], 25 MPa at Decatur, Illinois Basin [*Senel and Chugunov*, 2013] and 45 MPa at Cranfield, Mississippi [*Hovorka et al.*, 2013]. As a result, the analyses may over-estimate deformations during short-term well testing, and they will almost certainly under-estimate deformation during operation.

The fluid injected into the formation will be assumed to be at constant temperature and density, both of which are equal to the reservoir fluid. We recognize that the density of supercritical CO_2 is less than that of the brine expected to fill the pore space, and the temperature of the CO_2 may differ from that of the subsurface. However, the injection process and resulting pressure change is expected to dominate deformation effects caused by variation in fluid density and temperature, so those variations will be ignored.

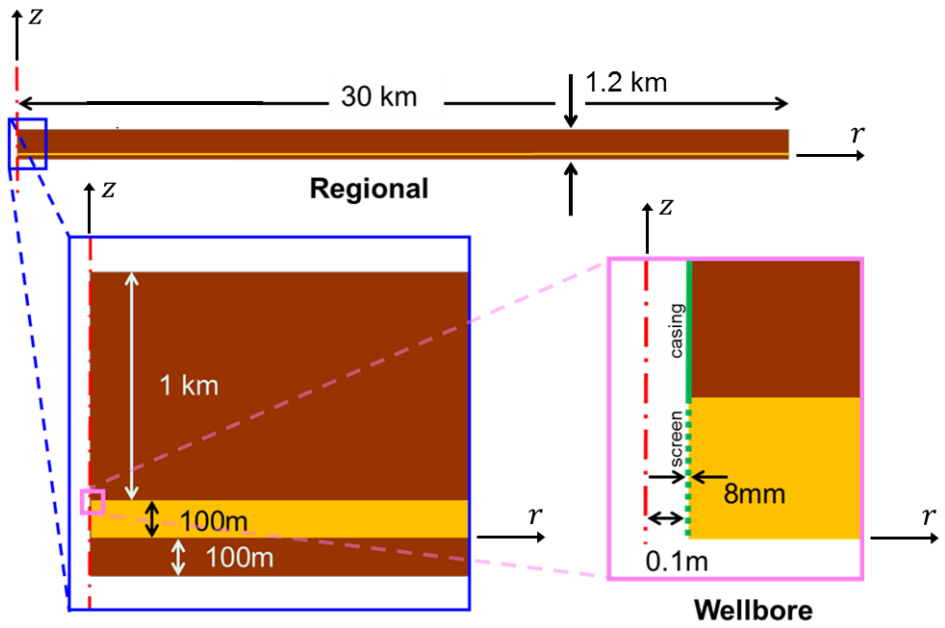

Figure 2.3-1. Configuration of model used in simulation spanning scales from casing to reservoir.

2.3.1 NUMERICAL MODEL

The numerical model used here represents the conceptual model by considering fluid flow and deformation in the vicinity of a well in a uniform, axisymmetric layer with the geometries defined in Figure 2.3-1.

Linear elastic poroelasticity [*Detournay and Cheng*, 1993; *Wang*, 2000] is assumed to describe the distribution of fluid pressure and deformation. Conservation of mass of a fluid at constant and uniform density gives [*Wang*, 2000]:

$$-\nabla \cdot q = \frac{1}{M}\frac{\partial h}{\partial t} + \alpha \frac{\partial \varepsilon_{kk}}{\partial t} \tag{2.3-1}$$

where q is the volumetric flux, h is the hydraulic head, α is the Biot-Willis coefficient, ε_{kk} is the volumetric strain, and M is the Biot modulus.

The hydraulic head is defined as:

$$h = z + \frac{P}{\gamma} \tag{2.3-2}$$

and the volumetric flux is given by:

$$q = -K\nabla h = -\frac{k}{\mu}\left(\nabla P + \rho g \nabla D\right) \tag{2.3-3}$$

where K is hydraulic conductivity, k is permeability, γ is the unit weight of the fluid, μ is fluid viscosity, g is gravitational acceleration, and z is the upward coordinate.

Conservation of momentum with Hooke's Law gives [Wang, 2000]:

$$\frac{E}{2(1+\nu)}\nabla^2 u_i + \frac{E}{2(1+\nu)(1-2\nu)}\frac{\partial \varepsilon}{\partial x_i} = \alpha \frac{\partial P}{\partial x_i} \qquad (2.3\text{-}4)$$

where P is pressure, u_i is displacement of the solid in the i^{th} direction, $i = x, y, z$, and E is drained Young's modulus, and ν is drained Poisson's ratio. In polar coordinates, the strain components are:

$$\varepsilon_{rr} = \frac{\partial u_r}{\partial r}, \quad \varepsilon_{\theta\theta} = \frac{u_r}{r}, \quad \varepsilon_{zz} = \frac{\partial u_z}{\partial z} \qquad (2.3\text{-}5)$$

Initial and Boundary Conditions

The initial conditions assume there is no fluid flow, and the formation is in static equilibrium. Pressures and displacements are determined relative to the initial conditions.

Conditions at the boundaries follow directly from the conceptual model and are given in Table 2.3-1. Boundary conditions at the wellbore are particularly important. In all cases, the total stress on the wellbore face is assumed to be equal to the fluid pressure.

Table 2.3-1 Boundary conditions used in analysis.

Boundary		Fluid Flow	Elasticity
top (z = 1,100 m)		pore pressure = 0 Pa (p = 0 Pa)	traction free (σ_{ij} =0)
bottom (z = -100 m)		impermeable (dp/dz =0)	roller (u_z = 0)
outer (r = 30,000 m)		pore pressure = 0 Pa (p = 0 Pa)	roller (u_r = 0)
inner (r = 0.1 m)	lower confining layer (-100 m < z < 0 m)	impermeable (dp/dr = 0)	roller (u_r = 0)
	sand aquifer (0 m < z < 100 m)	pore pressure = 1 MPa (p = 1 MPa)	total stress = fluid pressure ($\sigma_{ij} = -\alpha p$)
	upper confining layer (100 m < z < 1,100 m)	impermeable (dp/dr = 0)	total stress = fluid pressure ($\sigma_{ij} = -\alpha p$)

Material Properties

Material properties characterizing formations considered for CO_2 sequestration span a considerable range, and the magnitudes of these properties affect the resulting response to injection. To evaluate effects of this variability, the analysis was done in two stages. Properties typical of a depleted oil reservoir were used to conduct a baseline during the first stage of the analysis. Additional analyses described in the next section were conducted using distributions of formation properties typical of the five geologic settings currently considered for CO_2 storage. These properties are presented in Table 2.3-2.

Table 2.3-2. Representative material properties for a depleted reservoir used for CO_2 storage.

	Young's modulus (GPa)	Poisson ratio	porosity	permeability (mD)	Biot-Wills coefficient
sand reservoir	15	0.25	0.20	100	1
shale confining	15	0.25	0.20	0.1	1
casing (steel)	200	0.30	0.01	0.01	1
screen (steel)	200	0.30	0.20	100	1

Solution method and codes

The analyses were solved early in the investigation using three different codes (ABAQUS, COMSOL, and FLAC) designed to solve problems of coupled poroelasticity. These codes are widely used and readily available. Boundary conditions and the governing equations can be modified as needed to represent a particular problem using these codes. We avoided using dedicated reservoir geomechanics codes because the problem we solve is somewhat unconventional and it was difficult to implement in some dedicated codes. In other cases, prohibitive license fees limited code accessibility and would make our results difficult to duplicate.

COMSOL and ABAQUS use the Galerkin finite element method to solve the coupled problem defined by Eqs. 2.3-1 through 2.3-4 and the boundary conditions in Table 2.3-1. Both COMSOL and ABAQUS use adaptive time stepping and provide considerable flexibility in meshing. FLAC uses a finite difference formulation that is integrated with a fixed time step.

Preliminary analyses conducted using FLAC showed that results were generally similar to the other codes, but the run times using FLAC were much longer. Moreover, mesh refinement was limited in FLAC and this restricted the fidelity of displacement measurements in the vicinity of the well. Early evaluations of FLAC indicated that modification of the code would be needed before it was practical to simulate the conditions outlined above, so the use of this code was discontinued.

2.3.2. RESULTS

The constant pressure at the wellhead results in an injection rate of that decreases with time, but is approximately 0.6 L/s (100 gpm) throughout all but the first few hours of the simulation.

Verification

Initial verification was done using the 1D analytical solution by *Wang* [2000]. An analytical solution to a 2D problem resembling a well is unavailable to our knowledge, so verification was accomplished by evaluating the internal consistency of analyses of the same problem using different numerical codes. Preliminary analyses were conducted with different mesh densities, and meshes were selected that were fine enough for the results to be relatively insensitive to mesh density. Pressures and displacements were determined along radial and vertical lines, and the results differ by less than a few percent in most places. The largest relative error is approximately 3.7%, and it occurs in the vertical displacement in the confining unit

(Figure 2.3-2c). Details of the errors varied with the mesh design and size. A few percent is an acceptable level of numerical error for this study.

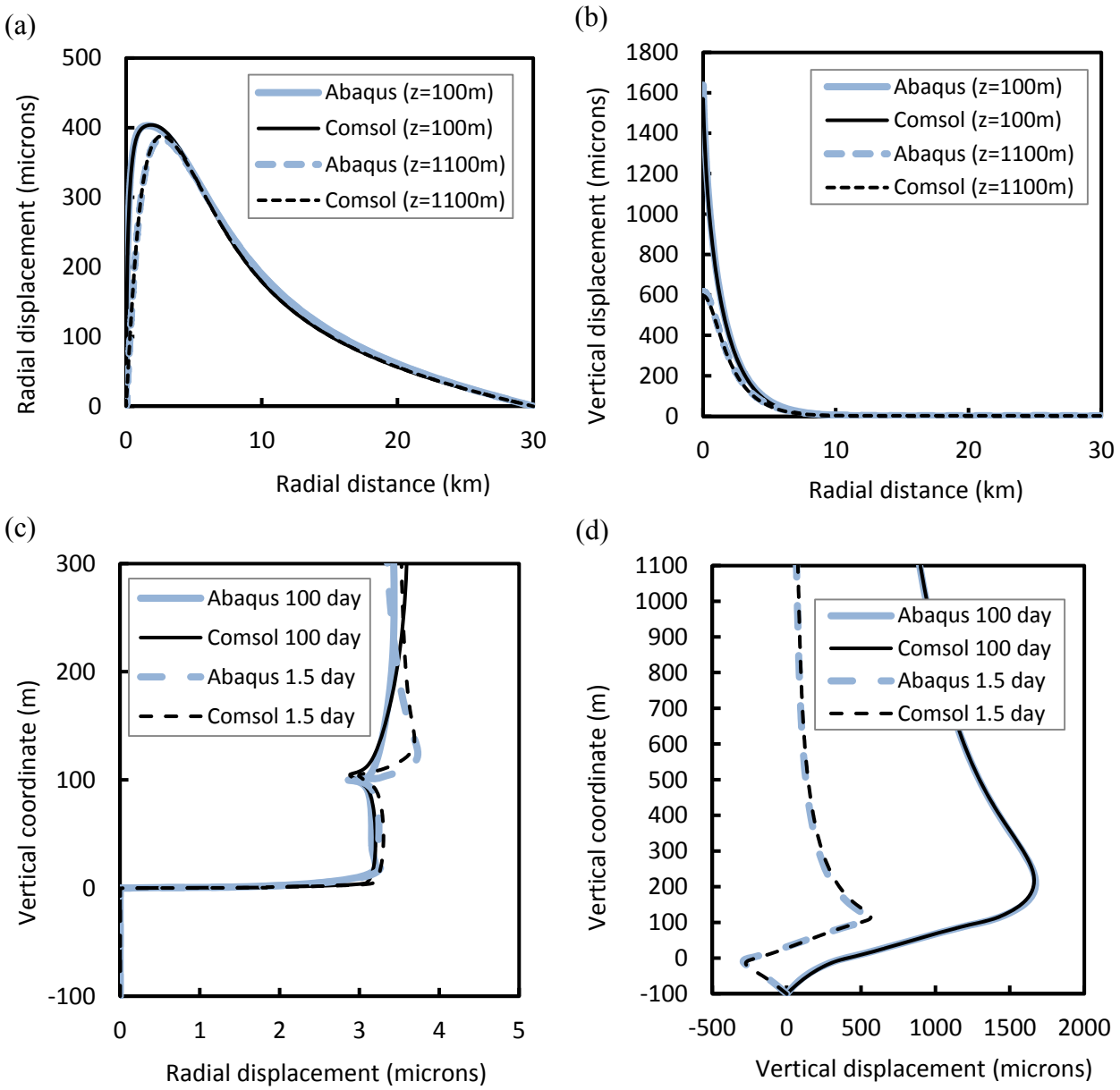

Figure 2.3-2. Displacements at t = 100 days in (a) radial displacement as a function of radial distance at z = 100 m (solid line) and z = 1,100 m (dashed and labeled "surface" to indicate the line is at the ground surface, (b) vertical displacement as a function of radial distance at z = 100 m (solid line) and z = 1,100 m (dashed), (c) radial displacement profile , and (d) vertical displacement profile at r = 0.1 m (wellbore).

Displacement profiles

The profiles after 100 days of injection indicate that displacements are typically in the range of 100 to 1000s of microns. The radial displacement of the reservoir is 6 microns outward at the wellbore, but it increases with distance and reaches a maximum of 400 microns approximately 1.6 km from the well (Figure 2.3-2). The confining unit is displaced radially

outward, and the displacement diminishes with distance upward from the contact with the reservoir (Figure 2.3-2a). The pattern is similar to the underlying reservoir, but the radial displacement reaches a slightly smaller maximum of approximately 385 microns at a distance of 2.5 km. The mismatch between the radial displacements in the reservoir and at the ground surface causes shear within the confining unit that is parallel to the horizontal contact.

The confining unit displaces upward, with a maximum uplift of 600 microns at the ground surface wellbore. The vertical displacement decreases with radial distance and is approximately 4 microns at r = 10 km (Figure 2.3-2b). Maximum uplift of the upper contact with the confining unit (z = 100 m) is roughly 1600 microns, several times greater than at the ground surface, and it decreases to 6 microns at approximately r = 10 km.

Radial displacement along the well casing is approximately 3 microns at t = 100 days and this is slightly less than the displacement at t = 1.5 days. A similar radial displacement is observed in the confining layer, and the overall radial displacement is nearly uniform along the well (Figure 2.3-2c).

Deformation pattern in the formation

The pattern of deformation evolves as the pressurized region spreads outward away from the injection well (Figure 2.3-2). The reservoir is displaced radially outward in the direction of flow and it also expands upward in the direction of the ground surface. This causes the reservoir to dilate and the overlying confining unit is lifted upward, doming the ground surface with a maximum of approximately 0.6 mm of uplift after 100 days of injection (Figure 2.3-2b and 2.3-2d).

Pressurization creates a pattern of compressive and tensile strain that evolves with time (Figure 2.3-3). After 1 day of injection, the pressure front has moved roughly 600 m from the well and the reservoir is characterized by tensile vertical strain (relative to initial conditions) within the pressurized region. The zone of tensile vertical strain greater than 1E-8 forms a bulb that extends ahead of the pressure and into the confining units (Figure 2.3-3a). The vertical strain is compressive in the confining units overlying and underlying the pressurized region. Vertical strain is the derivative of the vertical displacements in Figure 2.3-2.

The radial strain is tensile in the vicinity of the well, but it decreases and becomes compressive with distance from the well. Radial strain is particularly large in proximity of the well screen, but the entire thickness of the confining unit is also affected. The region of compressive radial strain approximately corresponds to the bulb-like region of tensile vertical strain that extends beyond and above the pressure front (Figure 2.3-3a).

The circumferential strain is tensile everywhere, which differs from the radial and vertical strains, which are tensile in some locations and compressive in others. The tensile radial strain is particularly large in the vicinity of the well bore, and it drops off with distance much like the pressure does (Figure 2.3-3a).

The pressure and general pattern of deformation expand outward with time. After 10 days of injection the pressure front in the simulation is approximately 1,500 m from the injection well, and it moves out to 4,000 m after 100 days of injection. The vertical strain is compressive overlying the pressurized zone and it remains tensile within the reservoir (Figure 2.3-3a). The bulb of tensile vertical strain and compressive radial strain moves outward with time and stays in

the vicinity of the pressure front (Figure 2.3-3a). The circumferential strain also moves outward with the pressure.

The strain field evolves in a distinctive pattern in the vicinity of the reservoir, but the evolving strain field also extends into the confining unit. This comes as no surprise because it is well known that the ground surface deforms in response to injection at depth, but it is clear that all the strain components are affected, even at depths that are shallow relative to that of the reservoir.

Borehole tiltmeters measure deformation gradients, dv/dz and du/dz, or du_r/dz in axial symmetry, where u_r is the displacement in the radial direction. A bulb of negative tilt evolves at early time in the confining unit over the pressurized zone, and a thin zone of positive tilt occurs in the underlying confining unit (Figure 2.3-3b). These tilts are a response to the outward radial displacement of the pressurized zone. A zone of positive tilt developed at the ground surface after 10 days and it grew considerably between 10 and 100 days (Figure 2.3-3c). This zone of positive tilting is a result of the uplift of the ground surface.

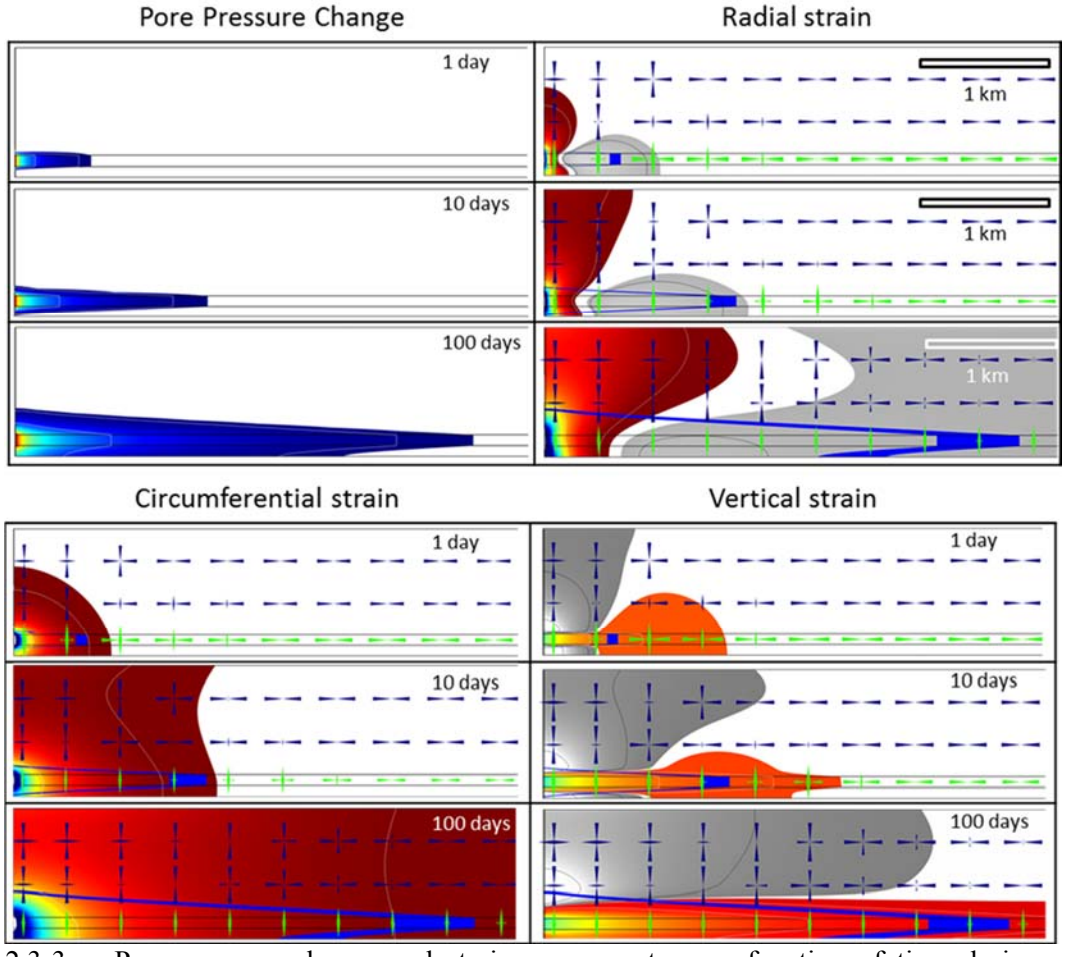

Figure 2.3-3a. Pore pressure change and strain components as a function of time during constant pressure (1 MPa) injection. For Pore Pressure plot the lower limit for plotting is 0.5E4 Pa, and contour lines are at 0.01 and 0.1 MPa. In strain plots, the color flood is tensile vertical strain > 5E8, grey is compressive strain < -5E-8. Strain in the white region is between +/- 5E-8. Arrow symbols show normalized vertical and horizontal strain. Strain contours are at +/- 1E-7 and +/- 1E-6. Blue band in the strain plots is where the pore pressure ~0.01 MPa.

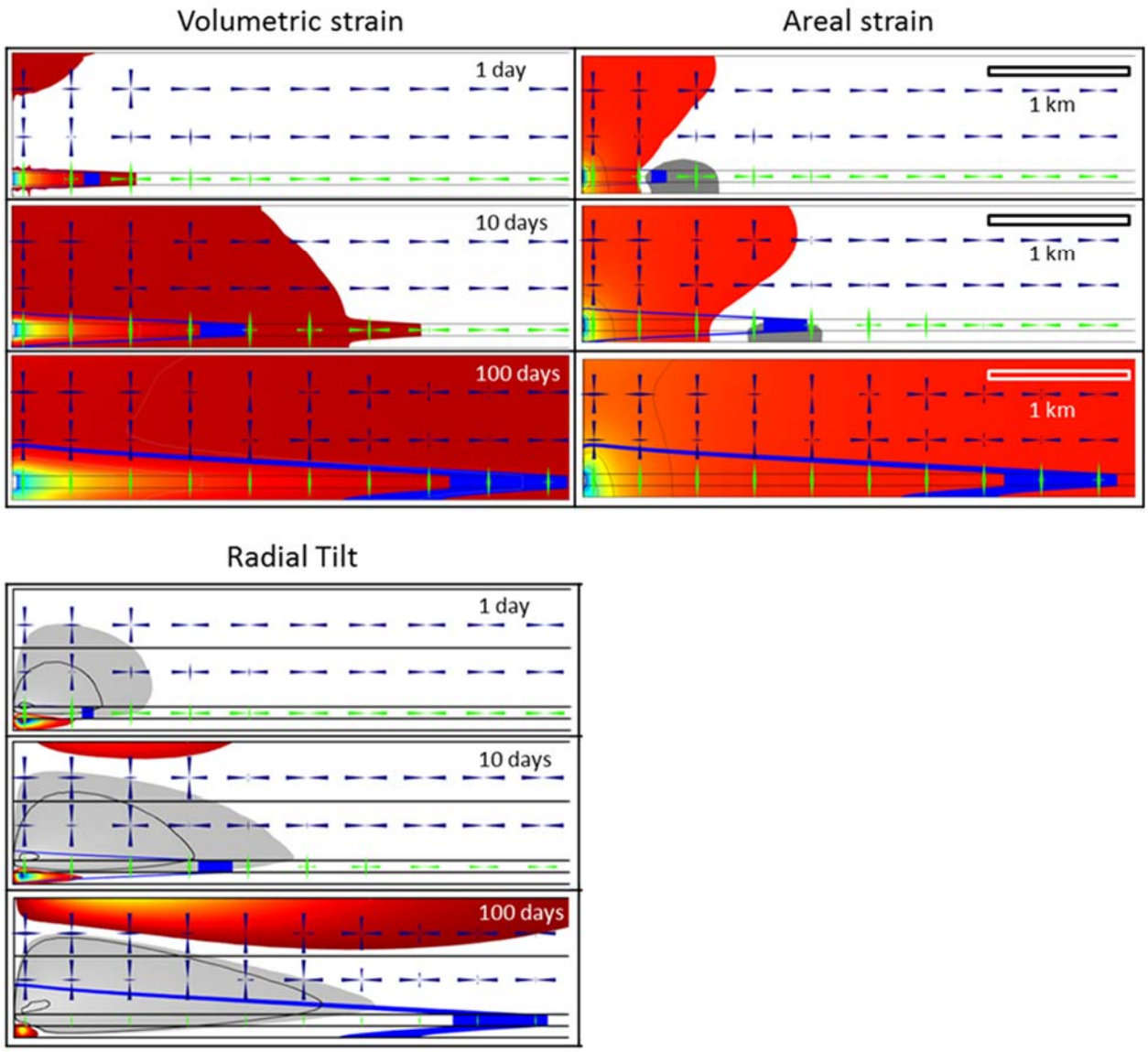

Figure 2.3-3b. Volumetric and areal strain components and radial tilt as a function of time in cross-section during constant pressure (1 MPa) injection. The well is at the lower left. The color flood is tensile strain or positive tilt > 5E8, grey is compressive strain or negative tilt < -5E-8. Strain in the white region is small and between +/- 5E-8. Arrow symbols show normalized vertical and horizontal strain. Strain contours are at +/- 1E-7 and +/- 1E-6. Blue band in the strain plots is where the pore pressure change > 0.01 MPa.

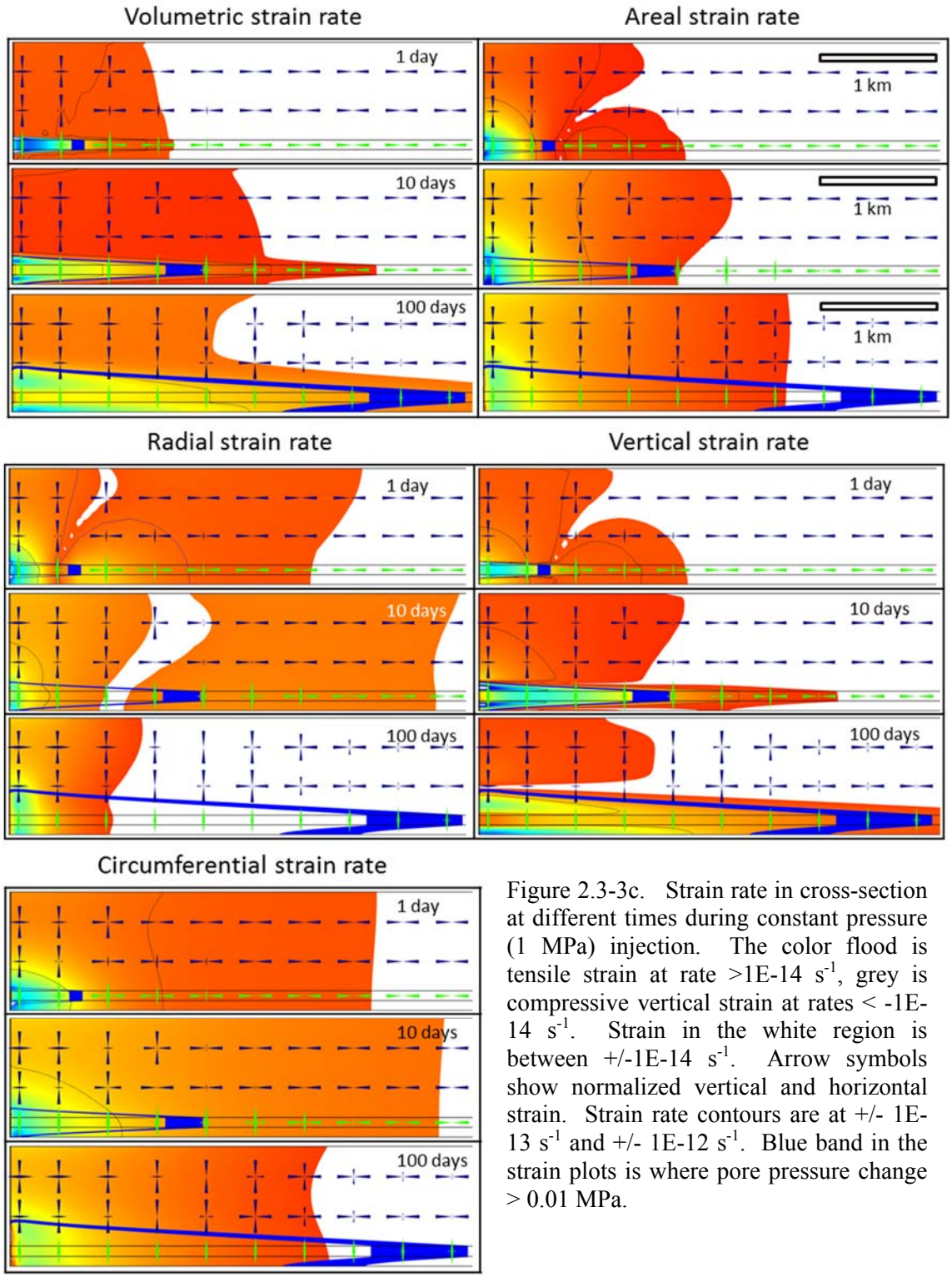

Figure 2.3-3c. Strain rate in cross-section at different times during constant pressure (1 MPa) injection. The color flood is tensile strain at rate >1E-14 s^{-1}, grey is compressive vertical strain at rates < -1E-14 s^{-1}. Strain in the white region is between +/-1E-14 s^{-1}. Arrow symbols show normalized vertical and horizontal strain. Strain rate contours are at +/- 1E-13 s^{-1} and +/- 1E-12 s^{-1}. Blue band in the strain plots is where pore pressure change > 0.01 MPa.

Radial deformation in the vicinity of the wellbore

Radial displacement is generally outward in the vicinity of the well, but it appears that details of this process may be surprising. The outward displacement is a few microns at the borehole face, but it increases to more than 10 microns at a radial distance of 1 m in the baseline example (Figure 2.3-4). The radial displacement appears to result from two primary effects. One is caused by the stress loading the face of the bore and it will be called "elastic only" loading. The other effect results from fluid pressure within the formation, and it will be called "poroelastic only" loading.

The elastic-only case was analyzed by setting the fluid pressures at the inner and outer radial boundaries equal to zero, and keeping the total stress on borehole face equal to the injection pressure. This eliminates flow caused by the boundary conditions, but it is still possible for flow to occur as a result of applying the elastic load. An analysis of the poroelastic-only case was conducted by setting the total stress on the borehole face equal to zero and keeping the fluid pressure as specified in the original problem.

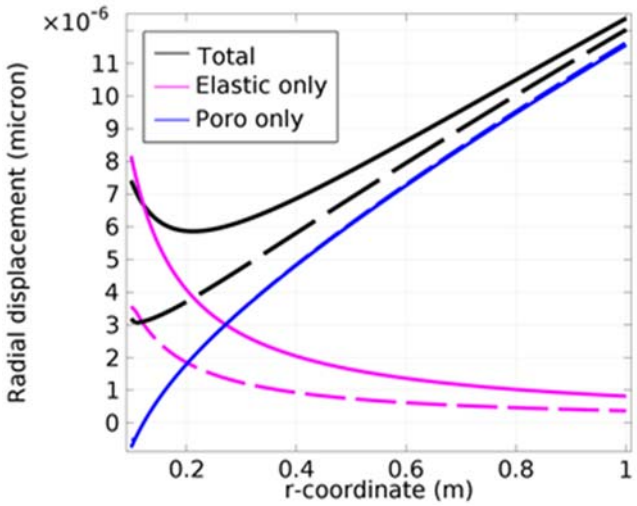

Figure 2.3-4. Radial displacement in the vicinity of the borehole. Displacements due to pressure on an impermeable elastic solid (magenta). Displacement due to internal fluid pressure only (blue). Open hole (solid) and cased hole (dashed). $t = 100d$. $z = 50$ m. Borehole pressure = 1 MPa.

Displacements in the vicinity of a pressurized open hole (without casing) are approximately 7.4 microns at the borehole face, they decrease to 6 microns at $r = 0.2$ m, and they increase beyond that. Thus, the minimum displacement is in the formation approximately 10 cm out from the borehole wall, rather than at the screen itself. This occurs because of the two loading effects. The elastic-only load creates displacements of approximately 8.1 microns at the borehole face, but they decrease sharply in the formation and are less than 1 micron at $r = 1$ m (Figure 2.3-4). In contrast, displacements from the poroelastic-only case are actually inward by -0.7 micron at the borehole face. They increase with distance and are roughly equal to the displacements from the elastic-only loading at $r \approx 0.3$ m. The total displacement is approximately the sum of the two effects, so it is dominated by the elastic loading of the borehole face at $r < 0.1$ m, and by poroelastic loading for $r > 1$ m.

Including a casing and well screen in the analysis reduces the displacement from the elastic-only loading, so the total displacement in the vicinity of the well bore is reduced to roughly half of the case that considers only an open hole (Figure 2.3-4). Negative displacements at the well face due to poroelastic loading also occur when a casing is present.

Displacements from poroelastic processes are small at the borehole face, but they may be significant. Poroelastic effects cause inward displacements in a small region near the borehole where the integrity of the seal between casing and the formation is important. Negative

displacements would tend to hold incipient flaws closed, potentially limiting their growth and reducing the onset of leakage.

2.3.3 VERTICAL PROFILES ALONG THE INJECTION WELL AND A MONITORING WELL

Deformation of the injection wellbore evolves with time in response to the fluid pressure transient, and both elastic-only and poroelastic effects are important. The wellbore pressure increases abruptly and is held constant, but the fluid pressure in the formation changes with time, even in close proximity to the well (Figure 2.3-5a). The fluid pressure at r = 1 m increases and stabilizes in a few days in the formation, but the transient in the confining unit persists for the duration of the simulation. Pressurization causes the screen to bulge outward by several microns, with slightly more displacement in the reservoir than in the confining unit at t = 20 s (Figure 2.3-3a). This occurs because the effective elastic modulus of the low permeability confining unit is greater (more similar to the undrained modulus) than that of the higher permeability reservoir at this time.

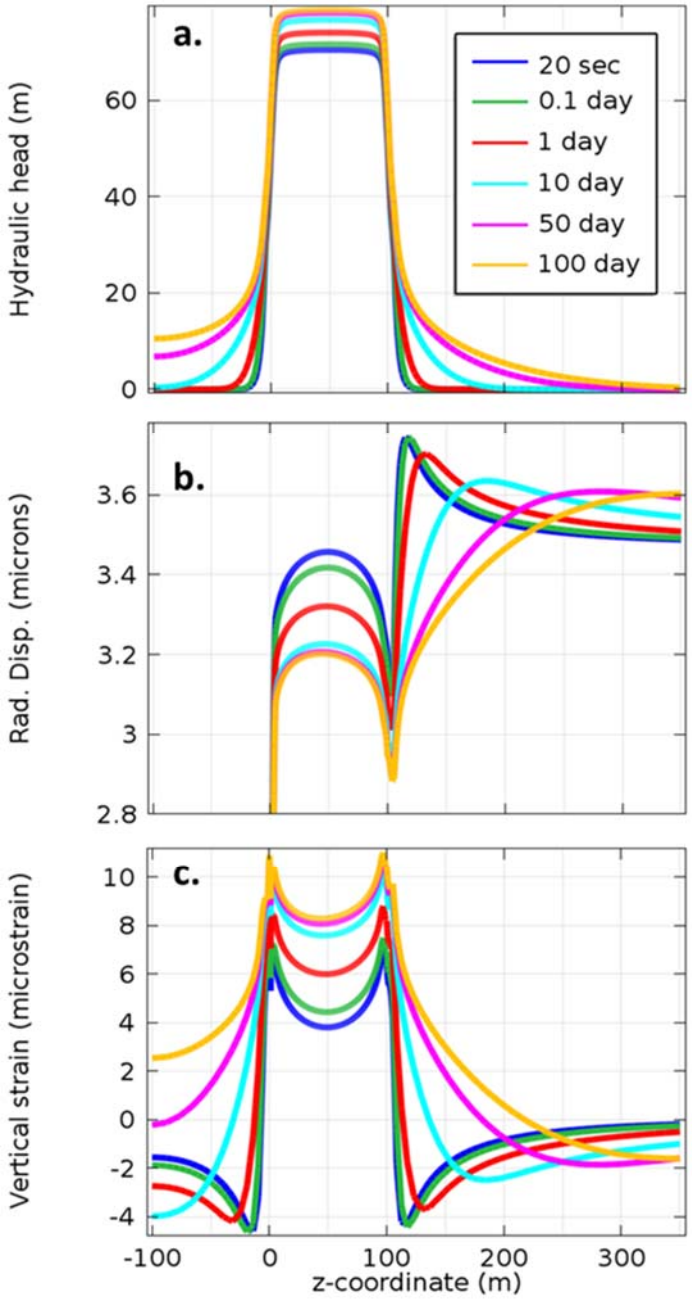

Figure 2.3-5. Profiles along the wellbore. a.) fluid pressure in formation at r = 1.0 m as function of time. b.) radial displacement of casing, r = 0.1 m. c.) vertical strain of casing. All lines use legend in a.).

The relative magnitudes in radial displacement reverse with time, however, and after a few hours the radial displacement in the confining unit is greater than that in the reservoir (Figure 2.3-5b). This occurs because of the near wellbore poroelastic effect that causes negative displacements in close proximity to the wellbore, as explained in the previous section (e.g. Figure 2.3-4). The inward displacement grows for several days and then equilibrates as the pore pressure equilibrates.

Radial displacement at early time in the confining unit increases relative to the initial, elastic-only effect, (the casing bulges outward from 3 to 3.2 microns). This occurs radially

outward displacements within the reservoir (Figure 2.3-2a and Figure 2.3-4) drag the confining unit outward. Radial displacements in the confining unit decrease with time as the pore pressure increases.

Vertical strain along the axis of the casing also changes with time, with tensile strain increasing to approximately 10^{-5} adjacent to the reservoir. Axial compression occurs in the casing completed in the confining units early in the injection history. The region of axial compression moves into the confining unit with time, roughly tracking the pressure change within the formation (Figure 2.3-2).

Strains along a vertical line 1 km from the injection well are smaller and have a somewhat different pattern than those at the injection well (Figure 2.3-6). The axial strain increases with time as the reservoir expands and it becomes negative in the confining unit. This patter resembles the one at the well, except the magnitudes are less. Radial strain is approximately and order of magnitude smaller than the axial strain, and it also changes sign from the reservoir into the confining unit. It is approximately +/-0.2 με after 4 months. The deformation gradient (tilt) increases with time and reaches a maximum of 0.8 μrad approximately 100 m above the upper contact of the reservoir (Figure 2.3-6).

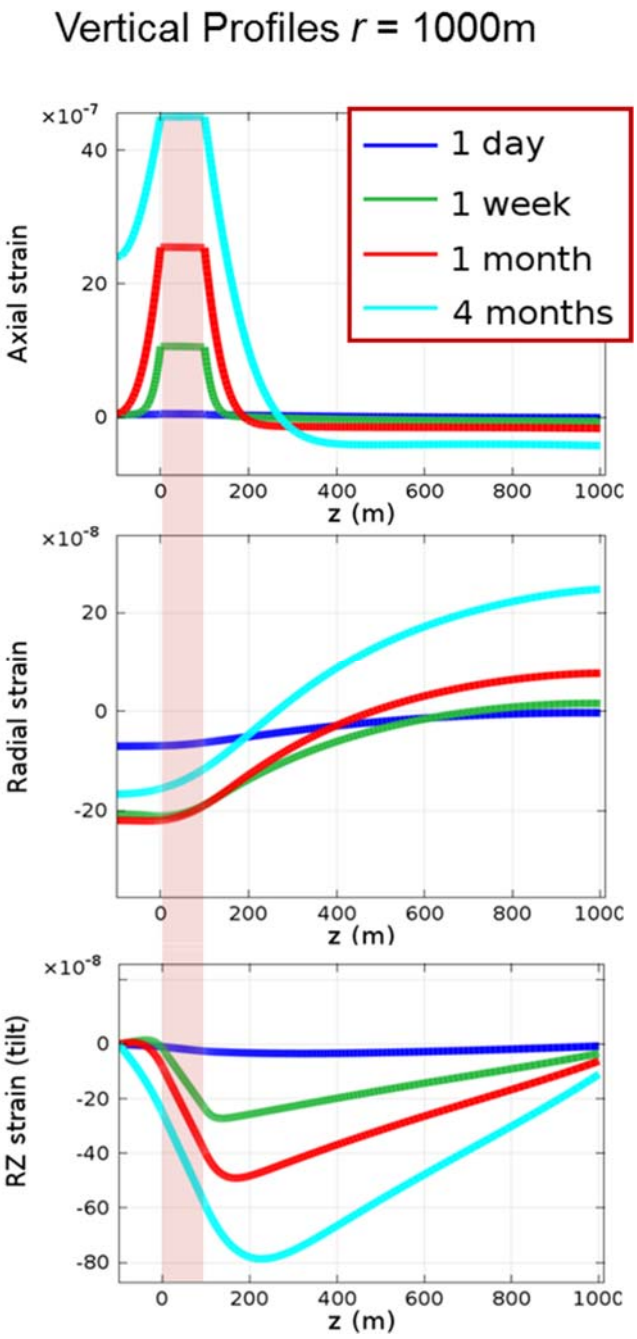

Figure 2.3-6. Vertical profiles of axial strain, radial strain and tilt at r = 1,000 m as a function of time.

2.3.4 Deformation Time Series

Deformation at the well was simulated as a function of time and the plot of these data give the hydromechanical type curves (Figure 2.3-7). This signal simulates the data from an in situ instrument. The data increase rapidly as the well is pressurized and they continue to increase with time in the range of με and μm (Figure 2.3-7).

Similar data were measured at four points, in the reservoir and confining unit, and two at the injection well. r = 0.1 m is the injection well, and at r = 1,000 m represents a monitoring well.

Deformation at the well is characterized by an abrupt change when the well is pressurized (not shown, but all variables start at 0), and then gradual changes after that. The casing stretches circumferentially by as much as 30 με and compresses radially by 15 με and transient changes in magnitude are less than 10 percent over $0.1d < t < 100d$. (Figure 2.3-8a1 and 2.3-8b1). The casing stretches axially (vertical strain) from 4 to 8 με in the center of reservoir (z = 50 m), but the signal is much different in the overlying confining unit (z = 150 m). Here the casing is compressed axially and the compression increases to 3 at t = 3 days. After that, the casing unloads axially and begins to stretch, ultimately reaching 3 με tensile strain at t = 100 days (Figure 2.3-5c).

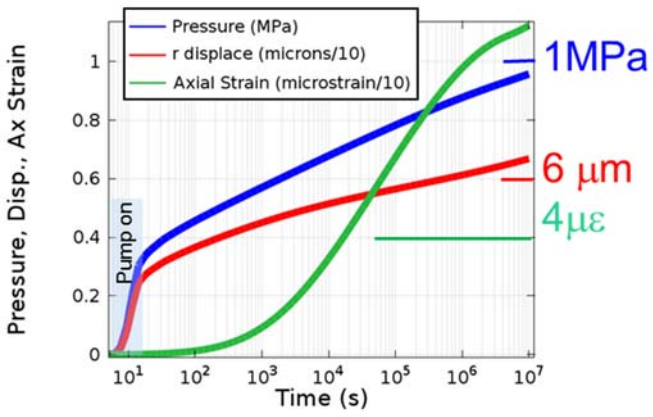

Figure 2.3-7. Pressure, displacement and axial strain at the casing adjacent to the mid-height of the reservoir (z = 50 m).

Reversal of the sign of the axial strain of the casing occurs as the confining unit becomes pressurized (Figure 2.3-5a). The strain occurs in the steel casing, but it results from the pressure change in the adjacent formation. This suggests that it may be feasible to track the pressure change in the confining unit behind a solid casing by measuring deformation of the casing, a technique that could be used to characterize the hydraulic diffusivity of the confining unit.

Strain magnitudes are in the microstrain range in the reservoir at r = 1,000 m, and they are in the tenths of a microstrain range in the overlying confining unit (r = 1,000 m, z = 500 m). The pattern of the time series in the reservoir is quite different from the pattern in the confining unit. In the reservoir, the formation compresses radially and extends vertically and circumferentially. The radial strain decreases (compresses) in advance of the pressure change. This suggests that radial strain could be an indicator of a future change in pressure. Interestingly, this effect also occurs in the confining unit, with compressive radial strains and tensile circumferential strain occurring in advance of the arrival of the pressure front in the underlying reservoir. This suggests that horizontal strains in confining units could be used to estimate pressure distribution at depth.

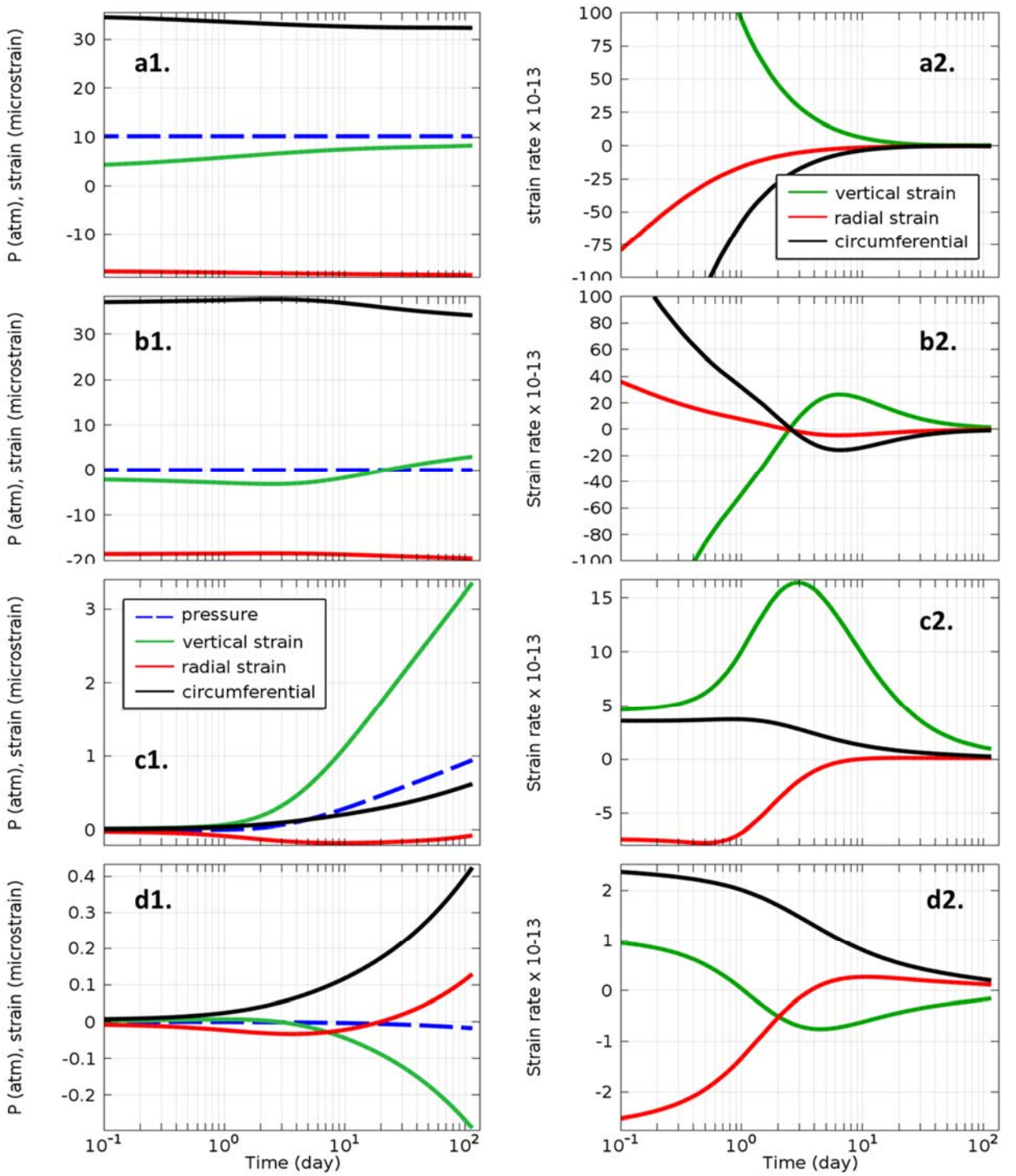

Figure 2.3-8. Pressure and strain (left column) and strain rates (right column) at selected points (a.) well screen; r = 0.1 m, z = 50 m; and (b.) well casing; r = 0.1 m, z = 150 m, (c.) monitoring point in reservoir; r = 1,000 m, z = 50 m, (d.) monitoring point in confining unit; r = 1,000 m, z = 500 m.

2.4 EFFECTS OF RESERVOIR TYPE

CO_2 storage is proposed for a variety of formations and the properties of those formations will affect the magnitude of the deformation signal. For example, the strain is expected to increase when Young's Modulus decreases and all else remains constant. The magnitude of the change will depend on the magnitude of the change in properties, of course, but it would also be affected by variability in other properties.

The objective of this section is to evaluate how changes in material properties within the range constrained by the types of reservoirs proposed for CO_2 storage. This will allow us to evaluate the uncertainty in predictions of deformation in Section 2.3 that result from uncertainty in material properties.

2.4.1 METHODS

The general approach we used was to identify the distribution of material parameters described in the literature for different formation types, then sample that distribution and conduct analyses of deformation with the resulting combinations of parameters. This approach resembles a Monte Carlo analysis. This resulted in approximately 1000 different parameter sets, which were used in the simulation described in Section 2.3. The strain and tilt signals resulting from this suite of simulations were evaluated to characterize the variability caused by changes in material properties.

CO_2 storage is being considered in five different types of formations; a.) depleted oil-gas reservoirs; b.) deep saline aquifers; c.) coal beds; d.) organic shales; d.) basalts. We reviewed the poroelastic properties in these, and other types of formations and we compiled the results in a database. We considered three of these formations (depleted gas/oil reservoir, deep saline aquifer and coal beds) for further analysis. We did not consider organic shales because their permeability is extremely low and it will be infeasible to store CO_2 in shales using the conceptual model for flow through porous media adopted in Section 2.3. Fracturing techniques would be needed to increase the rate at which CO_2 could be injected into shales, and including the effects of hydraulic fractures in the simulation was beyond the scope of the analysis we conducted for this research. It could be considered later, however. Basalts were also omitted from the analysis because the poroelastic parameters available for basalts were too limited to provide an adequate basis for evaluation.

Poroelastic Parameters Database

Poroelastic parameters describing naturally occurring rocks relevant to CO_2 storage were compiled from published sources. We conducted a literature review and compiled a database of parameters (Table 2.4-1). The database contains formation properties and geometries from approximately 45 locations, including 12 European and 33 US sites. The data include permeability, porosity, elastic modulus, Poisson's ratio, Biot-Willis poroelastic coefficient, and geometric aspects like depth and formation thickness. The data can be grouped by the type of storage reservoir, including depleted oil and gas reservoir, deep saline aquifer, coal bed,-organic shale, and basalt formation. The database also includes measurements of poroelastic properties of geologic materials from other settings. These data are included to provide estimates of properties of confining units, or to generate realistic bounds of parameters.

Table 2.4-1. Poroelastic Parameter Database.

	Rock Type		Permeability, *k* [mD]	Young's Modulus, E [Gpa]	Poisson's ratio (ν)	Biot-Willis Coefficient (α)	Biot Modulus, M [Gpa]	Reference
Igneous	**Tuff**	Daqing Rhyolite/ tuff	0.29	54.32				Qingling et al. (2008)
		Yucca Mountain	1.01E-02	35	0.3	1		Mabmann et al. (20110
	Basalt	DSDP Hole 504B (316 - 326m)		53				Bauer et al. (1985)
		DSDP Hole 504B (579 - 584m)		59				Bauer et al. (1985)
		DSDP Hole 504B (888 - 898m)		23				Bauer et al. (1985)
		DSDP Hole 504B (1116 - 1126m)		67				Bauer et al. (1985)
		DSDP Hole 504B (1171 - 1176m)		66				Bauer et al. (1985)
		DSDP Hole 504B (1279 - 1288m)		75.5				Bauer et al. (1985)
		DSDP Hole 504B (1327 - 1332m)		52				Bauer et al. (1985)
		Hanfold				0.23	23.69*	Palciauskas and Dominico (1989), Domenico and Schwartz (1998)
	Granite	Charcoal	1.00E-04	~48.28*	0.27	0.27	83.52*	Detourney and Cheng (1993) from Rice and Cleary (1973)
		Westerly	4.00E-04	37.5*	0.25	0.47	75.96*	Detourney and Cheng (1993) from Rice and Cleary (1973)
		Intensely Fractured		640	0.25			Arslan and Rosassanchez (2008)
		Weathered		750	0.2			Arslan and Rosassanchez (2008)
		Competent		74	0.2			Arslan and Rosassanchez (2008)
		Barre	~2.84	60	0.13	0.72		Paterson (1978)
		Barre	1.62E-4.06E-	60	0.13			Selvadurai et al. (2005)

			4					
		Avro (Dry)		~71.6				Hudson et al. (2009)
		Avro (Distilled)		~68.5				Hudson et al. (2009)
		Avro (Formation)		~66.6				Hudson et al. (2009)
		Avro (Saline)		~66.8				Hudson et al. (2009)
		Aue		48	0.19			Yoon et al. (2012)
		Stripa (6.03m)		59.97	0.19			Carlsson (1977)
		Stripa (7.68m)		56.46	0.17			Carlsson (1977)
		Stripa (8.53m)		59.94	0.19			Carlsson (1977)
		Stripa (10.10m)		61.68	0.22			Carlsson (1977)
		Stripa (11.44m)		59.06	0.19			Carlsson (1977)
	Granodiorite	Coso Geothermal Field, California		74.75	0.274			Morrow et al. (2006)
		Coso Geothermal Field, California		102.9	0.312			Morrow et al. (2006)
	Diorite	Aspo		76	0.25			Andersson (2007)
	Stillwater Complex	Ingeous intrusion: valley site		124.8	0.31			Johnson et al. (2003)
		Ingeous intrusion: mountain site		48.3	0.29			Johnson et al. (2003)
		Ingeous intrusion: mountain site		86.2	0.3			Johnson et al. (2003)
Metamorphic	**Marble**	Tennesse	1.00E-04	60*	0.25	0.19	118.11*	Detourney and Cheng (1993) from Rice and Cleary (1973)
		Morawica				0.23		Fabre and Gustkiewicz (1997)
		Vermont				0.64		Paterson (1978)
Sedimenta	**Coalbeds**	Subbituminous Anderson	262	1.38	0.35			Wang et al. (2009)
		High-volatile Bituminous Gilson	0.04	1.38	0.35			Wang et al. (2009)

		High-volatile Bituminous Blackwater-high pressure (A)	4.29	1.6	0.38			Wang et al. (2009)
		High-volitaile Bituminous Blackwater-low pressure (B)	1.83	1.8				Wang et al. (2009)
		Ardley	2	3	0.3			Bustin et al. (2009)
		Wolf Mountain	5	3	0.3			Bustin et al. (2009)
		Quinsam	3	3	0.3			Bustin et al. (2009)
		Krasnodonetsk Coal		5.5	0.21			Nasedkina et al. (2008)
		No. 10		1	0.39			Yao et al. (2011)
	Chalk	Lixhe				0.91	2.19*	Fabre and Gustkiewicz (1997)
	Limestone	Tonnerre				0.53	8.26*	Fabre and Gustkiewicz (1997)
		Villeperdue				0.41		Fabre and Gustkiewicz (1997)
		Chauvigny				0.69	8.73*	Fabre and Gustkiewicz (1997)
		Lavoux				~0.77	~7.76*	Fabre and Gustkiewicz (1997)
		Louny				0.8		Fabre and Gustkiewicz (1997)
		General				0.69	14.57*	Palciauskas and Dominico (1989), Domenico and Schwartz (1998)
		Indiana		30.51*	0.17	0.71	20.21*	Palciauskas and Dominico (1989), Domenico and Schwartz (1998)
		General		6.6	0.2			Yao et al. (2011)
		Salem				0.66		Paterson (1978)
		Anstrude				0.82		Nguyen et al. (2011)
		wacke texture	0.03	199.37*	~0.3			Adam (2004)
		mud texture	0.03	222.67*	~0.3			Adam (2004)
		grain texture	5.5	201.88*	~0.3			Adam (2004)
		grain texture	1.2	200.95*	~0.3			Adam (2004)
		grain texture	0.43	201.88*	~0.3			Adam (2004)
		bound texture	0.31	198.39*	~0.3			Adam (2004)

		pack texture	25	239.70*	~0.3			Adam (2004)
		wacke texture	103	222.67*	~0.3			Adam (2004)
		mud texture	432	219.03*	~0.3			Adam (2004)
		Pure $CaCO_3$		83.8*	.17*			Averbakh et al. (2010) from Mavko et al. (1998) and Bass (1995)
	Marl/ Muddy Dolomite	Lower Russ (Weathered)	~86.79	~42.75	~0.22			Abdullatif (2010)
		Lower Russ (Less Weathered	~53.68	~42.75	~0.22			Abdullatif (2010)
		Middle Russ	~84.57	~80.32	~.21			Abdullatif (2010)
		Kamenishy mine of Buturlin Region	123		0.12			Averbakh et al. (2010)
		Pure $CaMg(CO_3)_2$		118.82	0.29			Averbakh et al. (2010) from Mavko et al. (1998) and Bass (1995)
	Periclase	Pure MgO		309.56	0.18			Averbakh et al. (2010) from Mavko et al. (1998) and Bass (1995)
	Mudstone	General				0.95	8.82*	Palciauskas and Dominico (1989), Domenico and Schwartz (1998)
		General		~2.78	~0.32			Peng (2007)
		General		1.3	0.37			Yao et al. (2011)
		Sandy Mudstone		5.68	0.23			Peng (2007)
		Sandy mudstone: Xinji coal mine, Huainan coalfield		22.96	0.22			Meng et al. (2006)
		Rhinestreet, dark gray silty		31	0.18			Evans et al. (1989)
		Rhinestreet, black silty		20	0.19			Evans et al. (1989)
		Middlesex, black silty		17	0.13			Evans et al. (1989)
		West River, dark gray silty		26	0.17			Evans et al. (1989)
		Mercia			250			Chandler and Davis (1973)

		Mercia			2			Chandler and Davis (1973)
		Xinji coal mine, Huainan coalfield		10.35	0.24			Meng et al. (2006)
		Callovo-Oxfordian Argillite	1.01E-05	6*	.25*	0.75		Giraud et al. (2009)
	Shale	Sandy Shale		3.24	0.35			Peng (2007)
		Shale		~4.79	~0.35			Peng (2007)
		Krasnodonetsk Clay Shale		44	0.2			Nasedkina et al. (2008)
		Krasnodonetsk Sand Shale		30	0.4			Nasedkina et al. (2008)
		General Shale	1.00E-05	4.4	0.219			Roshan and Rahman (2011)
		Gulf of Mexico Shale	10 - 2500	6.96*	~0.20			Odumosu et al. (2007)
	Siltstone	Xinji coal mine, Huainan coalfield		32	0.3			Meng et al. (2006)
		Pipe Creek		30	0.11			Evans et al. (1989)
	Salt Dome	Bottom Layer (elastic)						Morency et al. (2011)
		Top Layer (elastic)						Morency et al. (2011)
		Brine-saturated aquifer						Morency et al. (2011)
		CO_2-saturated aquifer						Morency et al. (2011)
		Damaged salt matrix filled with brine		0.2	0.33			Dell-Isola et al. (2010)
	Sandstones	Ruhr	0.2	~29.38*	0.12	0.65	40.62*	Detourney and Cheng (1993) from Rice and Cleary (1973)
		Berea	190	~13.74*	0.17	~0.78	~12.72*	Detourney and Cheng (1993) from Rice and Cleary (1973)
		Weber	1	27.45*	0.15	0.64	~28.72*	Detourney and Cheng (1993) from Rice and Cleary (1973)
		Boise	800	~11.13*	0.15	0.85	4.88*	Palciauskas and Dominico (1989), Domenico and Schwartz (1998)

		Ohio	5.6	~16.09*	0.18	0.74	8.78*	Palciauskas and Dominico (1989), Domenico and Schwartz (1998)
		Pecos	1	~13.68*	0.16	0.83	10.29*	Palciauskas and Dominico (1989), Domenico and Schwartz (1998)
		Miechowice				0.4		Fabre and Gustkiewicz (1997)
		Thorez 2				0.1		Fabre and Gustkiewicz (1997)
		Thorez 1				0.14		Fabre and Gustkiewicz (1997)
		Nowa Ruda 1				0.39		Fabre and Gustkiewicz (1997)
		Nowa Ruda 2				0.29		Fabre and Gustkiewicz (1997)
		Nowa Ruda s				0.67		Fabre and Gustkiewicz (1997)
		Centrum				0.41		Fabre and Gustkiewicz (1997)
		Pniowek				0.55		Fabre and Gustkiewicz (1997)
		Fontainebleau before thermal treatment				0.12	70.83*	Fabre and Gustkiewicz (1997)
		Fontainebleau after thermal treatment				0.77	11.04*	Fabre and Gustkiewicz (1997)
		Vosges Brown				0.74		Fabre and Gustkiewicz (1997)
		Vosges Yellow before thermal treatment				0.58	22.13*	Fabre and Gustkiewicz (1997)
		Vosges Yellow after thermal treatment				0.59	21.75*	Fabre and Gustkiewicz (1997)
		Vosges Red before thermal treatment				0.64	15.56*	Fabre and Gustkiewicz (1997)
		Vosges Red after thermal treatment				0.76	13.1*	Fabre and Gustkiewicz (1997)
		Kayenta				0.76	16.31*	Palciauskas and Dominico (1989), Domenico and Schwartz (1998)
		Rotliegend (GS10)	2.15		0.22	0.78		Trautwein and Huenges (2005)
		Rotliegend (GS19)	16.5		0.24	0.9		Trautwein and Huenges (2005)
		Rotliegend (GS20)	0.14		0.21	0.61		Trautwein and Huenges (2005)

		Fine-grained		~19.65	.11-.18			Peng (2007)
		Medium-grained		~12.53	.1-.16			Peng (2007)
		General		3.8	0.22			Yao et al. (2011)
				17.97*	0.12			Odumosu et al. (2007)
		Gulf of Mexico	10 -2500	6.14*	~0.24			Odumosu et al. (2007)
		Xinji coal mine, Huainan coalfield		59.54	0.2			Meng et al. (2006)
		Rhinestreet (Grimes), fine-grained		48	0.17			Evans et al. (1989)
		Rhinestreet (Grimes), fine-grained		46	0.17			Evans et al. (1989)
		SNOK	120		0.39*		1	Schutjens et al. (2004)
		SNOK	80		0.39*		1	Schutjens et al. (2004)
	Mesaverde Formation Southern Piceance Basin, CO - 1	Sandstone (4300.3 - 4300.7 ft)	~ 6E-4 - 0.1	27.79	0.19			Green (2006)
		(c sand) (4301.7 - 4322.8 ft)	~ 6E-4 - 0.1	33.19	0.18			Green (2006)
		(4321.6 - 4322.8 ft)	~ 6E-4 - 0.1	36.89	0.16			Green (2006)
			~ 6E-4 - 0.1	38.49	0.2			Green (2006)
			~ 6E-4 - 0.1	44.79	0.36			Green (2006)
			~ 6E-4 - 0.1					Green (2006)
		Very fine sandstone with carbonate stringers (4492.7 - 4493.7 ft)	~ 6E-4 - 0.1	48.99	0.16			Green (2006)
		Very fine sandstone with carbonate stringers	~ 6E-4 - 0.1	51.79	0.17			Green (2006)
		Very fine sandstone with carbonate stringers	~ 6E-4 - 0.1	14.50	0.13			Green (2006)
		Mudstone (4498.4 - 4498.9 ft)	~ 6E-4 - 0.1					Green (2006)
		Sandstone (94550.6 - 4551.1 ft)	~ 6E-4 - 0.1	28.19	0.19			Green (2006)

		(B sand)	~ 6E-4 - 0.1	34.89	0.2			Green (2006)
			~ 6E-4 - 0.1					Green (2006)
		Carbonaceous Mudstone (4612.6 - 4613.6 ft)	~ 6E-4 - 0.1					Green (2006)
		Mudstone (4713.3 - 4714.4 ft)	~ 6E-4 - 0.1	16.70	0.13			Green (2006)
			~ 6E-4 - 0.1	37.19	0.17			Green (2006)
		Siltstone (4893.5 - 4894.0 ft)	~ 6E-4 - 0.1	38.09	0.17			Green (2006)
			~ 6E-4 - 0.1	42.69	0.17			Green (2006)
			~ 6E-4 - 0.1	23.59	0.13			Green (2006)
		Silty Mudstone (4922.6 - 4923.3 ft)	~ 6E-4 - 0.1	24.59	0.13			Green (2006)
			~ 6E-4 - 0.1	13.90	0.17			Green (2006)
		Sandstone (4946.0 - 49246.7 ft)	~ 6E-4 - 0.1	22.59	0.17			Green (2006)
		(A sand) (4947.2 - 4948.6 ft)	~ 6E-4 - 0.1	25.89	0.2			Green (2006)
			~ 6E-4 - 0.1	26.69	0.17			Green (2006)
			~ 6E-4 - 0.1	32.99	0.31			Green (2006)
	Mesaverde Formation Southern Piceance Basin, CO - 2	Muddy Siltstone (4871.5 - 4872.9 ft)	~ 6E-4 - 0.1					Green (2006)
			~ 6E-4 - 0.1	28.19	0.24			Green (2006)
			~ 6E-4 - 0.1	30.09	0.2			Green (2006)
			~ 6E-4 - 0.1	27.79	0.22			Green (2006)
		Muddy Siltstone (4894.5 - 4895.6 ft)	~ 6E-4 - 0.1	22.29	0.24			Green (2006)
			~ 6E-4 - 0.1	23.29	0.21			Green (2006)
			~ 6E-4 - 0.1	23.39	0.27			Green (2006)
		Sandstone (4913.0 - 4913.8 ft)	~ 6E-4 - 0.1	22.99	0.19			Green (2006)
		(A sand)	~ 6E-4 - 0.1	30.99	0.21			Green (2006)

			~ 6E-4 - 0.1	33.49	0.2			Green (2006)
			~ 6E-4 - 0.1	34.19	0.18			Green (2006)
		Sandstone (4932.7 - 4933.7 ft)	~ 6E-4 - 0.1	22.19	0.18			Green (2006)
		(A sand) (4933.7 - 4934.7 ft)	~ 6E-4 - 0.1	29.89	0.17			Green (2006)
			~ 6E-4 - 0.1	32.49	0.17			Green (2006)
			~ 6E-4 - 0.1	33.69	0.18			Green (2006)
	Mesaverde Formation Southern Piceance Basin, CO - 3	Sandstone (4913.9 - 4914.9 ft)	~ 6E-4 - 0.1					Green (2006)
		(A sand)	~ 6E-4 - 0.1	23.89	0.28			Green (2006)
			~ 6E-4 - 0.1	28.19	0.22			Green (2006)
	Mesaverde Formation Southern Piceance Basin, CO - Monitoring well	Sandstone (4316 - 4321 ft)	~ 6E-4 - 0.1					Green (2006)
		(C sand)	~ 6E-4 - 0.1	37.23				Green (2006)
			~ 6E-4 - 0.1	37.23	0.22			Green (2006)
			~ 6E-4 - 0.1	32.41	0.28			Green (2006)
			~ 6E-4 - 0.1	35.16	0.23			Green (2006)
			~ 6E-4 - 0.1	40.68	0.22			Green (2006)
			~ 6E-4 - 0.1	44.13	0.16			Green (2006)
	Mesaverde Formation, Piceance Basin	A: 15.2 feet gross height	2.00E-03	45.53	0.22			Green (2006)
		A: 15.8 feet	0.00E+00	49.04	0.22			Green (2006)
		A: 18.4 feet	8.00E-03	47.96	0.22			Green (2006)
		A: 14 feet	2.00E-02	48.61	0.22			Green (2006)
		A: 21.6 feet	4.00E-03	44.80	0.22			Green (2006)
		S: 22.2 feet	0.00E+00	53.20	0.22			Green (2006)
		S: 29.6 feet	2.00E-03	46.32	0.22			Green (2006)
		S: 21.9 feet	1.00E-02	45.48	0.22			Green (2006)
		S: 16.1 feet	3.00E-03	45.42	0.23			Green (2006)

		S: 40.9 feet	2.00E-03	46.32	0.21			Green (2006)
		G: 23.8 feet	7.00E-03	40.51	0.22			Green (2006)
		G: 20 feet		62.80	0.24			Green (2006)
		G: 38.1 feet	3.00E-03	52.38	0.22			Green (2006)
		G: 36.2 feet	6.00E-03	47.57	0.22			Green (2006)
		G: 18 feet	1.60E-02	55.26	0.22			Green (2006)
		M: 16.5 feet	2.70E-02	51.40	0.23			Green (2006)
		M: 15.2 feet	2.90E-02	49.28	0.22			Green (2006)
		M: 15.2 feet	3.10E-02	46.33	0.22			Green (2006)
		M: 21.6 feet	1.10E-02	46.50	0.22			Green (2006)
		M: 14 feet	9.00E-03	43.92	0.22			Green (2006)
		T: 21.4 feet	9.00E-03	48.90	0.22			Green (2006)
		T: 27.1 feet	1.00E-02	45.03	0.22			Green (2006)
		T: 42.9 feet	1.90E-02	45.26	0.23			Green (2006)
		T: 20 feet	1.00E-03	42.10	0.22			Green (2006)
		T: 20 feet	2.00E-03	45.37	0.23			Green (2006)
		T: 12.9 feet	1.00E-03	45.08	0.22			Green (2006)
		O: 17.2 feet	1.40E-02	36.27	0.22			Green (2006)
		O: 31.5 feet	4.00E-03	38.13	0.23			Green (2006)
		O: 36.57 feet	1.00E-03	46.34	0.22			Green (2006)
		O: 15.7 feet	2.80E-02	45.33	0.23			Green (2006)
		O: 11.7 feet	0.032	50.27	0.22			Green (2006)
		I: 12.85 feet	0.002	49.00	0.24			Green (2006)
		I: 25.72 feet	0.003	49.39	0.23			Green (2006)
Unconsolidated material	**Clay**	General				1	6.14*	Palciauskas and Dominico (1989), Domenico and Schwartz (1998)
		La Bouzule Clay					~5.5	Djeran-Maigre and Gasc-Barbier (2000)
		Marais Poitevin Mud					~4.35	Djeran-Maigre and Gasc-Barbier

								(2000)
	Silt	General		0.08*	0.25			Hsieh (1996)
		Clay-Silt Aquitard		0.01	0.3			Hernandez-Marin and Burbey (2010)
		Illite of Salins					~4	Djeran-Maigre and Gasc-Barbier (2000)
	Bentonite	Industrial	1.01E-06	1	0.35	1		Mabmann et al. (20110
	Kaolinite	St. Austell					~5.15	Djeran-Maigre and Gasc-Barbier (2000)
	Sand	Alaskan (P_c = 0)		0.63		0.68		Kapustyanskii et al. (2003)
		Alaskan (Pc = 2.6 MPa)		1.99	0.2	0.66		Kapustyanskii et al. (2003)
		Alaskan (Pc = 5.1 MPa)		3.05	0.19	0.44		Kapustyanskii et al. (2003)
		Alaskan (Pc = 10.1 MPa)		3.71	0.17	0.16		Kapustyanskii et al. (2003)
		Alaskan (Pc = 17.8 MPa)		4.45	0.17	0.02		Kapustyanskii et al. (2003)
		Clayed		1	0.3			Kapustyanskii et al. (2003)
		General		0.75*	0.25			Hsieh (1996)
		Del Monte Sand	4.56E+02	0.0013	0.4			Lewis and Schrefler (1999)
		Del Monte Sand	~2.56E5	0.0003	0.2			Mabmann et al. (2011)
		Sand Aquifer		1	0.25			Hernandez-Marin and Burbey (2010)
		Sand Vadose Zone		1	0.25			Hernandez-Marin and Burbey (2010)
		Sand in Fault Zone		1	0.3			Hernandez-Marin and Burbey (2010)
		N LA tight-gas		57.09*	~0.12			Odumosu et al. (2007)
	Texas Bossier Formation: Unconsolidated Shaley Sand	Depth: 11927.25 ft./ pressure: 50 psi		0.18	0.28			Odumosu et al. (2007)
		Depth: 11927.25 ft./ pressure: 686 psi		0.47	0.08			Odumosu et al. (2007)
		Depth: 11927.25 ft./ pressure: 1372 psi		1.44	0.18			Odumosu et al. (2007)

		Depth: 11934.9 ft./ pressure: 50 psi		0.16	0.2			Odumosu et al. (2007)
		Depth: 11934.9 ft./ pressure: 686 psi		0.79	0.21			Odumosu et al. (2007)
		Depth: 11934.9 ft./ pressure: 1372 psi		1.20	0.37			Odumosu et al. (2007)
		Depth: 11962.7 ft./ pressure: 50		0.08	0.28			Odumosu et al. (2007)
		Depth: 11962.7 ft./ pressure: 686 psi		0.77	0.21			Odumosu et al. (2007)
		Depth: 11962.7 ft./ pressure: 1372 psi		0.97	0.15			Odumosu et al. (2007)
	North Louisiana Sand Formation	Depth: 25.35 feet/ Confining Stress: 1000 psi		34.20	0.17			Odumosu et al. (2007)
		Depth: 25.35 feet/ Confining Stress: 2000 psi		41.05	0.18			Odumosu et al. (2007)
		Depth: 25.35 feet/ Confining Stress: 3000		40.93	0.17			Odumosu et al. (2007)
		Depth: 41.35 feet/ Confining Stress: 1000		57.97	0.11			Odumosu et al. (2007)
		Depth: 41.35 feet/ Confining Stress: 2000 psi		65.40	0.21			Odumosu et al. (2007)
		Depth: 41.35 feet/ Confining Stress: 3000 psi		69.38	0.22			Odumosu et al. (2007)
		Depth: 55.4 feet/ Confining Stress: 1000 psi		47.12	0.12			Odumosu et al. (2007)
		Depth: 55.4 feet/ Confining Stress: 2000 psi		52.19	0.18			Odumosu et al. (2007)

		Depth: 55.4 feet/ Confining Stress: 3000 psi		52.43	0.19			Odumosu et al. (2007)

*Values calculated in this work using poroelastic relations

References for Poroelastic Database

Abdullatif, O., (2010). Geomechanical properties and rock mass quality of the carbonate Rus Formation, Dammam Dome, Saudi Arabia. *Arabian J. Sci. & Eng.,* 35(2A):173-197.

Adam, L., (2004). *Elastic and Visco-elastic laboratory properties in carbonates.* (Doctorate of Philosophy), Colorado School of Mines.

Andersson, J.C., (2007). *Rock mass response to coupled mechanical thermal loading. Aspo pillar stability experiment, Sweden.* (Doctorate), Royal Institute of Technology, Stockholm.

Arslan, H., and L. Rosassanchez, (2008). Failure analysis of the granite for a dam foundation. *Environ. Geo.,* 54:1165-1173. doi: 10.1007/s00254-007-0885-5

Averbakh, V.S., V.V. Bredikhin, A.V. Lebedev, and S.A. Manakov, (2010). Acoustic spectroscopy of fluid saturation effects in carbonate rock. *Acoustical Physics, 56*(6), 794 - 806. doi: 10.1134/S1063771010060035

Bass, J. D. (1995). *A Handbook of Physical Constants*. In T.J. Ahrens (Ed.), (Vol. 2, pp. 45 - 63). Washington, DC: Amer. Geophys. Union.

Bauer, S. J., and J. Handin, (1985). Mechanical properties of basalt from Deep Sea Drilling Project Hole 504B. doi: 10.2973/dsdp.proc.83.122.1985

Bustin, R.M., X. Cui, and L. Chikatamarla, (2008). Impacts of volumetric strain on CO_2 sequestration in coals and enhanced CH_4 recovery. *AAPG, 92*(1), 15 - 29. doi: 10.1306/08220706113

Carlsson, H. (1977). Stress measurements in the Stripa Granite. In S. N. F. S. Program (Ed.), *KBS Teknisk Rapport 49* (pp. 13).

Chandler, R. J., and A.G. Davis (1973). Further work on the engineering properties of Keuper Marl. *Constr. Ind. Res. and Info. Assoc. Rep., 47*.

Dell'Isola, F., G. Sciarra, and R.C. Batra. (2010). A second gradient model for deformable porous matrices filled with an inviscid fluid. *HAL*.

Detournay, E., and A.H.-D. Cheng, (1993). Fundamentals of Poroelasticity, *Comprehensive Rock Engineering: Principles, Practice and Projects* (Vol. 2, pp. 113 - 171): C. Fairhurst, Pergamon Press.

Djeran-Maigre, I., and M. Gasc-Barbier, (2000). Hydromechanical Modelling of Experimentally Compacted Saturated Argillaceous Porous Media. *Transport in Porous Media* 41(1):81-103.

Domenico, P. A., & (1998), S. (1998)). *Physical and Chemical Hydrogeology* (2 ed.). New York: John Wiley and Sons, Inc.

Evans, K. F., Oertel, G., & Engelder, T. (1989). Appalachian stress study 2. Analysis of Devonian shale core: Some implications for the nature of contemporary stress variations and Alleghanian deformation in Devonian rocks. *J. Geophys. Res., 94*(B6), 7155 - 7170. doi: 0148-0227/89/88JB-04341

Fabre, D., & Gustkiewicz, J. (1997). Poroelastic properties of limestones and sandstones under hydrostatic conditions *Int. J. Rock Mech. Min. Sci., 34*(1), 127 - 134. doi: 0148-9062/97

Giraud, A., Giot, R., & Hommand, F. (2009). Poromechanical modelling and inverse approach of drying tests on weakly permeable porous rocks. *Transport in Porous Media, 76*(1), 45 - 66. doi: 10.1007/s11242-008-9229-5

Green, C. A. (2006). *Hydraulic fracture model sensitivity analyses of massively stacked lenticular reservoirs in the Mesaverde formation, southern Piceance Basin, Colorado.* (Master of Science), Colorado School of Mines.

Hernandez-Marin, M., & Burbey, T. J. (2010). Controls on initiation and propagation of pumping-induced earth fissures: insights from numerical simulations. *Hydrogeology J., 18*(8), 1773 - 1785. doi: 10.1007/s10040-010-0642-9

Hsieh, P. A. (1996). Deformation-induced changes in hydraulic head during ground-water withdrawal. *Groundwater, 34*(6), 1082 - 1089. doi: 10.1111/j.1745-6584.1996.tb02174.x

Hudson, J. A., Backstrom, A., Rutqvist, J., Jing, L., Backers, T., Chijimatsu, M., . . . Shen, B.-T. (2009). Characterizing and modelling the excavation damaged zone in crystalline rock in the context of radioactive waste disposal. *Environ. Geo., 57*, 1275 - 1297. doi: 10.1007/s00254-008-1554-z

Johnson, J. G., Brady, T. M., Maclaughlin, M. M., Langston, R. B., & Kirsten, H. A. D. (2003). *In situ stress measurements at the Stillwater Mine, Nye, Montana*. Paper presented at the Proc., 39th U.S. Rock Mech. Symp., Cambridge, Mass.

Kapustyanskii, S. M., Nikolaevski, V. N., & Schmidt, J. H. (2003). Elasticoplastic model of sludge injection into a weak water-pressurized reservoirs. *Fluid Dynamics, 38*(2), 293 - 302. doi: 0015–4628/03/3802–0293

Lewis, R. W., & Schrefler, B. A. (1999). *The Finite Element Method in the Static and Dynamic Deformation and Consolidation of Porous Media*: John Wiley & Sons.

MaBmann, J., Ziefle, G., Kohlmeier, M., & Zielke, W. (2011). Thermo-Hydro-Mechanical Modeling of Coupled Processes in Clay

Materials *Modelling, Simulation and Software Concepts* (pp. 29 - 74). Berlin: Springer-Verlag.

Mavko, G., Mukeji, T., & Dvorkin, J. (1998). *The rock physics handbook. Tools for seismic analysis in porous media*. Cambridge, MA: Cambridge Univ.

Meng, Z., Zhang, J., & Peng, S. (2006). Influence of sedimentary environments on mechanical properties of clastic rocks. *Environ. Geo., 51*(1), 113-120. doi: 10.1007/s00254-006-0309-y

Morency, C., Luo, Y., & Tromp, J. (2011). Acoustic, elastic and poroelastic simulations of CO2 sequestration crosswell monitoring based on spectral-element and adjoint methods. *Geophy. J. Inter., 185*(2), 955 - 966.

Morrow, C. A., & Lockner, D. A. (2006). Physical properties of two core samples from well 34-9RD2 at the Coso Geothermal Field, California. *Open-file Report 2006-1230*, 32.

Nasedkina, A. A., Nasedkin, A. V., & Iovane, G. (2008). A model for hydrodynamic influence on a multi-layer deformable coal seam. *Comput. Mech., 41*, 379 - 389. doi: 10.1007/s00466-007-0194-6

Nguyen, N. B., Giaud, A., & Grgic, D. (2011). A composite sphere assemblage model for porous oolitic rocks. *Int. J. Rock Mech. Min. Sci., 48*, 909 - 921. doi: 10.1016/j.ijrmms.2011.05.003

Odumosu, T., Torres-Verdin, C., Salazar, J. M., Ma, J., Voss, B., & Wang, G. L. (2007). *Estimation of dry-rock elastic moduli based on the simulation of mud-filtrate invasion effects on borehole acoustic logs.* Paper presented at the SPE Annual Technical Conference and Exhibition, Anaheim, CA.

Palciauskas, V. V., & Domenico, P. A. (1989). Fluid pressures in deforming porous rocks. *Water Resources Research, 25*(2), 203 - 213. doi: 0043-1397/89/88 WR-036865

Paterson, M. S. (1978). The role of pore fluids *Experimental Rock Deformation — The Brittle Field* (pp. 71 - 87): Springer Berlin Heidelberg.

Peng, S. (2007). Rock strength experiments and failure criteria *Engineering Geology for Underground Rocks* (pp. 75 - 100): Springer Berlin Heidelberg.

Qingling, W., Haibo, Z., Lailin, L., & Xingcai, F. (2008). Analysis of rock physics response of gas-bearing volcanic reservoir based on three-phase poroelastic theory. *Applied Geophy., 5*(4), 277 - 283. doi: 10.1007/s11770-008-0035-1

Rice, J. R., & Cleary, M. P. (1976). Some basic stress diffusion solutions for fluid-saturated elastic porous media with compressible constituents. *Reviews of Geophy., 14*(2), 227 - 241. doi: 10.1029/RG014i002p00227

Roshan, H., & Rahman, S. S. (2011). Analysis of Pore Pressure and Stress Distribution around a Wellbore Drilled in Chemically Active Elastoplastic Formations. *Rock Mech. and Rock Eng., 44*(5), 541 - 552. doi: 10.1007/s00603-011-0141-x

Schutjens, P. M. T. M., Hanssen, T. H., Hettema, M. H. H., Merour, J., de Bree, P., Coremans, J. W. A., & Helliesen, G. (2004). *Compaction-induced porosity/ permeability reduction in sandstone reservoirs: data and model for elasticity-dominated deformation*. Paper presented at the SPE Annual Technical Conference and Exhibition, New Orleans.

Selvadurai, A. P. S., Boulon, M. J., & Nguyen, T. S. (2005). The permeability of an intact granite. *Pure and Applied Geophy., 162*, 373 - 407. doi: 10.1007/s00024-004-2606-2

Trautwein, U., & Huenges, E. (2005). Poroelastic behaviour of physical properties in Rotliegend sandstones under uniaxial strain. *Int. J. Rock Mech. Min. Sci., 42*(7 - 8), 924 - 932. doi: 10.1016/j.ijrmms.2005.05.016

Wang, G. X., Massarotto, P., & Rudolph, V. (2009). An improved permeability model of coal for coalbed methane recovery and CO2 geosequestration. *Int. J. Coal Geo., 77*, 127 - 136. doi: 0166-5162/j.coal.2008.10.007

Yao, D., Xu, J., & Lu, H. (2011). Nonlinear coupling analysis of coal seam floor during mining based on FLAC. *J. of Coal Sci. & Eng., 17*(1), 22 - 27. doi: 10.1007/s12404-011-0105-5

Yoon, J., Zang, A., & Stephansson, O. (2012). Simulating fracture and friction of Aue granite under confined asymmetric compressive test using clumped particle model. *International Journal of Rock Mechanics & Mining Sciences, 49*, 68 - 83. doi: 10.1016/j.ijrmms.2011.11.004

Parameter Distributions

Poroelastic parameters were compiled for different formation types under consideration for CO_2 storage, and we summarize the means and standard deviations of the distributions in Table 2.4-2. The database was also used to estimate properties of confining units.

Table 2.4-2. Means and standard deviations of poroelastic parameters and geometry for various reservoir types.

	depleted oil/gas reservoir	deep saline aquifer	coal bed
Observations	9	15	11
Young's modulus (GPa)	16.2 / 8.3	16.2 / 8.3	2.4 / 1.4
Poisson ratio	0.18 / 0.04	0.18 / 0.04	0.31 / 0.05
Porosity	0.18 / 0.08	0.18 / 0.08	0.095 / 0.094
hydraulic conductivity (m/s)	$9.1\text{x}10^{-7}$ / $1.3\text{x}10^{-7}$	$2\text{x}10^{-6}$ / $2\text{x}10^{-7}$	$4.7\text{x}10^{-8}$ / $4.6\text{x}10^{-8}$
Biot-Willis coefficient	0.57 / 0.22	0.7 / 0.22	0.7 / 0.07
thickness (m)	71 / 57	107 / 89	11 / 8
depth (m)	1720 / 531	1702 / 716	725 / 429

The distributions of the parameters were used to evaluate the ranges of expected magnitudes of deformation. The distribution of many of the parameters is approximately Beta or log-normal (Figure 2.4-1). More specifically, the Beta distribution is used for the parameters bounded between 0 and 1 (such as Poisson ratio, porosity and Biot coefficient), and log-normal distribution is used for all the other positive-valued parameters (such as Young's modulus, hydraulic conductivity, depth, and thickness) (Table 2.4-1). The proposed distributions can provide the values of mean (μ) and standard deviation (σ) for the individual parameters (Table 2.4-2). Five poroelastic parameters (Young's modulus, Poisson ratio, porosity, hydraulic conductivity, and Biot-Willis coefficient, were chosen among three possible magnitudes (i.e., $\mu - \sigma$, μ, and $\mu + \sigma$), whereas the reservoir thickness and depth were fixed as their mean values. This resulted in a set of 243 (3^5) unique combinations of parameters.

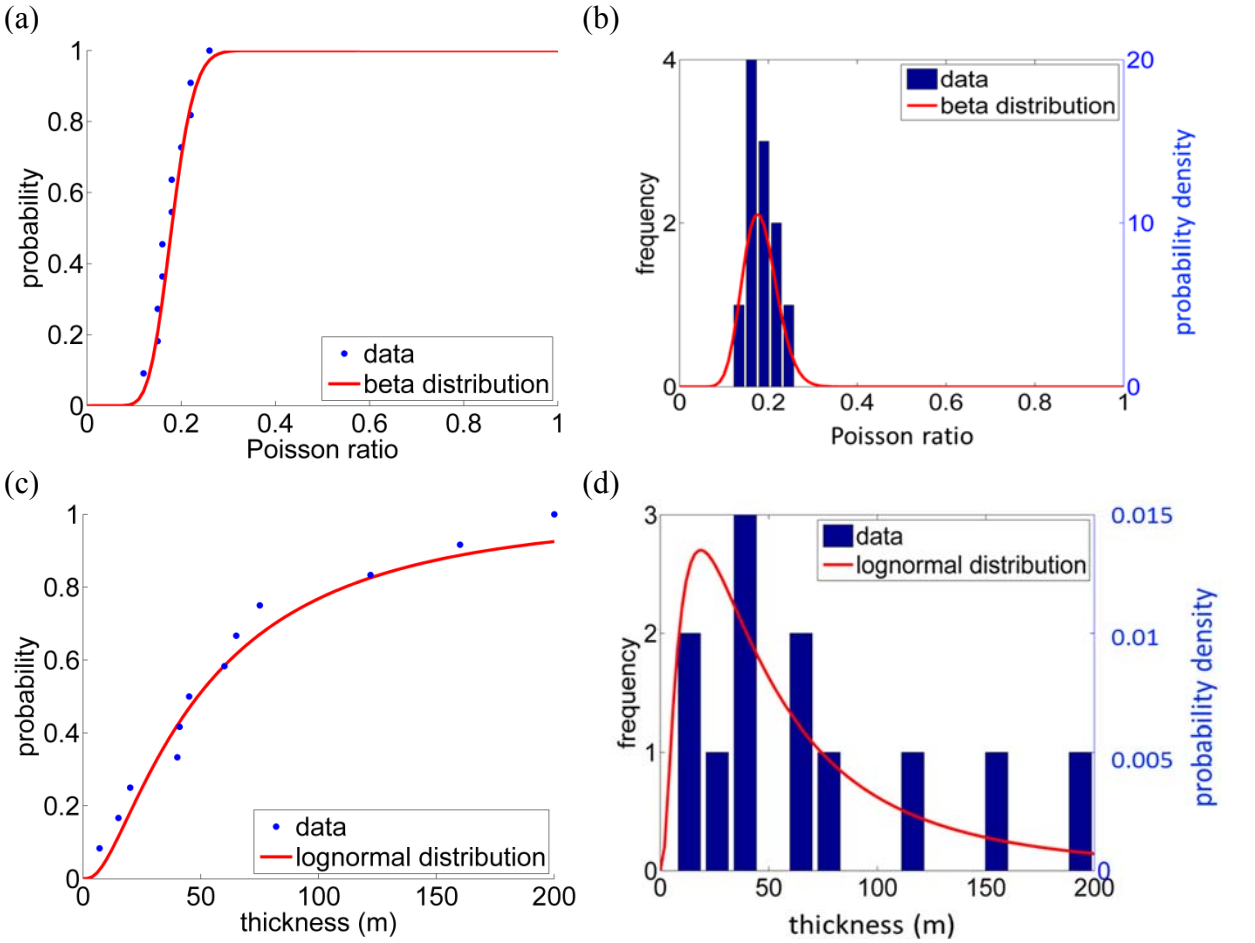

Figure 2.4-1. Statistical distribution applied to estimate mean and standard deviation values of parameters of depleted oil/gas reservoir. (a) raw data and CDF (cumulative distribution function) for Poisson ratio, (b) histogram and PDF (probability distribution function) for Poisson ratio, (c) raw data and CDF for reservoir thickness, (d) histogram and PDF for reservoir thickness.

The model configuration used in Section 2.3 was used to represent a typical case. In this model, the reservoir is a circular, horizontal layer of uniform thickness. The well is at the center of the reservoir, so axial symmetry will be assumed. The model resembles idealized field conditions with a 100-m-thick reservoir overlain by a uniform confining layer (2,000 m thick), and underlain by a 100-m-thick confining layer resting on impermeable, rigid basement rock (Table 2.4-4). The radial extent is 30 km. The well is represented as a cylindrical open hole in the formation. The properties of a depleted oil/gas reservoir in Table 2.4-1 were used to define a baseline case.

An initial test was conducted to show results of the sensitivity analysis as a function of time. An individual simulation takes roughly 5 minutes on a PC (i7-3770, 3.4 GHz), and 243 simulations were done using a cluster in roughly 35 minutes. Radial and vertical displacements were obtained at 9 observation points shown in Figure 2.4-2. In each point, pore pressure, radial and vertical displacements were recorded during the injection process.

The results show that radial displacement increases rapidly at first and the rate of increase diminishes with time (Figure 2.4-3). This general response occurs for all combinations of

material properties (Figure 2.4-3). The magnitude of the response is affected by the properties, with the maximum displacement occurring at the end of the simulation and ranging from 0.3 x 10^{-4} to 1.3 x 10^{-4} m, and with the mean of 0.75 x 10^{-4} m.

The general result from the sensitivity analysis is that the range of material properties (as shown in Table 2.4-3) for a depleted oil and gas reservoir is expected to cause the radial displacement to vary by approximately a factor of 2. This is a relatively small range. One implication of this is that if the analysis indicates that it is feasible to measure the radial displacement for the average case, then it will be likely that the radial displacement for any combination of parameters could also be measured.

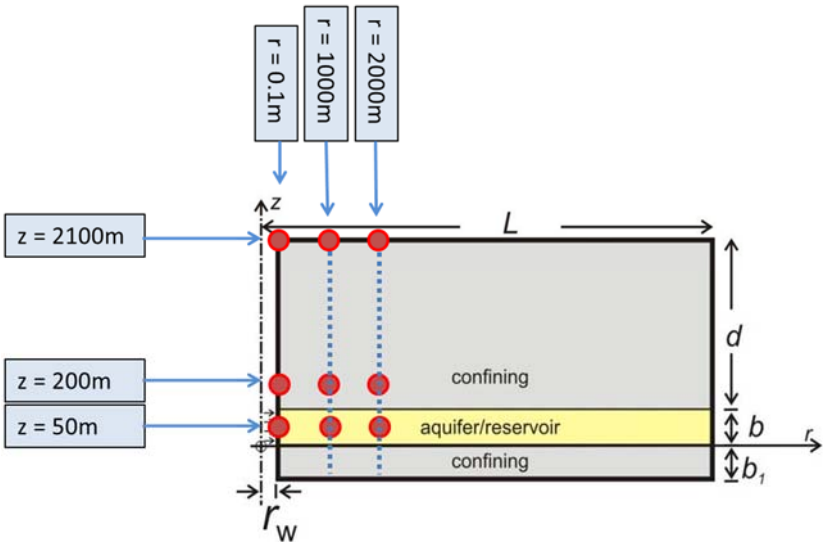

Figure 2.4-2. Cross section of reservoir and confining units with the observation points used in the code comparison.

Table 2.4-3. Representative poroelastic material properties for confining unit and casing for generic model and wellbore completion.

	Young's modulus (GPa)	Poisson ratio	porosity	permeability (mD)	Biot coefficient
shale	15	0.25	0.18	10^{-4}	1
cement	40	0.33	0.01	10^{-5}	1
fractured cement	40	0.33	0.18	10^{2}	1
steel	100	0.25	0.01	10^{-5}	1
perforated steel	100	0.25	0.18	10^{2}	1

Table 2.4-4. Representative geometry for generic model and wellbore completion

Geometry	Value (m)
thickness of upper confining layer	2,000
thickness of aquifer	100
thickness of lower confining layer	100
inner radius of steel pipe	0.1
outer radius of steel pipe	0.10813
outer radius of cement casing	0.14
Radial distance of monitoring well from wellbore	1,000
Outer radius	30,000

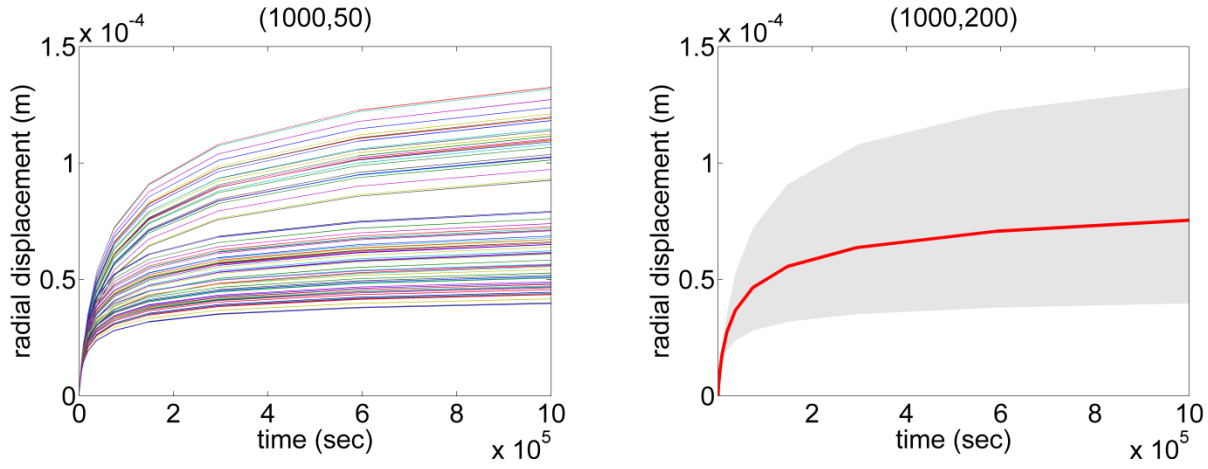

(a) (b)

Figure 2.4-3. Radial displacement at r = 1,000 m and z = 200 m for (a) all 243 simulations and (b) mean curve and envelope showing range of results.

We wanted to evaluate the sensitivity with a more quantitative analysis. The sensitivity of the displacement to changes in a parameter was calculated as:

$$s = \frac{\lambda_m}{u_{rm}} \left(\frac{\partial u_r}{\partial \lambda} \right)_{\lambda=\lambda_m} \qquad (2.4\text{-}1)$$

and in finite difference form as:

$$s = \frac{\lambda_m}{u_r(\lambda_m)} \frac{u_r(\lambda_{m+\sigma}) - u_r(\lambda_{m-\sigma})}{\lambda_{m+\sigma} - \lambda_{m-\sigma}} \qquad (2.4\text{-}2)$$

where λ_m is a mean value of a parameter, $\lambda_{m-\sigma}$ the value of the parameter one standard deviation below the mean, and $\lambda_{m+\sigma}$ the parameter one standard deviation above the mean.

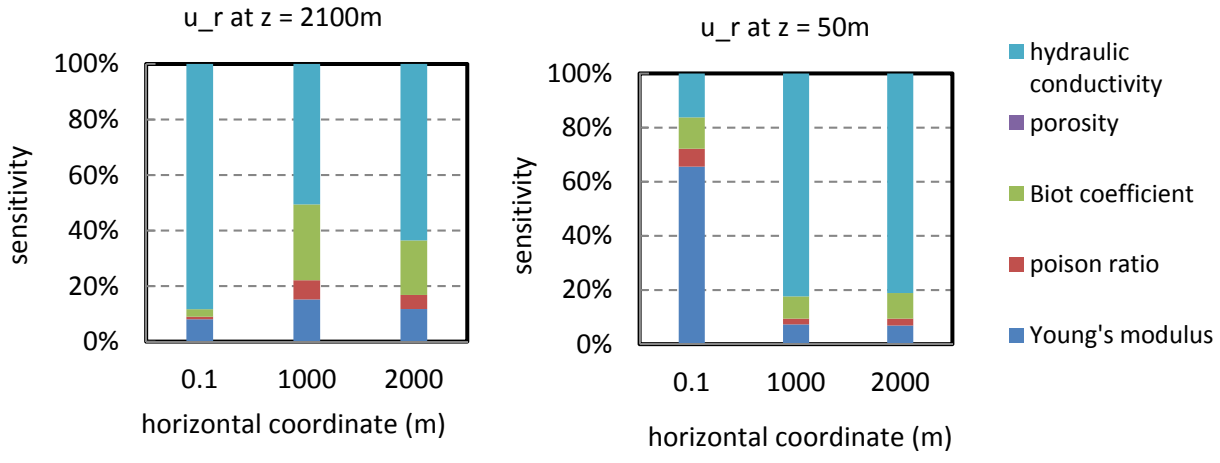

(a)

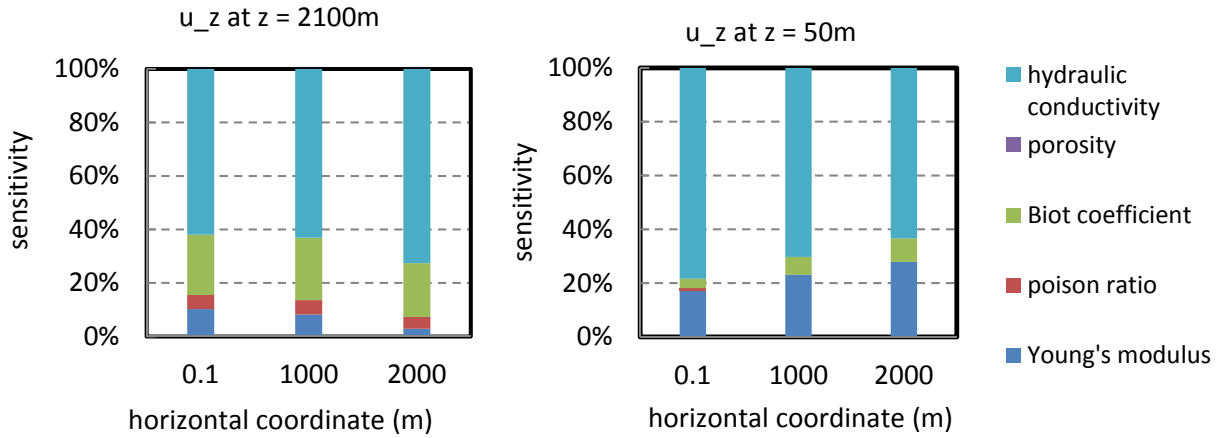

(b)

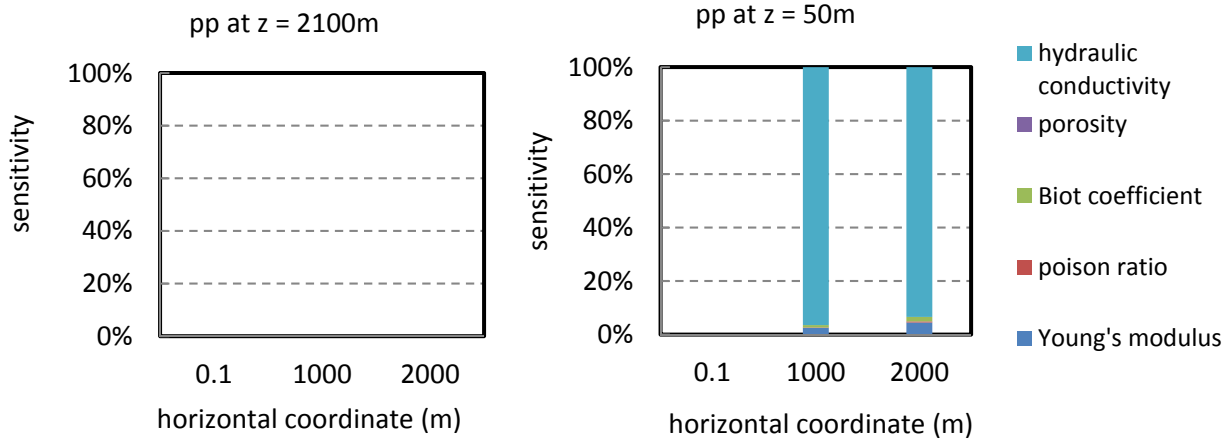

(c)

Figure 2.4-4. Sensitivity of displacements and pore pressures to individual poroelastic parameters at the corresponding coordinates at time $t = 10^6$ sec. (a) radial displacement, (b) vertical displacement, and (c) pore pressure

2.4.2 RESULTS

Sensitivity values of individual poroelastic parameters were calculated and presented at various locations in Figure 2.4-4. The displacements are typically most sensitive to hydraulic conductivity. An exception is the radial displacement at the injection point (0.1 m, 50 m), where Young's modulus has the highest sensitivity value (Figure 2.4-4a). Displacements are relatively insensitive to Biot coefficient and Poisson ratio, but the sensitivity increases for displacements at the ground surface (at z = 2100 m). Biot coefficient has, in general, larger sensitivity values than Poisson ratio. Effect of porosity is negligible. Sensitivity values of pore pressure at the surface and the injection point are zero because they are boundary conditions.

Results from 243 analyses were combined to evaluate the effects of ranges of parameters. The results for the dataset describing the depleted oil/gas reservoir gives plots of strains, stresses, pressure at selected points as functions of time for all the combinations of parameters (Figure 2.4-5). This results in many plots similar to Figure 2.4-3, which offer a comprehensive view of the response time series.

A more condensed perspective is available by plotting the representative strains and the pressure as functions of time at two locations near the middle of reservoir and the top of confining layer (e.g., r = 1 km, z = 40 m and 900 m for depleted oil/gas reservoir) (Figure 2.4-6). The created envelopes with the variability (Figure 2.4-6) that show the general tendency of the strain response is consistent with the baseline analysis.

The variability caused by parameter uncertainty differs among the different strain components, time, and location. This complex data set (Figure 2.4-5) can be simplified by normalizing the results of a particular variable to the mean value at a particular time. This gives the range of the variable scaled to a mean value of unity. We used this procedure and normalized the strains to their mean value at t = 100 days. This was done for all of the monitoring locations, and for each reservoir type.

The results for the depleted oil/gas reservoir show that the maximum variation in normalized strain is for the vertical strain at the injection well and it ranged from 0.3 to 2.4 (Table 2.4-5). The variability of all the normalized strains at the monitoring well is approximately 0.5 to 1.5. The radial and circumferential strain in the casing adjacent to the confining unit are essentially unaffected by the formation properties, likely because these strains are dominated by the properties of the casing. The uncertainty in pore pressure at the reservoir (r = 1 km, z = 40 m) is relatively small, with the scaled value varying between 0.93 and 1.05.

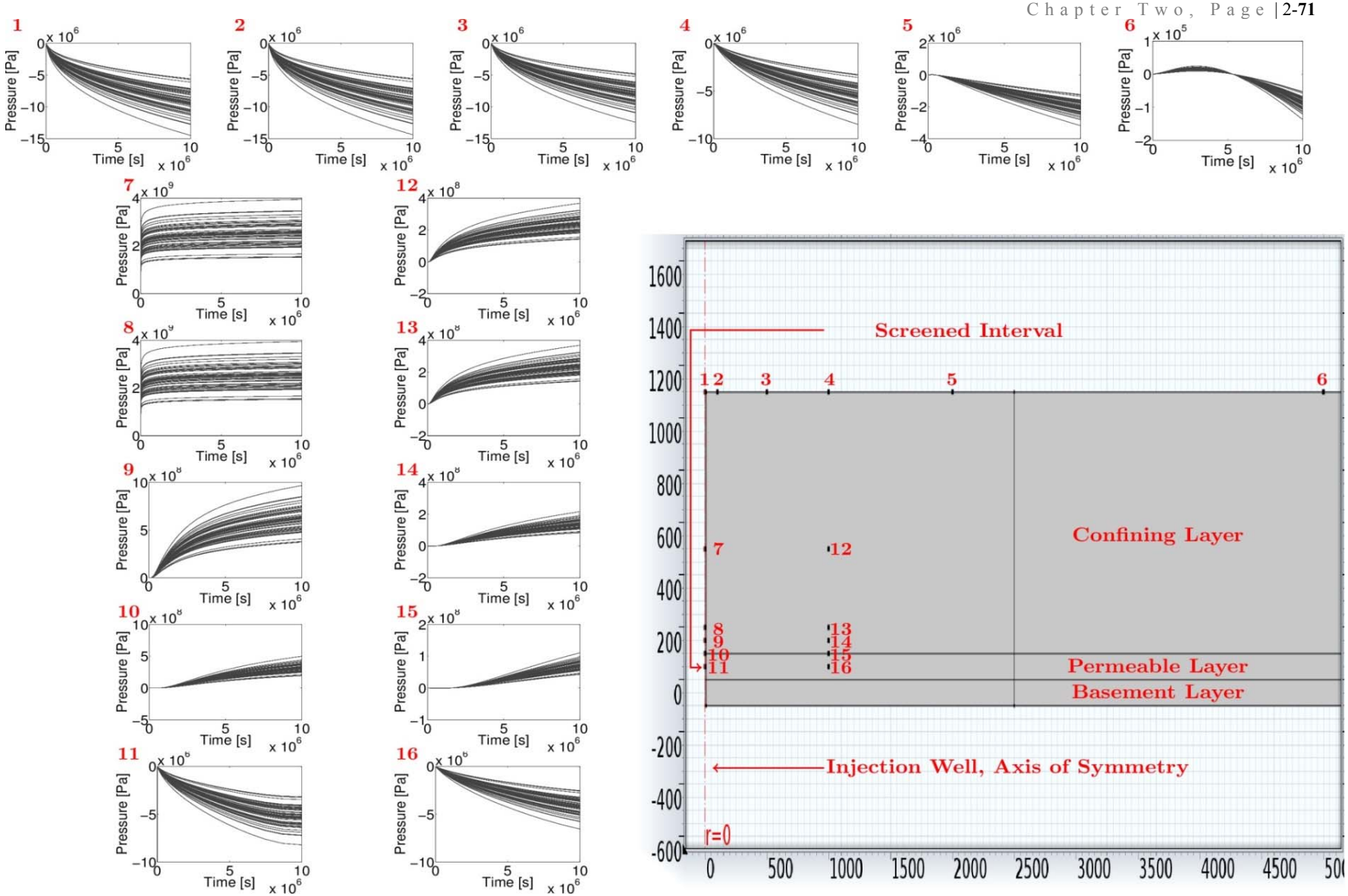

Figure 2.4-5a. Pressure as a function of time at different locations for ranges of parameters typical of a depleted reservoir.

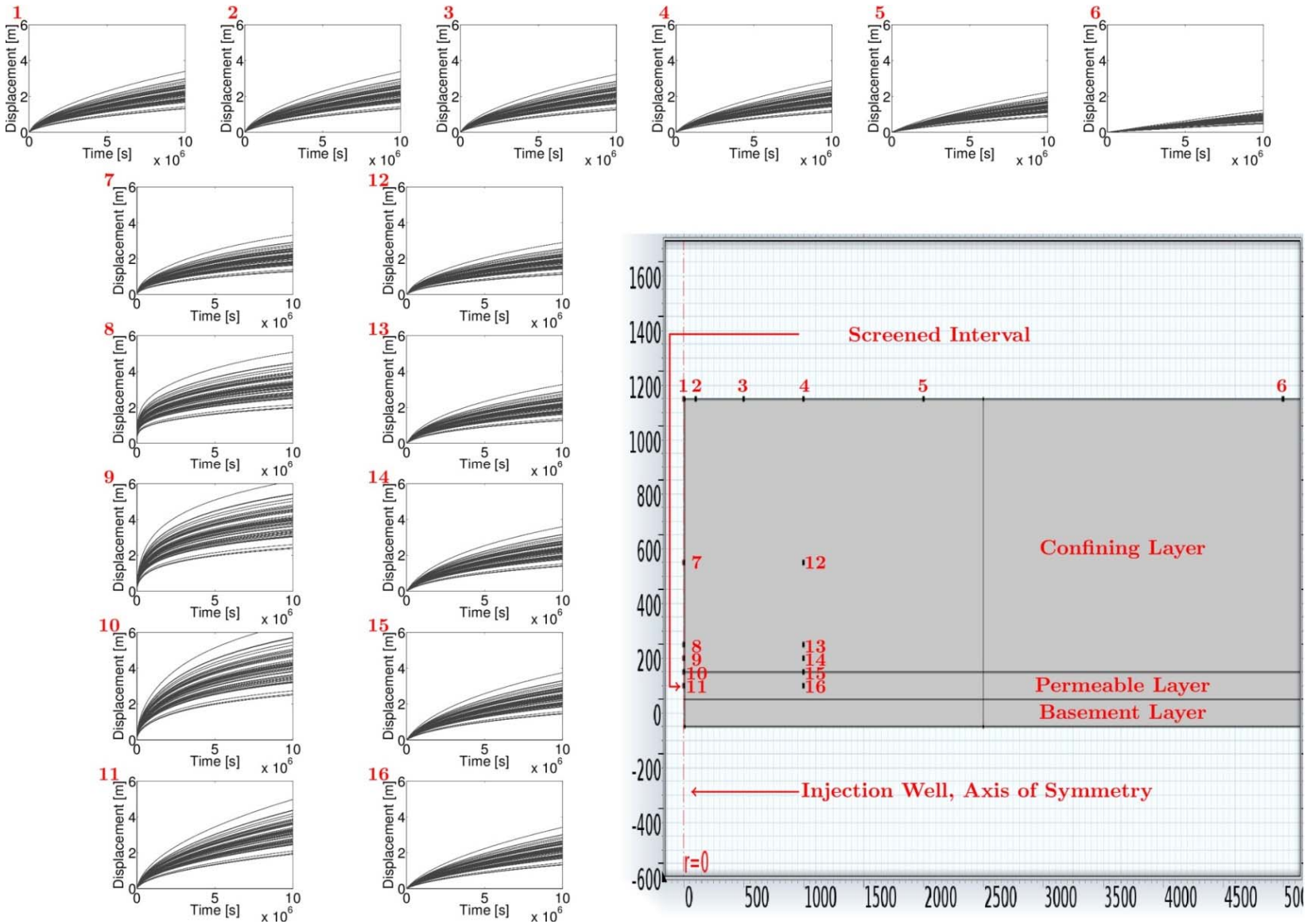

Figure 2.4-5b. Radial displacement as a function of time at different locations for ranges of parameters typical of a depleted reservoir.

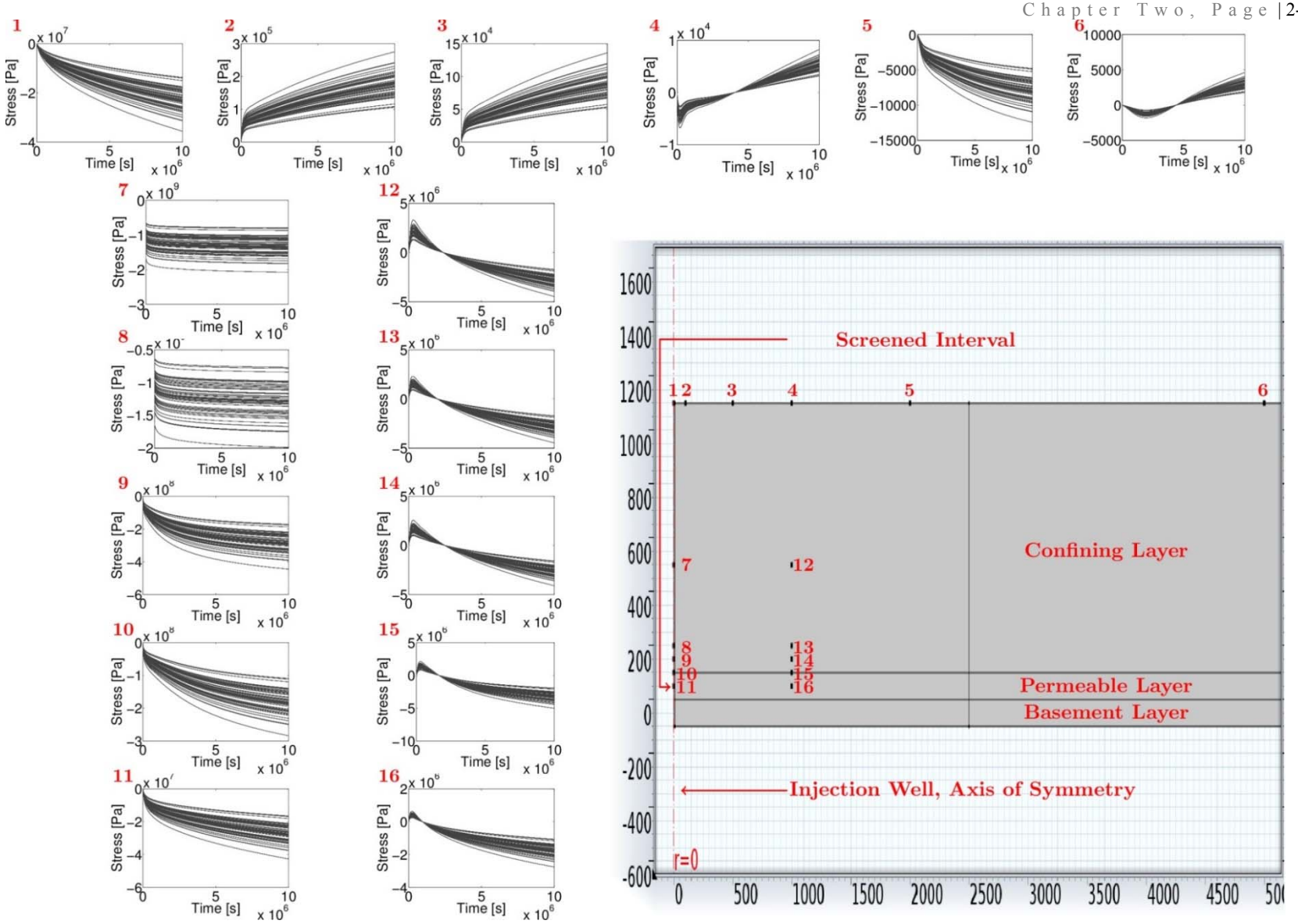

Figure 2.4-5c. Vertical stress as a function of time at different locations for ranges of parameters typical of a depleted reservoir.

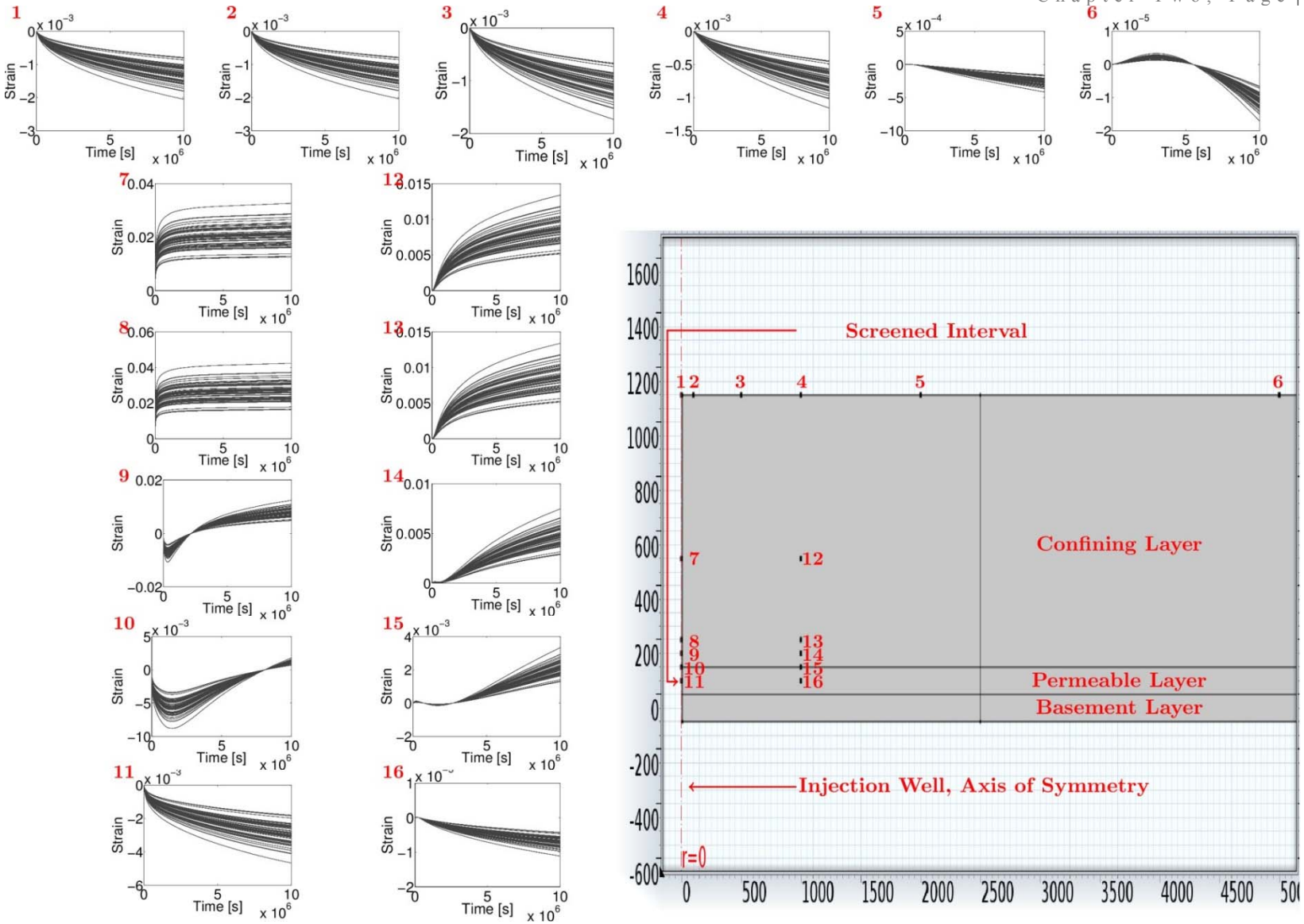

Figure 2.4-5d. Vertical strain as a function of time at different locations for ranges of parameters typical of a depleted reservoir.

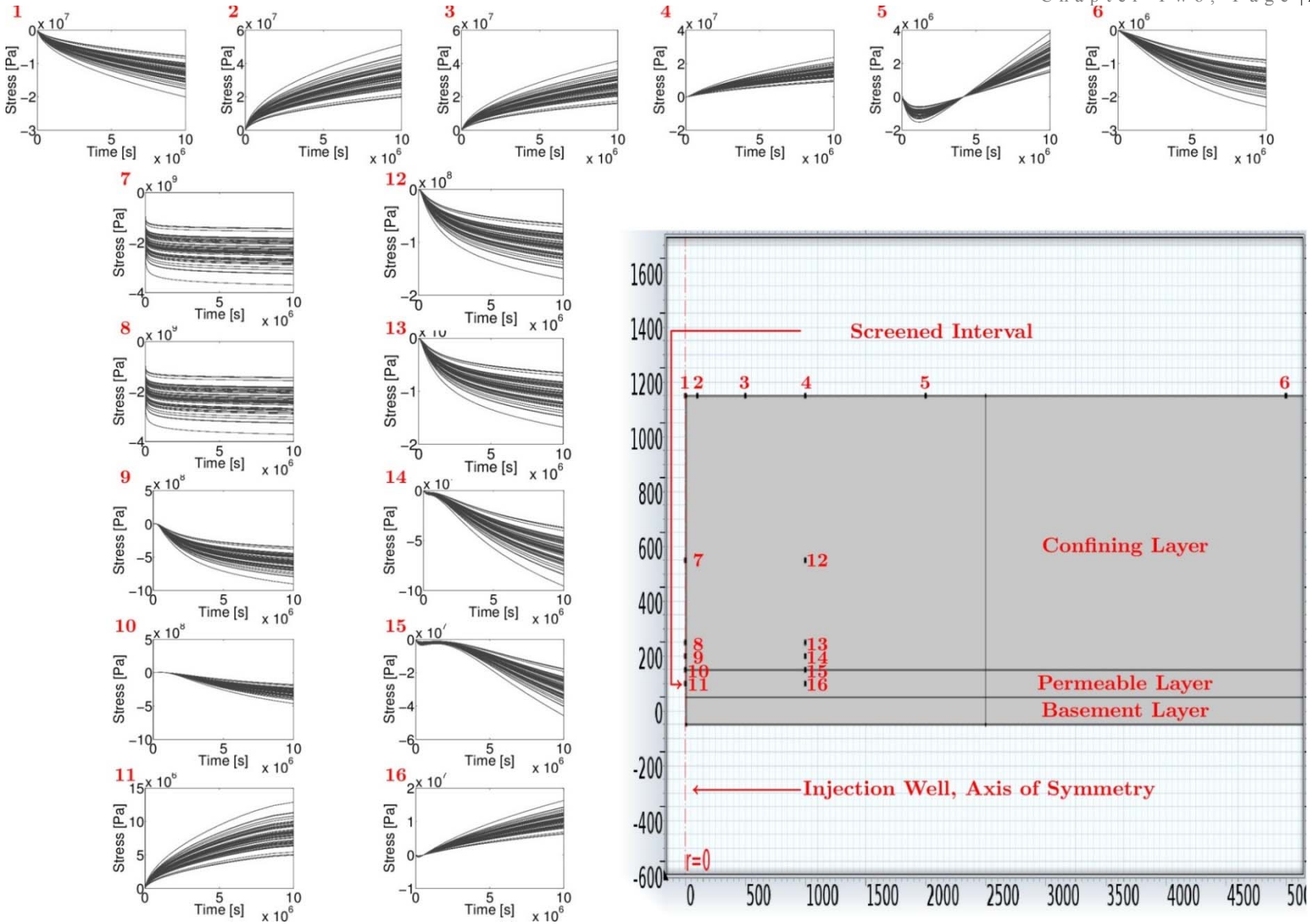

Figure 2.4-5e. Horizontal stress as a function of time at different locations for ranges of parameters typical of a depleted reservoir.

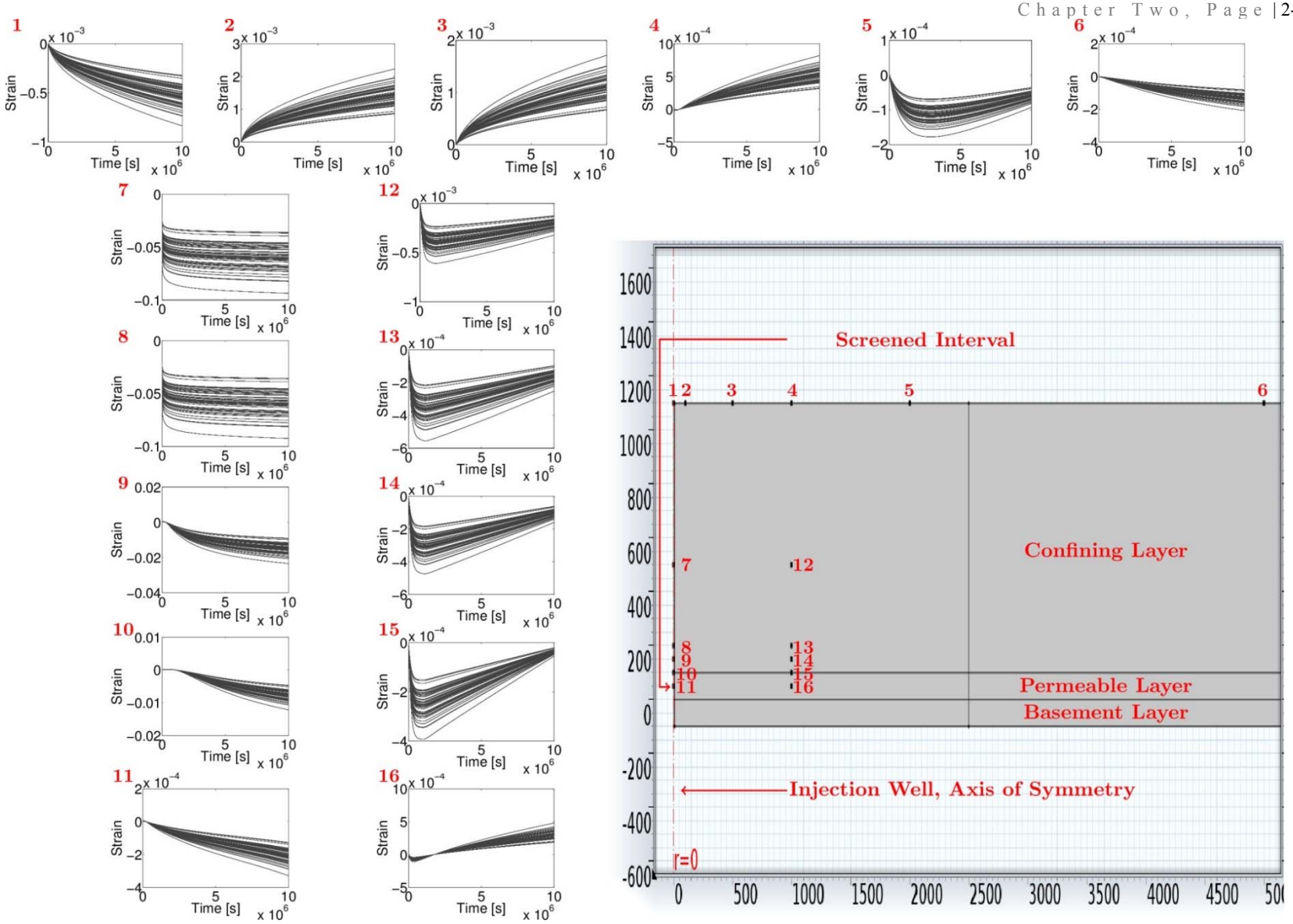

Figure 2.4-5f. Horizontal strain as a function of time at different locations for ranges of parameters typical of a depleted reservoir.

Table 2.4-5. Maximum/mean/minimum strains (με) at observation points at t = 100 days determined using distribution of parameters for a particular reservoir type. Max and min normalized to mean in parentheses. Positive is tensile, negative is compressive strain.

Coord. (m, m)	Location	Radial strain	Circumferential strain	Vertical strain
Type: Depleted oil/gas reservoir				
(0.1, 40)	middle of the reservoir at the injection well	-29/ -19/ -12 (1.5/ 0.6)	63/ 43/ 30 (1.4/ 0.7)	44/ 18/ 5 (2.4/ 0.3)
(0.1, 900)	middle of the confining at the injection well	-38/ -38/ -38 (1.0/ 1.0)	103/ 103/ 103 (1.0/ 1.0)	-2.6/ -1.0/ -0.6 (1.6/ 0.6)
(0.1, 1800)	ground surface at the injection well	-38/ -38/ -38 (1.0/ 1.0)	103/ 103/ 103 (1.0/ 1.0)	-1.5/ -1.3/ -1.1 (1.2/ 0.9)
(1000, 40)	middle of the reservoir at monitoring well	0.8/ 0.5/ 0.3 (1.5/ 0.5)	2.4/ 1.3/ 0.6 (1.8/ 0.4)	17/ 7.5/ 2.3 (2.3/ 0.3)
(1000, 900)	middle of the confining at monitoring well	0.8/ 0.5/ 0.2 (1.7/ 0.5)	0.9/ 0.5/ 0.3 (1.7/ 0.5)	-1.7/ -1.0/ -0.5 (1.7/ 0.5)
(1000, 1800)	ground surface at the monitoring well	0.5/ 0.3/ 0.2 (1.6/ 0.5)	0.5/ 0.3/ 0.2 (1.6/ 0.5)	-0.7/ -0.4/ -0.2 (1.6/ 0.5)
Type: Saline aquifer				
(0.1, 40)	middle of the reservoir at the injection well	-90/ -52/ -33 (1.7/ 0.6)	87/ 68/ 31 (1.3/ 0.5)	246/ 95/ 25 (2.6/ 0.3)
(0.1, 900)	middle of the confining at the injection well	-39/ -38/ -38 (1.0/ 1.0)	104/ 103/ 103 (1.0/ 1.0)	-3.4/ -1.7/ -0.7 (2.1/ -0.4)
(0.1, 1800)	ground surface at the injection well	-38/ -38/ -38 (1.0/ 1.0)	104/ 103/ 103 (1.0/ 1.0)	-2.9/ -1.8/ -1.2 (1.7/ 0.7)
(1000, 40)	middle of the reservoir at monitoring well	0.6/ 0.2/ -0.3 (3.9/ -2.2)	2.5/ 1.5/ 0.8 (1.6/ 0.5)	114/ 46/ 13 (2.5/ 0.3)
(1000, 900)	middle of the confining at monitoring well	0.9/ 0.5/ 0.3 (1.7/ 0.5)	1.3/ 0.7/ 0.3 (1.8/ 0.5)	-1.9/ -1.2/ -0.6 (1.6/ 0.5)
(1000, 1800)	ground surface at the monitoring well	1.0/ 0.5/ 0.2 (1.9/ 0.5)	1.4/ 0.6/ 0.3 (2.2/ 0.4)	-1.6/ -0.8/ -0.3 (2.1/ 0.4)
Type: Coalbed				
(0.1, 5)	middle of the reservoir at the injection well	-100/ -57/ -35 (1.8/ 0.6)	83/ 60/ 17 (1.4/ 0.3)	291/ 120/ 35 (2.4/ 0.3)
(0.1, 380)	middle of the confining at the injection well	-39/ -39/ -38 (1.0/ 1.0)	103/ 103/ 103 (1.0/ 1.0)	-1.1/ -0.5/ -0.1 (2.2/ 0.1)
(0.1, 740)	ground surface at the injection well	-38/ -38/ -38 (1.0/ 1.0)	103/ 103/ 103 (1.0/ 1.0)	-1.6/ -1.2/ -0.9 (1.4/ 0.8)
(1000, 5)	middle of the reservoir at monitoring well	-0.20/ -0.08/ -0.01 (2.6/ 0.1)	0.38/ 0.17/ 0.004 (2.3/ 0.02)	28.0/ 10.0/ 0.01 (2.8/ 0.0009)
(1000, 380)	middle of the confining at monitoring well	0.09/ 0.01/ -0.06 (7.7/ -5.3)	0.23/ 0.11/ 0.005 (2.1/ 0.04)	-0.29/ -0.11/ 0.004 (2.6/ -0.03)
(1000, 740)	ground surface at the monitoring well	0.12/ 0.03/ -0.06 (4.7/ -2.4)	0.23/ 0.11/ 0.008 (2.1/ 0.07)	-0.20/ -0.09/ 0.003 (2.3/ -0.03)

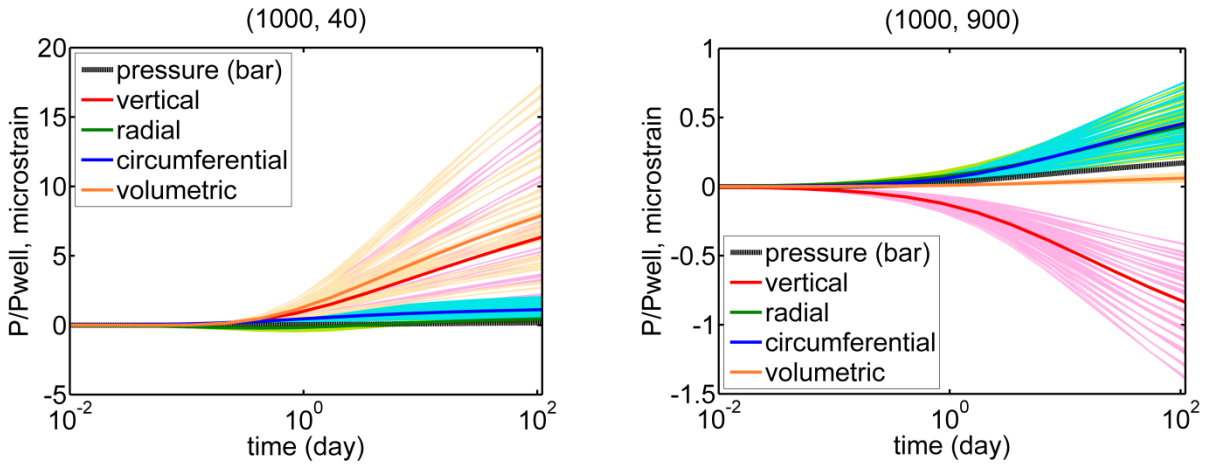

(a) (b)

Figure 2.4-6. Strain and pore pressure at r = 1 km as a function of time for a dataset of parameters representing a depleted oil/gas reservoir. Mean values are plotted as solid lines. a.) the middle of reservoir (z = 40 m) and b.) the top of confining unit (z = 900 m).

2.4.3 SUMMARY

We assembled datasets describing the properties of different reservoir types, and distributions of the important properties have been determined. The parameter distributions were sampled and 243 combinations of parameters were generated to characterize the range of expected properties for each reservoir type. Forward simulations were conducted using the 243 datasets and the resulting strains and displacements at selected locations were characterized as a function of time.

Sensitivity analyses were conducted to evaluate the relative importance of the different parameters on the displacement and strain. The displacements are typically most sensitive to hydraulic conductivity and are relatively insensitive to Biot coefficient and Poisson ratio. The values of the sensitivity changed based on the locations of the observation points. The sensitivity to porosity is negligible.

The variability caused by parameter uncertainty differs among the different strain components, time, and location. In general, however, strain magnitudes vary by less than a factor of 2. The deformation pattern remains unaffected.

The resulting conclusion relevant to this project is that the range of strains resulting from expected variations in average material properties is likely to have little effect on the ability to characterize strain at a particular point. If the strain calculated from a baseline analysis using typical parameters can be measured in the field, then it is likely that the strain from any combination of likely material properties can also be measured.

2.5 EFFECTS OF STRUCTURE AND HETEROGENEITIES

Hetereogenieties in aquifer properties are expected to affect the deformation pattern, altering it from the patterns given above that assume uniform properties. It seems reasonable that the pattern of deformation could be affected by a.) steeply dipping faults that are either sealing or permeable; b.) multiple sealing faults causing compartmentalization; c.) facies changes leading to pinch outs, or elongate structures like channels; d.) localized permeable zones (e.g. fault, sand dike) in overlying cap rock; e.) localized interbeds of shale within the aquifer/reservoir. The presence of these, or other related heterogeneities, may affect CO_2 storage, so it would be useful if these they could be recognized and characterized.

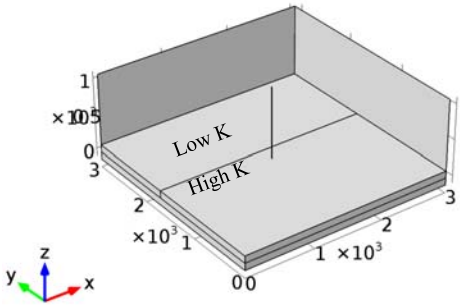

Figure 2.5-1. Configuration of 3D case with a contact.

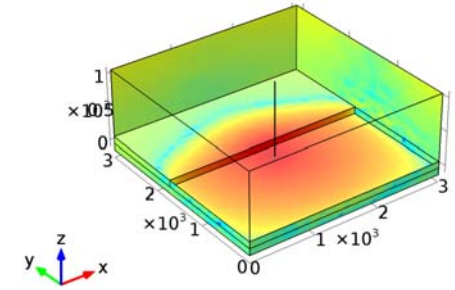

Figure 2.5-2. Volumetric strain after 2 weeks of injection.

Inversion of deformation data is one way that heterogeneities could be characterized. The general approach would be to set up forward models that allowed for the presence of heterogeneities, and then use inverse methods described in Chapter 3 to identify characteristics of the heterogeneities by comparing predicted and observed values. Forward models capable of including heterogeneities are needed to use in the inverse analysis.

The objective of this section is to outline an analysis that considers heterogeneities in material properties during calculations of deformation.

2.5.1 METHODS

The analysis developed here is a fully coupled, poroelastic simulation of flow and deformation in the vicinity of a well. The basic geometry and parameters are similar to those used in Sections 2.2 and 2.3, except the analysis is 3D and the total size of the region is only 3 km. The well is represented as a line source.

The aquifer consists of two zones with different permeability. The permeability distribution is described as a function, and, in principle, the function is arbitrary and can include a large number of parameters describing a complex distribution. However, we intend to control the function with the inversion algorithm, so we have conducted the analysis using simple shapes of heterogeneities that are described by simple functions.

Two examples are shown here. One example consists of a vertical planar contact where the permeability on one side of the contact differs from that on the other side. The well is completed in the zone with relatively high hydraulic conductivity K, and the boundary between high and low K is 300 m from the well in the +y direction. Hydraulic conductivity of the low K zone is 0.1 K in the aquifer. This is a modest contrast in K. The configuration of this analysis is shown in Figure 2.5-1.

2.5.2 RESULTS FOR PLANAR CONTACT

Simulations of injection for 11 days were conducted to evaluate the expected deformation signal during a well test. The presence of the heterogeneity affected the distribution of the strain. For example, the volumetric strain is smaller in the +y direction compared to other directions (Figure 2.5-2).

Time series of strain were evaluated at two points at depths of 200 m located +/- 500 m from the injection well. One point is in the +*y* direction and it overlies the low K zone. Data from this point are shown as blue curves in Figure 2.5-3. The other point is at *y* = -500 m, and data from this

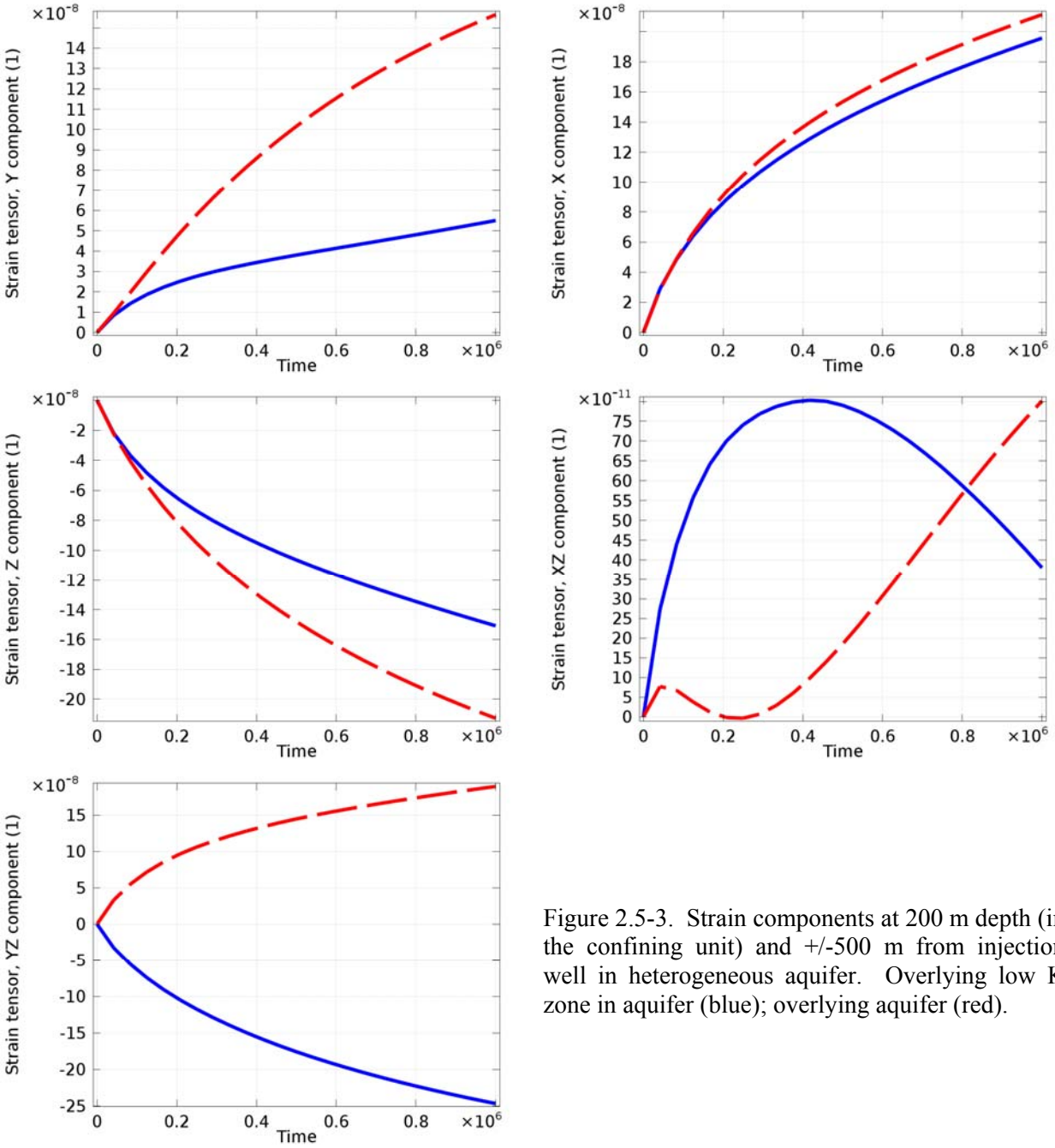

Figure 2.5-3. Strain components at 200 m depth (in the confining unit) and +/-500 m from injection well in heterogeneous aquifer. Overlying low K zone in aquifer (blue); overlying aquifer (red).

point are shown in red in Figure 2.5-3. These points are symmetrically located about the injection well, so responses at these locations are the same when the aquifer is homogeneous.

The results from the time series analyses show that the strains from the two locations are different from each other in all cases. The normal strains at the location underlain by the low K zone are less than the normal strains under the aquifer. The shear strain at these two locations differ in sign. Magnitudes of the strains are greater than 10^{-8} within a few hours of injection in all cases except the shear strain in the ZX direction. This shear strain parallel to the contact.

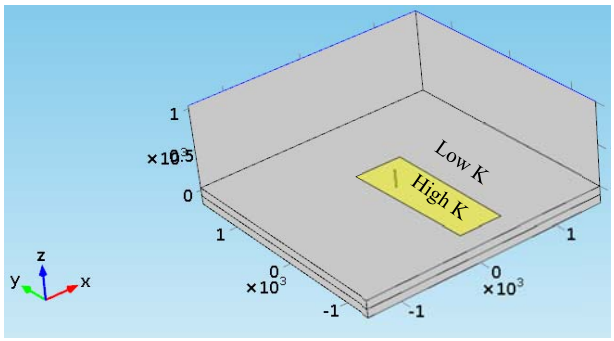

Figure 2.5-4. Rectangular high permeability zone used to test model.

Technology exists to measure all the strains in the figure with a resolution of ~10^{-8}. We conclude that the signals resulting from this injection test could be resolved in the field. Moreover, the signals from the two monitoring locations are strongly sensitive to location and orientation of the heterogeneity.

2.5.3 Results for a Bounded Reservoir

In this example, a heterogeneity is represented by a rectangular zone 225 m wide by 1,300 m long. This zone consists of material with a permeability of k = 10^{-13} m^2 and the permeability of the enveloping material is 10^{-16} m^2. This type of heterogeneity resembles a thick channel sand, for example. The well penetrates the reservoir and it is located asymmetrically within the permeable zone (Figure 2.5-4).

Simulations of injection for 11.6 days were conducted to evaluate the expected deformation signal during a well test. The presence of the heterogeneity affected the distribution of the total displacements (Figure 2.5-5), which has an elongated shape along the heterogeneity. The total displacement would be axisymmetric if the formation was homogeneous. With increasing time, the deformed shape becomes more elongated, but the maximum remains in the vicinity of the injection well location. In this example, the borehole has a diameter of 1 m. This is larger than an actual well, and this increased diameter was adopted to reduce the number of elements and speed the calculations. More discussions on this will be given below after the main results are presented.

Time series of strain were evaluated at 4 observation points at depths of 300 m (i.e., 700 m above the reservoir) located 500 m laterally from the injection well (Figure 2.5-6). Two points, in the $+y$ and $-x$ directions overly the low K zone. Data from these points are shown as blue and red curves, respectively, in Figure 2.5-7a for the volumetric strain and in Figure 2.5-7b for the radial strain. Two other curves correspond to the remaining two points located in the same horizontal plane in $-y$ and $+x$ directions. These four points are symmetrically located about the injection well, so responses at these locations should be the same when the aquifer is homogeneous.

The results from the time series analyses show that the strains from the four locations are different. It is interesting to note that the character of volumetric and radial strains differ for the first two locations as the blue line is higher than the red line in Figure 2.5-6a and the situation is reversed for Figure 2.5-6b. Yet, the volumetric strains at the location underlain by the low K zone are greater

than the volumetric strains under the aquifer. Magnitudes of the strains are greater than 10^{-8} within a few hours of injection in all cases except, and becomes greater than 10^{-7} in a few days.

Time series were also evaluated at 4 points at the borehole surface 50 m below the upper horizontal boundary of the reservoir (Figure 2.5-6). These points are located at distances 0.5 m in the $\pm y$ and $\pm x$ directions. Axial strains at these points (Figure 2.5-7c) differ only slightly. Radial displacements differ distinctly after about 3 hours of injection. The largest and smallest radial displacements are along the x-axis, which causes the borehole to deform into roughly an elliptical shape as a result of the heterogeneity. The curves in 2.5-7c would be the same if the reservoir was homogeneous.

The effect of the heterogeneity is illustrated by the deformation of the borehole, as shown in figure 2.5-8. The absolute position of the borehole moves laterally within the reservoir, and the magnitude of the movement depends on the extent of formation in a particular direction. For example, the lateral extent of the formation is larger in the $+x$ than the $-x$ direction. As a result, during injection the formation expands more on the $+x$ than the $-x$ side, and this causes the borehole to move in the $-x$ direction. Similarly, the extent of the formation in the $-y$ direction is greater than in the $+y$ direction, so the borehole also moved in the $+y$ direction within the reservoir. However, the lateral movement within the confining unit is less than in the reservoir. This causes the casing to bend, as shown in the Figures 2.5-8 and 2.5-9.

These results are noteworthy because they show that the borehole will bend in response to a heterogeneity. Instrumentation that could measure this type of bending was demonstrated in the field during the NAWC field test described starting on page 4-60 in Chapter 4.

Total displacement is asymmetrically distributed around the borehole at the depth of 300 m (Figure 2.5-10a). Arrows in this figure are also asymmetric and represent the tilt directions and magnitude. They can be seen more clearly in Figure 2.4-7b, where the displacement distribution is removed. Displacements and tilts at a depth of 300 m in the confining unit reflect the geometry of the underlying heterogeneity. Recognizing that the deformation of the confining unit is sensitive to the underlying heterogeneity is a first step toward using deformation to characterize formation heterogeneity.

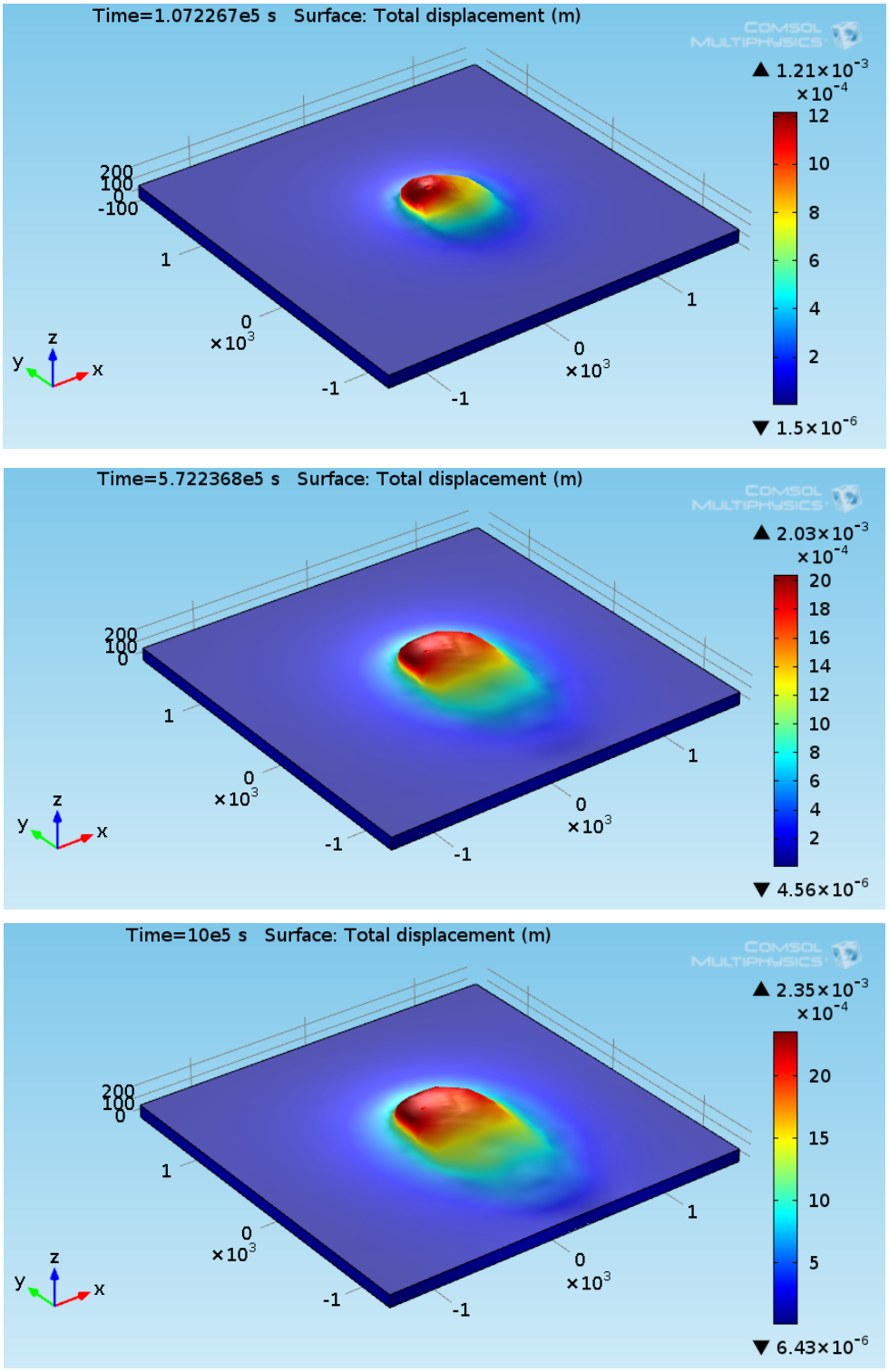

Figure 2.5-5. Total displacement at the top of the reservoir (m) at three different times. Injection into a rectangular reservoir with the well located as shown above in Figure 2.5-4.

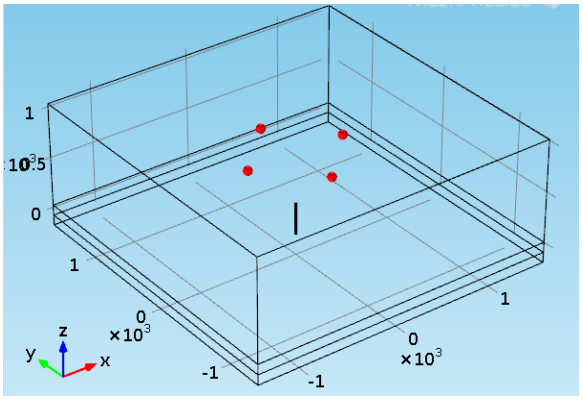

(a)

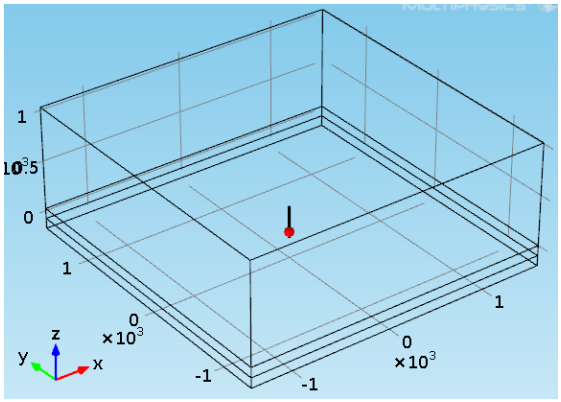

(b)

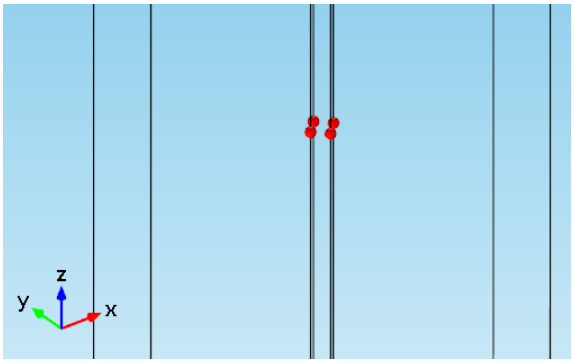

(c)

Figure 2.5-6. Location of points where the time series were taken. (a) 4 points at depths of 200 m located 500 m from the injection well. (b) 4 points on the surface of the injection well. (c) Close-up view of points at the surface of the injection well.

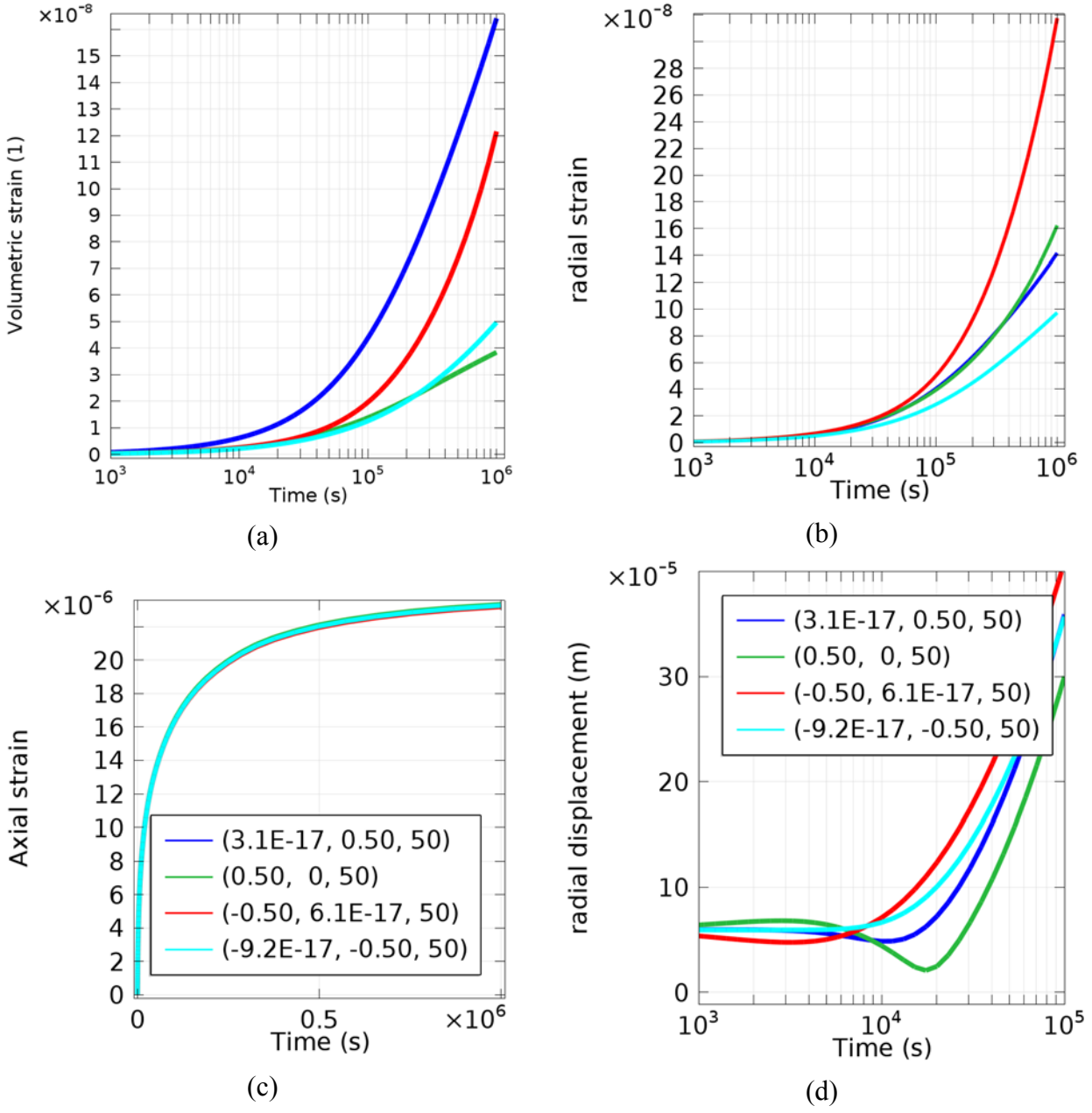

Figure 2.5-7. Time series of (a) volumetric and (b) radial strains at the observation points (±500, ±500, 800) (m), located at depths of 300 m and (c) axial strains and (d) radial displacements evaluated at 4 points (±0.5, ±0.5, 50) (m), located on the reservoir middle plane (i.e., 50 m above the reservoir bottom surface).

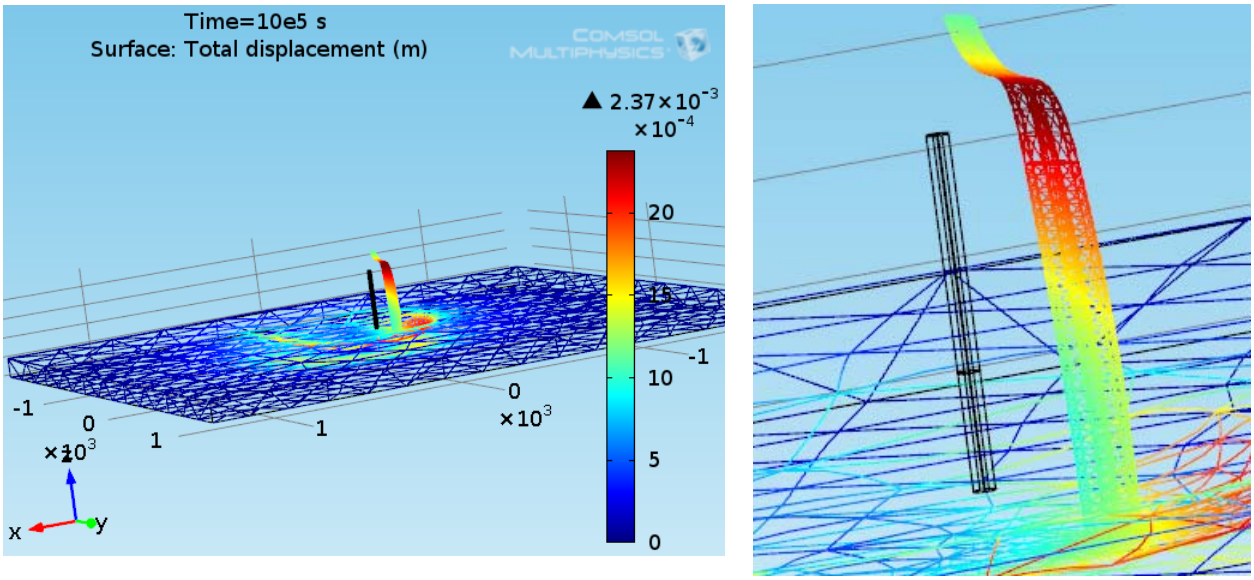

Figure 2.5-8. Total displacement (color) in m of the lower confining unit and the region around the borehole in deformed coordinates. The black frame is the original position of a 10-m radius cylinder around the borehole. The borehole is within this cylinder. The reservoir and upper confining unit have been removed to highlight the borehole. The contact between the reservoir and upper confining unit (i.e., the upper boundary of the reservoir located at the depth of 1,000 m) is marked by a kink in the borehole. Deformation magnified by a factor of 8.9×10^4.

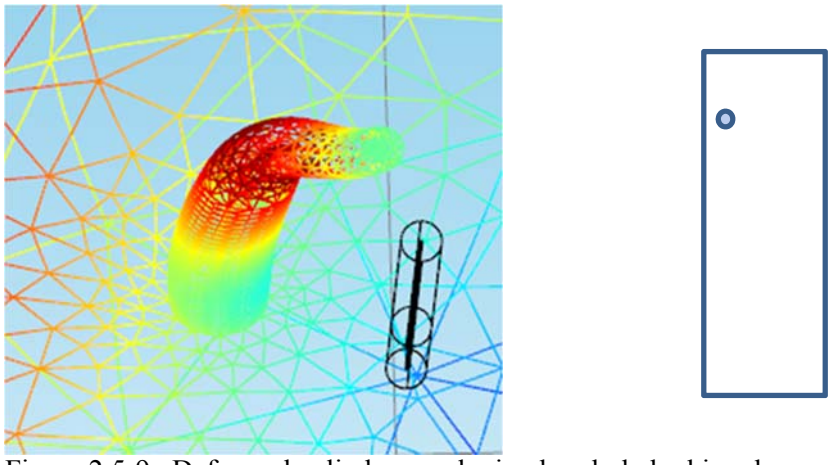

Figure 2.5-9. Deformed cylinder enveloping borehole looking down. Original location of cylinder shown as the black frame. Original borehole is heavy line at center of cylinder. Light black line is y axis. +x is to the right. The position of the borehole in the reservoir shown to the right. Pressurizing the formation causes the borehole to move away from the directions of more extensive formation. This effect is reduced in the confining unit, resulting in a kink in the borehole at the contact.

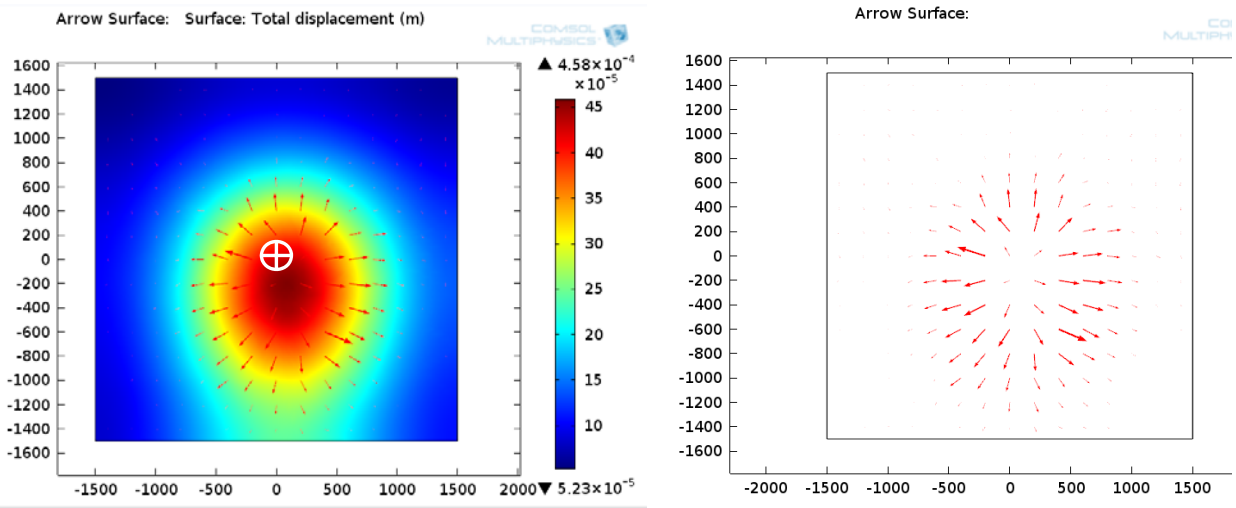

Figure 2.5-10. (a) Total displacement distribution (color) in m around the borehole (white cross in circle) at the depth of 300 m shown together with tilt direction and magnitude (arrows) and (b) tilt directions and magnitude with the displacement distribution removed. The length of the arrows is proportional to the tilt magnitude.

2.6 DEFORMATION OF AN INJECTION WELL

Injection will cause a well to expand outward and to stretch vertically in the vicinity of the well screen. Details of the displacement depend on both elastic and poroelastic effects, with the elastic effects dominating at the wellbore. In the confining unit, the casing extends outward and it can be compressed axially. This compression occurs as a response to the vertical stretching of the underlying reservoir. This basic response of the well casing is described in Section 2.3.

Additional analyses of the deformation of the injection well were conducted to evaluate details in the confining unit and as a result of leaks in the annular space.

2.6.1 INJECTION INTO AN IDEAL LAYER WITH CONFINING UNIT

This case evaluates deformation in the vicinity of an ideal layer and an overlying confining unit. The material properties and boundary conditions for this simulation are shown in Tables 2.6-1 and 2.6.-2, respectively. It consists of a 1 m thick permeable layer overlain by a 10 m thick layer with lower permeability (Figure 2.6-1a). The initial permeability of the confining layer is approximately 10^{-15} m^2 (1 md). The effects of the confining layer on deformation were evaluated by varying the permeability of the confining layer by a factor of 2.

Injection was assumed to occur at a constant pressure of 1 MPa. This condition was selected so the wellbore pressure was constant and the effects of casing deformation would only be due to processes in the formation.

Table 2.6-1. Properties

	formation	confining	screen
k	10^{-13} m^2	10^{-15} m^2+/-	10^{-13} m^2
E	1 GPa	1 GPa	200 GPa
υ	0.25	0.25	0.25
α	1	1	1

Table 2.6-2. Boundary conditions

Location	Fluid	Solid
Inner, $r = 0.1$, $0 < z < 1$ m	$p = 1$ MPa	$\sigma_n = p$
Inner, $r = 0.1$, $1 < z < 11$ m	No flow	$\sigma_n = p$
Upper and lower, $z = 0$, 21 m	No flow	Roller, $\tau = 0$
Outer, $r = 20$ m, $0 < z < 11$ m	$p = 0$	Roller, $\tau = 0$

Results

The results show that pressurization of the wellbore causes the casing and screen to bulge outward (Figure 2.6-1b). Radial displacement of the casing is roughly 7 microns, which is greater than the 2 microns or so of displacement at the screen. The maximum displacement of the casing occurs a few meters above the screen, with displacement diminishing above this point. These results assume the elastic modulus of the screen and casing are the same. With time, the displacement of the screen diminishes as does the radial displacement of the confining unit in the vicinity of the aquifer (Figure 2.6-1b). The radial displacement near the top of the confining unit increases with time, however.

The displacement signal at two points in the confining unit was evaluated for sensitivity to properties of the confining unit (Figure 2.6-1c). This analysis is intended to mimic data that could be measured in situ. Taking the displacements relative to the start of injection (after the initial pressurization) gives results that are somewhat surprising. The radial displacement initially is inward (negative displacements) 0.5 m above the contact, but it is outward 5 m above the contact. The displacements reach a maximum value at $z = 0.5$ m and then decrease, whereas at $z = 5$ m the displacements change sign and the casing moves outward after a few minutes (Figure 2.6-1c).

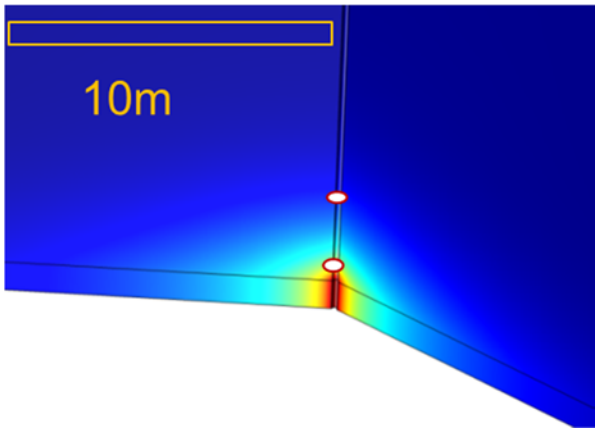

Figure 2.6-1a. Pressure distribution in aquifer and confining unit during constant rate injection. Observation points shown in confining unit.

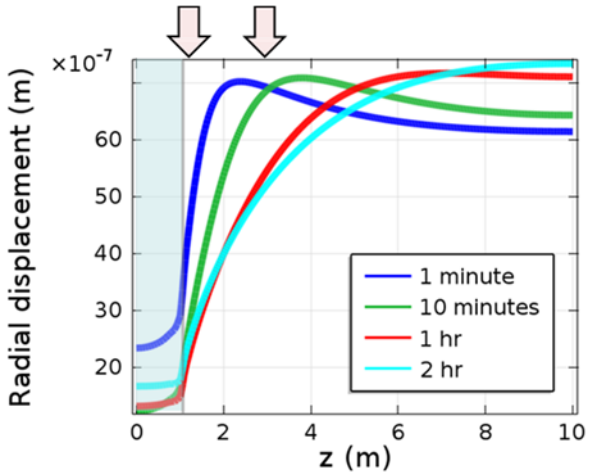

Figure 2.6-1b. Radial displacement of casing along the well as function of time. Aquifer is between $0 < z < 1$ m (blue). Location of observation points for transient data (arrows).

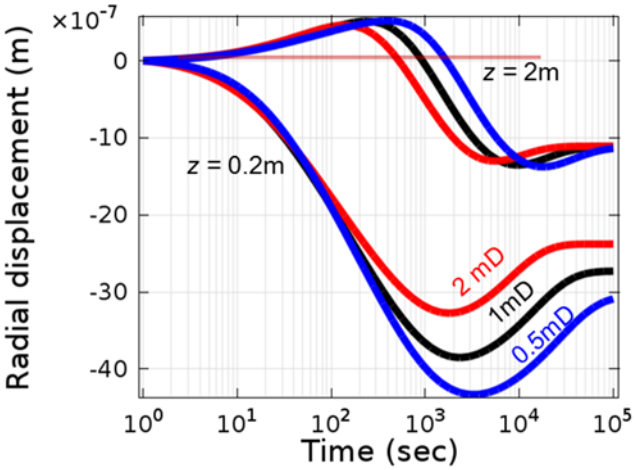

Figure 2.6-1c. Radial displacements as function of time at two observation points for confining units with 3 different permeabilities.

The effect outlined above apparently occurs as the pressure change in the aquifer/reservoir propagates upward and affects a progressively larger thickness of the confining unit. This pressure increase in the formation compresses the casing and accounts for the progression away from the screen. Compressing one interval of the screen will unload another interval in order to maintain equilibrium. This is why the casing bulges outward at z = 5 m when it contracts inward at z = 0.5 m.

Changing the permeability of the confining unit has a significant effect on radial displacement of the casing (Figure 2.6-1c). Doubling the permeability causes displacements to occur earlier and it can affect their magnitude. Cutting k by half has the opposite effect. The change in response caused by modifying k by a factor of 2 is a sizable fraction of the total signal. Moreover, peaks or troughs in the displacement signal occur at significantly different times when k is changed by a factor of 2.

Axial strains in the casing are also affected by the injection process (Figure 2.6-2). Pressurizing the aquifer causes tensile (positive) axial strain adjacent to the aquifer and compressive strain where the casing cuts the confining unit. With time, the tensile strain in the aquifer increases and moves further into the confining unit, while the compressive strain near the top of the confining unit also increases.

Axial strains at monitoring points z = 0.5 m and z = 2.0 m are approximate mirror images of the radial displacements (Figures 2.6-1 and 2.6-2). Changing the permeability by a factor of 2 causes a distinct change in the shapes and magnitudes of the axial strain time series.

One important distinction, however, is the magnitude of the axial displacement is one to two orders of magnitude larger than the magnitude of the radial displacement. As a result, it would be easier to measure the axial strain than the radial component. One possibility is that the axial strain could be measured with the WIRE system, which is installed in the annular region between the casing and the formation. The WIRE system is introduced in Section 4.2.

These results suggest that both radial displacement and axial displacement are sufficiently sensitive to the permeability of the confining unit that it may be possible to use these time series to estimate the vertical permeability of confining units during well tests.

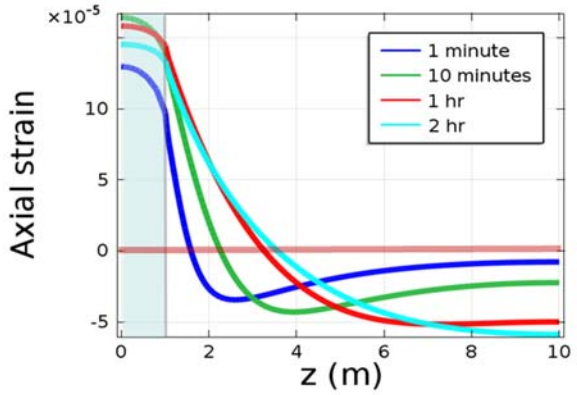

Figure 2.6-2a. Axial strain of casing along the well as function of time. Aquifer is between 0 < z < 1 m (blue).

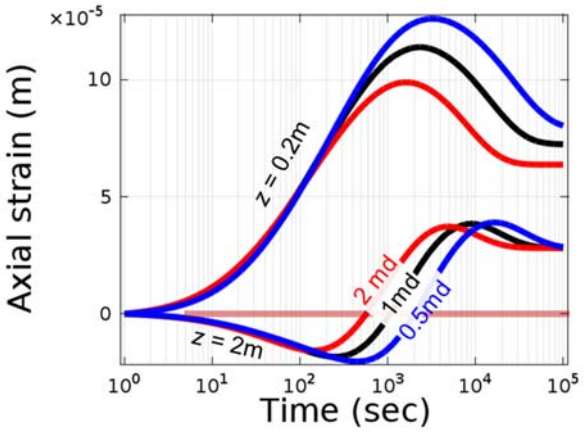

Figure 2.6-2b. Axial strain as function of time at two observation points for confining units with 3 different permeabilities.

2.6.2 Effect of Leakage Between Casing and Formation

The effect of leakage between casing and formation was evaluated by using the transient model outlined above and including a permeable annular zone. We assumed the permeability of this zone was 10^{-9} m^2 and it was 10^{-3} m thick. The specific storage of the fracture was assumed to be 10^{-9} Pa^{-1}.

The permeability of the confining unit used for this simulation is 10^{-17} m^2. This is a reasonable value for a confining unit, but it is lower than the value used in the previous case. With the exception of the permeability of the confining unit, the simulation used for this example is the same described in the previous section.

Results

The pressure enveloping the casing increases significantly when the high permeability zone is included in the simulation (Figure 2.6-3). Both radial displacement and axial strain are affected by the increased pressure enveloping the casing. The effect is to reduce the magnitude of displacement and strain and make the peak value occur sooner.

It appears that radial displacement and axial strain are sensitive to a high permeability zone adjacent to the casing for this example.

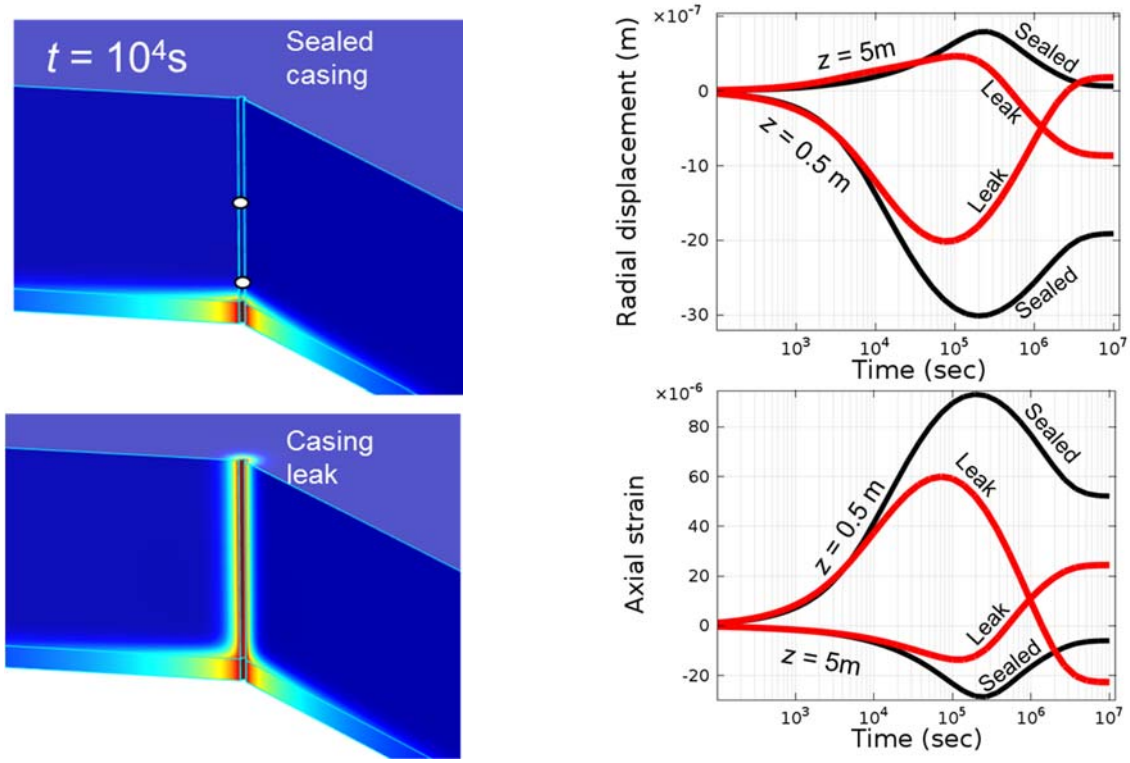

Figure 2.6-3. a.) Pressure distribution (color) after ~3 hrs of injection where casing is sealed or where it is enveloped by a high permeability layer. Observation points for transient displacement shown in upper diagram as white ellipses. b.) Radial displacement and axial strain as function of time at two locations (z = 0.5 and z = 5 m) on casing for sealed and leaking scenarios.

2.7 SUMMARY OF CHAPTER FINDINGS

The overall objective of this chapter was to estimate the magnitude and pattern of deformation associated with injecting fluid into reservoir. To meet this objective, we conducted a series of theoretical analyses using analytical and numerical models that solved problems in poroelasticity. We found that readily available computer codes (ABAQUS and COMSOL) can solve problems related to deformation in the vicinity of injection wells using finite element methods. We tested these codes in a variety of relevant example problems, and we developed a poroelastic benchmark model intended to be used by other investigators interested in validating other codes. The run times for fully coupled finite element codes can be time consuming and may be prohibitive for some inverse methods. To address this constraint, we developed two analytical asymptotic solutions that can be used to calculate deformation very quickly.

The magnitude and pattern of deformation were calculated using an idealized simulation that was based on properties typical of CO_2 storage operations. The analysis assumed an injection pressure of 1 MPa, which resulted in an injection rate of approximately 100 gpm, and the injection lasted for 100 days. This is a lower pressure and shorter duration than full scale operations, but it may be a higher pressure and longer than an injection test conducted for formation evaluation.

The results indicate that the axial strain will be tensile and approximately 10 με adjacent to the pressurized interval. It will decrease and change sign upward with axial compression of several με in the casing adjacent to the confining unit. Radial displacements of several microns are largely due to pressurizing the wellbore, but smaller changes in radial displacements occur with time as the formation pressure changes.

The pattern of strain in the casing is sensitive to the pressure in the annular space and in the confining unit. It may be feasible to estimate changes in pressure on the outside of solid casing by measuring casing deformation, and this could be used to characterize well bore integrity or the permeability of confining units.

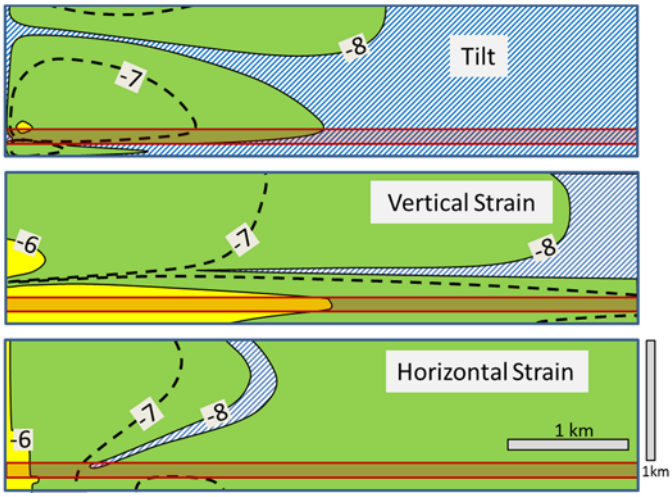

Figure 2.7-1. Summary strain magnitudes (as log of absolute value) in cross section after injecting for 100 days at 1 MPa according to baseline example. Colors show three categories (yellow: $\varepsilon > 10^{-6}$; green: $10^{-8} < \varepsilon < 10^{-6}$; hatched: $\varepsilon < 10^{-8}$). The aquifer/reservoir is shown in red, and the well is on the lower left.

Strain rates of 10^{-12} 1/s or greater are expected in the vicinity of the wellbore early in the injection. The strain rate will decrease with time to 10^{-13} 1/s or less in the first 100 days of injection. Strain rates of 10^{-13} 1/s occur in the confining unit and they also decrease with time.

The magnitude of strain at the well and in the formation increases roughly in proportion to the injection pressure (the results above are for 1 MPa)

The magnitude of the strain rate at the well and in the formation increases roughly in proportion to the injection rate (the results above are for approximately 100 gpm).

Formation properties will affect the magnitude of expected deformation, but the overall effect is generally less than a factor of two when using ranges of properties associated with a particular type of reservoir.

The distributions of strain components in the formation create varied patterns that evolve with time. An example of three components of the strain tensor after injecting for 100 days is summarized in Figure 2.7-1. The strain patterns depend on the magnitude and distribution of formation properties, so they are sensitive to heterogeneities in the aquifer and overlying confining unit. Patterns of horizontal and vertical strains, as well as displacement gradients (tilts) occur in the overlying confining unit in response to pressure changes in the underlying reservoir. The patterns result from both a.) radially outward and upward displacement of the reservoir, and b.) upward bending of the ground surface.

The strains predicted to occur in the vicinity of an injection well are in the range of available instrumentation. Strain in excess of 1 με ($>10^{-6}$) will likely occur in the vicinity of the injection well, according to the analysis. Strains of this magnitude can be measured by common strain gauges, and a system called WIRE, which consists of many strain gauges on a fiber optic cable, is available for downhole deployment along wellbores. Strains in excess of 10^{-8} can be measured by portable extensometers and tiltmeters, according to tests conducted in shallow aquifers. Vertical and horizontal strains and tilts of this magnitude occur within a few km of the injection well within 100 days of injection (Figure 2.7-1), according to the simulations. It appears that the strains that are expected to occur in the vicinity of injection wells are within the resolution of instruments that could be temporarily anchored in monitoring wells. Horizontal and vertical strains greater than 10^{-10} can be resolved by instruments that are grouted into boreholes. Strains of these low magnitudes will up to many km from injection wells, although distinguishing these small strains from background noise may be challenging.

2.8 REFERENCES

Agnew, D.C. (1986), Strainmeters and tiltmeters, *Reviews of Geophysics* 24(3):579-624.

Bellin, A., and D. Tonina (2007), Probability density function of non-reactive solute concentration in heterogeneous porous formations, *Journal of Contaminant Hydrology* 94:109-125, doi:10.1016/j.jconhyd.2007.05.005.

Benge, G. (2009), Improving wellbore seal integrity in CO_2 injection wells, *Energy Procedia* 1(1): 3523-3529.

Cappa, F., and J. Rutqvist (2011), Impact of CO_2 geological sequestration on the nucleation of earthquakes, *Geophysical Research Letters* 38(17), doi:10.1029/2011GL048487.

Chadwick, R.A., P. Zweigel, U. Gregersen, G.A. Kirby, S. Holloway, and P.N. Johannessen (2004), Geological reservoir characterization of a CO_2 storage site: The Utsira Sand, Sleipner, northern North Sea, *Energy*, 1371-1381.

Chiaramonte, L., M.D. Zoback, J. Friedmann, and V. Stamp (2007), Seal integrity and feasibility of CO2 sequestration in the Teapot Dome EOR pilot: geomechanical site characterization, *Environmental Geology* 54(8):1667-1675, doi:10.1007/s00254-007-0948-7.

Childers, B.A., F.H.K. Rambow, D.E. Dria, M.Y. Shuck, D.S. Homa, and S.H. Poland (2007), Downhole fiber optic real-time casing monitor, in *Industrial and Commercial Applications of Smart Structures Technologies, Proceedings of the SPIE, Volume 6527, article id. 65270J*, edited by L.P. Davis, et al., doi:10.1117/12.715289.

Crow, W., J. W. Carey, S. Gasda, D. B. Williams, and M. Celia (2010), Wellbore integrity analysis of a natural CO2 producer, *International Journal of Greenhouse Gas Control*, *4*, 186-197.

Davis, E. (2011), Interpretation of CO2 sequestration-induced surface deformatioin over KB-502 at Krechba, Algeria, in *Society of Petroleum Engineers*, edited.

Davis, S. N., F. L. Peterson, and A. D. Halderman (1969), Measurement of small surface displacements induced by fluid flow, *Water Resources Research*, *5*(1), 129-138.

Detournay, E., and A. H.-D. Cheng (1993), Fundamentals of Poroelasticity, in *Comprehensive Rock Engineering: Principles, Practice and Projects, Vol. II, Analysis and Design Method*, edited by C. Fairhurst, pp. 113-171, Pergamon Press.

Dusseault, M. B., M. S. Bruno, and J. Barrera (2001), Casing Shear: Causes, Cases, Cures, *SPE Drilling & Completion*(72060).

Ellsworth, W. L. (2013), Injection-induced earthquakes, *Science*, *341*, doi:10.1126/science.1225942.

Foerster, A., B. Norden, K. Zinck-Jørgensen, P. Frykman, J. Kulenkampff, E. Spangenberg, J. Erzinger, M. Zimmer, J. Kopp, Guenter Borm, C. Juhlin, C.-G. Cosma, and S. Hurter (2006), Baseline characterization of the CO2SINK geological storage site at Ketzin, Germany *Environmental Geosciences*, *13*(3), 145-161.

Gale, J. E. (1975), A numerical, field and laboratory study of flow in rocks with deformable fractures, Ph.D. thesis, 255 pp, University of California, Berkeley.

Ghomian, Y., G. A. Pope, and K. Sepehrnoori (2008), Reservoir simulation of CO_2 sequestration pilot in Frio brine formation, USA Gulf Coast, *Energy*, *33*, 1055-1067.

Gibson, R.I., (1995), Basement tectonics and hydrocarbon production in the Williston Basin: An interpretive overview: 7th Int'l. Williston Basin Symposium, 1995 Guidebook, p. 3-11

Gladwin, M.T. (1984), High precision multi-component borehole deformation monitoring, *Review of Scientific Instruments*, *55*, 2011-2016.

Gladwin, M.T., and R. Hart (1985), Design parameters for borehole strain instrumentation, *Pure and Applied Geophysics*, *123*, 59-80.

Gutierrez, M., D. Katsuki, and A. Almrabat (2012), Effects of CO2 Injection on the Seismic Velocity of Sandstone Saturated with Saline Water, *International Journal of Geosciences*, *3*, 908-917, doi:10.4236.

Hesler, G., Z. Zheng, and L. Meyer (1990), In-situ fracture stiffness determination, in *Rock Mechanics contributions and challenges*, edited by Hustrulid, et al., pp. 405-411, Balkema, Totterdam.

Hisz, D. B., L. C. Murdoch, and L. N. Germanovich (2013), A portable borehole extensometer and tiltmeter for characterizing aquifers, *Water Resources Research*, *49*, 1-11, doi:10.1002/wrcr.20500.

Hovorka, S. D., T. A. Meckel, and R. H. Trevino (2013), Monitoring a large-volume injection at Cranfield, Mississippi—Project design and recommendations, *International Journal of Greenhouse Gas Control*, *18*, 345-360.

IPCC (2005), Carbon Dioxide Capture and Storage*Rep.*, 431 pp, Intergovernmental Panel on Climate Change, Cambridge University Press, New York.

Liebschera, A., F. Möllera, A. Bannachb, S. Köhlerc, J. Wiebachd, C. Schmidt-Hattenbergera, M. Weinera, C. Pretschnerb, K. Ebertb, and J. Zemkec (2013), Injection operation and operational pressure–temperature monitoring at the CO2 storage pilot site Ketzin, Germany—Design, results, recommendations, *International Journal of Greenhouse Gas Control*, *15*, 163-173.

Lin, P., and T. G. Ray (1994), A New Method for Direct Measurement of In-Situ Stress Directions and Formation Rock Properties *Journal of Petroleum Technology*, *46*(3), 249-254.

Liu, G. (2012), Carbon Dioxide Geological Storage: Monitoring Technologies Review, in *Greenhouse Gases - Capturing, Utilization and Reduction*, edited by G. Liu, pp. 299-338, InTech.

Markley, M. E., N. Last, S. Mendoza, and S. Mujica (2002), Case Studies of Casing Deformation due to Active Stresses in the Andes Cordillera, Colombia., the IADC/SPE Drilling Conference, Dallas, Texas, 26–28 February.

Martin, C. D., C. C. Davison, and E. T. Kozak (1990), Characterizing normal stiffness and hydraulic conductivity of a major shear zone in granite, in *Rock Joints*, edited by Barton and Stephansson, pp. 549-556, Balkema, Rotterdam.

Maxwell, S. C., J. Du, and J. Shemeta (2008), Passive seismic and surface monitoring of geomechanical deformation associated with steam injection, *The Leading Edge*, *27*(9), 1176-1184.

Meertens, C., J. Levine, and R. Busby (1989), Tilt observations using borehole tiltmeters: 2. Analysis of data from Yellowstone National Park, *Journal of Geophysical Research*, *95*(B1), 587-601.

Morris, C., J. Vaeth, R. van Kuijk, and B. Froelich (2007), Enhanced ultrasoni measurements for cement and casing evaluation, in *AADE (American Association of Drilling Engineers) National Technical Conference and Exhibition*, edited, American Association of Drilling Engineers, the Wyndam Greenspoint Hotel, Houston, TX.

Phillips, S. P., C. S. Carlson, L. F. Metzger, J. F. Howle, D. L. Galloway, M. Sneed, M. Ikehara, K. W. Hudnut, and N. E. King (2003), Analysis of Tests of Subsurface Injection, Storage, and Recovery of Freshwater in Lancaster, Antelope Valley, California*Rep.*, 122 pp, U.S. Geological Survey, Sacramento, California.

Riddiford, F. A., A. Tourqui, C.D. Bishop, B. Taylor, and M. Smith (2003), A cleaner development: The In Salah Gas Project, Algeria., Proceedings of the 6th International Conference on Greenhouse Gas Control Technologies (GHGT-6), Pergamon, Kyoto, Japan, 1–4 October 2002.

Sacks, I. S., S. Suyehiro, D. W. Evertson, and Y. Yamagishi (1971), Sacks-Evertson strainmeter, its installation in Japan and some preliminary results concerning strain steps, *Papers in Meteorology and Geophysics*, *22*, 195-207.

Schweisinger, T., E. J. Svenson, and L. C. Murdoch (2011), Hydromechanical Behavior During Constant-Rate Pumping Tests in Fractured Gneiss, *Hydrogeology Journal*, *19*, 963-980.

Senel, O., and N. Chugunov (2013), CO2 injection in a saline formation: pre-injection reservoir modeling and uncertainty analysis for Illinois Basin Decatur Project, *Energy Procedia*, *37*, 4598-4611, doi:10.1016/j.egypro.2013.06.368.

Shafeen, A., E. Croiset, P. L. Douglas, and I. Chatzis (2004), CO2 sequestration in Ontario, Canada. Part I: storage evaluation of potential reservoirs, *Energy Conversion and Management*, *45*(17), 2645-2659, doi:10.1016/j.enconman.2003.12.003.

Svenson, E. J., T. Schweisinger, and L. C. Murdoch (2007), Analysis of the hydromechanical response of a flat-lying fracture to a slug test, *Journal of Hydrology*, *347*, 35-47.

Thompson, P. M., and E. T. Kozak (1991), In situ measurement of coupled hydraulic pressure/fracture dilation in stiff crystalline, in *Field Measurements in Geotechnics*, edited by Sørum, pp. 23-31, Balkema, Rotterdam.

Vasco, D. W., K. Karasaki, and K. Kishida (2001), A coupled inversion of pressure and surface displacement, *Water Resources Research*, *37*(12), 3071-3087, doi:10.1029/2001WR000391.

Vasco, D. W., A. Rucci, A. Ferretti, F. Novali, R. C. Bissell, P. S. Ringrose, A. S. Mathieson, and I. W. Wright (2010), Satellite-based measurements of surface deformation reveal fluid flow associated with the geological storage of carbon dioxide, *Geophysical Research Letters*, *37*(3), doi:10.1029/2009gl041544.

Verdon, J. P., J.-M. Kendall, A. L. Stork, A. Chadwik, D. J. White, and R. C. Bissell (2013), Comparison of geomechanical deformation induced by megatonne-scale CO2 storage at Sleipner, Weyburn, and In Salah, *Proceedings of the National Academy of Sciences, PNAS*, E2762–E2771.

Wang, H. F. (2000), *Theory of Linear Poroelasticity with Applications to Geomechanics and Hydrogeology*, 276 pp., Princeton University Press.

Zoback, M. D., and S. M. Gorelick (2012), Earthquake triggering and large-scale geologic storage of carbon dioxide, *Proceedings of the National Academy of Sciences, PNAS*, *109*(26), 10164–10168.

CHAPTER THREE
OPTIMIZATION AND PARAMETER ESTIMATION

CONTENTS

CHAPTER THREE
OPTIMIZATION AND PARAMETER ESTIMATION

3.1 EXECUTIVE SUMMARY

The goal of this task is to evaluate the potential of geomechanical data collected during injection operations as a constraint on reservoir model parameters. A major enabling contribution of this work was, therefore, the development of advanced optimization algorithms that leverage high performance computing to calibrate reservoir parameters. The approach developed here integrates several different sampling and optimization schemes (genetic algorithms, MCMC, naïve Monte Carlo, and Voronoi polygons) to balance algorithmic speed versus the evaluation of parameter uncertainty and tradeoffs in the data. This method was then used to study the ability of different types of data to constrain reservoir parameters and evaluate how this translates to predictions of long-term operational behavior. The key outcomes of the research are summarized in the three sections below that relate directly to the three goals outlined in the original project proposal. The rest of this report, however, is structured in a format that provides a clearer explanation of the results given substantial overlaps between the sections.

3.1.1 PARAMETER UNCERTAINTY AND UNIQUENESS

We have demonstrated that different combinations of geomechanical measurements such as pressure, tilt and strain can be used to estimate poroelastic parameter values and their uncertainties. Notably, the most accurate parameter estimates with the lowest uncertainties are obtained when pressure data are used in conjunction with measurements sensitive to all three components of reservoir strain. We have also investigated how measurement location impacts our ability to estimate parameters and found that measurements within cap rock theoretically provide sufficient information for calibrating the model parameters, thus suggesting that field studies may not require penetration of the target formation, thus reducing risk.

3.1.2 PREDICTION SENSITIVITY

Evaluating the sensitivity of predictions to uncertainty and error in model estimates was considered within the scope of this work. Using Monte Carlo simulations, we were able to produce forecasts of reservoir performance for different data constraint cases, i.e., where parameter uncertainty depended on the type of data used in the optimization. We found that the degree of uncertainty in the forecasts scaled with the degree of uncertainty in the parameter estimates. A second type of study we performed evaluated the effect of model errors on predictions, i.e., the case where a model does not capture key information about the underlying reservoir system, such as a preferential flow path through a fracture or along the borehole. We found that in these scenarios, significant errors in parameter estimates could occur, but model predictions were well outside reasonable uncertainties in the data thus providing a mechanism to identify and correct these model errors when geomechanical data are used as a constraint.

3.1.3 LARGE-SCALE OPTIMIZATION

We have investigated a number of stochastic and deterministic optimization methods, and evaluated their viability for large-scale optimization of poroelastic forward models. We have

observed that while some deterministic methods, e.g., gradient descent, converge quickly in ideal circumstances, they perform poorly in the presence of non-unique problems or non-convex error structures. By integrating these methods with stochastic techniques like genetic algorithms, Markov chain Monte Carlo, and naïve Monte Carlo with a novel sampling technique based on Voronoi polygons, we have developed a new hybrid algorithm that balances fast convergence with an improved exploration of the parameter space. As these stochastic methods require many simulation runs in order to perform adequately, we have used high-performance computing methods to distribute simulation runs over many computational nodes on a cluster computer. To support the analysis of these data, we implemented a statistical method for combining non-unique pieces of information into superior parameter estimates.

3.2 INTRODUCTION

Traditional reservoir characterization approaches have relied on utilizing in-situ fluid pressures as a means to quantify the control of transmission and storage properties of the reservoir rock on flow dynamics. The geomechanical behavior of the reservoir is therefore implicitly captured by constitutive storage properties that neglect the detailed evolution of the reservoir over time. The goal of this task is to evaluate whether the information captured by transient deformation measurements (i.e., strain, tilt, and displacement) can be used to improve the characterization of reservoirs. Key challenges exist that needed to be addressed in this project in order to evaluate the potential benefit of geomechanical measurements as a characterization tool. First and foremost was the need to develop new calibration methods that can account for the complexity and greater computational demands of poroelastic models. The problem here is not only that poroelastic models are themselves more computationally demanding that standard hydraulic models, but also that the increased number of parameters in these models leads to a greater number of tradeoffs between parameters and uncertainty in parameter estimates. A second key challenge was therefore to evaluate the information content of geomechanical data versus standard pressure measurements. Various scenarios were used to compare the information content of different measurement types and locations. These scenarios included standard reservoirs as well as cases where heterogeneity or wellbore leakage were considered as typical scenarios likely to affect geomechanical responses.

3.3 METHODS DEVELOPED

A key operational challenge addressed in this research was the development of advanced optimization methods that can be used to efficiently calibrate the parameters of poroelastic models. This work first reviewed and evaluated the advantages and limitations of different individual optimization techniques. We then developed a hybrid algorithm capable of overcoming the limitations of individual techniques while leveraging their advantages. This development represents a substantial effort in software development that is described here in some detail. The new method was evaluated using several different "hard" optimization benchmark problems before we applied it to the poroelastic optimization problem central to this project.

3.3.1 DISTRIBUTED COMPUTING

We have developed an object-oriented optimization framework in MATLAB that communicates with COMSOL using the LiveLink interface. At each iteration, the framework uses a suite of stochastic methods described below to generate sets of model parameters to be passed

into the forward model and simulated. It compiles these parameters into a single data structure, passes them into COMSOL, and retrieves the necessary geomechanical signals. Using this approach, we are able to take advantage of COMSOL's native cluster computing and job scheduling environment. This allows us to run multiple stochastic optimization algorithms in parallel using a single COMSOL session to perform the forward model evaluations.

Testing indicates a roughly linear speedup with additional computational resources (Figure 3.3-1); i.e., the simulation time for an individual run is not substantially reduced by adding nodes given that our current models run on a single node, though the run may be distributed across multiple processors on that node (16). Ultimately, we are limited by the number of available processors available per node on our cluster computer, as communication slowdowns between nodes become the ultimate limiting factor. Using 60 high-end nodes, we have been able to achieve a sustained average runtime of approximately 4 seconds per simulation for our reference poroelastic model, or roughly 20,000 simulations per day per node. As conceptual models become more complex, i.e., requiring 3D geometries, complex heterogeneous structures, multiphase flow, or non-isothermal effects, the average runtime will increase dramatically. Therefore, in order to be effective for near-real-time decision-making and monitoring of carbon sequestration operations, we require an optimization approach capable of converging reliably with only a few thousand function evaluations.

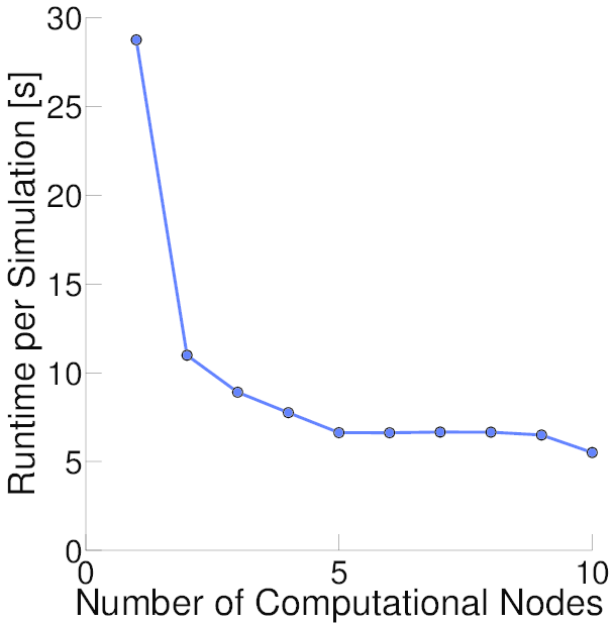

Figure 3.3-1. Computational time as a function of the number of computational nodes available. A stable computational time of about 4seconds per simulation is typical for our reference poroelastic model; note each node has 8 processor cores and 16 GB of memory.

3.3.2 INVERSE ALGORITHMS

We evaluated various optimization algorithms and created a hybrid algorithm to run them in parallel to leverage the strengths of each method. In particular, our approach allows us to modify each algorithm to also take advantage of the simulation results of its neighbors. Since each optimization strategy has its advantages and disadvantages, we use several different optimization strategies to explore the parameter space, while building a common pool of candidate simulations to draw inferences from.

Gradient Descent (GD)

One deterministic method implemented is the gradient-descent (GD) approach. At the initial iteration, GD uses the prior model to generate a random point within the parameter space, represented as a vector **x**. A set of points adjacent to this point is then evaluated in order to estimate the Jacobian of the forward model. The Jacobian is then used to determine the down-gradient direction, and an appropriate step is taken in the parameter space. This process continues until the gradient is below a given threshold, indicating a local minimum has been found. Once local convergence has been detected, the prior model is again used to generate a random point within the parameter space, and the gradient descent process continues. This algorithm is a very direct, efficient way to quickly identify promising local minima. However, it requires many function evaluations per step ($2n + 1$ per iteration, where n is the dimensionality of the parameter space), and is sensitive to non-uniqueness and to the choice of step size.

Monte Carlo (MC)

Rejection sampling via the naïve Monte Carlo (MC) approach is the slowest to converge for a high dimensionality parameter spaces, but is also the most stable and resistant to premature convergence. At each iteration, Monte Carlo uses the *prior* model to generate a set of parameters, and passes it to the forward model queue to be evaluated. The Monte Carlo approach is therefore not biased by the results of previous iterations thus enabling unexplored regions of the parameter space to be explored, but it also does not sample as thoroughly around areas of interest.

Metropolis-Hastings algorithm (MCMC)

The Metropolis-Hastings algorithm [*Metropolis et al.*, 1953] is an MCMC (Markov Chain Monte Carlo) method commonly used in optimization and parameter estimation problems. It is considered to be a stable, reliable method that converges to an ergodic distribution, and eventually 'forgets' or loses sensitivity to its prior model. However, it is slow and requires many iterations to thoroughly explore a complex parameter space. MCMC operates by a simple, iterative process. First, initial values are chosen for each parameter based on the best prior knowledge available (i.e., the prior models). The initial parameter values (θ_0) are run through the forward model, and the error or data misfit between the model and the measured or synthetic data (e_0) is computed. Each parameter is then modified by a small perturbation (referred to as a step), and the new set of parameter values (θ_i) is run through the forward model and compared against the real or synthetic dataset. The error of the new parameter set (e_{i+1}) is then compared to the error of the previous parameter set (e_i). If the new parameter set has a lower error, it is accepted and carried forward to the next iteration. If the new parameter has a higher error, it is accepted with a probability inversely proportional to the increase in error. This allows the model to occasionally move 'up-gradient' along the error surface, rather than becoming trapped in any local minima that may lie between θ_0 and the global minimum.

The series of steps making up the MCMC process is referred to as a chain. During the early iterations of a given chain, the solution will traverse the parameter space generally moving down-gradient. When it encounters a minima, it will sample more densely in and around that region, occasionally moving out of the minima and then either exploring the rest of the parameter space, or moving back into the previous minima.

When a single chain is used, it may be difficult to determine whether the chain has converged to the true global minima, or has simply found one of many local minima. However, when many MCMC chains are run with different starting points (Figure 3.3-2), we can be more confident that the parameter space has been thoroughly explored.

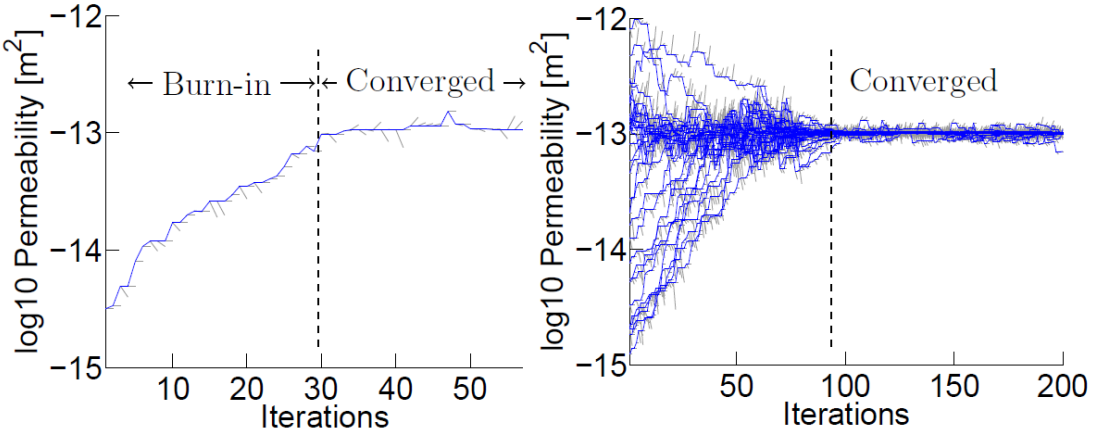

Figure 3.3-2. Comparison of single-chain and multi-chain MCMC. Blue lines indicate the series of accepted parameters. Gray lines (i.e., "hairs" extending from the blue line indicate rejected parameter sets.

Genetic Algorithms

Genetic algorithms use a heuristic approach designed to mimic the process of natural selection in nature. Like an MCMC, a genetic algorithm begins with initial parameter estimates based on prior models. These initial estimates are run through the forward model, and a data-model misfit is calculated. At each iteration, a percentage of the best parameter estimates are selected from the previous iteration based on their data-model misfits. Of this 'survivor' group, pairs are selected at random and their parameters are recombined to construct new parameters sets. The new parameter sets are then subject to small random perturbations in order to maintain 'genetic diversity' in the population, and are evaluated by the forward model. The process is repeated iteratively, and after enough generations the 'survivor' group should improve in its ability to fit the data.

Genetic algorithms can be very efficient at searching large parameter spaces. Instead of taking small steps like an MCMC method, the recombination operator causes genetic algorithm to frequently take large steps in the parameter space. While a multi-chain MCMC optimization may see many chains traversing the same area of the parameter space, genetic algorithms avoid this redundancy due to the effective communication that takes place between chains. However, genetic algorithms tend to exhibit a strong sensitivity to their starting estimates. This kind of non-ergodic behavior is called genetic drift.

Multiobjective Algorithms

We have implemented several common multiobjective algorithms, described below. We have also developed a hybrid MCMC/genetic algorithm approach which allows us to use the selection, crossover and mutation operators from one of the genetic algorithms, and also apply the Metropolis-Hastings criteria to ensure convergence.

Vector Evaluated Genetic Algorithm (VEGA)

The VEGA algorithm [*Schaffer*, 1984] allows each objective to act as the sole selection criteria for one segment of the population. During the selection operator, each of the *k* objectives is used to select a subpopulation. The subpopulations are then shuffled back together into a single population, and the normal crossover and mutation operators are applied. This strategy tends to bias the optimization in favor of the extreme edges of the Pareto front, which represents tradeoffs between equally-likely parameters, without effectively sampling the interior.

Multiple Objective Genetic Algorithm (MOGA)

The MOGA algorithm [*Fonseca and Fleming*, 1988a, *Fonseca and Fleming*, 1988b] uses a Pareto ranking approach to assign fitness, i.e., identifies models that satisfy multiple optimization (data fitting) criteria (Figure 3.3-3). The first set of non-dominated solutions (those where an improved model is not available that could produce an improved data fit for one or more objectives without increasing the misfit for another objective) is identified, assigned a rank of 1, and temporarily removed from the population. Then the next set of non-dominated solutions is identified, and assigned a rank of 2, etc. Once all solutions have been assigned a rank, an average fitness is computed from the members of each Pareto front, and assigned to each member of that Pareto front. Therefore, members of the same Pareto front are selected with equal probability. This strategy tends to suffer from genetic drift or premature convergence, where an optimal but non-unique solution is found and quickly saturates the 'gene pool' of the population. Where many equivalently good solutions exist, it is important to instead maintain genetic diversity while also continuously improving the fitness of the population. The MOGA algorithm accomplishes this by a process called niche induction, where solutions that are too similar to each other incur a fitness penalty. A niche radius is selected, and any two solutions whose Euclidean distance within the parameter space is less than the niche radius incur a fitness penalty. While this method can be effective at forcing the population to explore the remaining Pareto front, it requires the user to decide an appropriate niche radius.

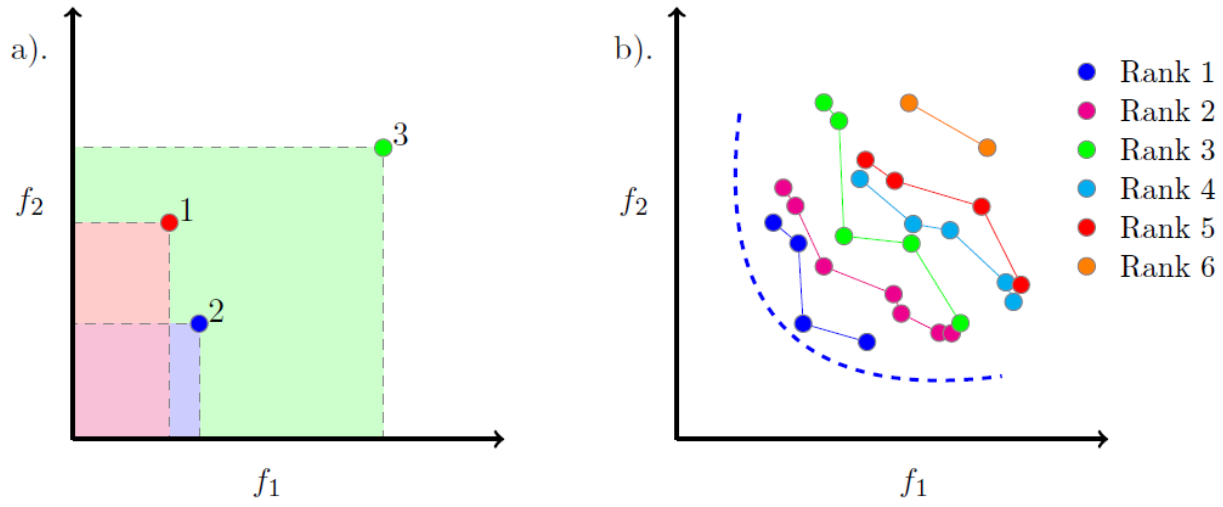

Figure 3.3-3. Pareto optimality example: points along the Pareto front are considered optimal in the sense that one objective cannot be improved at the expense of another. (a) Identification of ranked Pareto optimal points in the objective space (f_1 and f_2 represent competing data fitting objectives); points 1 and 2 are Pareto optimal in the sense that to reduce one objective (i.e., f_1 or f_2) would require the other objective

to increase, whereas point 3 is not Pareto optimal because moving to either points 1 or 2 would allow for both f_1 and f_2 to be reduced. (b) Estimation of the Pareto front based on sample data where Rank 1 consists of model estimates that provide the current best estimate of the true Pareto front (tradeoff curve) in our iterative fitting procedure.

Niched Pareto Genetic Algorithm (NPGA)

The NPGA algorithm [*Horn et al.*, 1994; *Erickson et al.*, 2002; *Abido*, 2003] uses a different approach to promote niche formation. Rather than the fitness proportional selection commonly used in standard genetic algorithms, NPGA uses a form of tournament selection. In fitness proportional selection, solutions are selected from the pool of candidates (members of the previous generation) such that each candidate has a selection probability directly proportional to its fitness. In tournament selection, *n* solutions are chosen at random from the pool of candidates, and the best candidate is added to the survivor pool. The size of the tournament therefore allows the user to control the selection pressure as needed, where $n = 2$ provides the smallest selection pressure. NPGA uses a variation of tournament selection where two candidates are chosen randomly for selection, and a number of candidates are also chosen as a comparison set. If one candidate has a lower rank than all members of the comparison set, it is selected as a survivor. If neither or both candidates have a lower rank, then the niche radius m_{ij} is used to identify the least 'crowded' solution. The degree of crowding is quantified by the niche count m_i, which uses the Euclidean distance d_{ij} between solutions to sum the relative distances of all solutions within the niche radius.

$$m_i = \sum_{j=1}^{nPop} Sh(d_{ij}) \tag{3.3-1}$$

$$Sh(d) = \begin{cases} d \geq \sigma & 0 \\ d < \sigma & 1 - {}^{d}/_{\sigma} \end{cases} \tag{3.3-2}$$

While this approach is less sensitive to the niche radius than MOGA, it does also require the user to choose the size of the comparison set.

Strength Pareto Evolutionary Algorithm (SPEA)

The SPEA algorithm maintains an external population of all non-dominated solutions that have been identified so far. At each generation, this external population is combined with the current population and included in the selection operator. A Pareto rank-based fitness is assigned, and used in the selection, crossover and mutation operators. A niching method is also used to penalize clustering.

Sparsest-point Sampling

Our last sampling method ensures dense sampling across the parameter space. This approach accesses all the parameter combinations that have been investigated so far by other algorithms, and uses an n-dimensional Voronoi tesselation to identify the largest empty hyperspheres [*Toussaint*, 1983], or the regions of the parameter space that have been most sparsely explored. Sampling is then performed within the sparest regions of the parameter space

to ensure that a possible solution that provides a global minimum to the optimization was not overlooked in this region. This safeguard allows us to avoid neglecting large regions within the parameter space which might contain superior solutions.

3.3.3 OBJECT-ORIENTED SOFTWARE DEVELOPMENT FRAMEWORK

Given the complexity of the hybrid algorithm employed in this work, we utilized modern programming paradigms to produce a robust and extensible software solution that provides the flexibility needed to take on a wide range of poroelastic problems. Specifically, we used an object-oriented programming approach to design an optimization framework general enough to be used with the Monte Carlo and MCMC methods, deterministic methods, or with any of the multiobjective genetic algorithms described here. By generalizing the concept of the inverse algorithm, we are able to run very different types of inverse approaches in parallel while still using identical data and model assumptions. Running our algorithms in parallel also allows us to aggregate parameters from each separate inverse method, distribute them over the Palmetto cluster using a single COMSOL software license, and distribute the results back to their respective data structures. This aggregated approach also allows us to share results *between* algorithms, which greatly improves the performance of genetic algorithms which thrive on genetic diversity.

A UML (Unified Modeling Language) diagram is given in Figure 3.3-4 to illustrate the overall structure of the optimization software developed in this project. Given that the development of this software was a substantial aspect of the project, details of the components of the object oriented algorithm are defined briefly below.

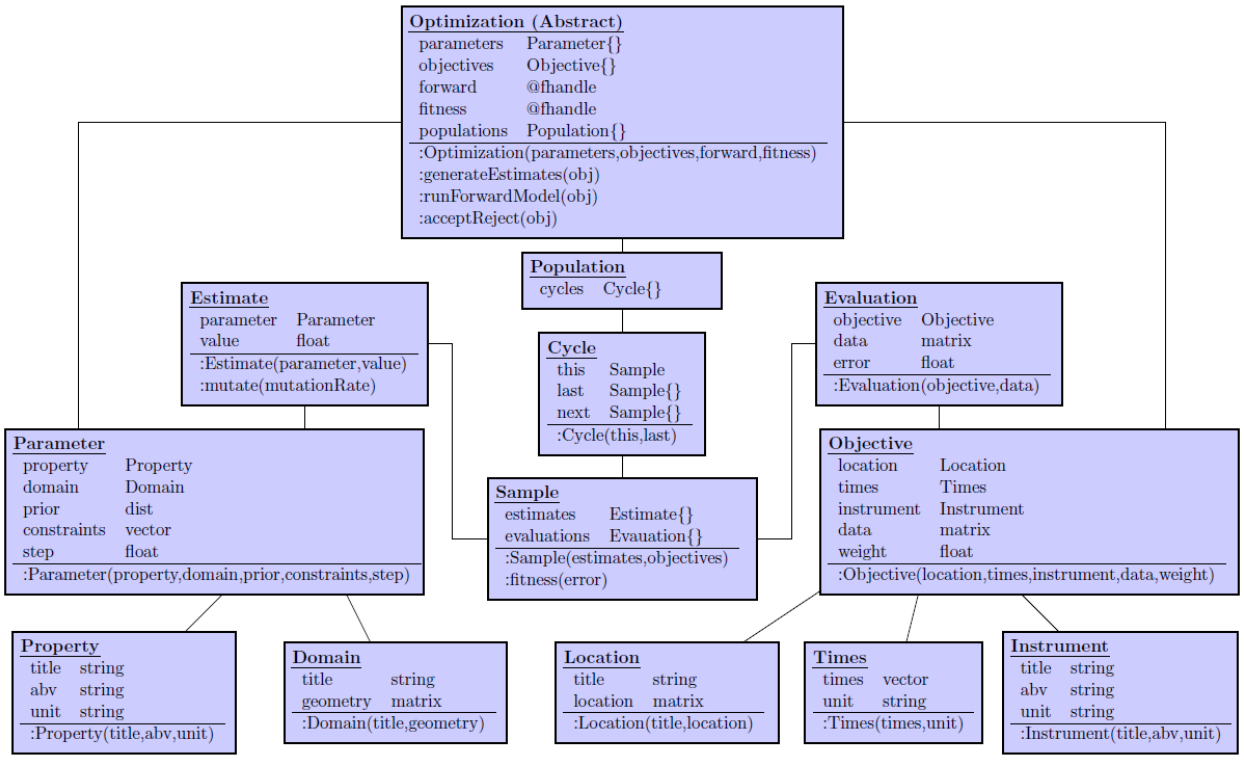

Figure 3.3-4. UML (Unified Modeling Language) diagram for the optimization framework.

A *property* object represents a physical quality or characteristic being solved for. A property must include specification of a name (e.g. Young's modulus, permeability, etc.), an abbreviation (e.g. E, K, etc.) and a unit (e.g. Pa, m/s). A *domain* represents a physical region where a property is defined. A domain object must specify a name (e.g. aquifer, bedrock, confining unit) and an array or matrix somehow specifying the geometry of the region. Geometry information is not used by the optimization routine itself, but is available for use in the forward model to define the simulation setup. A *parameter* object is composed of a property object, a domain object over which that property is defined, a prior model (MATLAB distribution object), a set of upper and lower bounds on the property, and a step size or scaling factor specific to the property that is used by the optimization algorithm.

A *location* object represents a point within the model space where a real or virtual instrument is located. A *times* object represents a series of times when measurements are taken by a specific instrument. An *instrument* object represents a particular type of measurement device employed in the field. An *objective* is composed of a specific *location* object, *times* object, and *instrument* object, as well as the measured or synthetic dataset collected by that instrument.

An *estimate* object represents a value approximating the true parameter value. An estimate is made up of a parameter object and a floating point value. An estimate can use the step size from its parameter object and a sampling algorithm to generate a new estimate, which can be used in the next iteration. An *evaluation* object represents model data associated with an objective, for a particular set of parameter values. The model data can be compared with the objective data to find a misfit or error. A *sample* is composed of an estimate of each parameter, and an evaluation of each objective. Each sample corresponds to one full function evaluation. A *cycle* object maintains the lineage relationships between different samples. Each cycle has a single accepted sample, and can have a number of rejected samples. It can also have any number of cycle objects preceding or following it. In the case of an MCMC, each cycle has a single preceding cycle (the last step in the chain), and a single following cycle (the next step in the chain). In the case of a genetic algorithm, each cycle has two parent cycles that it is derived from, and any number of child cycles.

A *population* object is composed of a group of cycles and therefore their corresponding samples. It can represent a particular iteration or generation, or it can represent a subset of samples of interest (the elite cohort, the survivor cohort, or a particular Pareto rank).

An *optimization* object is initialized by a set of parameters, a set of objectives, a forward model and a fitness function. The forward model and fitness function are passed into the optimization constructor using MATLAB function handles. The optimization uses the prior models contained in the parameter objects to construct an initial set of estimates, forming the first population object. Note that the Optimization class definition is an abstract class. It contains the methods necessary for manipulating the objects described here, but cannot be implemented itself. A group of specific optimization objects have been implemented including the Markov Chain Monte Carlo (MCMC) method, simple genetic algorithm (SGA) method, as well as the multiobjective genetic algorithms described in the previous section and our hybrid algorithm.

3.3.4 STATISTICAL INFERENCE

While the initial sampling strategy proposed for this project, i.e., MCMC, provides a robust theory for estimation of the posterior statistics of the model parameters, this is not true of the heuristic sampling algorithms used in our hybrid algorithm. As a result, we needed to develop a statistical estimation strategy appropriate for our non-statistical sampling methods. We opted to evaluate statistical moments based on a function approximation approach that allows for declustering of highly sampled regions and interpolation over sparsely sampled regions.

The fundamental definitions of the mean and variance are given by the statistical moments of the joint probability density function (pdf):

$$\mu = \int m\, \rho(m|d) dm, \text{ and} \tag{3.3-3}$$

$$\sigma^2 = \int (m-\mu)^2 \rho(m|d) dm. \tag{3.3-4}$$

In our case, the pdf is not known analytically, but is defined empirically through the samples obtained during the iterative inversion process. Estimation of the statistical moments therefore requires a non-parametric evaluation of the multi-dimensional integrals in Eqs. 3.3-3 and 3.3-4. Figure 3.3-5 illustrates a typical scenario for a case of two-parameters, which is easily visualized on a set of plots. In Figure 3.3-5, each point represents a sample of the model parameters visited during the inversion process (i.e., during the search of the parameter space for optimal solutions) and the color assigned to the point represents a measure of the quality of the data misfit provided by that specific set of model parameters for each data type (i.e., pressure vs. tilt). It is clear from this figure that there are regions of higher probability (i.e., lower data mistfit), but there are also tradeoffs (i.e., correlations) between the parameter estimates where different combinations of the parameter values produce equivalent (or nearly equivalent) approximations of the data. By combining the two figures together, i.e., using both pressure and tilt meter data, it would be possible to reduce the impact of these tradeoffs as only a small portion of the parameter space provides solutions that are consistent with both data types simultaneously. These figures together therefore represent a qualitative evaluation of the underlying joint pdf for each data type and, if appropriately recombined, for the overall dataset.

There are several challenges that must be addressed, however, in order to provide quantitative estimates of the parameter values and their uncertainties. First, is the question of how to recombine or weight the importance of different data types relative to each other in forming the posterior distribution of the model parameters. We make the assumption that the misfit from distinct data types can be combined into a single probability measure by selecting an appropriate probability model for the posterior pdf.

The second challenge is associated with the fact that our sampling of the parameter space is non-uniform, with a higher degree of (non-statistically representative) sampling in regions of low data misfit. Unlike formal statistical sampling strategies, like MCMC, the density of samples produced by our hybrid algorithm does not represent the posterior probability of the parameters. Instead, the color scales in Figure 3.3-5, i.e., the data misfit, provides the representation of the underlying pdf. We therefore take a function evaluation approach to solving the integrals (Eqs. 3.3-3 and 3.3-4), where Voronoi declustering is used to overcome the non-uniform sampling and facilitate approximation of the integrals required for the estimation of the statistical moments.

In order to combine multiple types of measurements into the estimate of the posterior pdf of the model parameters, our statistical inference method for approximating the posterior pdf of the model parameters is based on Bayes theorem. Bayes uses a data likelihood, $\rho(d|m)$, to relate a prior probability density function, $\rho(m)$, to a posterior probability density function, $\rho(m|d)$:

$$\rho(m|d) = \rho(d|m)\frac{\rho(m)}{\rho(d)} = k\rho(d|m)\rho(m) \tag{3.3-5}$$

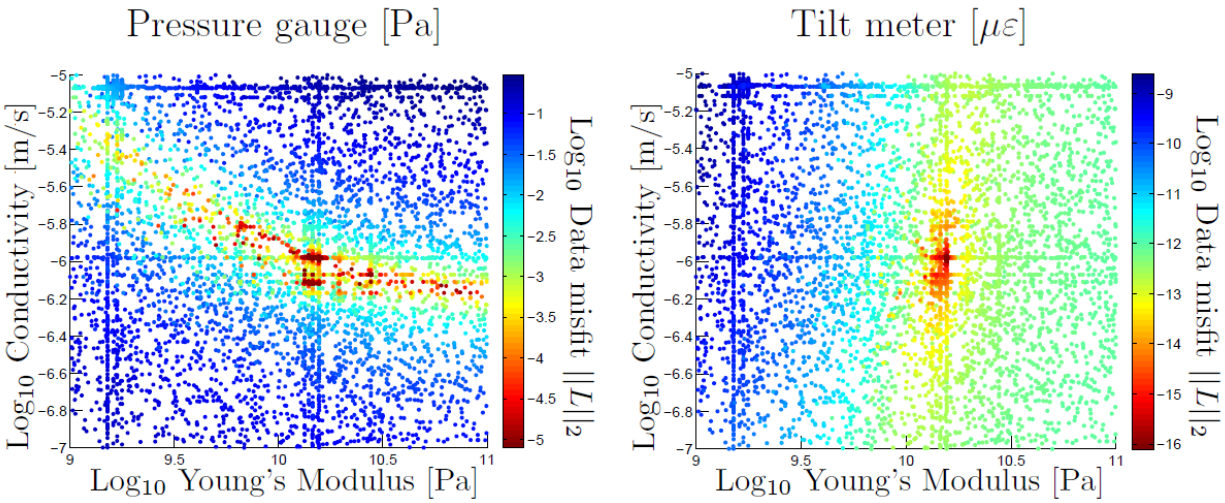

Figure 3.3-5. Inverse log error is shown as a function of conductivity and Young's modulus. Red points indicate points in the parameter space that produced models closely fitting the synthetic data. Black '+' indicates true parameter values.

If we assume that the prior model follows a Gaussian (or log-normal) distribution, we can represent it as:

$$\rho(m) \propto \exp(-\tfrac{1}{2}[m-\mu]^T \Sigma_m [m-\mu]), \tag{3.3-6}$$

where m is a vector of our model parameters, μ is a vector of expected values for each model parameter, and Σ_m is the prior model covariance matrix, representing our initial uncertainty for each parameter as well as the expected correlations between parameters. The covariance matrix has the form:

$$\Sigma_m = \begin{bmatrix} \sigma_{11} & \sigma_{12} & \sigma_{13} \\ \sigma_{21} & \sigma_{22} & \sigma_{23} \\ \sigma_{31} & \sigma_{32} & \sigma_{33} \end{bmatrix} \tag{3.3-7}$$

where off-diagonal values are zero if we assume that our parameters are uncorrelated (in this study we assume parameters are uncorrelated, but this is not necessary in general and future research will explicitly deal with spatial correlations between parameters). If we assume that the data noise also follows a Gaussian distribution, we can represent the likelihood as:

$$\rho(d|m) \propto \exp\left(-\tfrac{1}{2}[d-f(m)]^T \Sigma_d [d-f(m)]\right) \tag{3.3-8}$$

where d is the vector of all measured data values from multiple disparate sensors, and $f(m)$ is the vector of predicted data values for the specific set of model parameters m. In our case, $f(m)$ is the output from the COMSOL forward model. The data covariance $\sum_d$ represents the errors and

relationships within the dataset. As with the model covariance, each diagonal value of $\sum_d$ represents the variance of a data parameter, while the off-diagonals represent the correlation between measurement errors. If measurement errors are uncorrelated, which is assumed here, the off-diagonals will be zero. The probability density of the data is commonly treated as a constant, *k*. This allows us to substitute Eqs. 3.3-2 and 3.3-4 into Eq. 3.3-1 to construct an exact expression for the posterior distribution:

$$\rho(m|d) = k\, exp\left(-\frac{1}{2}[m-\mu]^T\Sigma_m[m-\mu]\right)\exp\left(-\frac{1}{2}[d-f(m)]^T\Sigma_d[d-f(m)]\right). \quad (3.3\text{-}9)$$

While *k* is difficult to derive analytically, we can estimate it by integrating the probability density function over the model space, which by definition is equal to unity:

$$\int \rho(m|d)dm = 1 \quad (3.3\text{-}10)$$

Substituting our posterior distribution expression allows us to solve for k:

$$\frac{1}{k} = \int exp\left(-\frac{1}{2}[m-\mu]^T\Sigma_m[m-\mu]\right)\exp\left(-\frac{1}{2}[d-f(m)]^T\Sigma_d[d-f(m)]\right) \quad (3.3\text{-}11)$$

In order to approximate this integral, we use a Voronoi grid approach to integrate numerically over the error function. Once we have estimated the *k* value, we directly evaluate the posterior probability density $\rho(m|d)$ of any point sampled, and can therefore perform numerical integrations to estimate the mean and standard deviation.

3.4 Benchmark Testing and Evaluation of Inversion Procedure

Given the complexity of the inversion procedures described above, it was important to evaluate different underlying techniques and our ultimate hybrid algorithm against benchmarks commonly used in the optimization literature. In addition to these abstract functions, we also utilized an analytical poroelastic model as a benchmarking tool for our algorithm. We briefly describe each of the benchmarks here and report briefly on the performance of our hybrid algorithm for each one.

3.4.1 Benchmark Functions

In order to test the hybrid MCMC/GA algorithm and verify its resilience against various types of error structures, we selected a set of benchmark problems from the optimization literature. These error structures vary in terms of the number of local optima, the connectivity between local optima, and the presence and utility of local gradient information. Benchmark results are presented below comparing MCMC and standard genetic algorithms to our hybrid approach. In all cases so far investigated, the hybrid algorithm matches or outperforms either the MCMC or genetic algorithm approaches, thus providing a robust methodology that performs well under many different circumstances.

Parabolic function

This objective function (Figure 3.4-1) has a single optima, and the local gradient points toward it at all points in the parameter space. The MCMC algorithm requires roughly 100 iterations to arrive at convergence. The genetic and hybrid algorithms are able to converge much more quickly (about 5 to 10 iterations), while continuing to passively search the remaining parameter space for better solutions (Figure 3.4-2). Note that while this performance difference is significant, this function also represents an ideal scenario for gradient-based methods, which

would find the optimum in a very low number of iterations (i.e., for some methods, the optimum could be reached in a single iteration).

$$z(x, y) = 79 - (x^2 + y^2)$$

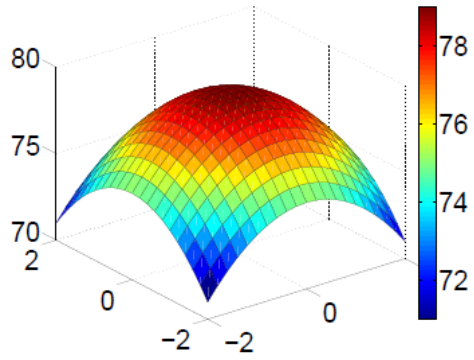

Figure 3.4-1. The parabolic objective function has two parameters with a single objective. The function has a single optimum.

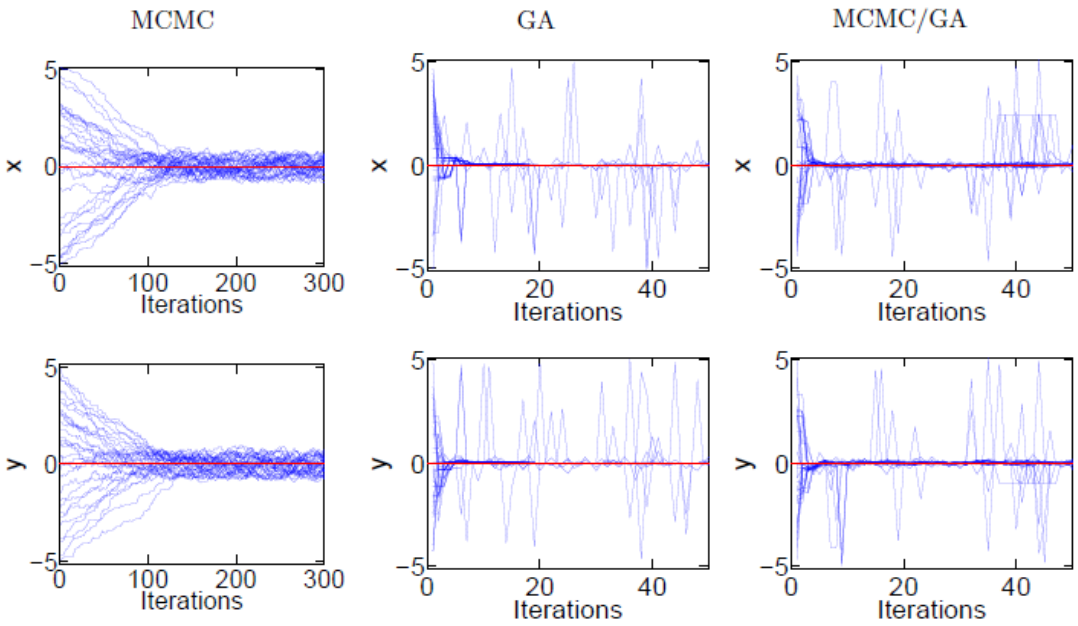

Figure 3.4-2. Benchmark results for the parabolic function illustrates substantially faster convergence of the parameters (x, y) with the genetic (GA) and hybrid (MCMC/GA) algorithms compared to Markov chain Monte Carlo (MCMC).

Rosenbrock function

This objective function (Figure 3.4-3) is composed of a large parabolic shape about the $x = 0$ axis, and a smaller-magnitude parabola perpendicular to $x = 0$. There are very high gradients in regions away from the origin, and very shallow gradients near the origin, making it a difficult function for gradient-based methods. The MCMC algorithm is able to arrive at the correct solution, but requires many iterations to do so. The genetic algorithm converges much more quickly, but fails to thoroughly explore the region surrounding the global optimum. The hybrid algorithm converges roughly as quickly as the genetic algorithm, but proceeds to thoroughly

search the region near the global optimum, yielding more useful information about the uncertainties and any tradeoff dynamics inherent to the problem (Figure 3.4-4).

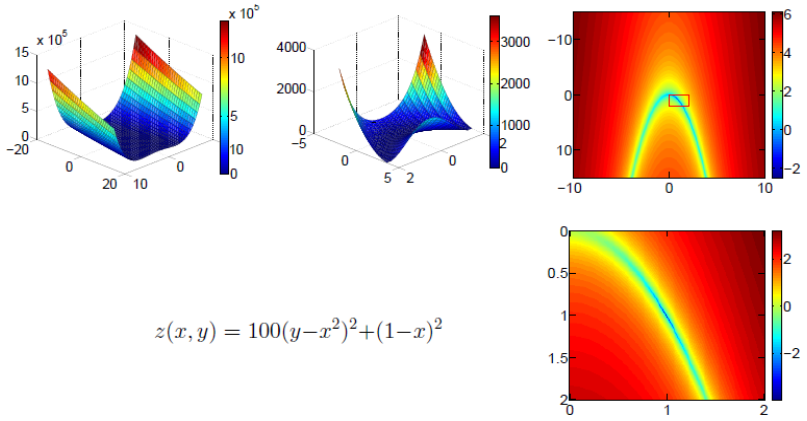

$$z(x,y) = 100(y-x^2)^2+(1-x)^2$$

Figure 3.4-3. The Rosenbrock function provides a single function minima, but has a deep trough of almost equal probability near this optimum, making it a challenge for gradient-based methods.

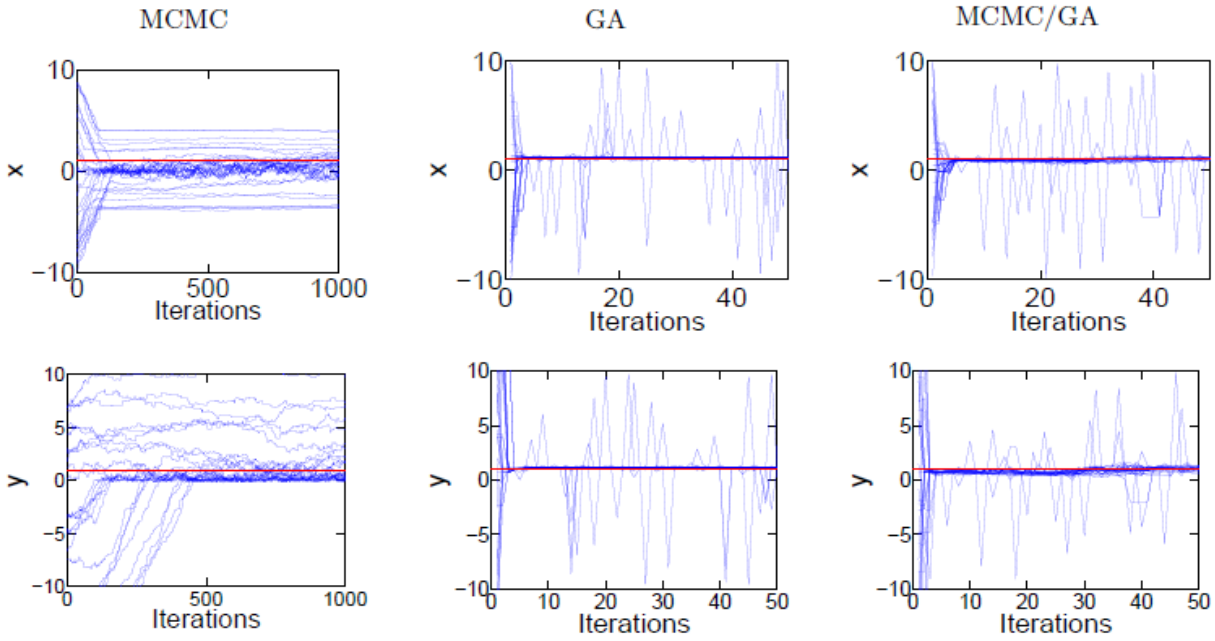

Figure 3.4-4. Benchmark results for the Rosenbrock function illustrates substantially faster convergence of the parameters (x,y) with the genetic (GA) and hybrid (MCMC/GA) algorithms compared to Markov chain Monte Carlo (MCMC), though the hybrid technique also explores the space around the optimum, whereas the GA does not.

Rounding function

In this case, local gradient information is removed by rounding parameter values to the nearest integer (Figure 3.4-5). Therefore gradient-based methods fail for this function and MCMC takes a much longer time to arrive at the optima. The genetic algorithm finds the lowest step very quickly, but fails to exploit the discovery and thoroughly define the shape of the optima. The hybrid algorithm converges quickly, and exploits the discovery by thoroughly sampling the entire optima (Figure 3.4-6).

$$z(x,y) = 26 - ||x|| - ||y||$$

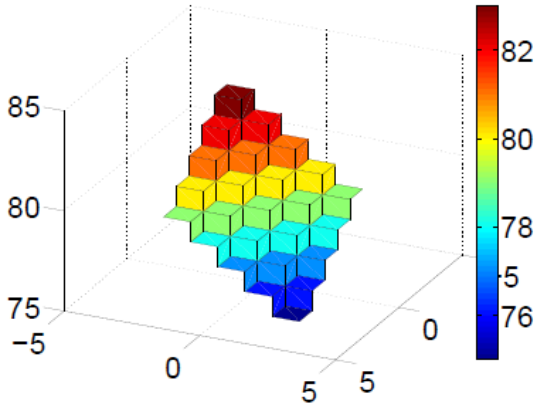

Figure 3.4-5. The rounding function is extremely challenging as it consists of flat regions and steps, i.e., has discontinuous derivatives.

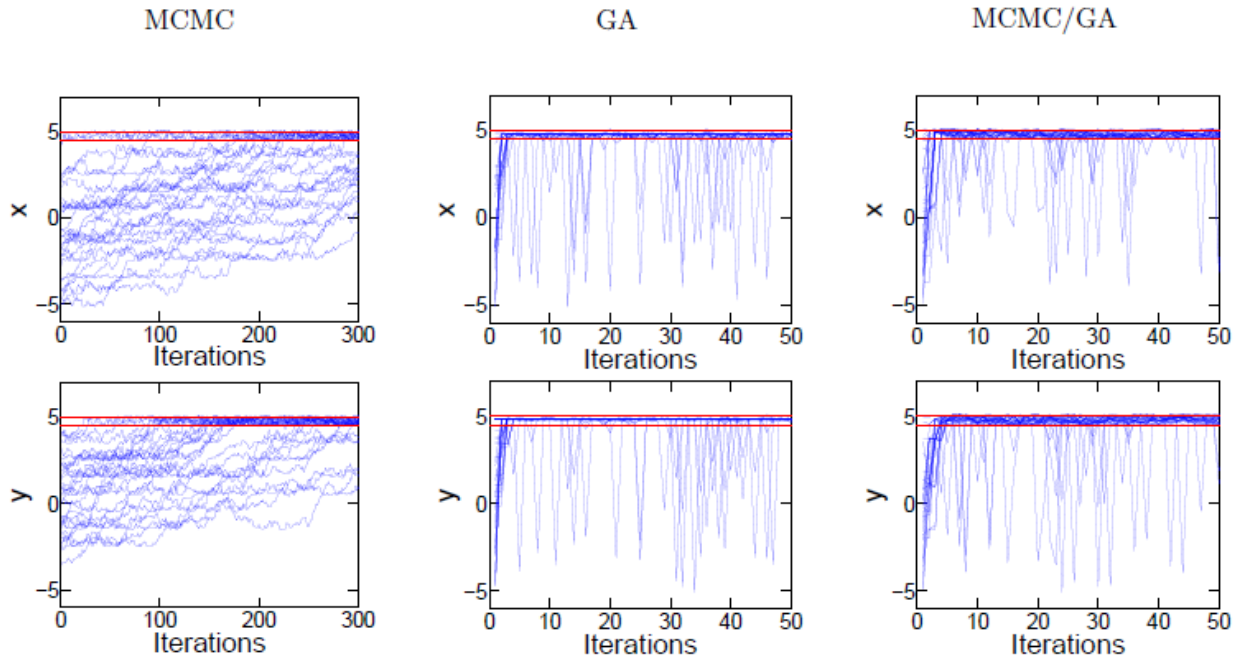

Figure 3.4-6. Benchmark results for the rounding function illustrates poor convergence of the parameters (*x*,*y*) using Markov chain Monte Carlo (MCMC). The GA is efficient, but does not explore the minima to define the shape of the space in this region, thus failing to define parameter tradeoffs. The hybrid method is efficient and explores the space around the minima, thereby leveraging the advantages of both MCMC and GA.

Ripple function

The ripple objective function has a global optima surrounded by a series of concentric rings of high and low error (Figure 3.4-7). The MCMC algorithm performs very poorly, since in this case the local gradient information is very uninformative about the location of the global optima, especially in regions far away from the optima. The genetic algorithm performs marginally better, but is unable to converge. The hybrid algorithm, however, is able to define both the location and the shape of the global optima. This is because the genetic algorithm

quickly brings the solutions near the global optima, where the MCMC can take advantage of the more informative local gradient information (Figure 3.4-8).

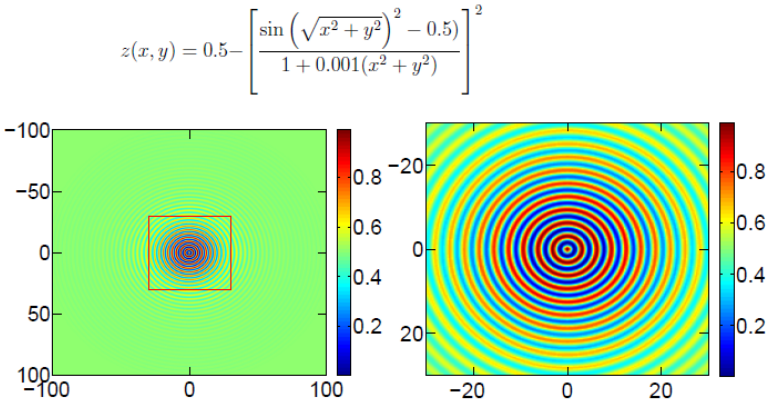

Figure 3.4-7. The ripple function has a well-defined global gradient and minima, but confounding local minima that make it extremely difficult to identify and proceed down the global gradient.

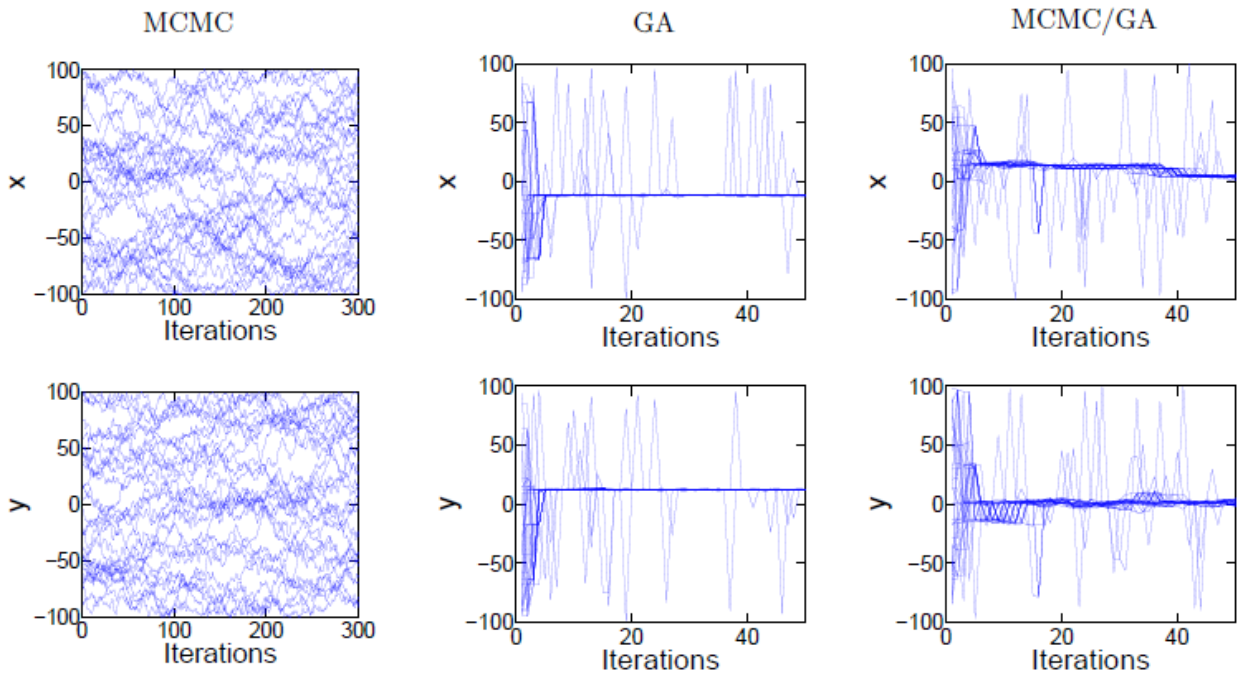

Figure 3.4-8. Benchmark results for the ripple function illustrates failure using Markov chain Monte Carlo (MCMC). The GA is efficient, but does not explore the minima to define the shape of the space in this region, thus failing to define the ring nature of the objective function around the global minima, whereas the hybrid method is effective in this regard.

Multiple peaks

This objective function has multiple, discontinuous but distinct optima with only a single poorly defined global minimum (Figure 3.4-9). The MCMC algorithm is able to solve this optimization problem, but with a high number of iterations and only when the step size is appropriately sized to traverse the lesser optima. The genetic algorithm is able to find the global optimum, but does not thoroughly sample its shape and relationship to the surrounding local

optima. The hybrid MCMC/GA algorithm quickly arrives at the global minimum and samples thoroughly around the peak, yielding valuable information about parameter uncertainty and the shape of the Pareto front (Figure 3.4-10).

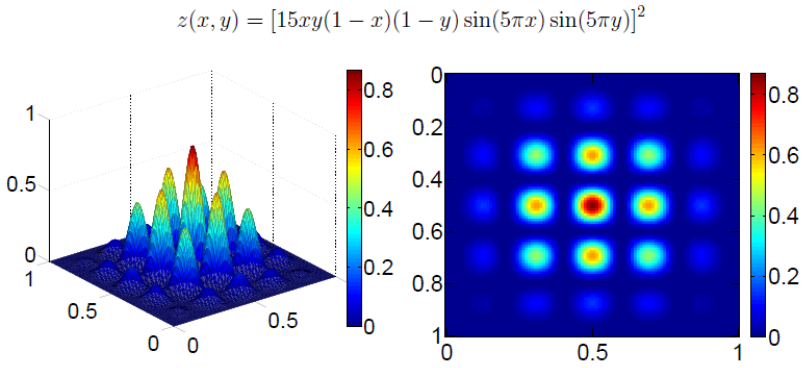

Figure 3.4-9. This function is pathologic in that it has many well defined local minima, with a single global minima that is not substantially different from the local minima.

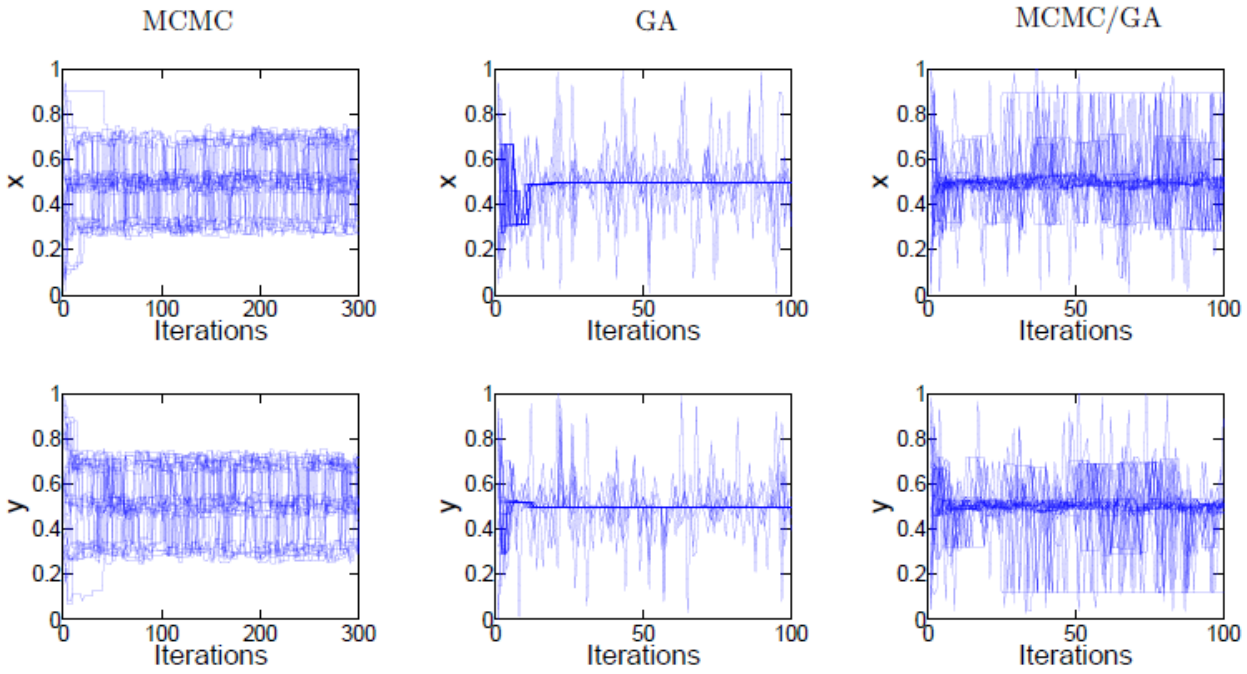

Figure 3.4-10. Benchmark results for the multiple peaks function illustrates failure using Markov chain Monte Carlo (MCMC). The GA is efficient, but does identify surrounding local minima whereas the hybrid method is able to explore both the global minimum and surrounding local minima.

3.4.2 Analytical Model Benchmark

To further test the hybrid inversion algorithm in a geologically relevant setting, we have implemented an analytical solution for the poroelastic response to injection from a continuous

line source [*Wang*, 2000]. We calculate the pressure and radial displacement, as a function of radial distance from the line source and time, using the equations:

$$p(r,t) = \frac{Q_0'\mu}{4\pi\kappa} E_1\left(\frac{r^2}{4ct}\right) \tag{3.4-1}$$

$$u_r(r,t) = \frac{Q_0'\gamma}{8\pi c} r\left\{\frac{4ct}{r^2}\left[1 - \exp\left(\frac{-r^2}{4ct}\right)\right] + E_1\left(\frac{r^2}{4ct}\right)\right\} \tag{3.4-2}$$

where Q_0' is the flux into the reservoir ($Q_0' = Q/h$), Q and h are the volumetric flow rate and thickness of the reservoir, κ, c, and γ are the permeability, diffusivity, and loading efficiency of the reservoir, μ is the dynamic viscosity of the fluid being injected, and r and t are the independent variables: radial distance from the line source, and time. We use the following parameter values as the true values, and treat the permeability and loading efficiency as free parameters to be estimated based on observed pressures and radial displacements.

Table 3.4-1. Parameters used to generate synthetic data for the analytical model inversions; permeability and loading efficiency are treated as unknowns in the benchmark study.

Name	Parameter	True Value	Range of free parameter	Units
Volumetric flow	Q	$-1x10^{-3}$	N/A	$\frac{m^3}{s}$
Aquifer Thickness	h	100	N/A	m
Flux	Q_0'	$-1x10^{-5}$	N/A	$\frac{m^2}{s}$
Permeability	κ	$1.02x10^{-13}$	10^{-15} to 10^{-11}	m^2
Loading Efficiency	γ	0.379	0 to 1	$unitless$
Dynamic Viscosity	μ	0.001	N/A	$Pa \cdot s$
Diffusivity	c	0.813	N/A	$\frac{m^2}{s}$

The parameter givens in Table 3.4-1 were used to generate synthetic records of radial displacement and pressure for a one day injection test (shown in the two inset plots on the top right corner of Figure 3.4-11; the blue lines indicate the simulated data records). Each of the algorithms (MCMC, GA, and hybrid) were used to estimate the log permeability and loading efficiency of the formation (Figures 3.4-11 through 3.4-13). The MCMC algorithm was able to converge fully within ~100 iterations, and then proceeded to explore the vicinity near the optimal solution (Figure 3.4-11). This yields a well-developed approximation of the Pareto front, which gives us valuable information about the tradeoffs implicit in the data fitting problem. The genetic algorithm approach was able to converge much faster – within only 10 iterations – but

was unable to thoroughly explore the surrounding parameter space, yielding a sparser Pareto front approximation (i.e., less information useful for defining uncertainty in the parameter estimates). Notably, the inability of the GA to adequately characterize parameter uncertainty directly translates to poor estimates of prediction uncertainty in Figure 3.4-12. In contrast, the hybrid algorithm was also able to converge within 10 iterations, but also sampled much more thoroughly around the global optimum, thus yielding a much denser and more informative Pareto front approximation (Figure 3.4-13). This improved characterization of parameter uncertainty also translates to fuller evaluation of prediction uncertainty more similar to that obtained by MCMC.

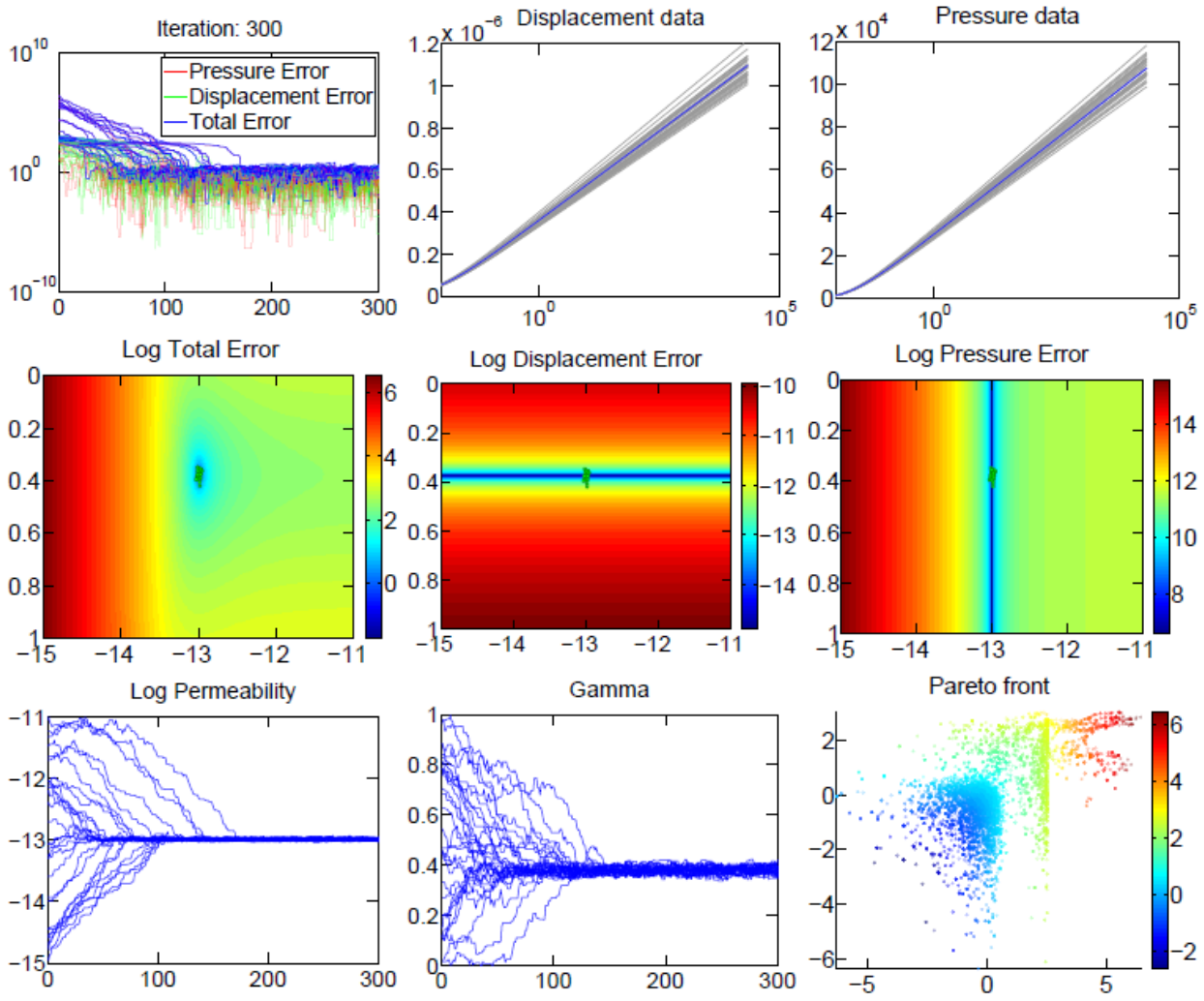

Figure 3.4-11. Results of the MCMC optimization using the analytical poroelastic benchmark. (Top left: Objective function evaluations as a function of iteration; top center/right: true synthetic data (blue line) and ensemble of data predicted from estimated parameter values (gray lines); Center row: objective function as a function of log permeability (*x*-axis) and loading efficiency (*y*-axis) for different data scenarios; Bottom row (left and center): convergence of parameter estimates during the optimization; Bottom (right): estimate of the Pareto front (color indicates rank).

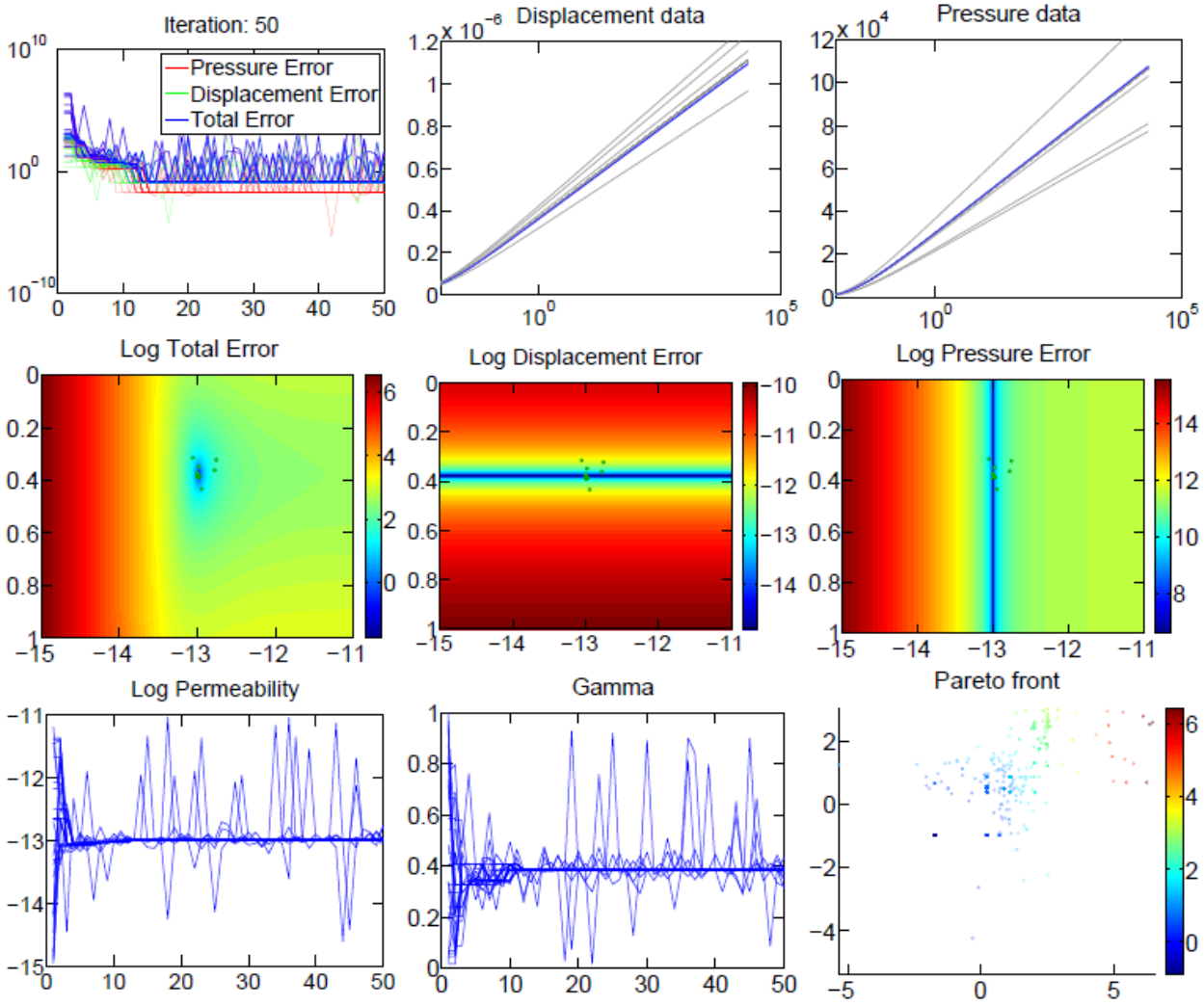

Figure 3.4-12. Results of the genetic algorithm optimization using the analytical poroelastic benchmark. (Top left: Objective function evaluations as a function of iteration; top center/right: true synthetic data (blue line) and ensemble of data predicted from estimated parameter values (gray lines); Center row: objective function as a function of log permeability (*x*-axis) and loading efficiency (*y*-axis) for different data scenarios; Bottom row (left and center): convergence of parameter estimates during the optimization; Bottom (right): estimate of the Pareto front (color indicates rank). Note fast convergence of the algorithm, but lack of diversity in parameter estimates and reservoir predictions.

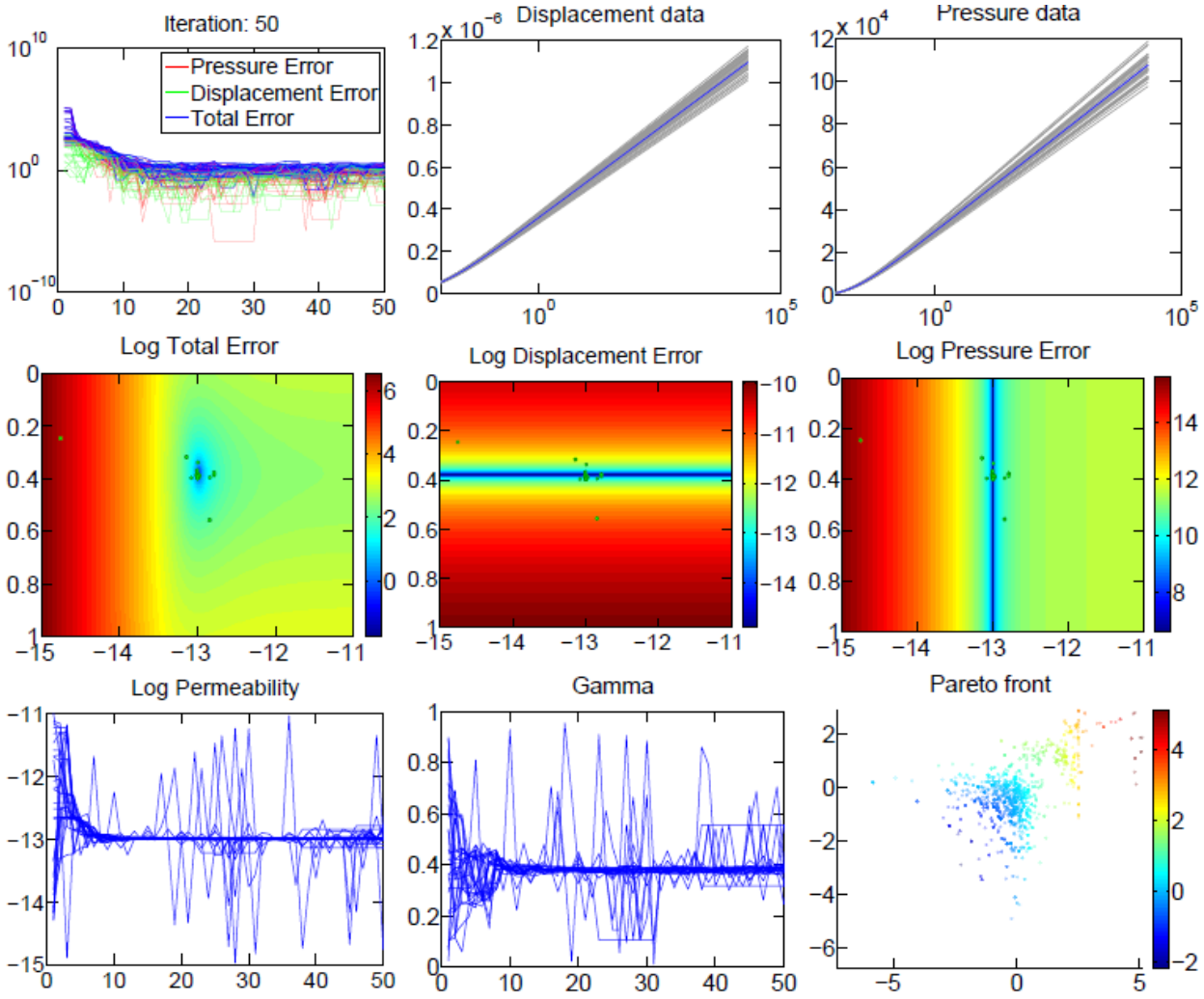

Figure 3.4-13. Results of the hybrid algorithm optimization using the analytical poroelastic benchmark. (Top left: Objective function evaluations as a function of iteration; top center/right: true synthetic data (blue line) and ensemble of data predicted from estimated parameter values (gray lines); Center row: objective function as a function of log permeability (*x*-axis) and loading efficiency (*y*-axis) for different data scenarios; Bottom row (left and center): convergence of parameter estimates during the optimization; Bottom (right): estimate of the Pareto front (color indicates rank). Note that the hybrid algorithm achieves both fast convergence and an improved estimate of parameter uncertainty and reservoir predictions.

3.5 NUMERICAL MODEL TESTS

To evaluate the efficacy of utilizing geomechanical data for estimation of reservoir properties, we performed a wide variety of model calibration studies based on the scenario described in Benchmark Example 4 from Chapter 2 of this report. The goal of these studies was to evaluate: (1) the value of different types of geomechanical data relative to pressure alone for constraining reservoir properties, (2) the influence of measurement noise on the inversions, (3) the role of measurement location (i.e., within the reservoir versus the caprock), and (4) the impact of reservoir heterogeneities and model errors on the inversion results and reservoir predictions. The results provided here are considered high-level summaries of some of our findings, but do not capture all relevant details reported through the quarterly reports prepared during the project.

3.5.1 MODEL DESCRIPTION

We have developed a poroelastic forward model based on Benchmark Example 4 using the COMSOL Multiphysics (COMSOL Inc., Burlington, MA). The reservoir geometry is a 3-layer system that is axially symmetric about the injection well, thus equivalent to a 3d cylindrical model space. The 3 layers are a bedrock, permeable formation, and impermeable cap rock. The bedrock is at the bottom, and 100 m thick. The permeable formation is overlying bedrock, and is 100 m thick. The cap rock overlies the formation, and is 1,000 m thick. All three layers have a radial extent of 30 km. An overview of the reservoir geometry is shown in Figure 3.5-1 and its material properties are shown in Table 3.5-1.

We constructed a finite element mesh with a dense set of elements within the formation and near the injection well (where the highest gradients will occur), and a sparser set of elements within the cap rock. We then initialize the model with a steady state constant pressure condition, and evaluate the coupled partial differential equations representing flow through porous media according to Darcy's law, and elastic pressure response according to Hooke's law. We use a constant pumping rate of 0.6 m^3/s for a duration of 10^7 s (~ 4 months) to produce data records for multiple types of instruments (discussed below). Note that the model was setup to evaluate differential deformations induced by the injection and thus does not consider changes in boundary conditions imposed by regional stresses.

For the purposes of inverting the (computationally expensive) numerical poroelastic forward model, we use our hybrid method that integrates multiple algorithms. Two hybrid MCMC/GA algorithms are used within the algorithm. The first is based on NPGA, and tends to converge well when the data are insufficiently informative about the system to converge to a unique solution, but rather identifies a parameter tradeoff relationship. The second hybrid algorithm is based on SPEA, and tends to perform well where a unique solution is indicated by the data. We also use the Monte Carlo and Markov Chain Monte Carlo algorithms, and the sparsest-point sampling approach.

3.5.2 NUMERICAL MODEL EVALUATION RESULTS

A variety of cases were investigated in this work to evaluate the use of geomechanical data as a reservoir constraint. Each of these experiments targeted a different aspect of the inversion problem and are therefore discussed individually below.

Table 3.5-1. Physical properties of the reservoir and confining materials used in the forward model to simulate the true synthetic data used in the inversions.

	Young's Modulus	Conductivity	Poisson Ratio	Porosity	Biot-Willis Coefficient
Cap Rock and Bedrock	20 GPa	10^{-12} m/s	0.15	0.2	1
Formation	15 GPa	10^{-6} m/s	0.25	0.2	1

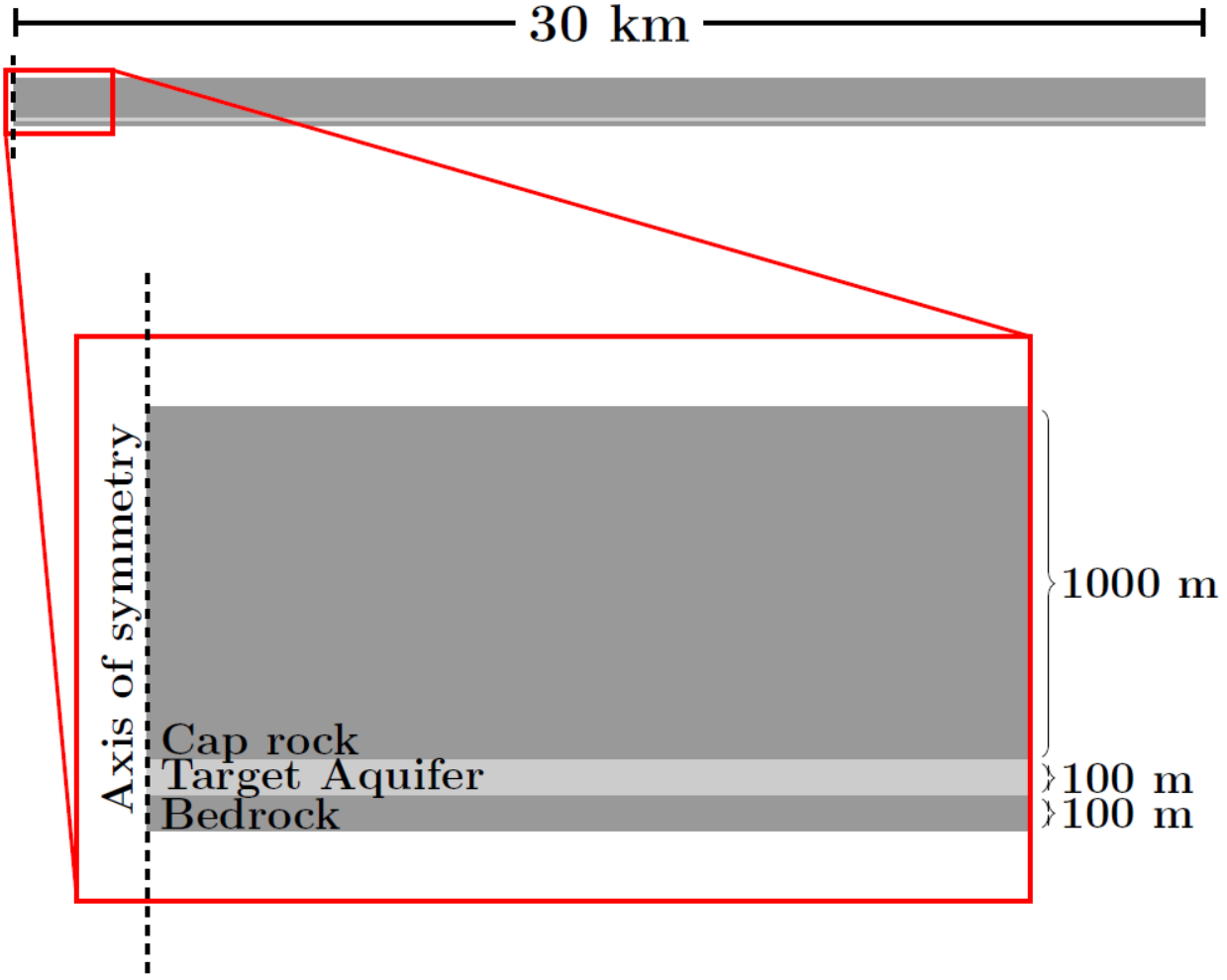

Figure 3.5-1. Geometry of the conceptual model used for the inversion analyses. The reservoir model is a 2-dimensional axially symmetric approximation of a 3-dimensional cylindrical injection aquifer with a radius of 30 km. The injection well is located along the axis of symmetry, screened in the target aquifer.

Instrument Type

The first experiment compared the use of hydraulic data (i.e., pressure) versus different geomechanical measurements (i.e., pressure, tilt, and local strain measurements). Using synthetic measurements of pressure and tilt within the formation, we are able to estimate the Young's modulus and permeability of the formation (Figure 3.5-2). However, we are unable to resolve a precise estimate of the Poisson ratio. This represents a distinct type of convergence

failure, as we are able to generate samples with a broad range of incorrect Poisson ratios that agree with our measured dataset. Rather than a weakness in our algorithm, this dataset is insufficiently informative about the parameters we are interested in, and additional information is required. In contrast, using synthetic measurements of pressure and vertical strain within the formation as data constraints, we are able to resolve the Young's modulus, permeability and Poisson ratio of the formation Figure 3.5-2, indicating that vertical strain data is more sensitive to Poisson ratio than tilt meter data. Adding tilt or other components of strain did not provide significant improvements in any of the parameter estimates, suggesting that pressure and vertical displacement data contain sufficient information to constrain the reservoir model. We point out, however, that given the simplicity of this benchmark model, we may not yet be taking full advantage of the information available from measuring multiple strain components that would be useful in a field scenario in the presence of 3D heterogeneities.

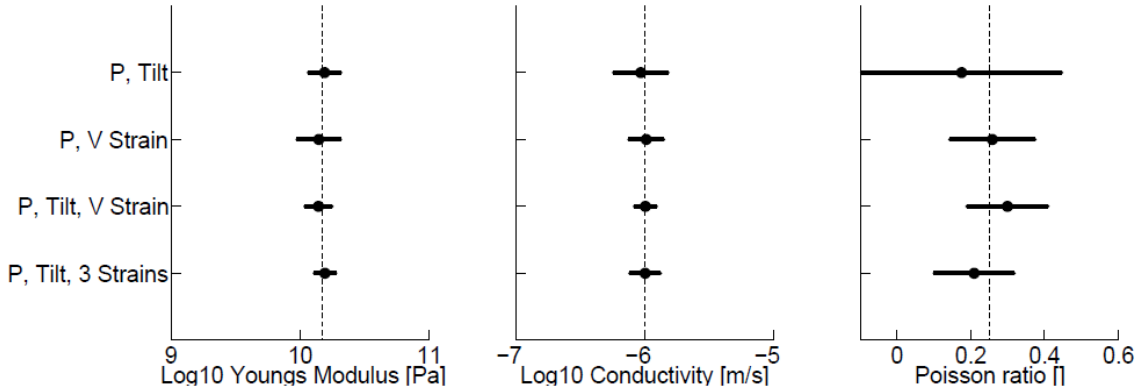

Figure 3.5-2. Parameter estimates obtained using various combinations of pressure, tilt, and strain measurements taken from inside the target formation to constrain formation properties. Note the dot indicates the mean value of each parameter estimate and the bars indicate uncertainty (one standard deviation).

Instrument Noise

The role of instrument noise on the inversion was investigated by adding proportional Gaussian random noise to the "true" measurements at various different error levels (0, 5, 10, 15, and 20%), which are considered to be more than ample to cover the range of measurement errors expected from the instrument error studies described in Chapter 4 of this report. We then performed the inversion for each corrupted data set, considering pressure, radial displacement, vertical displacement, vertical strain, and circumferential strain as data constraints. Contrary to our expectations, the noise had relatively little influence on the inversion results. Figure 3.5-3 shows that increasing the noise level did not significantly increase the number of iterations required for convergence nor the degree of uncertainty in the parameter estimates (note variations in the histograms shown are associated with ergodic variations resulting from the stochastic nature of the inversion algorithm and do not reflect significant differences in parameter error). Our interpretation of this result is that there is sufficient redundancy in the relatively simple transient model that the different parameters compensate for each other to provide a reliable estimate. In other words, use of multiple measurements (i.e., pressure, tilt, and strain) allowed the influence of the unbiased random noise to effectively be filtered out of the signal. The result suggests that use of geomechanical measurements therefore have a significant

benefit to monitoring as a means of effectively overcoming noisy, poor-quality signals obtained in non-optimal monitoring scenarios. While these results are promising, we feel that additional studies are likely needed to assess the general applicability of our finding before applying this finding to operational settings.

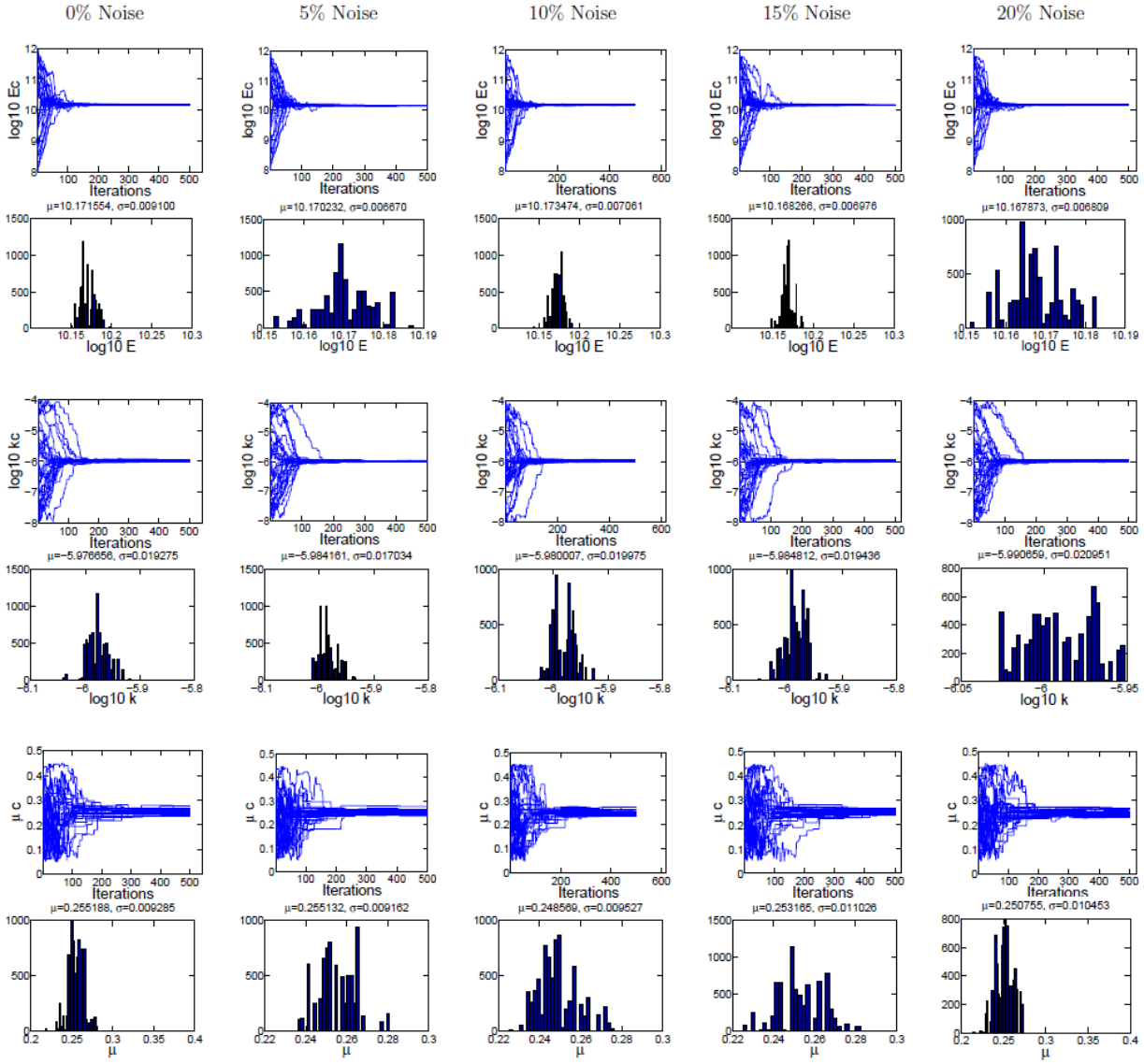

Figure 3.5-3. Evaluation of the influence of data noise on inversion results. The top two rows indicate the convergence result and posterior histogram of parameter estimates for Young's modulus, whereas the middle two rows show the same for permeability, and the bottom two rows for Poisson's ratio. Each column represents results for a different level of proportional noise used to corrupt the measurements.

Instrument Location

We investigated the importance of the measurement location in constraining the reservoir parameters. The three locations we consider include: (i) in the injection well, (ii) within the reservoir but far from the injection well, and (iii) within the caprock. This study used synthetic measurements of pressure, tilt and all three components of strain as the data constraint.

Data taken at the injection site is able to resolve all three parameters, and in particular provides an excellent estimate of the formation Poisson ratio (Figure 3.5-4). Vertical deformation rates are high in this high-pressure region, and are strongly dependent on the Poisson ratio of the formation. This strong, informative signal allows us to make precise estimates of the Poisson ratio. However, these measurements are also difficult to collect due to the noise and logistical complication of the injection process. Observations collected inside the formation far from the injection well were also able to resolve the Young's modulus, permeability and Poisson ratio of the formation with a similar level of uncertainty as the measurements collected at the injection well, with the exception of Poisson's ratio (Figure 3.5-4). While these instruments provide a good estimate of the formation parameters, taking such measurements can be hazardous and expensive as it requires puncturing the entire thickness of the cap rock and drilling into the formation. This procedure is expensive due to the drilling depth, and creates a potential pathway for leakage and escape of the stored carbon. In contrast, measurements collected within the caprock would reduce drilling expenses and eliminate CO_2 leakage risks. In this study, the observation well was located in the upper 10% of the cap rock, i.e., near the ground surface. This approach to monitoring is promising given that we observed that data collected in this region were also able to constrain the three reservoir parameters targeted in the study, albeit with a somewhat greater degree of uncertainty (Figure 3.5-4). The result also suggests that ground deformation measurements themselves may provide sufficient information to constrain reservoirs at substantial depth. An issue that was not considered in the context of this study, however, was how the contributions of errors from near surface noise, regional and teleseismic deformations, and heterogeneities may impact our ability to utilize surficial or near surface data. Such a study would be a valuable contribution to future work. The results of this study do suggest, however, that combinations of multiple data types would be a good strategy for providing the best parameter estimates possible.

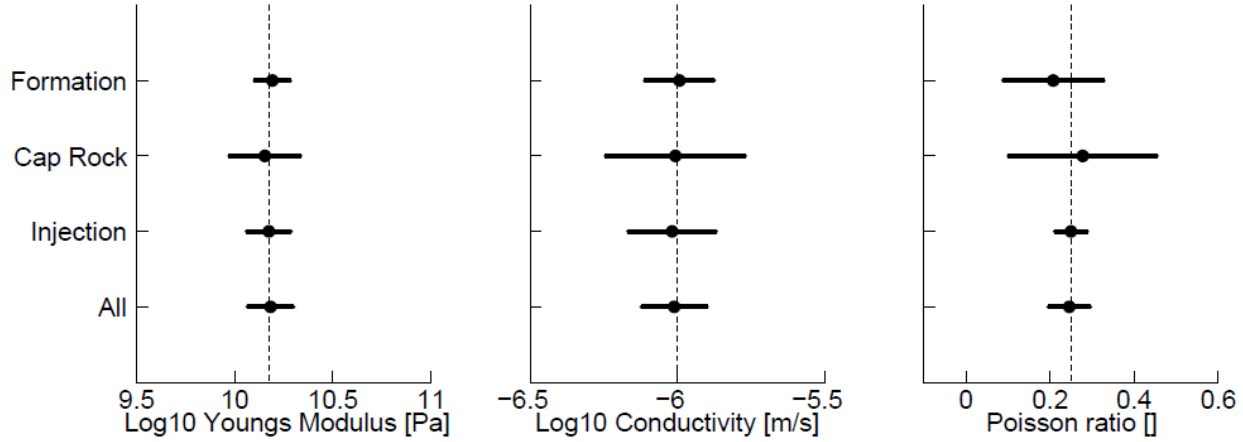

Figure 3.5-4. Optimization results using pressure, tilt, and strain measurements taken from various points in the model space to constrain formation properties.

Heterogeneities

In contrast to random noise, we found that systematic noise – such as that introduced by a model error – significantly impacts our ability to constrain an accurate predictive model. We studied this problem by studying scenarios where heterogeneities were introduced into the models used to produce the "true" synthetic data, but these features were not included within the

model used for inverting the data. The data being fit and the model being used to fit the data therefore have some intrinsic incompatibility, or model error.

In order to investigate the influence of model error on the inversions, we introduced a 150 m long by 20 m thick heterogeneity parallel to the formation with either a higher or lower permeability than the surrounding material. This heterogeneity was present in the forward model used to generate the synthetic data, but not in the forward model used to fit the data. It therefore represents a case where our forward model is incorrect and cannot adequately capture the true flow field.

Figure 3.5-5 demonstrates when the reservoir inclusion is a high permeability, i.e., the inclusion acts as a preferential flow path, there is a much greater degree of parameter uncertainty than for the case where the inclusion has a low permeability. An important characteristic of the data that we observed throughout our studies was that even though the inverse algorithm may converge to a solution despite the model errors, it was still not possible to fit the data when the inclusion was a preferential flow path.

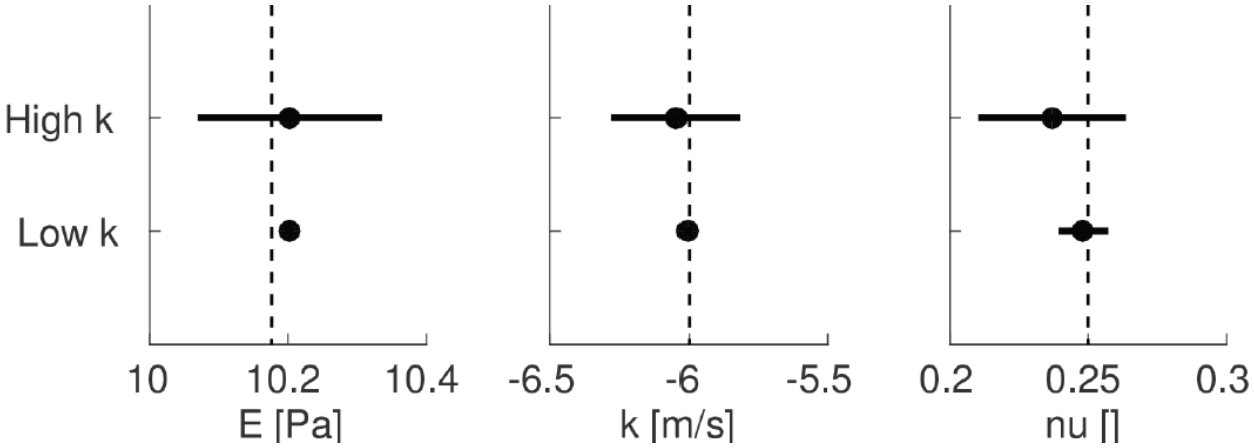

Figure 3.5-5. Optimization results using pressure, tilt, and strain measurements taken from all three points in the model space (formation, cap rock, injection point) to constrain formation properties. A high or low-permeability heterogeneity in the formation interferes with each optimization.

Figure 3.5-6 illustrates the sensitivity of the measurements to the presence of heterogeneities in the formation; the heterogeneity in this case is a permeable (3x formation permeability) near-well inclusion filling 60% of the formation thickness over a length of 100 m. Although the changes observed in this particular scenario are small, it is clear that the heterogeneity does in fact cause a systematic shift in the observed data. Although the length of the heterogeneity extends only about 100 m from the injection well, its influence is detectable in measurements collected 20 times this distance from the injection well, i.e., in an observation well located 2,000 m away from the injection site. The magnitudes of vertical and radial strain observed in this base case are above the expected measurement limit of the strain sensors developed in this project, which is on the order of 10 nanostrain over short time periods. The detectable deformations in the near-well region produced by the heterogeneity suggest that the properties of the heterogeneity may be estimated from the measurements.

Absolute Measurement **Data Differences**

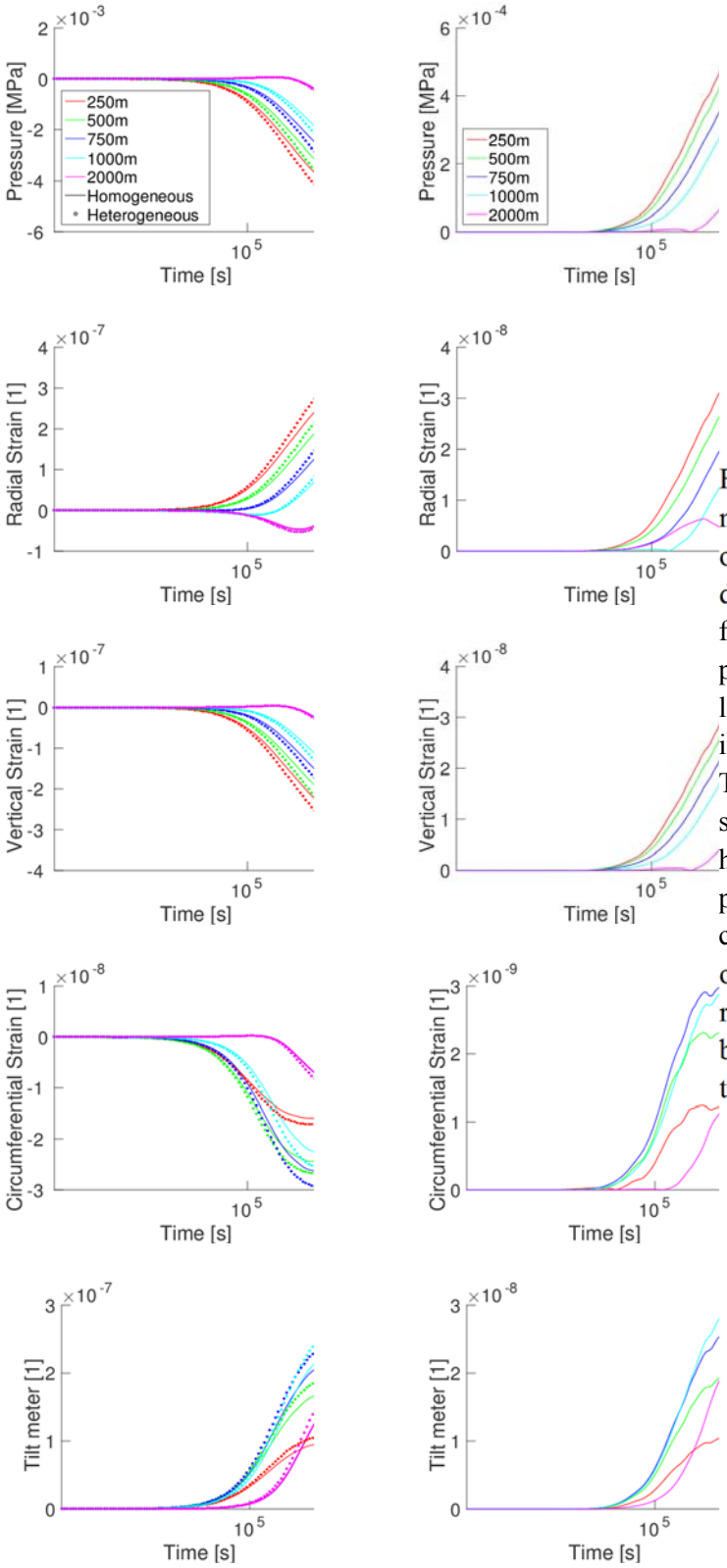

Figure 3.5-6. Comparison of measurements collected at an observation well located various distances from the injection well for the cases when a (100 m) permeable zone is and is not located in the vacinity of the injection well (left column). The difference between the signals expected when the heterogneity is and is not present are shown in the right column. The magnitude of the observed deformations is in the range expected to be detectable by strain sensors developed in this project.

In a related study, we evaluated whether measurements obtained from locations near (1.3x) the boundary of the near-well heterogeneity and far (3.3x) from the boundary could be used to determine information about the inclusion. Figure 3.5-7 shows that it was possible to constrain the Young's modulus and permeability of the formation as well as the permeability of the inclusion with a high degree of precision. Though less accurately determined, we also found that was possible to narrow the range of uncertainty for the position of the boundary itself. These results suggest that use of multiple geomechanical measurement locations in the optimization, similar to the process used in tomographic imaging, shows promise for constraining heterogeneous reservoirs.

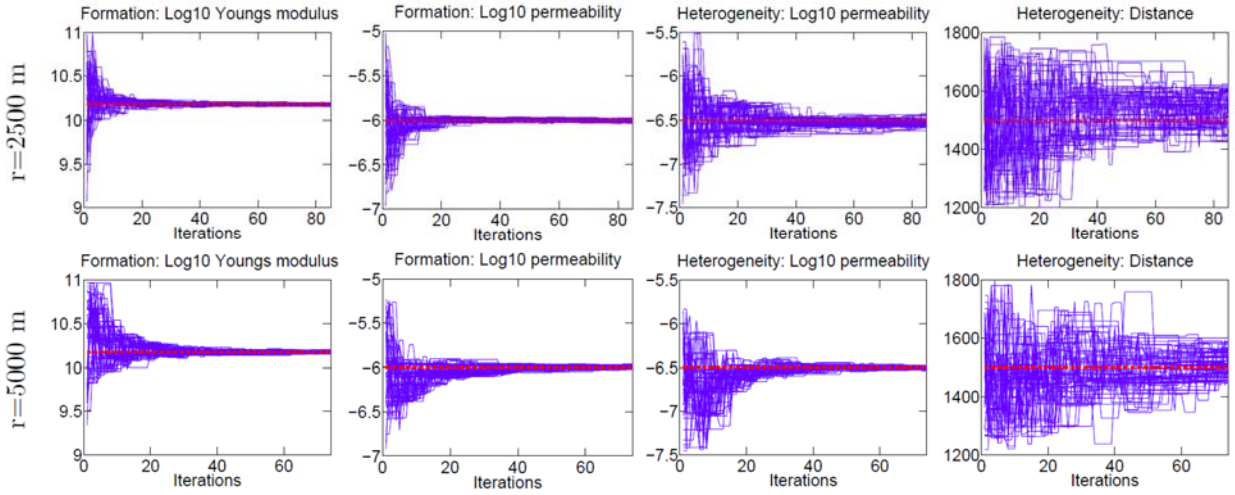

Figure 3.5-7. Comparison of convergence properties for the optimization of reservoir and inclusion properties in a heterogeneous reservoir. Results are shown when the measurement well is located near (1.3x) the inclusion boundary (top row) and far (3.3x) from the inclusion boundary (lower row).

3.5.3 RESERVOIR FORECASTING

In order to examine how our predictions of reservoir performance might vary with respect to the types of data used to calibrate the model, we have used our optimized parameter distributions from Section 3.4.1 to forecast pressure data beyond our data collection phase. We first use these parameter distributions to generate a set of 1,000 random parameter sets. We then run these parameter sets through the forward model and plot them against our measured data. In this case, we used 4 months of synthetic data to forecast 4 years of carbon sequestration. The model maintain the same trajectory over this period with an appropriate level of uncertainty, reflective of the parameter estimates, captured in the prediction results (Figure 3.5-8). Notably, the prediction uncertainties do not grow in an unreasonable manner as could happen in unstable systems.

Given that regional stresses are not included in the model used here, to further perturb the system to investigate the impact of parameter uncertainty on prediction errors we increased the injection rate by a factor of 300%. The magnitude of the reservoir responses clearly increases due to the perturbation (Figure 3.5-9), but not in an unreasonable way as might occur in an unstable system. Furthermore, the prediction uncertainty remains unchanged in a proportional sense (Figure 3.5-10). This result therefore indicates that stable estimates of reservoir behavior with well-defined bounds on prediction uncertainty will be possible.

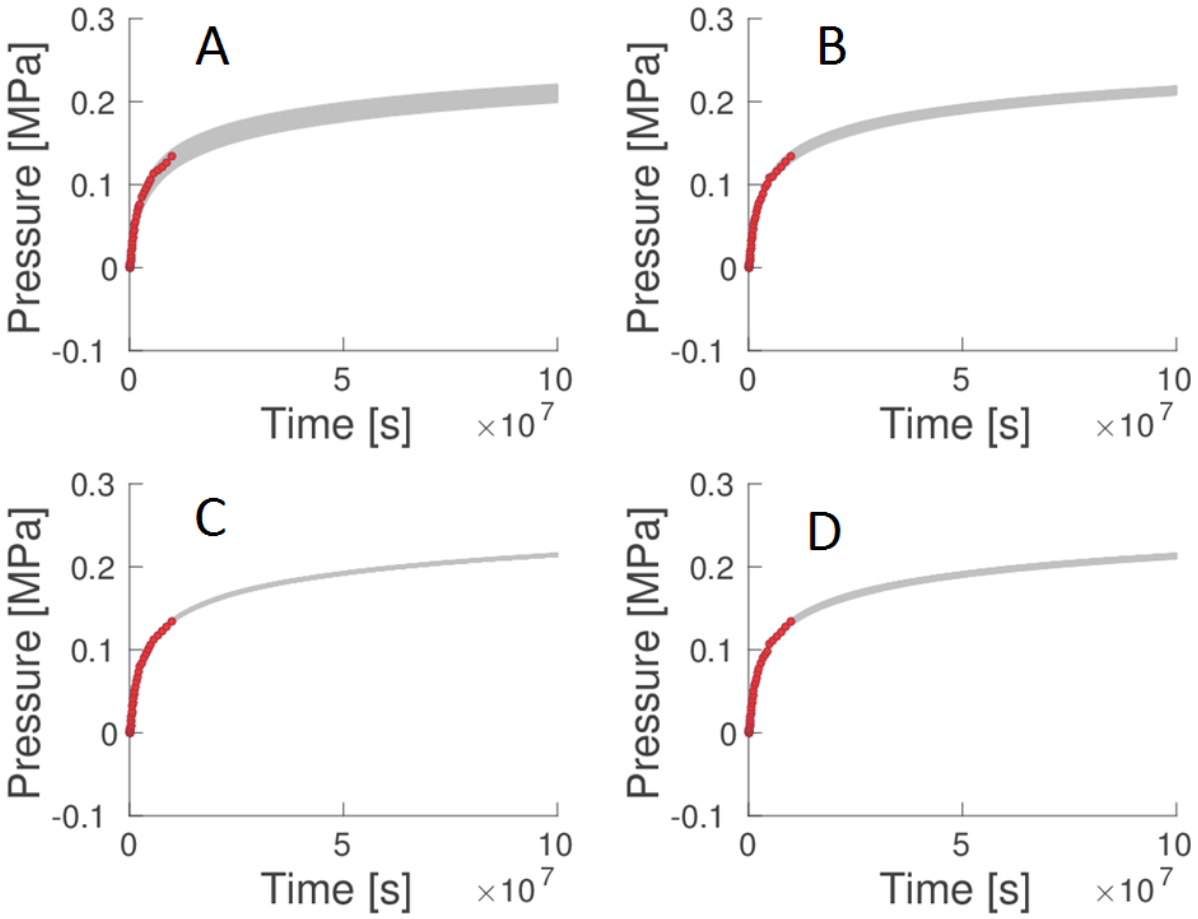

Figure 3.5-8. Parameter distributions are used to generate a set of forecasted models. Subplot A uses 4 months of synthetic pressure and tilt data to forecast pressures over 4 months. Subplot B uses pressure and vertical strain data, subplot C uses pressure, tilt and vertical strain data, and subplot D uses pressure, tilt and vertical, radial and circumferential strain data.

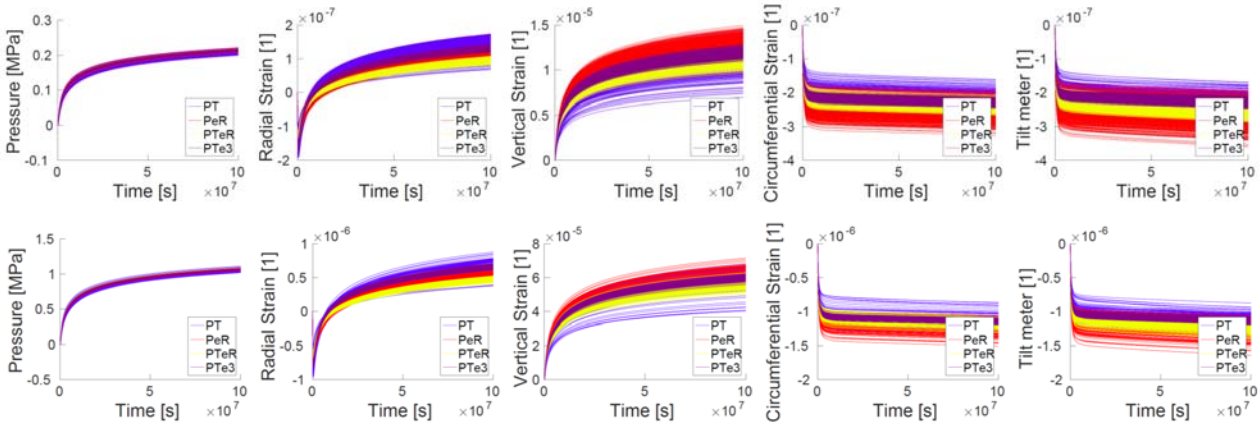

Figure 3.5-9. Forecasts of various reservoir behaviors are presented as a function of the data used to generate the forecast, i.e., PT = pressure & tilt data, PeR = pressure & radial strain, PTeR= pressure, tilt, and radial strain, PTe3 = pressure, tilt, & 3 component strain (radial, vertical and circumferential). The top row represents the reference case, whereas the bottom row represents a scenario where the injection rate is increased by 300%.

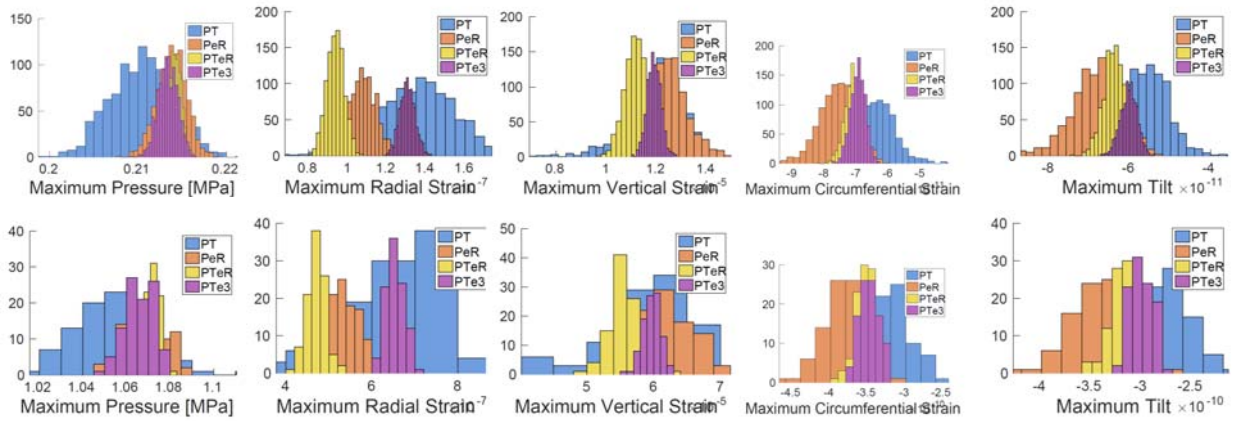

Figure 3.5-10. Comparison of forecasts of the maximum reservoir response between the long-term reference operational scenario (top row) and a case where the injection rate is increased by 300% (bottom row). As before, i.e., PT = pressure & tilt data, PeR = pressure & radial strain, PTeR= pressure, tilt, and radial strain, PTe3 = pressure, tilt, & 3 component strain (radial, vertical and circumferential). Notably, the shapes of the histograms do not change significantly, indicating a simple scaling of prediction uncertainty proportional to injection rate.

3.6 CHAPTER SUMMARY

This task was effective in developing a new inversion methodology for the calibration of poroelastic models using geomechanical data. Applying the model to various case studies, we clearly demonstrated that geomechanical data have substantial value for improving estimates of reservoir properties. We also found that there is flexibility in where these measurements are made (i.e., at the injection point, in the reservoir, or in the caprock), but that using multiple measurements is likely to be the most effective strategy as the complimentary information in the data set is likely to aid in identification and filtering of random and systematic noise. This work also showed that geomechanical data have substantial potential for detecting and identifying heterogeneities within formations. Based on the findings of this study and the availability of the inversion algorithm developed, we feel that the next step would be to test the approach on a real data set to evaluate the efficacy of calibrating poroelastic models with real data.

3.7 REFERENCES

Deb, K. (2002). A fast and elitist multiobjective genetic algorithm: Nsga-ii. IEEE Transactions on Evolutionary Computation, 6(2):182–197.

Chang, H., Y. Chen, and D. Zhang, Data Assimilation of Coupled Fluid Flow and Geomechanics via Ensemble Kalman Filter, *SPE Journal*, SPE-118963-PA, 2010.

Cholathat, R., Ge, L., and Li, X. (2011). Monitoring geologic carbon sequestration with radar remote sensing. Proceedings published 2011 in Australian Space Science Conference Series, ed. W. Short & I. Cairns, *10th Australian Space Science Conf*., Brisbane, Australia, 27-30 September 2010, 187-198

Fonseca, C.M., and Fleming, P.J. (1998a) Multiobjective optimization and multiple constraint handling with evolutionary algorithms- part i: A unified formulation. IEEE Transactions on Systems, Man, and Cybernetics, Part A: Systems and Humans, 28(1), 26-37.

Fonseca, C.M., and Fleming, P.J. (1998a) Multiobjective optimization and multiple constraint handling with evolutionary algorithms- part ii: Application example. IEEE Transactions on Systems, Man, and Cybernetics, Part A: Systems and Humans, 28(1), 38-47.

Iglesias, M.A. and McLaughlin, D. (2012). Data inversion in coupled subsurface flow and geomechanics models.

Khakim, M.Y.N., Tsuji, T., and Matsuoka, T. (2012). Geomechanical modeling for InSAR-derived surface deformation at steam-injection oil sand fields. Journal of Petroleum Science and Engineering, 96-97, 152—161.

Metropolis, N., A.W. Rosenbluth, M.N. Rosenbluth, and A.H. Teller, (1953). Equations of state calculations by fast computing machines. *The Journal of Chemical Physics* 21(6): 1087-1092.

Schaffer, J.D., (1984). *Some experiments in machine learning using vector evaluated genetic algorithms*. PhD Thesis, Vanderbilt University.

Toussaint, G. T. (1983). Computing largest empty circles with location constraints. *International Journal of Computer and Information Sciences* 12(5): 347-358.

Wang, Z., Cates, M.E., and Langan,. R.T. (1998). Seismic monitoring of a CO_2 flood in a carbonate reservoir: A rock physics study. *Geophysics* 63(5): 1604-1617.

Wang, H.F. (2000). Theory of Linear Poroelasticity with Applications to Geomechanics and Hydrogeology, (Princeton Univ. Press, Princeton, New Jersey, 2000).

White, D. J., (2011). Geophysical monitoring of the Weyburn CO_2 flood: Results during 10 years of injection. *Energy Procedia* 4(2011): 3628-3635.

Zitzler, E., Laumanns, M., and Thiele, L. (2001). Spea2: Improving the strength pareto evolutionary algorithm. Technical Report 103, Computer Engineering and Networks Laboratory (TIK), ETH Zurich, Zurich, Switzerland.

CHAPTER FOUR
INSTRUMENTATION

CONTENTS

CHAPTER FOUR
INSTRUMENTATION

The objective of this task is to evaluate instrumentation that could measure multi-dimensional displacements in a borehole during CO_2 storage. We first consider in Section 4.1 sensors that can measure strain in various forms, including deformation and tilt. These are sensors that could be packaged in various instruments to measure wellbore deformation. This is followed in Section 4.2 by a review of instruments capable of measuring deformation in situ. We consider existing instruments, as well as a new instrument that was developed and evaluated for this project. The major findings of the evaluation are summarized in Section 4.3.

The organization of this chapter differs slightly from the organization of the SOPO. The reason for this is because it became apparent during the investigation that we should evaluate sensors and instruments under shallow, in-situ field testing conditions. This provided some important insights that contributed to the overall objective of the task, but it was beyond the scope of the tasks explicitly identified in the SOPO, which only included laboratory tests. As a result, we have organized the following chapter to describe these shallow, pilot-scale field evaluations, along with the other tasks identified in the original SOPO. An example of this is that Section 4.3 of the SOPO included evaluating anchors and registration systems, which are components of downhole instruments. Instead of evaluating them as isolated components, we describe functional downhole instruments that included these components and we evaluate the instruments under field conditions. These downhole instruments are described in Section 4.2. The SOPO also included Sections 4.1 and 4.2 that focused on evaluating sensors. We evaluate sensors explicitly in Section 4.1 below, but the performance of sensors in the field is also evaluated in Section 4.2.

4.1 SENSORS

The objective of this section of the report is to evaluate sensors that could be useful for measuring deformation of boreholes during changes in fluid pressure in the subsurface. We reviewed available sensors and obtained representative examples that seemed most promising. Suitable candidates were sensors that had the potential to be used in downhole conditions, and to resolve the general magnitude of expected strain. In particular, we were interested in sensors that could

1.) function under harsh conditions; e.g. exposed to water, or CO_2 at downhole temperatures

2.) function remotely; minimal power requirements, data transmission capabilities

3.) provide high resolution data on strain, displacement or tilt

We identified two electromagnetic and two optical sensors that meet these requirements to varying degrees for strain and displacement sensing. Sensors were also identified for tilt measurements.

The evaluation consisted of a review of the functionality based on published descriptions, and in some cases we evaluated the performance based on data we obtained ourselves. Some of the sensors were identified early in the research and we had time to evaluate them in the lab and field. Other sensors, like the eddy current sensor, were identified relatively late in the project so the data we were able to generate was more limited. As a result, we provide example data for the

potential sensors, but only some of these examples are suitable for evaluating the resolution of the sensor under field conditions. Additional evaluation of many of the sensors was done by including them in field instruments, and this is described in section 4.2.

4.1.1 DVRT

Differential Variable Reluctance Transducers, or DVRTs, have an internal core surrounded by an outer coil (Figure 4.1-1) [*Pierson*, 1999; *Feipel et al.*, 2003; *Ferrari and Marioli*, 2008]. The internal core moves axially within the outer coil in response to displacement. The core position is determined by measuring the differential reluctance of the coil using a sine wave excitation and demodulator [*Pierson*, 1999].

DVRTs are similar to Linear Variable Differential Transformers (LVDT) in that both systems use the interactions between an inner core with low magnetic susceptibility and an outer coil to measure displacement. There are some important differences, however, and the most notable is that DVRTs are available with a resolution of 10^{-8} m, whereas the resolution of commercially available LVDTs is an order of magnitude or greater. LVDTs are widely available with a dozen or so manufacturers, whereas to our knowledge the company MicroStrain (http://www.microstrain.com/displacement/dvrt) is only current commercial manufacturer of DVRTs.

The packaging of DVRTs includes a threaded housing to facilitate mounting of the outer coil. The inner core moves on a bearing to improve the alignment within the outer coil. A spring within the outer coil is used to push the inner core outward in order to keep the end of the core in contact with a target. The core can be threaded onto a target, or the core can be terminated in a sphere to provide a relatively bearing surface on the target that is relatively free of bending moments that could bind the core within the coil.

Figure 4.1-1. DVRT (cylinder on left) with signal conditioner (black triangle). DVRT consists of an outer coil in a cylindrical housing with an inner core tipped with a ball. The inner core slides on a bearing at the end of the cylindrical housing. From: http://www.microstrain.com/displacement/sg-dvrt

During deployment, the threaded core is mounted on a reference piece and the ball on the inner coil is placed on the target. The spring keeps the ball in contact with the target, but it also applies a force to the target. Non-contact DVRTs are available that do not have a spring loaded core, but their resolution is less than the highest resolution model with a core.

Uses

DVRTs are marketed by MicroStrain for general applications requiring displacement measurement. The sensors are cylindrical and either smooth or threaded to facilitate mounting. The coil configuration in DVRTs is more compact than LVDTs, so DVRTs can be made smaller than LVDTs. Sensor packages a few mm in diameter and one cm or so long are available. This small form factor facilitates applications to monitoring civil engineering infrastructure, industrial processes, and biomedical applications.

Performance

We evaluated a MicroStrain DVRT-S configured to "nano" resolution at the factory. The sensor is 34 mm long and housed in a threaded stainless steel cylinder with 3/8-24 UNF threads. The frequency output of the DVRT was demodulated to a 0-5 VDC using a MicroStrain Model DEMOD-DC. The output voltage was converted to a 24-bit digital signal using a Symmetric Research model SER1CH Analog to Digital converter.

The sensor can function under downhole conditions with few ill effects. An application of this sensor is described below in Section 4.2.2. The DVRT sensor can be vulnerable to electromagnetic interference. A periodic noise of significant amplitude (~60 nm) was produced when two DVRTs operating at slightly different frequencies interfered with each other, even though they were separated by more than 10 m. Downhole pumps can also cause interference under some circumstances, although the extent of the interference appears to depend on the design of the data cable, proximity of the pump and other factors.

We evaluated the performance of the Lord MicroStrain NANO-G-DVRT-0.5 sensors both in the laboratory and field. The lab tests were conducted by running the instruments in a static fixture over the weekend when human activity is minimal. The field test involved deploying the sensor on the Tilt-X frame, described below, and monitoring while in place in a borehole. A nine-day long section of the field record was selected for analysis. The results were analyzed using a Fourier transform to determine the magnitude spectra.

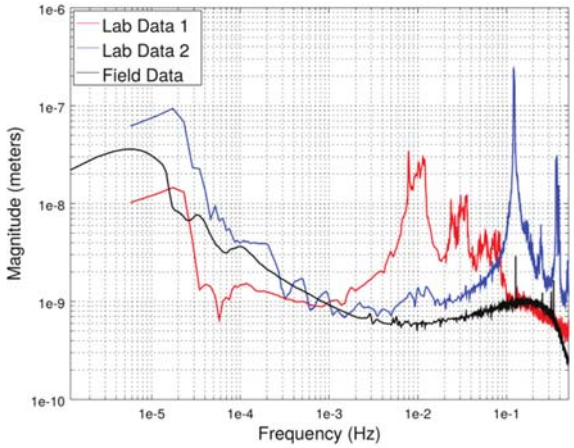

Figure 4.1-2. Magnitude spectra from lab and field DVRT data.

The results (Figure 4.1-2) shows the magnitude spectra reaches minima at approximately 1 nm both in the lab and the field. The minima in the lab is in the range of 10^{-3} to 10^{-2} Hz, and the magnitude increases substantially at higher frequencies in the lab. The large magnitudes at high frequency are probably vibrations of the building, and probably do not reflect limitations in the sensor performance. The noise in the field is generally less than that in the lab, with the lowest noise levels of less than 1 nm occurring at approximately 10^{-1} Hz (Figure 4.1-2).

4.1.2 EDDY CURRENT

Eddy current displacement transducers are electronic devices that operate by generating a magnetic field that induces eddy currents in an electrically conductive target (typically aluminum), which in turn induces an opposing magnetic field. The strength of this coupled field depends upon the output of the transducer, the conductivity of the target, and the electrical impedance of the gap between the transducer and the target. Assuming the conductivity to be constant, the impedance only depends upon the physical gap between the sensor and the target. It is this impedance that is being measured and converted to a voltage output using a resistive bridge circuit.

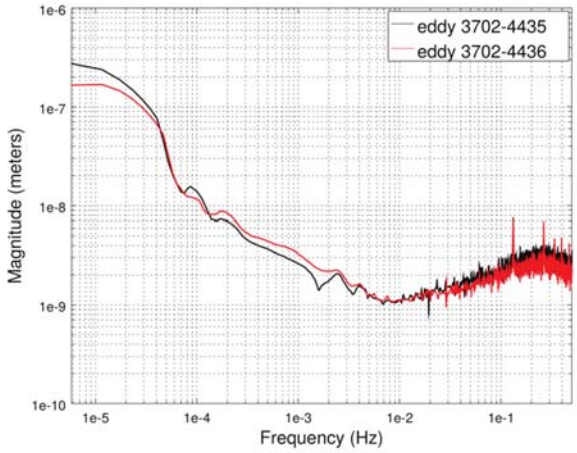

Figure 4.1-3. Magnitude spectra from a pair of single-ended eddy current displacement transducers.

The primary advantages of the eddy current sensors are their very high resolution, small size, and non-contact operation. Their precision is typically stated to be around 1 nm for the single-ended units and 0.1 nm when using a pair of sensors in differential mode. The sensors themselves can be quite small at several mm in diameter and 1-2 cm long. The lack of contact between the sensor and its target eliminates potential noise caused by friction as well as any drift caused by abrasion.

Uses

There are a handful of manufacturers of eddy current displacement transducers that are marketed for industrial positioning and vibration measurement applications. Micro-Epsilon (http://www.micro-epsilon.com/displacement-position-sensors/eddy-current-sensors/index.html) and Kaman Precision Products (http://www.kamansensors.com) appear to be the two main competitors for the highest resolution sensors, and both offer single-ended and differential systems.

Performance

We conducted baseline tests of the performance of the a Micro-Epsilon 3702 single-ended eddy current displacement sensing system deployed on a fixed target in the laboratory to evaluate intrinsic noise in the instrument. Figure 4.1-3 shows the magnitude spectra from two instruments. The data are consistent with single-digit nanometer performance between 10^{-4} and the Nyquist frequency (0.5 Hz). Noise spectra from eddy current sensors in a differential configuration are expected to be less than those from a single ended system, but those data were unavailable. As a result, we expect that sensors in a differential configuration will perform better than the data in 4.1-3, but additional testing is required to establish the performance.

4.1.3 FIBER BRAGG GRATING

Fiber Bragg Grating (FBG) sensors are fine grooves etched into the circumference of an optical fiber and spaced a fixed distance apart. The evenly spaced grooves form a grating that acts as a wavelength-specific reflector. When light is injected into the fiber, the grating will either reflect or refract a specific wavelength defined by the spacing between the gratings and the effective refractive index of the grating in the optical fiber. Maximum reflectivity occurs at the *Bragg wavelength* [*Grattan and Sun*, 1999]:

$$\lambda_B = 2n_e\Delta \qquad (4.1\text{-}1)$$

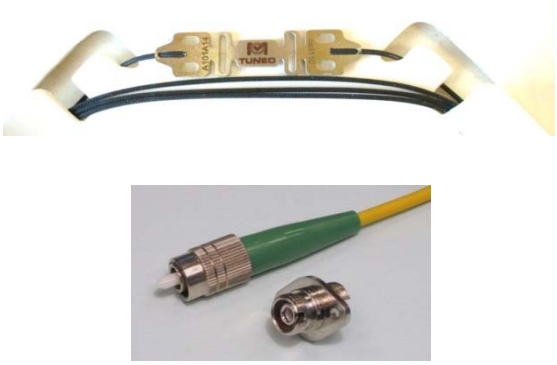

Figure 4.1-4. The top picture is the FBG sensor. The fiber optic cable is in the middle of the steel carrier which keeps the FBG etchings in tension. The bottom picture is the FP/APC connector and the adapter.

where n_e is the effective refractive index of the grating in the fiber core, Δ is the grating spacing. When the sensor extends, the spacing between the grating, ΔL, increases and the Bragg wavelength shifts towards a higher wavelength. The spacing between the etchings decreases when compression occurs, and the reflected wavelength decreases. The change in wavelength due to displacement is given by [*Schmidt-Hattenberger et al.*, 2003]:

$$\Delta\lambda_B = \lambda_B\left(C_S\frac{\Delta L}{L} + C_T\Delta T\right) \qquad (4.1\text{-}2)$$

where C_S is a strain calibration coefficient, L is the length of the sensor, and ΔL is displacement, C_T is a temperature coefficient, and ΔT is temperature change.

FBG sensors are typically used on a platform that reduces their compliance and holds them in tension. An FBG strain gauge made by Micron Optics consists of an optical fiber bonded to a stainless steel plate containing elongate holes (Figure 4.1-4).

The signal conditioner for FBGs is called an interrogator. It sends light down the fiber and measures the frequency of the reflected light. Measurement rates of 1 Hz are common, but rates of several hundred Hz are also possible. Up to several dozen FBGs can be read on a single fiber with currently available interrogators.

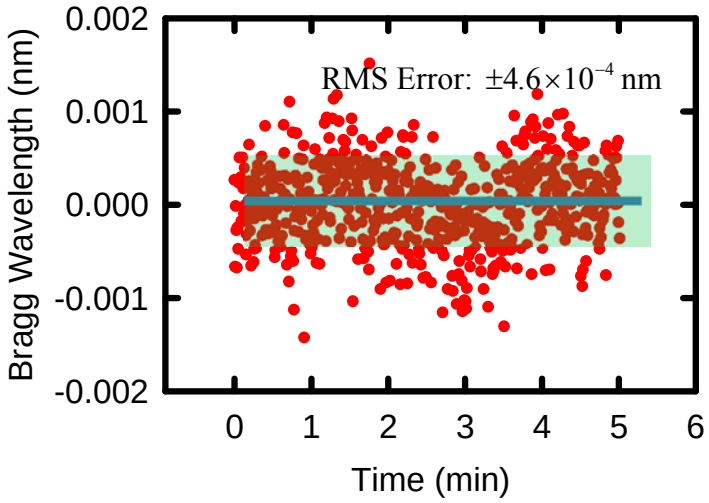

Figure 4.1-5. Bragg wavelength as a function of time measured on unstress FBG to indicate level of instrument noise.

Uses

FBGs are widely used to measure strain in industrial and civil engineering applications. The strain gauge shown in Figure 4.1-4 can be welded to metal, so it is well suited to deployment on steel infrastructure, like bridges or the frames of buildings. The FBG itself is a narrow glass fiber that can be embedded along with other fibers in composite materials.

FBGs are sensitive to temperature as well as mechanical strain, according to Eq. 4.1-2. This has resulted in applications for FBGs as thermometers. Two FBGs can be integrated to allow temperature compensation of strain measurements.

FBGs are primarily used in optical circuits. This is unrelated to the application that is relevant to this work.

Performance

The resolution of FBGs depends on the performance of the interrogator and the gauge. The FBG gauges that we identified are rated with a resolution of slightly less than 1 με when used with readily available interrogators. For example, the Micron Optics FBG is rated as 1.4 pm /με. We tested the Micron Optics SM 125 interrogator and found it had an RMS error of ±0.46 pm at 1 Hz (Figure 4.1-5). This corresponds to an RMS error of 0.46/1.4=0.3 με. Other vendors of FBGs give similar estimates of the resolution.

The displacement resolution of FBGs can be estimated as the product of their strain resolution and their length. FBGs are approximately one cm long, so their displacement resolution is estimated as $\sim 10^{-8}$ m. This is consistent with our field measurements (e.g. 4.2-68 or 4.2-70).

4.1.4 FIBER INTERFEROMETER

The length of an optical fiber can be measured with very high precision using the principle of laser interferometry. The most basic configuration is the Michelson interferometer shown in Figure 4.1-6. A light source is injected into one of the four arms of a 2×2 fused optical fiber coupler where the light is split equally into two paths. The light within these two fibers reflect off mirrors and returns back through their same paths and recombine at the 2×2 coupler to form interference fringes. These emerge from each arm of the coupler where the intensity of one of the two returning beams is measured by a photodetector.

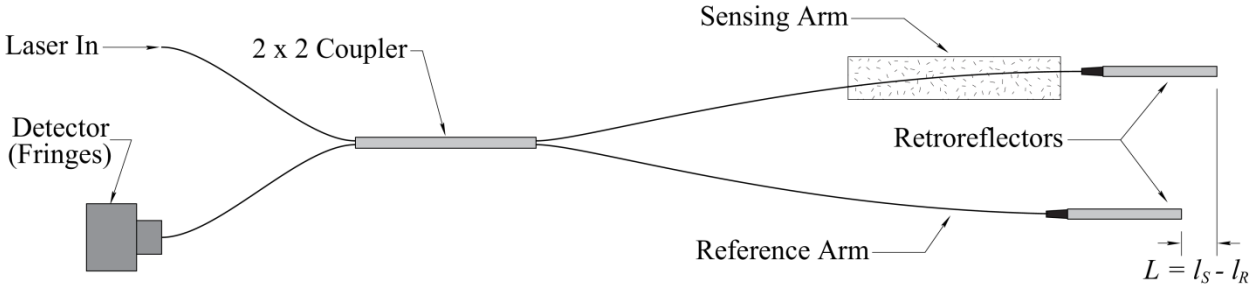

Figure 4.1-6. The optical fiber Michelson interferometer, where light is divided into two paths and recombines to form interference fringes. While it is customary to depict one path (the "Sensing Arm") as being lengthened with respect to the other ("Reference Arm"), it is the net change between the two that is measured.

To derive the relationship between the mechanical elongation of the fiber and the observed fringe signal, consider the total optical phase of light propagating in an optical fiber:

$$\theta = \frac{2\pi nl}{\lambda} \tag{4.1-3}$$

where the index of refraction $n = c/v$ is the ratio of the speed of light in air c and the speed in the material v, l is the path length, and λ is the wavelength. The optical phase shift ϕ is related to the difference between the optical phase of the light propagating in the sensing arm θ_S and reference arm θ_R, respectively, as:

$$\phi = \theta_S - \theta_R = \frac{2\pi nl}{\lambda}(l_S - l_R) = \frac{2\pi nL}{\lambda} \tag{4.1-4}$$

where $L = l_S - l_R$ is the physical length difference between the two interferometer arms. The intensity at the output of the 2×2 coupler as seen by the output (voltage) x of the photodetector can be expressed as:

$$x = x_0 + a\cos(2\phi) \tag{4.1-5}$$

where x_0 and a are the offset and amplitude, respectively, and the factor of 2 is a result of the reflection (i.e., the light travels through its path twice).

There is a bidirectional phase ambiguity present in Eq. 4.1-5 that can be resolved using a 3×3 fiber coupler. Consider when the output intensity is a maximum, i.e., where the optical phase is $\phi = \pi$ or optical path length difference $nL = \lambda/2$. An increase in L results in the same decrease in intensity seen by the photodetector as an equal decrease in L, thereby making it impossible to discriminate between expansive and contractive path length changes. Fused optical fiber couplers function by allowing light to "leak" from one waveguide to the other when fused together. In addition to the amplitude being split, there is also a phase shift induced in proportion to the distance between the waveguides and the wavelength of light. For an ideal 3×3 coupler (1/3:1/3:1/3 splitting ratio), the light in each adjacent arm is phase-shifted by 120º from the other (Sheem 1980), implying that the intensity measured by a second photodetector, y, is:

$$y = y_0 + b\,sin(2\phi + 120°) \tag{4.1-6}$$

where y_0 and b are the offset and amplitude, respectively. Therefore, by employing a 3×3 rather than a 2×2 coupler, two fringe signals emerge whose photodetector voltages form a Lissajous curve that sweeps out an ellipse as the optical path length difference changes. The orbital direction of the x, y voltage pair around this ellipse depends upon whether one path is lengthening or shortening with respect to the other. Many signal processing techniques can be employed to extract the directional optical phase information from these two voltages [*Zumberge et al.*, 2004; *Pozar and Mozina*, 2011; *Li et al.*, 2003].

Uses

The primary advantages of optical fiber interferometers are their very high sensitivity to strain and temperature [*Hocker*, 1979], and their complete immunity to electromagnetic interference. The very thin fibers (125 μm in diameter) are easy to wrap around or embed in other materials [*Hocker*, 1979; *Sirkis and Mathews*, 1993]. The low attenuation in an optical fiber (typically 0.2 dB/km) implies that sensors can be made using an almost arbitrarily long length of fiber to increase the sensitivity of a small sensing area or to perform a spatial average over a large area.

These advantages lead to the extensive and diverse applications of optical fiber interferometers. For example, Sagnac interferometers are widely used for optical fiber gyroscopes, whose sensitivity is proportional to the area enclosed by a loop of fiber [*Vali and Shorthill*, 1976]. Given the small fiber diameter and low attenuation, many thousands of wraps can be wound about a small cylinder to achieve very precise rotation rate measurements for applications such as inertial navigation. Optical fiber accelerometers and hydrophones are widely used in the oil and gas industry. This is in partly due to the fact that one expensive active interrogation system can read out many thousands of inexpensive passive sensors in permanent reservoir monitoring deployments. The Petroleum Geo Solutions (PGS) OptoSeis:

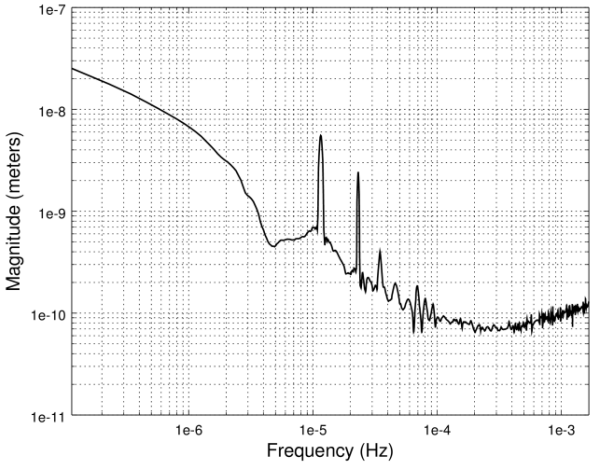

Figure 4.1-7. Magnitude spectra from 125 m of fiber wrapped on a quartz mandrel.

http://www.pgs.com/Geophysical-Services/4D-Seismic/Permanent-Monitoring/

is one of many such systems.

The main disadvantage of optical fiber interferometers is the relatively large temperature coefficient of the index of refraction of the glass fiber. This has been estimated at approximately 1.2×10^{-5} per degree Celsius [*Zumberge et al.*, 1988], and is the primary limiting factor in designing sensing systems. However, this becomes less of a limitation in deep borehole environments where the temperature is generally very stable.

Performance

We conducted tests to evaluate the stability of an optical fiber Michelson interferometer similar to the one shown in Figure 4.1-6. The test consisted of 125 m of optical fiber wrapped about a 20-cm-diameter quartz cylinder, which was deployed 3-m below the ground surface in an underground vault. No external loads were applied to the system.

The results (Fig. 4.1-7) show that the system is capable of resolving changes in length of less than 10^{-10} m (0.1 nm) between 1×10^{-4} and 1×10^{-3} Hz (10,000 and 1,000 second periods, respectively). The two peaks at roughly 1.2 and 2.4 x 10^{-5} Hz correspond to 1 and 2 cycles per day. These peaks are likely due to small changes in temperature.

The displacement resolution of the fiber interferometer was approximately 0.1 of the resolution of the electromagnetic sensors (DVRT or Eddy Current). The measurement made by the interferometer is over a reference length of more than 100 m, whereas the reference length of the electromagnetic sensors is approximately 1 cm, 4 orders of magnitude smaller than the fiber interferometer. As a result, the strain resolution of the fiber interferometer is approximately 5 orders of magnitude finer than the electromagnetic sensors.

4.1.5 ELECTROLYTIC TILT SENSOR

Electrolytic tilt sensors are created by monitoring the position of a gas bubble in a curved glass tube (Figure 4.1-8). This is accomplished by placing fine gauge wires inside of the tube and monitoring the resistance between the wires. The liquid in the tube is electrically conductive, whereas the gas is a poor conductor. As a result, the overall resistance between the wires is a strong function of the length of the wire in contact with the gas bubble, which changes with the tilt.

Figure 4.1-8. Eletrolytic tilt sensor. This example is from Spectron sensors:

http://www.spectronsensors.com/tilt-sensors.php

The tilt sensing system requires the sensor itself along with a signal conditioner capable of measuring changes in resistance to high resolution. The signal conditioner is designed to eliminate current flow through the sensor, and an alternating current is used to eliminate electrode polarization in an effort to improve resolution. (e.g. http://www.aositilt.com/ma/applicat/).

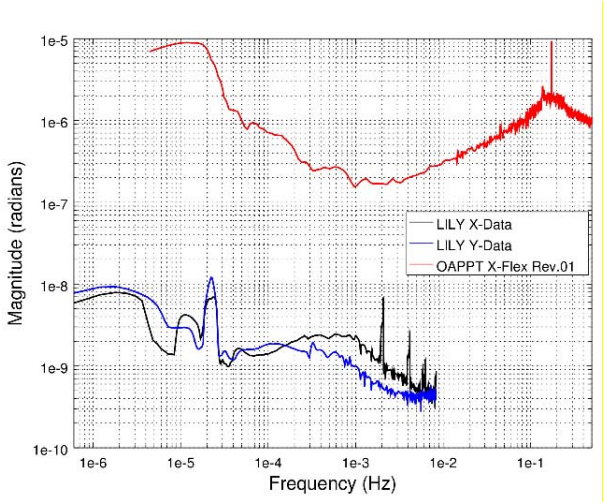

Figure 4.1-9. Magnitude spectra from the LILY electrolytic tiltmeter experiment described in Section 4.2.2, and from the OAPPT employing differential eddy current sensors. The peak in the OAPPT spectrum at 0.18 Hz is the free period of the tiltmeter.

Other styles of tilt sensors are available, but electrolytic sensors occupy an important niche relevant to applications for CO_2. Micromachining techniques are used to make electronic sensors capable of measuring tilt. One design uses an accelerometer to measure the change in the direction of gravitational acceleration during tilting. These Micro-Electromechanical Systems (MEMS) sensors are rugged and can be more robust than electrolytic sensors, but we are unaware of MEMS sensors that can rival the resolution of electrolytic tilt sensors at this time. It is also possible to measure tilt by measuring the displacement of a pendulum. This approach has been used in research instruments for many years, but to our knowledge, tilt sensors based on a macro-sized pendulum are currently unavailable from commercial sources.

Uses

Electrolytic tilt sensors configured for a wide span and relatively low resolution are used as electronic substitutes for a carpenter's level, with similar applications. Higher resolution configurations are used to characterize the inclination of equipment, or infrastructure.

Electrolytic tilt sensors are available in a configuration that can be deployed in a borehole. The most readily available instrument is a Lily Self-leveling Borehole Tiltmeter, originally made by Applied Geomechanics and currently marketed by Jewell Instruments

(http://www.jewellinstruments.com/?s=lily). This device consists of two orthogonal horizontal tilt sensors that can be adjusted with an internal motor after the instrument is in place.

Components similar to the Lily tiltmeter have been used for applications in the oil and gas industry for many years. Other applications include monitoring deformation associated with volcanos and plate tectonics. For example, 26 borehole tiltmeters were installed to monitor crustal deformation as part of the Plate Boundary Observatory (http://www.unavco.org/instrumentation/geophysical/borehole/tiltmeter/tiltmeter.html).

Performance

The resolution of the Lily Tiltmeter is cited as 5 nrad by the manufacturer. We evaluated the performance spectrum from roughly 20 days of data while being deployed in a 152-foot deep borehole for the experiment described in Section 4.2.2. The Lily tiltmeter was deployed using the retractable anchor system outlined in the section below describing the Tilt-X instrument.

This analysis also includes data from a precision pendulum tiltmeter that we recently developed. This device (called a One Axis Physical Pendulum Tiltmeter, or OAPPT) is a 10-cm-long pendulum suspended on cross-flexures. A pair of Kaman 15N eddy current displacement transducers is configured to monitor tilt by measuring the position of the mass at the end of the pendulum.

The magnitude spectra in Figure 4.1-9 illustrates some of the differences between the two instruments and the environmental conditions under which they are deployed.

The overall spectral level of the Lily tiltmeter is quite good with a noise level in the single digit nanoradian range (~10^{-9} rad) at frequencies above 10^{-5} Hz. The two peaks between 1 and $2x10^{-5}$ Hz are from barometric fluctuations and earth tides.

The magnitude from the OAPPT in the laboratory is approximately $2x10^{-7}$ rad at 10^{-3} Hz and it increases at higher and lower frequencies. These data are included to demonstrate proof-of-concept of the OAPPT tiltmeter, but they should not be considered a measure of the resolution of the instrument. The spectra from the OAPPT in Figure 4.1-9 results from vibrations or movements of the building, temperature changes in the laboratory, and other factors that cause tilting. As a result, the signal from the OAPPT tiltmeter likely reflects actual deformation, rather than a limit of resolution of the instrument.

Temperature changes during the Lily downhole test are expected to be roughly 2 orders of magnitude less than those during to OAPPT test (several hundredths of a degree compared to several degrees). As a result, temperature changes alone may account for the 2 orders of magnitude difference between the Lily and OAPPT data in Figure 4.1-9. Tests in a down-hole environment will be needed to generate performance data from OAPPT that can be compared to that from Lily.

4.1.6 DISCUSSION

All the sensors described in the previous pages appear to have potential applications associated with measuring deformation of boreholes. Characteristics of the sensors vary and the details will affect suitability for particular application.

Size

Eddy Current, DVRT and FBG sensors are approximately 1 to 2 cm in size and could be deployed in a variety of configurations. DVRT and Eddy Current sensors require signal conditioning electronics within several meters of the sensors. The signal conditioning electronics are in enclosures that are approximately 7 cm in maximum dimension. No downhole signal conditioner is required for FBGs, but it does require a sophisticated signal conditioner and computer above ground.

Electrolytic tilt sensors are also several cm in size, but they require larger signal conditioners. Nevertheless, the signal conditioner for the Lily tiltmeter is designed to fit in a 5-cm-diameter, pressure tight cylinder, and this size should not limit most downhole applications.

Optical fiber interferometers can be as small or as large as needed for the desired application, but are similar to FBGs in that they require an interrogation system. Simple displacement sensors such an intrinsic Fabry-Pérot interferometer can be made as small as several mm. The limiting factor in embedding geometries is typically the bend radius of the optical fiber, but newer fibers such as the Corning ClearCurve ZBL allow for many tight bends as small as 5 mm in radius.

Durability

The optical fiber sensors (FBG and interferometer) have several advantages over the other sensors. By far the most attractive feature is that no electronic components are required downhole. This permits their use in high temperature and corrosive environments inaccessible to electronics. Standard telecommunications optical fiber is also very inexpensive ($0.10 per meter) and allows for the sensors themselves to be expendable. Optical fiber sensors are also completely immune to electromagnetic interference (and lightning) unless deliberately designed using high Verdet constant materials.

However, optical fibers are fragile and they must be embedded in some material or packaged in a configuration that protects them during deployment downhole. The calibration factor of FBGs can be changed, or the fiber can be broken when FBGs are subjected to excessive strains. The optical fiber in interferometers will also be vulnerable to excessive strains (>1%), and this will need to be considered during the design of instruments that use these sensors.

DVRT and Eddy Current sensors are more robust and will be less vulnerable than fibers to damage. The magnetic core on the DVRT is delicate and must be protected during deployment. However, the spring-loaded core helps to protect the DVRT from damage. This is because the ball on the end of the core can slip laterally, or it will harmlessly disengage when the target is extended beyond its range. There is no contact between the Eddy Current sensor and its target, so this further protects it.

The FBGs we tested were unaffected after being immersed in supercritical CO_2 for 1 week. We were unable to evaluate the effects of supercritical CO_2 on other sensors, but we expect that they will function properly when built with appropriate materials.

Compliance

The compliance of a sensor (displacement per unit of applied force) can affect its suitability for applications involving high resolution. The force applied by the sensor may affect the measurement. A good example of this is measuring the location of a pendulum. In this case, a force applied by the sensor to the pendulum will affect the position of the pendulum. This may influence the results, and it should be considered in applications.

Eddy Current sensors have the highest compliance of the sensors we evaluated. There is no physical contact between an eddy current sensor and its target, so effects of compliance can be ignored. DVRT sensors have a light spring that applies force on the target. The spring is light (it is quantified in the section describing Tilt-X), but it is certainly strong enough to influence some results; it would influence a pendulum for example.

The compliance of the FBG strain gauge we tested was relatively low by comparison to other gauges. The gauge was made from a steel sheet containing flexures that must deform with the component being measured. The load created by the compliance of the FBG should be considered for high resolution applications, but in many cases it will be negligible.

The compliance of bare fiber in an interferometer will be midway between that of a relatively stiff FBG and a compliant DVRT. Nevertheless, it seems likely that some type of matrix will be required to stabilize the fiber, which would affect the compliance. It is possible to configure an interferometer using light that passes through free space and reflects off a target. The compliance of this configuration would be essentially infinite.

Resolution

The preceding section presents data on the resolution of displacement and tilt sensors. Spectral plots like (4.1-9) show the magnitude of a signal as a function of frequency. Ideally, these plots show data where there is no displacement on the sensor, so the resulting signal is only affected by instrument noise. The instrument noise would be a lower limit of the resolution of the sensor. Obtaining conditions needed to identify instrument noise for high resolution sensors can be challenging. In some cases, the data we present are from field tests characterized by stable downhole temperatures that facilitate identifying instrument noise. Some ambient displacements may occur in these tests, in response to barometric pressure or earth tides for example, so the signal may overestimate the instrument noise at the frequencies of the ambient signals.

In other cases, data are from the laboratory where a frame was used to create a null, or constant displacement. Temperature fluctuations are difficult to eliminate from the laboratory, and thermoelastic effects may cause displacements in the frame. Temperature fluctuations of signal conditioners will also cause apparent displacements in the laboratory. These thermal effects are likely larger than the temperature variations experienced downhole, so these data are an upper estimate of the resolution.

At least two factors will increase the resolution of displacement measurements compared to the data shown in this section. Random noise can be reduced by oversampling and averaging bins of data. The resolution can be improved, or the noise level reduced, by a factor approaching the square root of the number of points included in the average. For example, sampling 100 points at 1 Hz and taking the average will give one value at 0.01 Hz. The random noise associated with the 0.01 Hz data will be 1/10 that of the noise in the original data.

Another approach is to extend the span of the measurement using a rigid, stable reference bar. For example, attaching a small sensor to a reference bar may increase the effective length of the measurement from 1 cm to 1 m. Assuming the strain in the rock over this distance is uniform, the reference bar will amplify the displacement measurement by a factor of 100. This is equivalent to increasing the resolution by a factor of 100.

4.2 FIELD INSTRUMENTS

At least three classes of in situ instruments are available for measuring deformation of wellbores associated with pressure changes in aquifers or reservoirs. The different classes trade logistics for resolution. *Annular strain sensors* provide the most flexible logistics because they are mounted on the outside of casing so the wellbore is open and use is unaffected. The WIRE system developed by Baker Hughes is the currently the only available system for making this measurement, to our knowledge. *Portable strain instruments*, including extensometers, tiltmeters and strainmeters, are temporarily anchored to the inside of a wellbore. This will affect the logistics of well operation, but operations can continue during deployment and the instrument can be removed afterwards. The portable instruments can measure smaller deformations than embedded fiber sensors, but many hundreds of embedded fiber sensors can be used to provide high spatial resolution. The other class is *grouted strain meters*. These instruments were developed by the geodesy community and they are the most sensitive strain meters available. They are designed to be grouted into the bottom of a boring, so the bore can no longer be used for other purposes.

The objective of this chapter is to review the instruments available for measuring in situ deformation associated with fluid pressure change. We will consider embedded fiber sensors, portable instruments, and grouted strain meters. Most of the information in the chapter is based on published descriptions, but we also included material that has not yet been published. The information about WIRE is based on material recently presented. Portable instruments called 3DX and 5DX were developed for this project and they have not been described previously.

ANNULAR STRAIN SENSORS

4.2.1 WIRE

The WIRE system was developed by a team led by Roger Duncan at Baker Hughes, the industry partner on this project. WIRE has been under development for nearly a decade and has recently matured to commercial field testing.

The WIRE system has yet to be described in published form, but public presentations about the technology have been given. The following images and description are based on a presentation by Roger Duncan from the winter of 2015.

Principle

The WIRE system uses optical fibers with Bragg gratings to measure strain in the direction of the fiber. It departs from the typical use of Bragg gratings as strain gauges, which relies on the gauges to reflect light at a wavelength that depends on the strain. Instead, WIRE measures the interference between reflections from different Bragg gratings. Many pairs of gratings can be used, with the resulting signal multiplexed into many discrete measurement points. This allows the system to measure more locations along a single fiber and potentially with higher resolution than the conventional Bragg grating approach.

Another innovation in the WIRE system is the helical wrapping of optical fibers around a core. This causes the measurements to have axial and circumferential components, instead of the axial-only measurement from a standard fiber. The spatial resolution of the measurements along the fiber can be sub-meter, so the multi-component displacement data can be processed to

determine the 3D trajectory of the fiber (Figure 4.2-1). Data from coils of the fiber can be analyzed to correctly show details of the shape (Figure 4.2-1).

WIRE is deployed on the outside of casing (Figure 4.2-2). The deployment involves securing the helically wrapped cable to casing using specialized locking collars (Figure 4.2-3). The collars protect the cable during deployment. The current embodiment of WIRE requires securing the cable to the outside of casing during completion of the well. After the casing is in place, the annular space is filled with cement, mechanically coupling the optical fiber cable to the casing and formation.

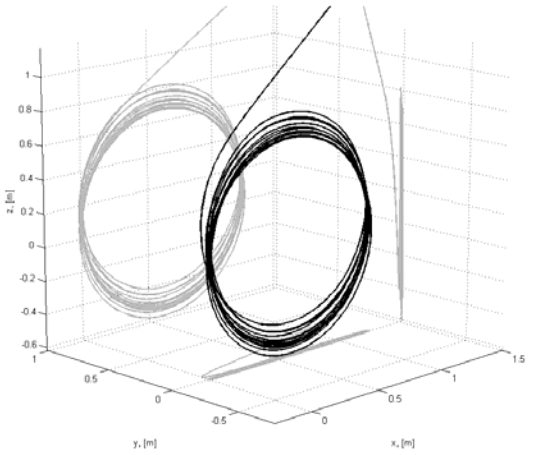

Figure 4.2-1. WIRE data used to reconstruct 3D trajectory.

Data from WIRE can be used to characterize a variety of shapes of casing deformation. Strain measurements are made with high enough spatial resolution to show patterns that indicate different styles of deformation. For example, periodic bending results in periodic variations in strain (Figure 4.2-4). A localized offset (dog leg), resulting from shear of the borehole for example, is characterized by fluctuations of high and low strain separated by a straight interval. Localized buckling can be distinguished from localized offset by periodic deformation between the characteristic end signals (Figure 4.2-4).

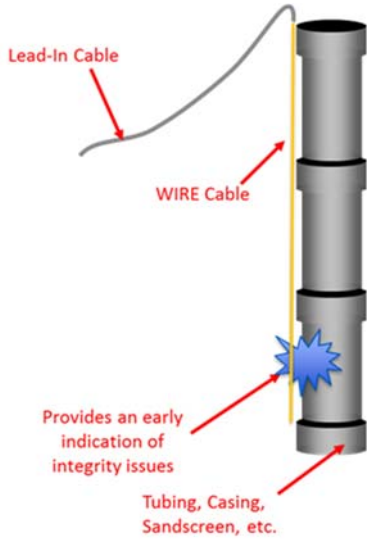

Figure 4.2-2. Conceptual application of the WIRE system deployed on the outside of casing. WIRE deployed with locking collars on the outside of casing.

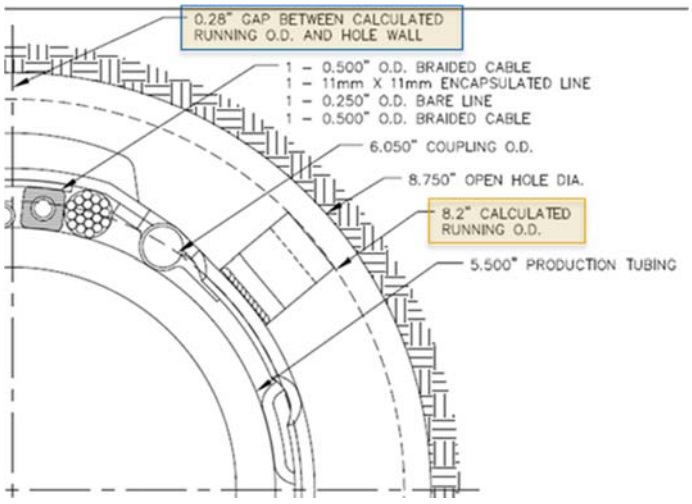

Figure 4.2-3. Axial view of WIRE on the outside of casing.

Performance

In the laboratory, the strain resolution is better than 1 με. For example, lab tests (Figure 4.2-5) show the displacement precision is approximately 0.25 mm over 350 m of cable, a precision of 0.7 με.

The WIRE system has been successfully demonstrated on a commercial basis at a handful of wells used for petroleum production. One of the first applications was at a well drilled into the Diatomite/Tulare formation in California. The well was drilled to approximately 1,500 feet and the WIRE system was deployed on the casing during completion (Figure 4.2-6). The Diatomite/Tulare formation is relatively shallow and soft, so it readily deforms during production.

At the Diatomite/Tulare well, the WIRE system showed that the compressive displacement over a 90-foot-long interval increased with time over a 5 month period, reaching maximum values of approximately 800 με (Figure 4.2-7). The time series of displacement shows that the overall strain rate is approximately 3E-11 s^{-1} over a representative, 90-foot-long interval (Figure 4.2-8). The strain is compressive in this case as a result of a net loss of fluid from the reservoir. The rate varies with time, however, apparently in response to reservoir activities. For example, the strain rate decreased at the end of the monitoring period. The rate of water injection into the formation increased from approximately 2,600 bbl/day to 3,000 bbl/day (Figure 4.2-8).

The WIRE system in the Diatomite/Tulare well includes hundreds of measurement points that are measured approximately every minute. This provides data that are highly resolved in space and time (Figure 4.2-9). For example, a compilation of the data shows the total strain increasing along the entire produced interval, with the maximum strain at a depth of approximately 1,475 feet (Figure 4.2-9).

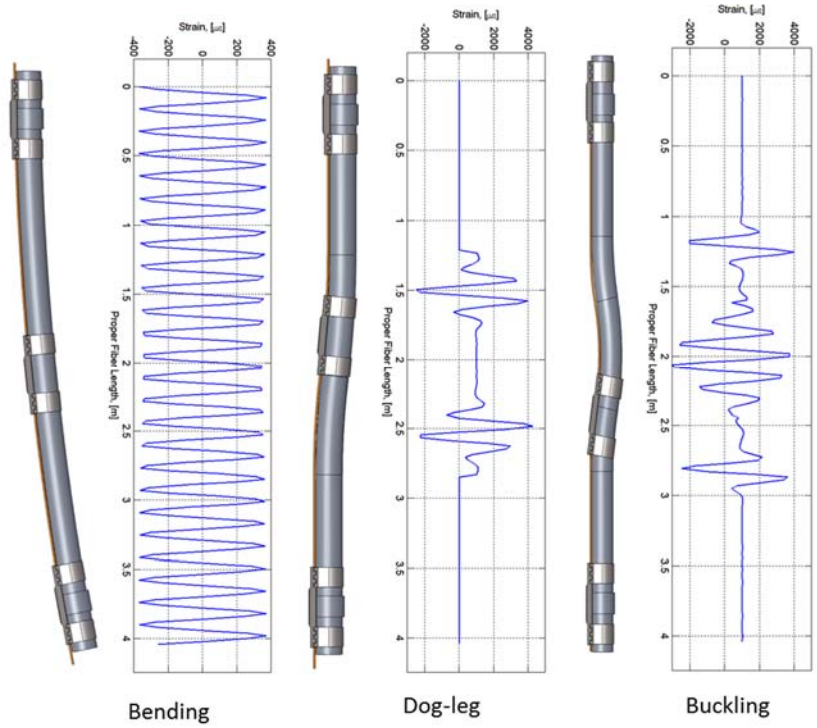

Figure 4.2-4. Patterns of strain distribution along casing.

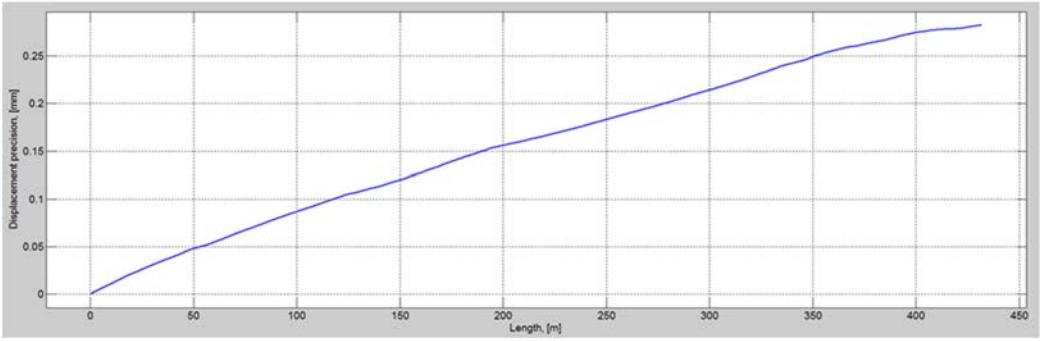

Figure 4.2-5. Displacement precision as function of distance along the fiber. Overall slope is approximately 0.7E-6.

Bending strains can be localized along the tops of produced intervals because this occurs because of the sharp strain gradient near the contact between a producing interval and an overlying confining unit. This effect is difficult to see in data that include the entire produced interval, but are readily apparent in a plot of data at a localized scale (less than 1 m) at the top of the formation (Figure 4.2-10).

Figure 4.2-6. WIRE cable being installed at a well in Diatomite/Tulare Formation.

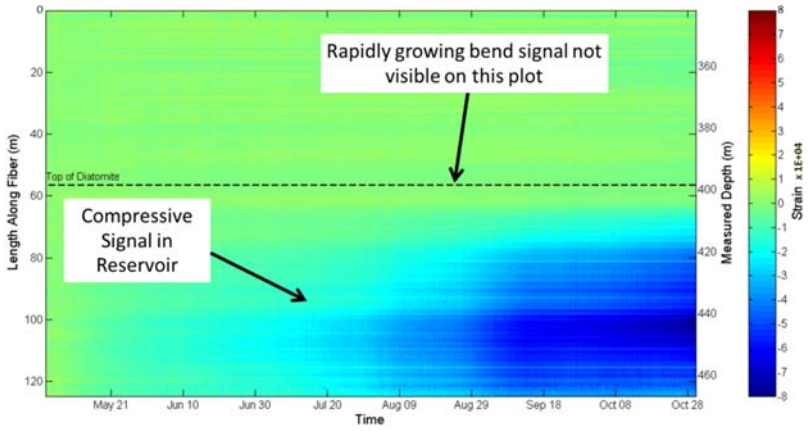

Figure 4.2-7. Strain as a function of location and time over approximately 160 days. Dark blue is a strain of 8E-4 (800 με).

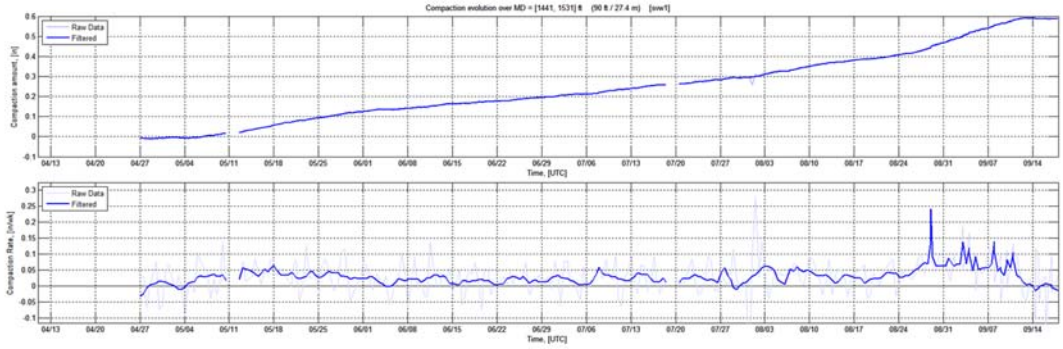

Figure 4.2-8. Axial deformation in inches along a 90 foot interval in Diatomite/Tulare formation as a function of time (upper plot). Deformation rate as function of time (lower plot). Average strain rate is 3E-11 s^{-1}. The decrease in rate during the last week occurs when the water injection rate was increased from approximately 2,600 bbl/day to 3,000 bbl/day.

The WIRE system has also been deployed at well in the overburden of a steam injection project. This application is particularly noteworthy because it shows the compressive strain that occurs in a confining unit as a result of injection, a process that closely resembles what is expected to occur during injection of CO_2.

Time series data from this application show that the compressive strain increases abruptly at the onset of injection. Total strains of several 10s of me occur during approximately 1 week of injection during these tests (Figure 4.2-11). The time series also shows small variations of approximately 1 mm with a period of 0.5 to 1 day. This corresponds to a strain of approximately 2 με. It is possible that this signal is instrument noise and represents the lower resolution of the instrument. However, signals with these periods are expected from barometric loading, temperature and Earth tides. If this is the case, then data correction schemes could be developed to remove this signal and improve the resolution to strains resulting from injection.

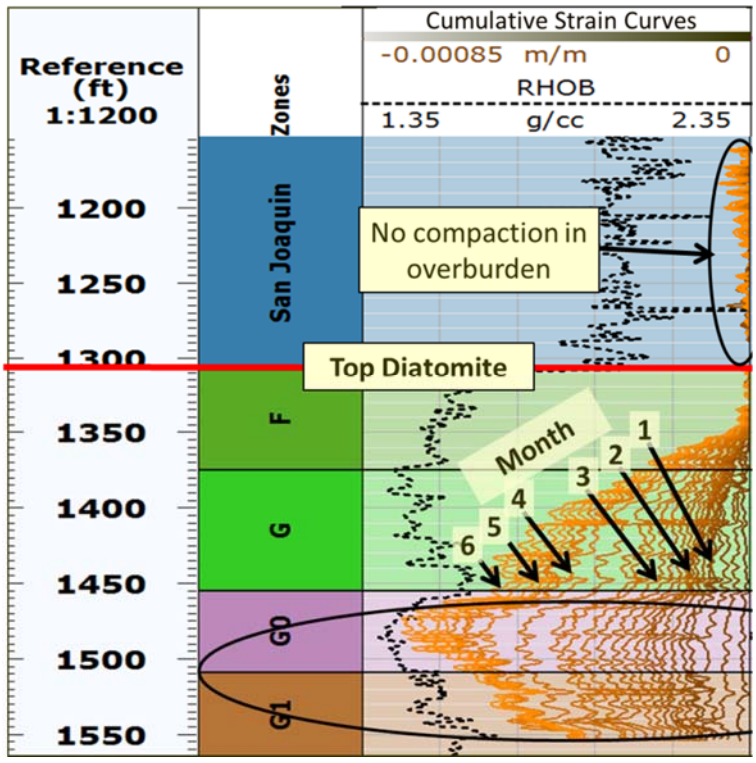

Figure 4.2-9. Strain as a function of location and time measured using WIRE in the Diatomite/Tulare Formation.

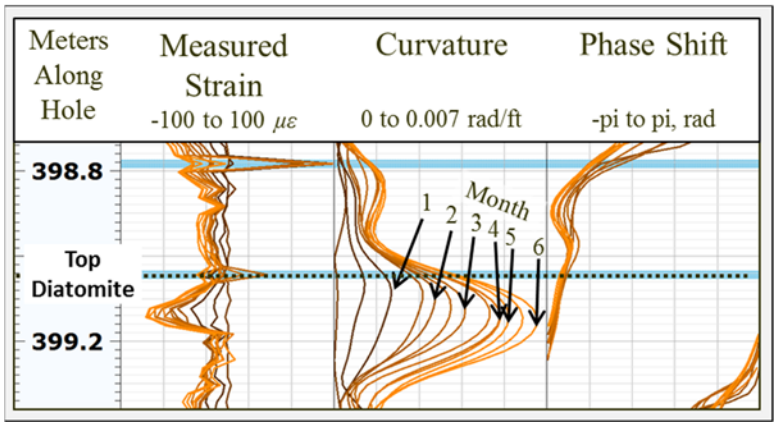

Figure 4.2-10. Strain, Curvature and Phase shift over a short interval at the top of Diatomite formation. This signal shows the increase in localized curvature resulting from production.

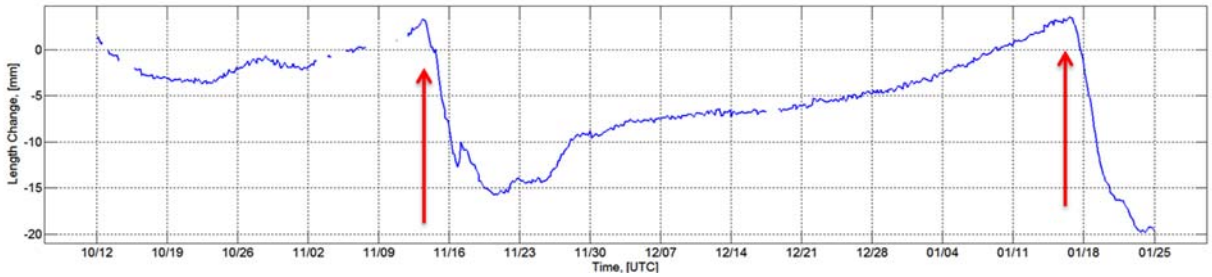

Figure 4.2-11. Displacement as a function of time over 432 m of observation in a confining unit overlying a steam injection project. Steam is injected twice (red arrows), resulting in displacements of 15-20 mm. The maximum displacement corresponds to 35 με.

PORTABLE STRAIN INSTRUMENTS

This class of instruments include extensometers, tiltmeters, and combination instruments. Early investigations of hydromechanical well tests used extensometers that measured displacement over the entire length of a well [*Riley*, 1961, 1969; *Lofgren*, 1961; *Davis et al.*, 1969; *Poland et al.*, 1979; *Pope and Burbey*, 2004]. These instrumented wells were typically completed in sedimentary aquifers and they measured deformations of both aquifers and confining units. These devices provide remarkable insights, but they span a long length and so they fall short of characterizing spatial distributions of hydromechanical response. They also require considerable effort to install in a dedicated well. More recent research has led to the development of portable, compact extensometers, which can be moved along a wellbore to characterize hydromechanical responses at many locations [*Gale*, 1975; *Hesler et al.*, 1990; *Martin et al.*, 1990; *Thompson and Kozak*, 1991; *Cappa et al.*, 2005, 2006, 2007; *Svenson et al.*, 2008; *Murdoch et al.*, 2009; *Schweisinger et al.*, 2011].

Portable extensometers

Portable extensometers used for well testing measure the change in distance between two anchors set along the borehole. The anchors are spaced 1 m to 2 m apart, providing displacement measurements averaged over that length scale. The anchors can be retracted and the device moved to create a profile of properties along a wellbore [*Svenson et al.*, 2008], or the device can be used to characterize known hydraulically active intervals in a borehole [*Cappa et al.*, 2005, 2007; *Schweisinger et al.*, 2011]. The development of portable extensometers has enabled hydromechanical well tests to be conducted with little more effort than typical straddle packer tests.

Portable extensometers have made it practical to measure displacements during well tests, but currently available devices have an important shortcoming: they are limited to measurements of displacement along the axis of a borehole (an exception briefly outlined by Guglielmi et al., 2009). This may be sufficient when characterizing the response of widely spaced fractures oriented normal to boreholes in tight rock where displacement measured by the extensometer can be assumed to be equal to the displacement of the fracture walls. This seems to be a reasonable assumption in some cases, but in cases where fractures are dipping, the axial displacement along a vertical borehole will underestimate the displacement normal to a fracture. Other types of heterogeneities may cause shear along the borehole that is not resolved by measurements of axial displacements.

Tiltmeters

Another approach to conducting a hydromechanical well test is to measure deformation with tiltmeters instead of extensometers. Tiltmeters are sensitive to shear displacements, where two reference points on the instrument move normal to the line between them. Tiltmeters have been used for hydrological applications, but according to Agnew (2003) they were initially developed to study Earth tides. Early tiltmeters were water-filled, horizontal pipes with precision sensors of the water surface at either end [*Agnew*, 2003]. These long-baseline tiltmeters are remarkably accurate, and refined designs continue to be used today for hydrologic studies and other applications [*Beavan and Bilham*, 1977; *Wyatt et al.*, 1982; *Klein*, 1984; *Agnew*, 1986; *Meertens et al.*, 1989; *Longuevergne et al.*, 2009; *Jacob et al.*, 2010]. The simplicity and high resolution of long baseline tiltmeters makes them attractive for applications in settings where the necessary horizontal access is available (e.g. mines, caves, or similar), but their size and geometry make them cumbersome to deploy for well testing applications.

Tiltmeters using high precision electrolytic bubble sensors developed in compact containers [*Agnew*, 1986] are readily deployed in boreholes. Recent refinements [*Castillo et al.*, 1997; *Hunter*, 2002] have achieved resolution to roughly 10^{-8} rad, which is sufficient to detect deformations associated with changes in pressure during pumping in aquifers or reservoirs [*Fabian and Kumpel*, 2003; *Fabian*, 2004]. Borehole tiltmeters at depths of less than 50 m have been used to determine deformation caused by aquifer well testing [*Vasco et al.*, 1998; *Karasaki et al.*, 2000; *Vasco et al.*, 2002; *Weise et al.*, 1999; *Fabian and Kumpel*, 2003; *Fabian*, 2004] and earth tides [*Wyatt and Berger*, 1980; *Wyatt et al.*, 1982; *Levine et al.*, 1989; *Kohl and Levine*, 1995; *Meertens et al.*, 1989].

High resolution borehole tiltmeters are a standard tool in the petroleum industry, where they are deployed to monitoring hydraulic fracturing [*Davis et al.*, 2000], and secondary and tertiary recovery operations [*Dusseault et al.*, 1993]. Analyses have been developed to interpret tiltmeter measurements and estimate characteristics of hydraulic fractures [*Pollard and Holzhausen*, 1979; *Evans et al.*, 1982; *Davis*, 1983; *Evans and Holzhausen*, 1983; *Holzhausen et al.*, 1985; *Castillo et al.*, 1997, *Warpinski et al.*, 1997]; the distribution of hydrocarbon recovery [*Dusseault et al.*, 1993; *Vasco and Karasaki*, 2001, *Vasco et al.*, 2002], steam distribution [*Holzhausen et al.*, 1985; *Du et al.*, 2005] and water injection [*Kumpel et al.*, 1996; *Vasco et al.*, 1998; *Fabian and Kumpel*, 2003; *Jahr et al.*, 2006]. The many applications in the petroleum and geothermal energy extraction [*Vasco et al.*, 1998, 2000, 2002] highlight the potential that tiltmeters have for understanding changes in fluid distribution, even though Lecampion et al. (2005) point out that tiltmeter interpretations applied to hydraulic fractures are vulnerable to non-uniqueness.

Despite their potential applications, the use of borehole tiltmeters to study aquifers has been limited to a handful of investigations. Most recent applications have used the LILY borehole tiltmeter by Applied Geomechanics, which is housed in a meter-long cylinder. The device is lowered into a dedicated boring, the annulus is packed with sand and then allowed to equilibrate. This provides a stable coupling between the borehole and the formation, but it is commonly deployed in shallow boreholes where temperature fluctuations can cause spurious signals requires dedicated borings [*Haneberg and Friesen*, 1995; *Sleeman et al.*, 2000; *Fabian and Kumpel*, 2003]. Some designs [*Levine et al.*, 1989; *Kohl and Levine*, 1993] make use of mechanical coupling between the tiltmeter and the borehole. This design allows tiltmeters to be installed deep enough to avoid significant thermal fluctuations, which improves accuracy. Those

applications were intended for geodetic applications (e.g. Levine et al., 1989), so the tiltmeter was rested on the bottom of the borehole, which would limit applications during well testing where measurements from multiple depths would be ideal.

4.2.2 TILT-X

Tiltmeter measurements compliment data from extensometers. Both of devices respond to displacement, but they measure different components. Mounted in a vertical boring, an extensometer is sensitive to vertical normal strain, *dw/dz*, whereas a biaxial borehole tiltmeter responds primarily to displacement gradients *du*/*dz* and *dv*/*dz*, [*Wang and Kumpel*, 2003] where *u, v, w* are displacements in the *x*, *y* and *z* directions, respectively, and *z* is assumed to be vertical. Integrating between two anchors allows three orthogonal displacements to be resolved.

Inversion of tilt [*LeCampion et al.*, 2005] and axial deformation [*Svenson et al.*, 2008; *Schweisinger et al.*, 2011] alone can produce non-unique interpretations, but combining these signals can reduce this ambiguity. Consider as an example the characterization of a dipping fracture. The axial displacement during a pumping test is a function of both the normal displacement across the fracture walls, and the dip of the fracture. The measured axial displacement will decrease as the dip of a fracture increases, so a dipping compliant fracture would be indistinguishable from a flat-lying stiff fracture. However, pressure change in the dipping fracture would induce horizontal shear, which would cause tilting in the up-dip direction during pumping [*Burbey et al.*, 2011]. Resolving displacements in 3-D using a tiltmeter and extensometer would presumably allow both the compliance and the orientation of a dipping fracture to be characterized.

The complementary nature of extensometer and tilt data has motivated the development of an instrument capable of measuring both signals. Additional motivation has come from the need for a portable device that can be remotely anchored to facilitate the deployment of tiltmeters during pumping tests in aquifers. The device is called, *Tilt-X,* which is short for *Tiltmeter Extensometer*. Tilt-X was described by Hisz et al. (2013), and the following description is based on that paper and related work.

Design

The Tilt-X consists of two anchors separated by rods (Figure 4.2-12) [*Hisz*, 2013]. The basic design of the anchors follows from concepts introduced by Schweisinger et al. (2007), where a bar pushes the body of the device up against the borehole wall. Fixing the device to one side of the borehole minimizes cavity effects induced by distortion of the borehole [*Levine et al.*, 1989]. The tiltmeter is fixed between two connecting rods and forms the body of the Tilt-X, whereas the extensometer makes use of a third connecting rod between the anchor bars. The connecting rods are made from invar, an iron-nickel alloy with a low coefficient of thermal expansion of 1.18 x 10^{-6} cm/cm/°C

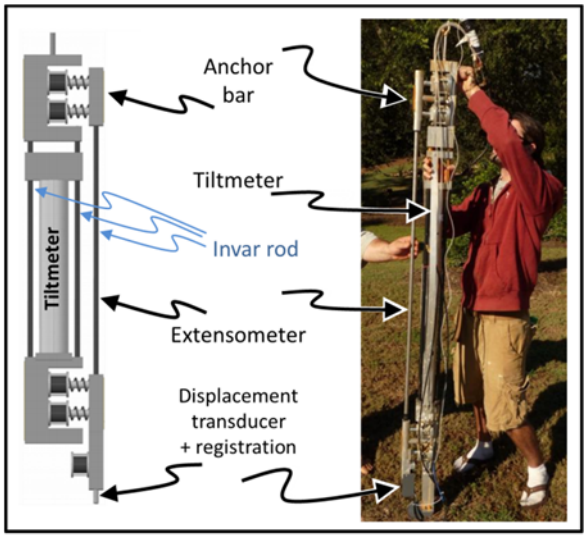

Figure 4.2-12. Major components of Tilt-X.

(Eagle Alloys Corporation, 2012), so they create a frame that is relatively insensitive to temperature variations.

Anchors

The anchors consist of a frame with two pneumatic cylinders and a spring attached to a bar (Figure 4.2-12) [*Hisz*, 2013]. Coarse carbide abrasive strips (1.2 cm by 15 cm) were fixed to outer edges of the anchors where the bar and the frame contact the borehole wall. The system behaves like a single-acting cylinder, with the spring pushing outward and the cylinders retracting the bar. The cylinders have a throw of 3.75cm, and the span of the anchor ranges from 13.0 cm when fully retracted to 16.2 cm when fully extended. This set of anchors was designed for a 15-cm-diameter borehole, so they have ample clearance when retracted and can extend outward to grip regions of the borehole that are slightly enlarged.

The anchors use an epoxy-coated spring, which created a force of 450 N (~100 lbs) when the span on the anchor is 16.2 cm, and 730 N when the anchor bar was fully retracted. The air cylinders were 5 cm in diameter and the pair of anchors create enough force to retract the spring when they are energized with 0.25 MPa of pressure.

The cylinders were pressurized to retract the anchors so the tool could be moved in the borehole. Reducing the air pressure in the cylinder caused the spring to extend the anchor bar and press it and the opposing frame against the borehole wall. The carbide abrasive strips on the bar and frame were pushed against the borehole wall by the spring with a force of 500-700 N, which holds the device in place.

Extensometer

The extensometer measures the movement of one anchor relative to the other in a direction parallel to the axis of the borehole [*Hisz et al.*, 2013]. A reference rod is attached to the upper bar and spans the 1.1m length of the device and extends through the lower bar (Figure 4.2-12). A displacement transducer measures the change in position of the end of the reference rod relative to the lower bar, and in doing so it measures the change in the distance between the anchors.

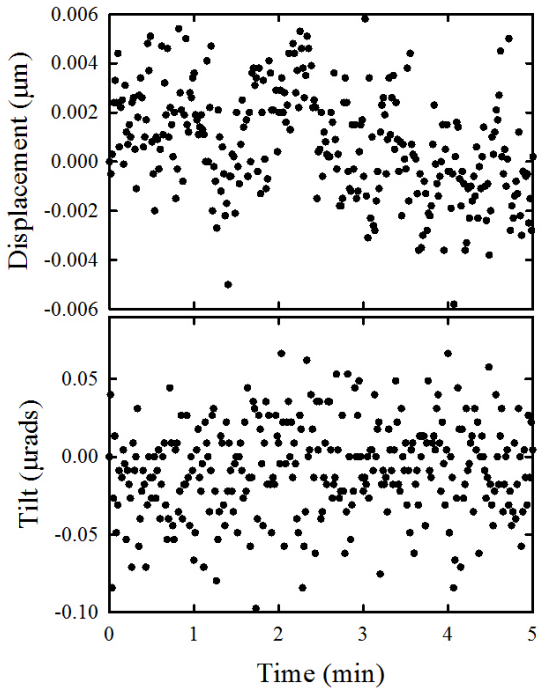

Figure 4.2-13. Displacement and tilt as functions of time during 5 minutes of sampling with no applied displacement. Based on Hisz et al. 2013.

DISPLACEMENT SENSOR

The design target was for displacement measurements to have a resolution of $\pm 10^{-8}$ m. Relatively stiff rock with an elastic modulus of 10^{10} Pa and a Biot-Willis coefficient of 0.1 [*Wang*, 2000] is expected to be strained by 10^{-8} in response to a pressure change of 10^3 Pa (0.1 m of head change). Most well tests would involve a pressure change of at least 10^4 Pa, which should create a strain of 10^{-7}. The gauge length of the device is 1.1 m, so 10^{-8} m

resolution should provide a measureable signal from many well tests in many rock types.

The required resolution was achieved with a Differential Variable Reluctance Transformer (DVRT; MicroStrain Model NANO-G-DVRT-0.5). This device (Figure 4.2-12) has a measurement range of $5x10^{-4}$ m and a manufacturer specified resolution of +/- 10^{-8} m.

Field tests demonstrate a RMS noise of approximately +/- 1.4 x 10^{-9} m (1.4 nm) over 5 minutes at 1 Hz using the system outlined above in a well.

EXTENSOMETER COMPLIANCE

The compliance of the extensometer itself is the distance the anchors move in response to a unit axial force. High compliance ensures that the anchors move with the rock, whereas a low compliance or stiff extensometer could create enough force to cause the anchors to move relative to the rock. Previous designs [*Schweisinger et al.*, 2007] used anchors that were uncoupled from each other to create high compliance, but the Tilt-X design required attaching the anchors to a stiff frame for mounting the tiltmeter and this will reduce the compliance. The compliance of the extensometer was determined by supporting the device in a vertical position by the top anchor, placing weights on the bar of the bottom anchor and measuring the displacement with the DVRT. This gives a compliance of approximately $1x10^{-6}$ m/N (+/- $0.05x10^{-6}$ m/N). This implies that the force generated on the anchors during displacements of 1 micron is approximately 1N.

The stability of the anchors themselves could be affected by either internal shear of the anchors or slip along the interface between the anchors and the rock. The anchor bar is a block of aluminum with a cross-section of approximately 2.7 cm x 21.6 cm, and the force created by the compliance of the system could cause shear within the bar [*Hisz et al.*, 2013]. The displacement caused by an axial force on the anchors due to shear of the anchors is:

$$v_s = \frac{FL}{AG} \tag{4.2-1}$$

where F is an applied axial force, L is the half thickness of the anchor bar (~1 cm), A is the longitudinal cross-sectional area (58 cm^2) and G is the shear modulus of aluminum (~25 GPa). Assuming the axial force exerted by the extensometer is 10 N (this force would accompany a displacement of 10 µm, which is relatively large for well testing applications) gives a displacement of $8x10^{-10}$ m. This is less than the resolution of the sensor, so it will be ignored.

It is possible that the anchor could slip along the borehole wall as a result of the force created by the compliance of the extensometer. The force required to cause the anchors to slip is:

$$F_y = CF_N \tag{4.2-2}$$

where F_N is the normal force and C is the coefficient of static friction between the anchor and the borehole wall.

The contact surface of the anchors is a sharp, coarse-grained carbide abrasive, which is harder than nearly any rock. The coefficient for the carbide abrasive and rock exposed in a borehole wall was not measured, but it is assumed to be approximately unity. The normal force generated by the anchors is greater than 450 N, and this is more than 40 times larger than the maximum expected force created by the compliance of the extensometer.

Even though the compliance of the Tilt-X is greater than that for earlier designs, it appears that the spurious displacement caused by compliance-induced forces on the instrument can be ignored.

REGISTRATION

One of the consequences of using a high-resolution sensor, like the DVRT, is that it measures displacement over a small span. The relatively high compliance of the extensometer can allow displacements to occur during deployment that exceed the span of the sensor. The system must then be registered so the sensor is roughly in the middle of its measurement scale prior to testing. To avoid the sensor going off scale and becoming non-functional, the Tilt-X design included a registration system.

The registration system on the Tilt-X includes a conical hole drilled in the side of the reference rod. A rod with a matching conical point is attached to a pneumatic cylinder mounted on the anchor bar. Extending the cylinder forces the conical point into the hole on the reference rod, and this moves the rod until it is centered under the point. The sensor can be registered to within ~10 microns in the field using this system [*Hisz et al.*, 2013].

Tiltmeter

The Tilt-X uses a bi-axial electrolytic tiltmeter manufactured by Applied Geomechanics Inc. (http://www.carboceramics.com/appliedgeomechanics/) under the model name "LILY Self-leveling Borehole Tiltmeter." The device uses sensors made from glass tubes, much like a carpenter's level. The tubes contain wires that are used to detect the location of a gas bubble, and tilt is characterized by a change in the position of the gas bubble. Electronics included with the sensors allow the position of the bubble to be resolved with remarkable accuracy.

Two tilt sensors and an electronic compass are included in the tiltmeter. The sensors are oriented at right angles and measure tilts in orthogonal directions. The compass allows those directions to be oriented to magnetic north.

Each sensor can measure tilt over a range of ±330 microradians. The RMS noise is $3x10^{-8}$ rad for a 5-minute-long signal sampled at 1 Hz when deployed in the subsurface (Figure 4.2-13).

Registration is important for the tiltmeter, just as it is for the extensometer. Servo motors rotate the sensors through an arc of 10° and software controls the motors to automatically position the sensors at an initial level.

A cable allows two-way communication with the device. Commands can be sent to level the device, or start or stop data transmission, and set sampling rates. During operation, the device sends digital output (RS422 protocol) describing tilt in two directions, orientation with respect to magnetic north, and temperature at a frequency up to 1 Hz.

The tiltmeter is sealed within a tube 51 mm in diameter and 0.9 m long, which is mounted between the invar rods on the Tilt-X frame (Figure 4.2-12).

Field Testing

The field site used to test the Tilt-X is a well field within the South Carolina Botanical Gardens in Clemson, South Carolina (Figure 4.2-14). The regional geology consists of highly deformed, high-grade metamorphic rocks of the inner Piedmont physiographic province [*Nelson*

et al., 1998]. The study site is underlain by medium-grained biotite gneiss with strong foliation that strikes northeast and dips between 40 and 80 degrees to the southeast [*Svenson*, 2006]. The rock is composed predominantly of quartz, plagioclase, and biotite with lesser amounts of hornblende, epidote, garnet, and chlorite.

Three of the wells (LAR-2, LAR-3, and LAR-4) are 60 m deep, and another one, LAR-1, is 120 m deep. The wells are cased through approximately 21 m of regolith, and they are open bores 15-cm in diameter below the casing. The wells are laid out in an L-shaped pattern, with 3 wells along a line trending 310 and another one perpendicular to the line (Figure 4.2-14) [*Hisz et al.*, 2013]. They are spaced approximately 5 m apart.

The density of visible fractures is 3 to 4 m^{-1} below the casing it decreases with depth and is 0.1 to 0.4 m^{-1} below 50 m. There are three significant zones of fractures that transmit water through the gneiss [*Svenson et al.*, 2008]. The shallowest one is a meter or two below the casing in LAR-3 and LAR-4 at a depth of ≈25 m. It is intersected by those two wells, but is absent in the other two wells. Two other permeable zones are intersected by all four wells and occur at depths of approximately 35 m and 50 m. The zone at ~35 m consists of multiple fractures over an interval roughly 2 m thick, whereas the zone at ~50 m is a single permeable fracture.

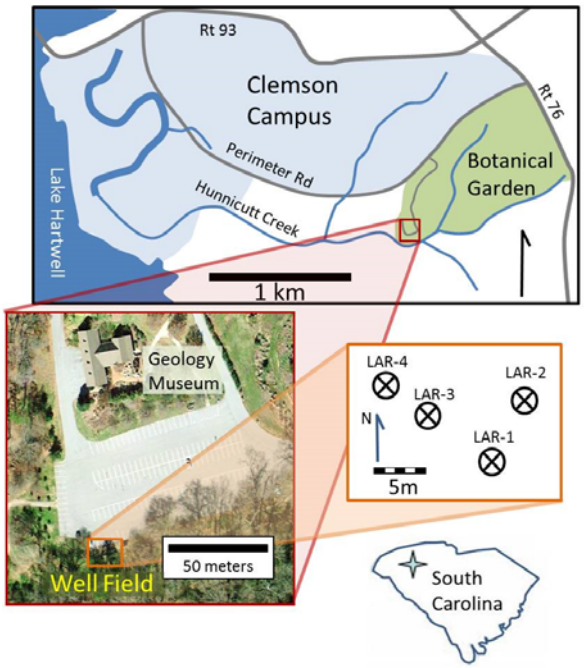

Figure 4.2-14. Location of the field testing. Measurements made in LAR-4. Pumping in LAR-3.

Method

Evaluation of the Tilt-X was done by monitoring signals during ambient conditions, and during several constant rate pumping tests. The ambient test was conducted by anchoring the Tilt-X at a depth of 25.9 m in LAR-4 and monitoring the signals for 7 days, from 3/14/2012 to 3/22/2012. The Tilt-X was anchored across the shallowest fracture zone, which is known to be intersected by 3 wells at the site. No packers were used during the test, and the well was open to the atmosphere.

Pumping tests were conducted using methods similar to those described by Schweisinger et al. (2011). The Tilt-X was anchored at a particular depth and allowed to equilibrate for at least 12 hrs. Both the tilt and displacements varied after the Tilt-X was anchored, but the rate of variation decreased with time and reached background values within several hours. The well was then pumped at constant rate for 4 hours (longer than the tests described by Schweisinger et al. 2011), and then allowed to recover for 20 hours. Each test was conducted at least twice. The Tilt-X was moved after a suite of tests was completed at a particular depth, and then allowed to re-equilibrate before another suite of pumping tests was started.

Field Results

The results show that ambient signals fluctuate with diurnal and semi-diurnal periods (Figure 4.2-15). Barometric pressure fluctuated with a diurnal period on most days, although there are extra peaks on days 3 and 6. The typical daily variation in barometric pressure is 300 to 400 Pa.

Water Level

Measurements of water-pressure head decreased in a long-term trend of approximately -6 mm/day and varied over approximately 2 cm with a diurnal period (Figure 4.2-15b). The long-term trend is the result of seasonal fluctuations. The well is open, so the changes in pressure head reflect changes in water level in the well. Maximum water-pressure head typically occurs in late afternoon, when the barometric pressure is lowest, and then it falls and reaches a minimum in early morning when barometric pressure peaks. This suggests that the fluctuations in water level in the well are due to changes in barometric pressure, a widely recognized effect [*Domenico and Schwartz*, 1998].

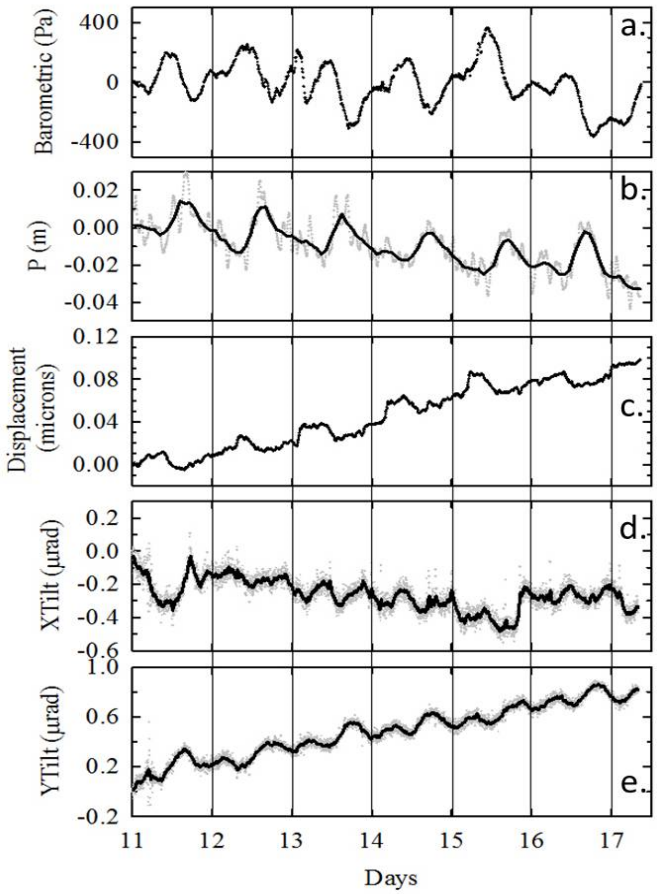

Figure 4.2-15. Time series of ambient measurements from Tilt-X anchored at 25.9 m from 3/14 to 3/21/2012 in a well completed in fractured gneiss near Clemson, SC. a.) barometric pressure; b.) water level (grey is raw data, black is smoothed); c.) axial displacement; d.) and e.) tilt in local X and Y directions (grey is raw data, black is smoothed). All data except the water levels and tilts is shown as obtained from the sensor without smoothing.

Displacement

The displacement includes a long-term trend with a diurnal variation (Figure 4.2-15c). The long-term trend is approximately 15 nm/day. There are periodic episodes where the fracture opens and closes over roughly 8 hours in the morning, and then it follows the long-term trend in the afternoon and evening (Figure 4.2-15c). The amplitude of the diurnal displacement is approximately 20 nm.

Tilt

The ambient tilt in both axes varies with a semi-diurnal period, with a maximum variation of approximately 0.1 µrad. Plotting the E-W and N-S tilt components forms a tight ellipse where the azimuth of the major axis goes between 340 and 160 daily. The tilt magnitude was decomposed with Fast Fourier Transform and the power spectrum contains peaks with periods of 12 hr and 24 hr, which are consistent with the O1, K1 and N2, M2 Earth tides [*Melchior*, 1964].

Pumping test

The pumping tests caused both displacement and tilt that were repeatable at each depth, but that varied when compared to tests at different depths. An example data set includes the drawdown following the typical pattern accompanying constant rate pumping followed by recovery (Figure 4.2.2-5) [*Theis*, 1935]. The displacements follow a generally similar pattern as the hydraulic heads, although the displacement lags the drawdown slightly, which is similar to the response observed by Schweisinger et al. (2011) in a neighboring well. The drawdown reaches a maximum of slightly more than 2m, and the fracture closes by slightly more than 3 microns.

The tilt signal accompanying the pressure head and displacement is the novel contribution of the Tilt-X, and the example test shows that the two components of the tilt vector follow patterns that are also similar to the drawdown (Figure 4.2-16). The signals increase sharply and then flatten with time, only to abruptly decrease during recovery.

The tilt vector can also be expressed by plotting the EW and NS components in map view (Figure 4.2-17). The results shows that the tilt vector reaches a magnitude of 35 µrad along an azimuth of 230 during one test and a magnitude of 30 µrad and azimuth of 245 during the next one (Figure 4.2-17).

The tiltmeter was moved and the test repeated at other depths. The azimuth of the tilts was remarkably consistent at the three depths, but the magnitude was greatest at the intermediate depth (35 m) and it decreased sharply to a few µrad at 50 m. Tilt magnitude decreased slightly to 25 µrad at shallower depths (25 m) (Figure 4.2-17).

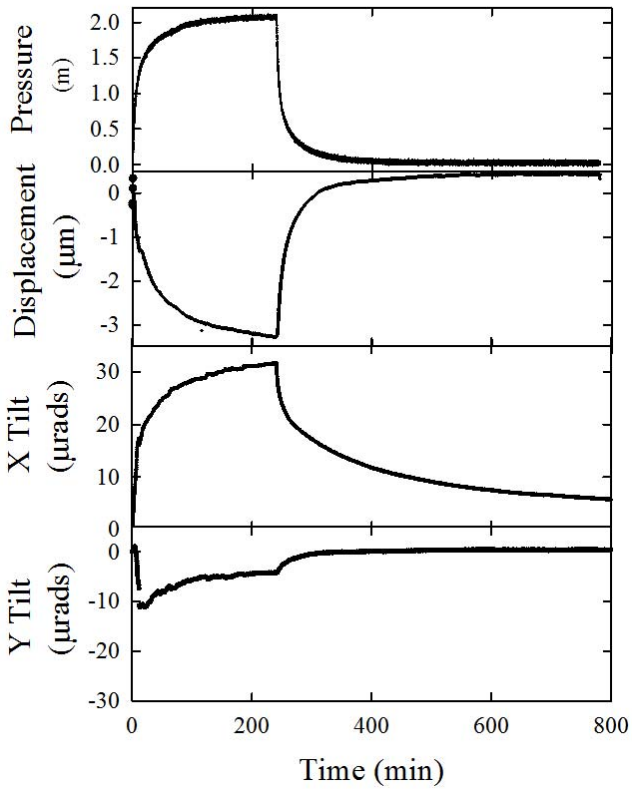

Figure 4.2-16. Data during pumping and recovery for a 4-hour-long pumping test. A.) drawdown b.) axial displacement; c.) and d.) tilt in local X and Y directions, respectively.

Discussion

The Tilt-X device generates data describing axial displacement and tilt of a borehole under both ambient or stressed conditions, and these data should have a variety of applications.

Sensitivity and Applications

Changes in loading at the ground surface will affect the fluid pressure and displacement at depth, and a good example of this is the effect of barometric pressure fluctuations (Figure 4.2-15). Hydrologic processes, such as changes in water content due to rainfall or evaporation, will also change the vertical load [*van der Kamp and Schmidt*, 1998] and may be detectable by the Tilt-X. For example, the sensitivity of the Tilt-X during both barometric loading and pumping is approximately 1 µm of displacement/m of

head change, or 10^{-9} m/Pa. The resolution of the Tilt-X is approximately 10^{-8} m at 1 Hz, which suggests that the device could resolve deformations that occur in response to load changes of 10 Pa. This is equivalent to 1 mm of water. Load changes of several tens of Pa are expected due to daily ET, and many rainstorms are greater than 1 mm of water. Averaging the 1 Hz Tilt-X signal to 0.01 Hz would increase the resolution by a factor of 10, while providing data every 100 s, which is a sufficiently short period to resolve many effects of hydrologic significance. Implementation of this approach would be facilitated by a packer in the casing that isolated the underlying wellbore from changes in barometric pressure.

Barometric effects on water levels in wells have long fascinated hydrologists [*Jacob*, 1940; *Clark*, 1967; *Weeks*, 1979], and Tilt-X will add the ability to collect another dataset describing the effects of barometric pressure on aquifers. The displacement caused by barometric pressure is consistent with the response of water levels. An increase in barometric pressure elevates the total head in the formation, but it increases the total head in the well even more [*Weeks*, 1979; *Furbish*, 1991; *Rasmussen and Crawford*, 1997; *Butler et al.*, 2011]. This change causes flow from the wellbore into the aquifer, which both lowers the water level and dilates the fractures causing the observed displacements.

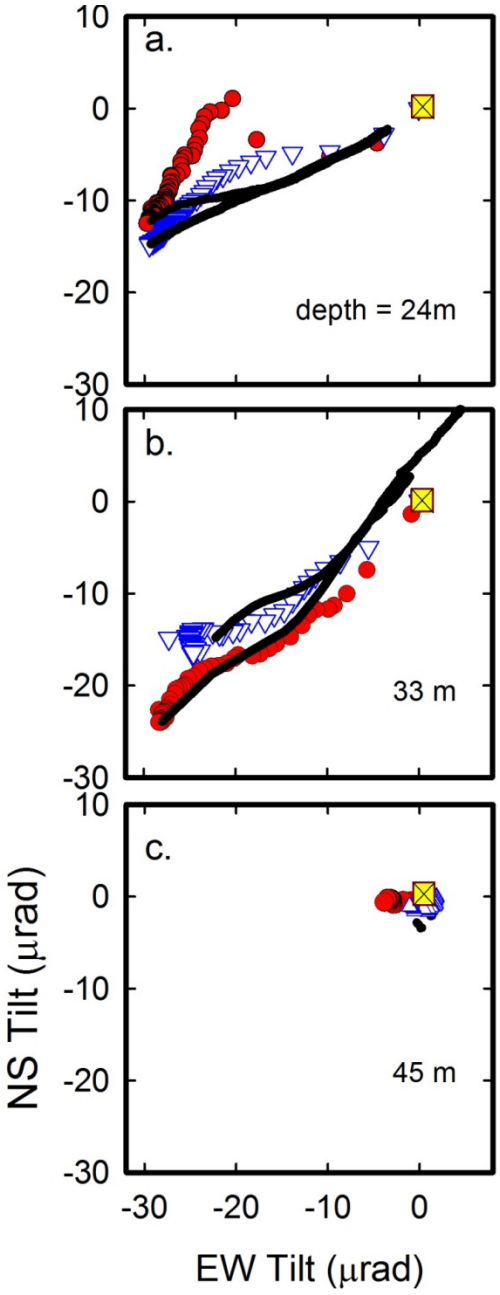

Figure 4.2-17. Tilt during pumping (points) and recovery (lines) during two tests (red circles or white triangle) at different depths. Yellow square with cross is start. Arrows show increasing time during pumping or recovery.

Changes in water level caused by barometric fluctuations have been used to estimate aquifer properties [*Jacob*, 1940; *Weeks*, 1979; *Rasmussen and Crawford*, 1997; *Spane*, 2002; *Burbey et al.*, 2011], and it appears that displacements may also be used in this way. For example, the hydraulic compliance estimated during pumping tests is 1.5 x10^{-9} to 4 x10^{-9} m of displacement/Pa of water pressure. The low value of compliance is the ratio of maximum displacement to maximum pressure change, whereas the high value is the late-time value of *dv*/*dp* [*Svenson et al.*, 2007; *Schweisinger et al.*, 2011]. For comparison, the compliance during ambient conditions appears to range from 1x10^{-9} m/Pa to 2.5x10^{-9} m/Pa. The low value is the ratio of maximum displacement to maximum change in water level in the well during diurnal barometric

fluctuations, whereas the higher value is the ratio of displacement to pressure for the long-term trend in the data.

Another extensometer with a different design was deployed in a nearby well when the dataset shown in Figure 4.2-16 was obtained. There was both a diurnal change and a long-term increase in the displacement measured by this second extensometer. This second instrument is important because it validates the Tilt-X data and it seems likely that the long-term increase in displacement in Figure 4.2-16 is occurring in the formation and is not a result of instrument drift.

The vertical aquifer compressibility, C_v, is the product of the hydraulic compliance and the spacing between the anchors. The data indicate that the vertical compressibility is $1x10^{-9}$ Pa^{-1} < C_v < $2.5x10^{-9}$ Pa^{-1}, or $1x10^{-5}$ m^{-1} < C_v < $2.5x10^{-5}$ m^{-1}. In most cases, specific storage is dominated by the aquifer compressibility, so it appears that the ambient measurements of displacement can be used to estimate specific storage.

Borehole tiltmeters are sensitive to hydrologic processes [*Ishii et al.*, 2001; *Agnew*, 1986; *Levine et al.*, 1989] and the tilt signal from Tilt-X could be used for hydrologic applications [*Jacob et al.*, 2010]. The device can readily resolve Earth tides, and many hydrologic signals are significantly greater than Earth tides. Tilt-X is straightforward to install in an open borehole, and this would facilitate temporary applications during campaign-style studies. Tilt is sensitive to heterogeneities in elastic properties [*Kohl and Levine*, 1993], so multiple measurements of tilt could be used to improve characterization of subsurface features.

One aspect that would be important for long-term applications is instrument drift, which may result from the tilt sensor itself [*Agnew*, 1986] or from the method of securing it to the rock. Instruments designed for long-term use are typically grouted permanently in place in an effort to create a stable connection to the rock [*Agnew*, 2007]. The mechanical anchors of the Tilt-X stabilize enough to be used for well testing applications in a few hours. Slow changes in tilt persist, however, it is possible that this is a result of drift caused by the instrument. Nonetheless, barometric pressure, water level, and displacement changed as systematic trends throughout the testing period (Figure 4.2-15), so it seems likely that the long-term trend in the tilt data is a result of the same effects causing those signals to change. We recognize that instrument drift will limit the Tilt-X during some long-term applications, but the results so far have been free from obvious spurious effects of instrument drift.

Well Tests

A portable tiltmeter and extensometer should improve evaluation of aquifer properties and the distribution of heterogeneities. The Tilt-X can resolve the background tilting from Earth tides and the periodic dilation and contraction due to barometric loading, and deformation induced by well testing is readily apparent above these background signals. Methods for interpreting measurements from extensometers are outlined in Cappa et al., (2005); Svenson et al., (2008); Murdoch et al., (2009); and Schweisinger et al., (2011), and similar methods could be used for the Tilt-X data. The resolution of the Tilt-X displacement data is more than 10x better than previous measurements made with a LVDT [*Schweisinger et al.*, 2009; *Svenson et al.*, 2008], and this is particularly important in settings where stiff rocks limit displacements.

Interpretation of the tiltmeter component is expected to follow the same approach as conventional well tests with a mix of conceptual, simple quantitative, and detailed numerical inversion methods. The data used to illustrate the Tilt-X performance (Figures 4.2-16 and 4.2-

17) serve as a good example of a conceptual interpretation. In this case, the tilt data are repeatable through three tests and the axial displacement data are similar to results from previous tests in that borehole [*Svenson et al.*, 2008; *Schweisinger et al.*, 2011]. The azimuth of tilt during the tests, 230 to 240, is surprising because the expectation is that tilting would occur on a radial path from the monitoring point to the pumping well (azimuth of 310°). This expectation is based on the basic configuration of tilting in the vicinity of a pumped well in a homogeneous aquifer. The analytical solution to this problem shows three primary zones based on the direction of tilt [*Urlaub and Fabian*, 2011]. Two lobe-shaped zones occur adjacent to the well screen. Tilt occurs toward the well from locations in the lower lobe and away from the well from locations in the upper one. This pattern occurs because radial pressure gradients cause inward radial movement of the aquifer material at the level of the well screen. The magnitude of displacement diminishes above and below the level of the screen, and this causes the different signs of tilt in the two lobes. A third zone occurs at shallow depths where tilting occurs toward the well.

One explanation for the non-radial tilt direction is that the direction is influenced by heterogeneities. It is possible that conductive fractures in the vicinity of the well are dipping, and the inclination causes a non-radial component of tilt. To evaluate this hypothesis, we conducted a numerical analysis of a dipping fracture zone embedded in a uniform tight porous matrix (Figure 4.2-18). The analysis assumes fully coupled poroelasticity [*Detournay and Cheng*, 1993; *Wang*, 2000]. A fracture zone is represented as a permeable layer with a dip of either 0 or 20° and nominal thickness of 0.1 m, and a well is represented as a vertical line sink pumping at $3x10^{-4}$ m^3/s at the fracture (Figure 4.2-18). The fracture intersects the well at a depth of 35 m. Material parameters are based on the expected scales at the field site and are given in Figure 4.2-19.

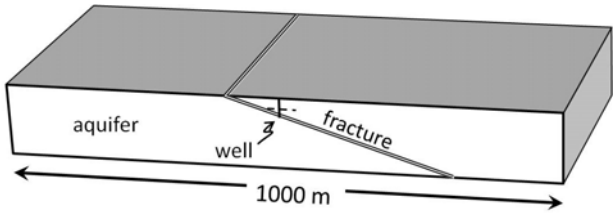

Figure 4.2-18. Geometry used in analysis of tilts in vicinity of a dipping fracture embedded in a homogeneous aquifer. Dashed line intersecting the well is the trace of the plane used to plot the tilt data.

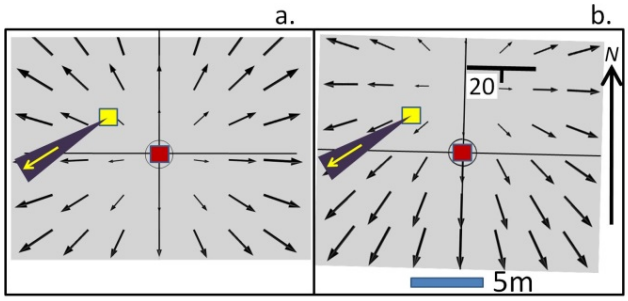

Figure 4.2-19. Tilt vectors (arrows) predicted at a depth of 25 m in the vicinity of the pumping well (red square). Observed azimuth of tilts (purple wedge and yellow arrow) at monitoring well (yellow square). a.) flat lying fracture. b.) fracture oriented as shown with strike and dip symbol. Predicted tilts are rotated to match orientation of observed tilts in b.

The results from the case with a flat-lying fracture show that tilt radiates away from the well at a depth of 25 m (Figure 4.2-19). This response resembles that for a uniform aquifer, and there is no configuration that matches the field data (Figure 4.2-19). However, a different pattern emerges when a dipping fracture is used. In this case, tilts at 25-m depth radiate from a point approximately 5 m up-dip from the well. This creates tilt vectors that form high angles with paths radiating from the pumping well (Figure 4.2-19).

The field data were overlain on top of the theoretical results and the overlay was rotated until the observed tilt direction matched the predicted one. The best match occurs for a fracture

that strikes approximately EW and dips to the south (Figure 4.2-19). This approach generates a unique strike and dip direction for the permeable zone affecting the vicinity of the well.

The significance of this interpretation is that it provides insight about the possible orientation of the fracture system that could not otherwise be obtained during a well test. More elaborate interpretation could be done using numerical techniques, but a simple qualitative interpretation of the tilts provides useful information. If this analysis was done during a site assessment program, for example, then the information about fracture orientation could be used to evaluate the locations of subsequent wells that would test the interpretation of fracture orientation. Numerical inversion techniques could refine the evaluation of the field data, and the dipping-fracture hypothesis appears to be a viable conceptual model for more detailed evaluation. Other conceptual models may also explain the observed data.

Conclusions

An instrument for measuring the axial displacement and tilt of a borehole during ambient conditions or during well tests, has been developed and demonstrated in the field. The Tilt-X instrument is roughly 1.5 m long and can be readily lowered into a well and fixed in place by remotely activating an anchoring system. It includes an axial extensometer with a resolution of 10^{-8} m and a bi-axial tiltmeter with a resolution of 10^{-8} rad. Both the extensometer and tiltmeter can be registered so their sensors are moved to the middle of the measurement span. The sensors typically equilibrate within several hours after being moved and registered, so it is practical to move the device and make measurements at multiple depths. The anchors are activated by springs, so they can be deployed without requiring power to hold them in place.

Field testing included measuring ambient tilts and displacements during several weeks in March in South Carolina, USA. This data set is characterized by displacements of roughly 0.02 μm with a diurnal period, which coincide with changes in water level and barometric pressure. Apparently the rock is deformed during barometric loading and the new device is able to characterize this process. We are unaware of previous direct measurements of displacements of rock associated with barometric fluctuations, although barometric effects on tilt are well known [*Agnew*, 1986; *Wyatt*, 1989].

The device was also demonstrated during pumping tests by deploying it at different depths in a monitoring well. Tilting occurs to the SW in the upper two locations and both the magnitude and direction of tilt are repeatable. Tilting deep in the well is roughly an order of magnitude less than it is at shallower depths. A theoretical analysis indicates that the observed tilting pattern can be explained by the occurrence of fracture zone at approximately 35m depth that strikes roughly EW and dips to the south.

This work demonstrates the feasibility of obtaining high resolution measurements of both axial displacements and tilts that are collocated in a borehole in a fractured rock aquifer. The Tilt-X device makes it possible to generate datasets describing transient deformations during ambient and stressed conditions in aquifers, which should lead to better interpretations of aquifer properties and structure.

4.2.3 MULTICOMPONENT STRAIN MEASUREMENT USING OPTICAL FIBERS, 3DX AND 5DX

During the course of our evaluation of technologies for measuring deformation of boreholes, it became apparent that the measurement of multiple components would be desirable to reduce uncertainty during inversion. Our experience with Tilt-X demonstrated that it was feasible to measure multiple strain components with a portable instrument, but it also highlighted a drawback in maintaining electrical sensors for extended periods down hole. While this was feasible, it required significant design and logistical consideration and it was clear that there would be advantages if these requirements could be reduced.

We evaluated the use of Fiber Bragg Gratings (FBGs) and it was clear that these sensors offered the potential for measuring strain without downhole electronics, but individual sensors were only capable of measuring a single component of strain. We were unaware of existing systems for measuring multiple strain components using optical fibers, but the project team developed some concepts for how this could be accomplished.

The objective of this section was to evaluate the feasibility of developing an instrument that could measure multiple components of strain using Fiber Bragg Gratings.

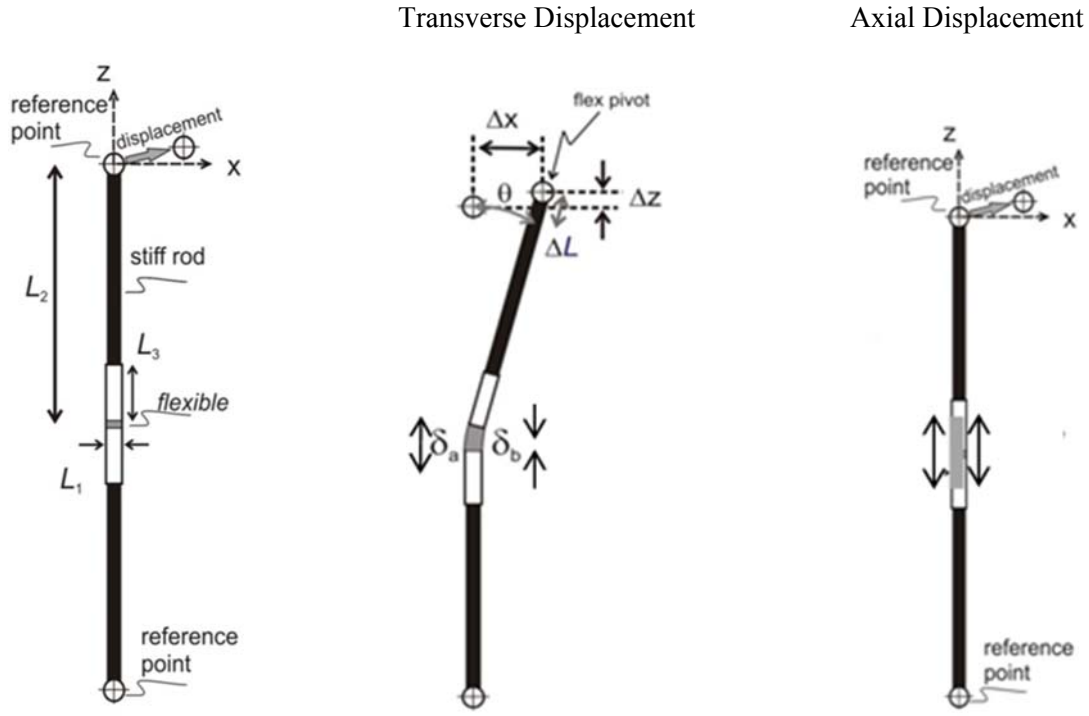

Figure 4.2-20: Conceptualization of how the two contact points on the device move relative to each other during 3D displacement.

Design

The design strategy for measuring displacement in three dimensions was to use two anchor points connected by a stiff rod with a specially designed flexure within the rod (Figure 4.2-20). The flexure can bend during transverse displacement, and it can extend or compress. When the two anchor points moved relative to each other, the displacement was concentrated

within the flexures. During axial displacement, the flexure compresses or extends when the anchors move relative to each other. When there is transverse displacement, one side of the flexure compresses while the other side extends (Figure 4.2-20). Three dimensional displacements can be determined by measuring the compressive or extensive displacement on each side of the flexure. Displacements of the flexures could be measured with FBGs.

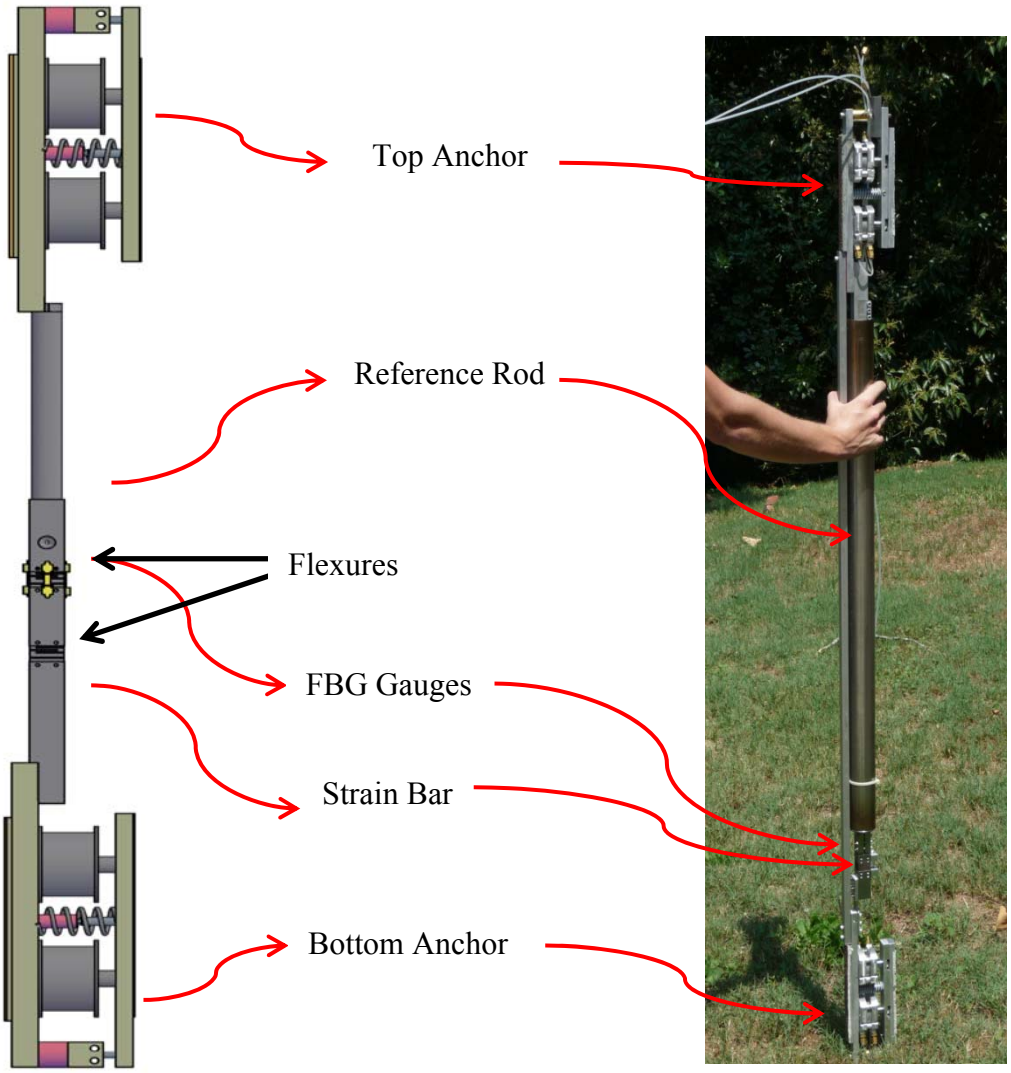

Figure 4.2-21: Conceptual diagram and an image of the 3DX.

The instrument used to implement this concept was developed in two stages. The initial development was done by instrumenting one set of flexures. This demonstrated proof-of-concept, but it also showed the potential for measuring addition degrees of freedom by instrumenting a second set of flexures. The drawing in Figure 4.2-21 shows both sets of flexures, but only one of them is monitored with FBGs. This was the first instrument we developed, and it was called 3DX because it could measure 3 normal displacements. The second instrument with FBGs on both flexures was called 5DX because it was designed to measure 3 normal displacements and 2 displacement gradients, or 5 degrees of freedom. Most of the effort involved developing and evaluating the 3DX, so it will be the focus of the following description.

The 3DX consists of seven main components (Fig. 4.2-21): 1.) two anchors that grip the borehole; 2.) a strain bar where displacement will be localized; 3.) a frame used to move the device; 4.) centralizers to locate the device in the center of the borehole; 5.) fiber optic sensors used to measure displacement; 6.) a reference rod between the anchors; 7.) and an interrogator used to process the fiber optic signals.

Fiber Bragg Grating Sensors

The sensor used to determine the strain uses a Fiber Bragg Grating (FBG), which consists of fine grooves etched into the circumference of the fiber and spaced a fixed distance apart. The evenly spaced grooves form a grating that acts as a wavelength-specific reflector. When light is injected into the fiber, the grating will either reflect or refract a specific wavelength defined by the spacing between the gratings and the effective refractive index of the grating in the optical fiber (Figure 4.2-22). Maximum reflectivity occurs at the *Bragg wavelength* [*Grattan and Sun*, 1999], which is given by:

$$\lambda_B = 2n_e\Delta \tag{4.2-3}$$

where n_e is the effective refractive index of the grating in the fiber core, Δ is the grating spacing. The change of the reflected Bragg wavelength is:

$$\Delta\lambda_B = \lambda_B\left(C_S\frac{\Delta L}{L} + C_T\Delta T\right) \tag{4.2-4}$$

where C_S is a strain calibration coefficient, L is the length of the sensor, and ΔL is displacement, C_T is a temperature coefficient, and ΔT is temperature change.

When the sensor extends, the spacing between the grating increases and the Bragg wavelength shifts towards a higher wavelength. The spacing between the etchings decreases when compression occurs, and the reflected wavelength decreases. The change in wavelength due to displacement is given by rearranging Eq. 4.2-4) [*Schmidt-Hattenberger et al.*, 2003].

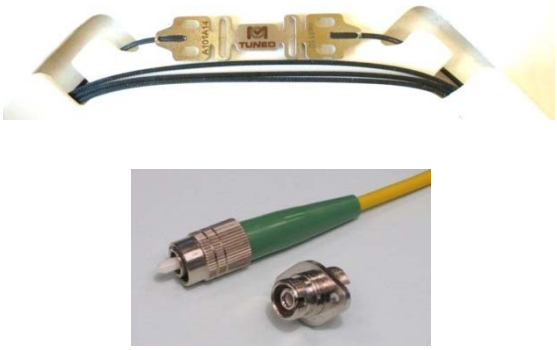

Figure 4.2-22: The top picture is the FBG sensor. The fiber optic cable is in the middle of the steel carrier which keeps the FBG etchings in tension. The bottom picture is the FP/APC connector and the adapter.

The strain gauges used in the device are thin stainless steel plates approximately 30 mm long, 10 mm wide and 1 mm thick. An optical fiber with a Fiber Bragg Grating strain gauge extends along the axis of the gauge and is the active component. Two holes give the stainless steel body of the gauge compliance. The gauges are manufactured by Micron Optics and sold under the product name os3100 (Figure 4.2-22). The gauges are packaged with a one meter-long strand of fiber optic cable extending from either side of the steel body with FC/APC connecters at the end of each fiber optic strand. The connectors allow multiple gauges to be attached in series. FC/APC connectors can be linked together with an adaptor. The maximum number of

gauges that can be connected to each other is limited by the number of Bragg wavelengths the interrogator can read on one channel.

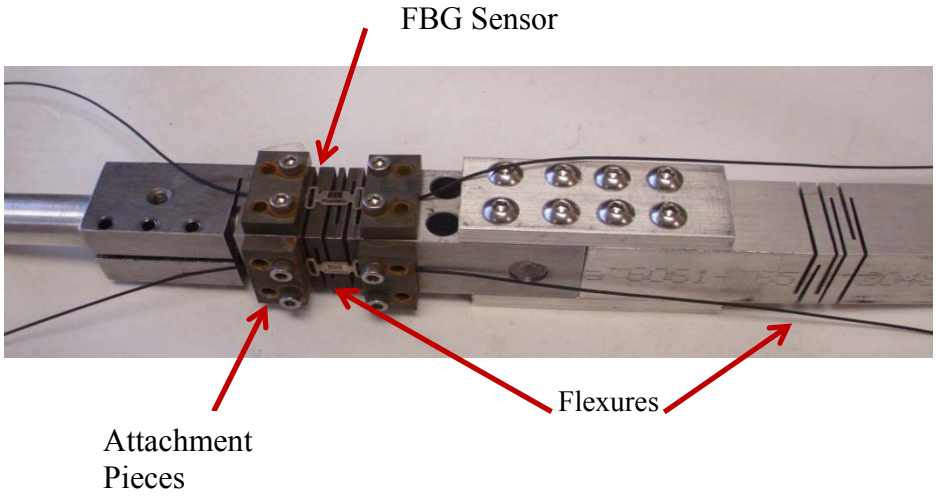

Figure 4.2-23: The strain bar used in the 3DX. The set of flexures on the left is where the gauges are secured by tightening the rectangular attachment pieces down holding the gauges in place.

Strain Bar

The strain bar is designed to accommodate two types of displacement; bending and extension. The strain bar is a 15.2 x 2.5 cm stainless steel bar with six, transverse parallel cuts that extend through approximately 80 percent of the thickness of the bar (Figure 4.2-23). Three cuts separate the bar into a pair of parallel plates joined to each other along one edge and to the bar along the other. The plates are approximately 3 mm thick and 2 cm long, and they act as flexures that are much more compliant than the bar itself. Axial or bending forces applied to the bar primarily cause displacement of the flexures. One set of cuts is arranged to create flexures that are joined along two opposing sides of the bar. These flexures allow bending about an axis normal to the axis of the bar and parallel to joined edge of the flexures (Figure 4.2-24). Another set of cuts creates flexures that allow bending in the orthogonal direction. Axial displacements can be accommodated at both sets of flexures.

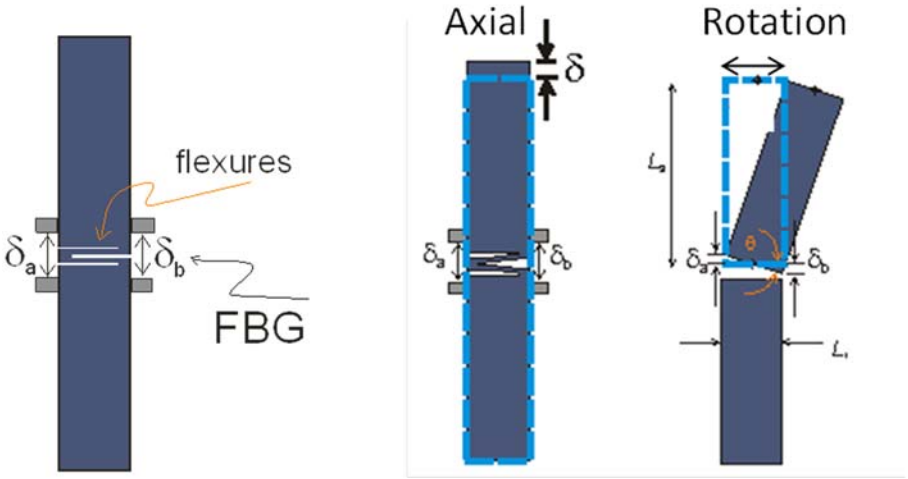

Figure 4.2-24: The conceptual model of how the strain bar moves during 3D deformation.

The strain gauges were placed axially along the strain bar to span the compliant interval containing the cuts. The gauges were clamped them onto the strain bar using two 6-32 bolts and a stainless steel plate. This was an important feature because it allowed the delicate strain gauges to be decoupled from the strain bar when the instrument was moved, and then secured in place prior to deployment in the field. It also allowed the gauges to be removed and replaced when they were damaged.

There are two strain bars attached to each other axially on the 3DX. Two strain bars are necessary to accomplish the range of motion needed. The strain bar rotates during transverse displacement and this would be impossible if there was only one set of flexures. When there is transverse displacement the flexures compress on one side and extend on the other causing rotation (Figure 4.2-24). The difference in displacement of the two opposing gauges gives the total transverse displacement of the strain bar with:

$$\delta_t = \frac{L_2}{L_1}(\delta_a - \delta_b) \tag{4.2-5}$$

where L_2 is the distance between the cuts and the end of the strain bar, L_1 is the width of the strain bar, and $\delta_{a,b}$ is the displacement of both gauges in line with the direction of displacement. The axial displacement is given by:

$$\delta_A = \frac{(\delta_a + \delta_b + \delta_c + \delta_d)}{4} \tag{4.2-6}$$

where the lower case subscript corresponds to each of four gauges.

Anchors

There are two anchors located at each end of the 3DX that are responsible for securing the instrument into the borehole and holding the frame in place during deployment. The features of the anchors are two air cylinders, a spring, frame clamp, spacers, and carbide friction strips (Figure 4.2-25). The top bar of the anchor retracts when the air cylinder is pressurized. When air is released from the air cylinders the center spring extends the top bar, and applies a force to the walls of the borehole (Figure 4.2-26). The carbide strips increase the friction between the wall of the borehole and anchor preventing the 3DX from slipping.

The frame clamping mechanism is composed of a hollowed brass cylinder connected to the bottom bar, and a steel rod attached to the top bar of the anchor. The brass cylinder is conical at the top. When the anchors retract the steel rod is driven through the brass cylinder reducing the distance between the top anchor and the brass cylinder (Figure 4.2-26). Thus, retracting the anchor disengages the extensometer from the wall and secures it to the frame so it can be moved safely.

The 3DX has the capability to be deployed in a wide range of borehole diameters. The top bar, where the carbide strips are attached, can be removed and spacers can be inserted between the sections. It also has interchangeable carbide pieces with different widths. Currently it has been deployed in holes ranging in diameter from 9 to 15 cm.

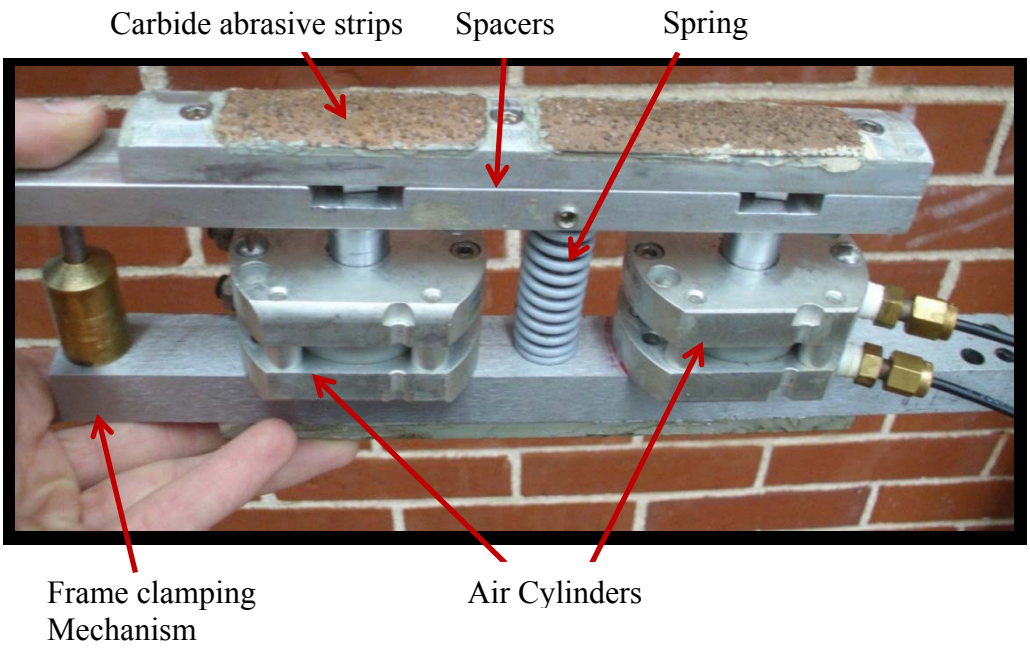

Figure 4.2-25. An anchor used in the 3DX. The air cylinders retract the anchor and the spring extends it. Sharp carbide abrasive strips increase friction on the wall of the borehole.

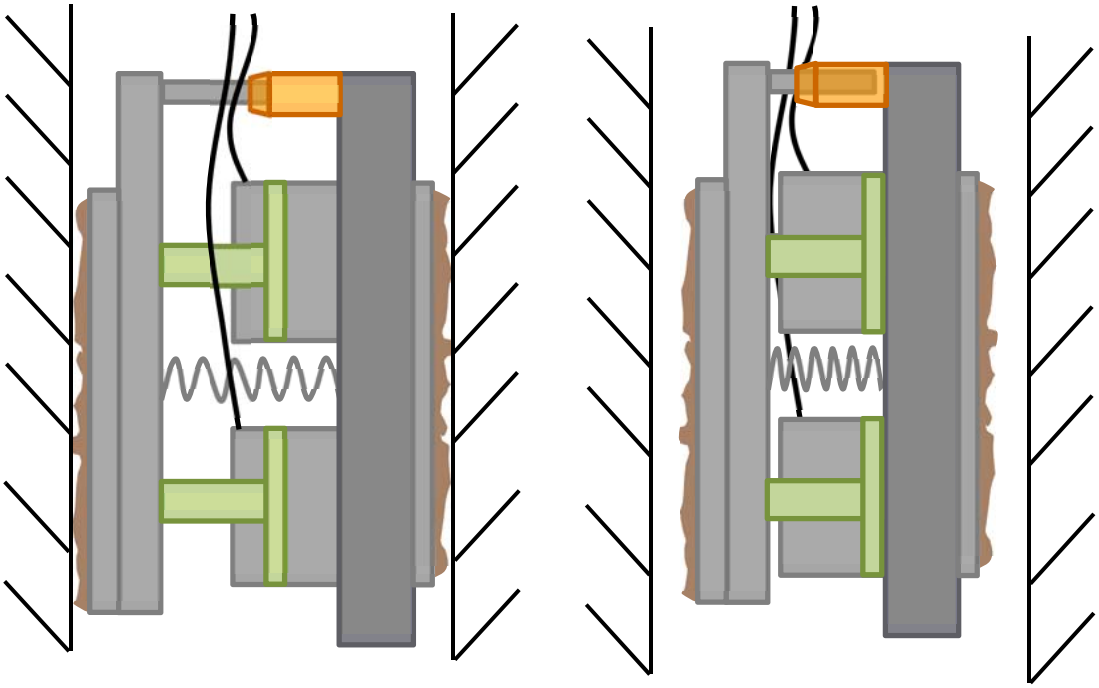

Figure 4.2-26. Idealized diagram of the 3DX anchor. The spring extends the anchor and applies a force to the borehole walls. Pressurizing the cylinders retracts the anchors and clamps it to the frame (not shown).

Interrogator

The interrogator is the signal processing instrument used to send a broadband light source through the fiber optic cable, and then detect the wavelength reflected by the FBG. The Micron Optics FBG gauges have been used with three different interrogators during this work: Micron Optics sm125, FOS&S Spectraleye version 3.0.25, and Anritsu AR4011A. The Spectraleye and Anritsu interrogators were used during the tests in Japan, and the Micron Optics device was used during tests in Clemson, SC. Interrogators have different specifications (i.e. size, scan frequency, number of optical channels, wavelength range, etc.), so tests can be optimized based on the benefits of the different interrogators.

The Micron Optics sm125 has a maximum scan frequency of 2 Hz. The device has 4 channels and each channel can detect up to 10 gauges. The sm125 requires a laptop or PC, and requires an external power supply. It has a wavelength range between 1510 and 1590 nm.

Reference Rod

The reference rod is a thin-walled steel tube that connects to the strain bar and one of the anchors (Figure 4.2-27). The reference rod has an outside diameter of 5.08 cm, an inside diameter of 4.915 cm, and a length of 1 meter

The reference rod is designed to be stiff and light weight. It needs to be stiff in order to concentrate bending displacement in the strain bar. The weight is low to reduce the load on the strain bar when the instrument is supported at one point. A light bar also reduces body forces in inclined or horizontal boreholes. A large diameter, but thin walled tube is used to balance the tradeoff between bending stiffness and weight.

The bending stiffness of a tube arranged as a cantilever with a transverse force, F at the end is given by:

$$\frac{F}{\delta} = \frac{3E\pi}{2L^3}\left[r_o^4 - (r_o - w_1)^4 \right] \tag{4.2-7}$$

where δ is the transverse displacement, E is Young's Modulus, L is length, r_o is outer diameter and w_1 is the wall thickness.

The weight of a tube is:

$$W = \pi\rho L\left[r_o^2 - (r_o - w_1)^2 \right] \tag{4.2-8}$$

The ratio of stiffness to weight is:

$$\frac{F}{W\delta} = C_1\left[\frac{w^2}{2} - w + 1 \right]$$

$$w = \frac{w_1}{r_o}$$

$$C_1 = \frac{3E\pi r_o^2}{\rho L^3} \tag{4.2-9}$$

The maximum value of stiffness to weight ratio is $2C_1$ and it occurs at $w \rightarrow 0$, whereas the minimum value is C_1 and it occurs at $w = 1$, which is a solid rod. This result indicates that the

maximum ratio of stiffness to weight occurs for a thin-walled tube with the largest possible radius, r_o. This is illustrated by the stiffness and weight of a one-m-long cantilever beam (Table 4.2-1). The solid cylinder is approximately 8x stiffer than the hollow cylinder of the same radius, but it is 16x heavier. However, the tube is more than 30x stiffer than a solid cylinder of the same weight.

Table 4.2-1: Stiffness and weight of rods and tubes.

Description	Radius (m)	Stiffness (N/m)	Weight (Kg)	Stiffness/Weight (N/m*kg)
hollow cylinder	Outer:0.0254 Inner:0.024575	24867	1.01	23867
Solid cylinder	0.0254	196144	15.9	12327
Solid cylinder	0.00635	766	0.99	770

The maximum diameter of the tube was determined by including other components in the design and evaluating the size required to fit in a borehole of 9.4 cm diameter. A tube of 2.54 cm diameter and 1.5mm wall thickness was selected as a balance of the various design criteria. The length is 1 m and the material is 304 stainless steel.

Frame

The frame consists of two aluminum bars approximately 183x2.5x.75 cm (72x1x0.3 in) (Figure 4.2-28). There are 4 cross pieces that connect the two outer bars. Conical holes are drilled through two of the cross pieces, whereas the other two are solid. The frame clamping mechanism on the 3DX anchor goes through the cross pieces with the conical holes.

The purpose of the frame is to support the weight of the 3DX during deployment, and prevent the anchors from moving relative to each other. Restricting the movement of the anchors limits the load on the strain gauges and reduces the risk that the gauges will be broken. There is a conical piece on each anchor that matches the conical holes in the frame. Retracting the anchor causes the conical piece on the anchor to seat in the conical hole on the frame. The conical shape is used to register the 3DX at the same position each time the anchors are retracted. This is how the load is taken off the strain bar and gauges (Figure 4.2-29).

During deployment a rope or steel cable is attached to an eye bolt on the top of the frame. A centralizer is attached to the bottom of the frame, and there are also centralizers on the upper side of the frame.

Centralizer

The centralizers hold the 3DX along the center axis of the borehole during deployment. This prevents the anchors from being off center when they are extended in the borehole, and it allows for easier deployment in a borehole with varying diameters. There are two sets of centralizers on the 3DX. This creates two points of contacts between the 3DX and the well bore preventing the 3DX from rotating. The bottom centralizer centers the 3DX in both the *x* and *y* plane, and the top centralizer only centers the 3DX in the *x* plane.

Figure 4.2-27. The reference rod is a tube with two end pieces used to attach to the top anchor and the top of the strain bar.

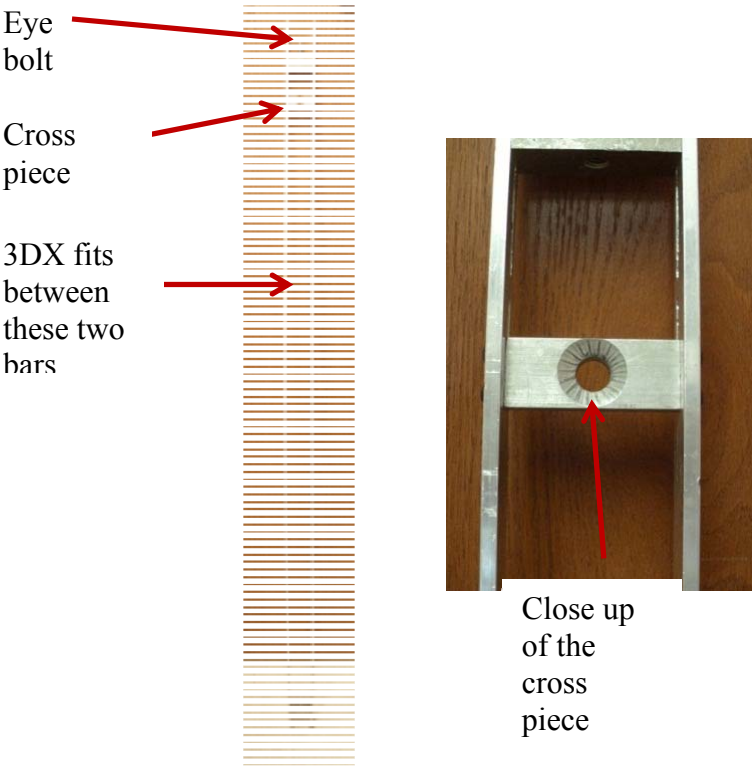

Figure 4.2-28. The frame is two aluminum bars attached by four cross pieces. The two middle cross pieces have a conical depression that connects to the anchor through the frame clamping mechanism. The top most cross piece holds the eye bolt, and the bottom most cross piece holds the bottom centralizer.

The bottom centralizer is made of four strips of spring steel that attach to a threaded rod (Figure 4.2-30). The top centralizer is two strips of spring steel that attach to the sides of the frame.

The centralizers are bow-shaped springs. They flex and are compressed to maintain contact with the borehole wall when the 3DX is deployed.

Calibration

The functionality of the 3DX was evaluated and the instrument was calibrated in the laboratory prior to field deployment. This includes measuring the response to displacement axially and transversely, and evaluating the resolution of the FBG gauges.

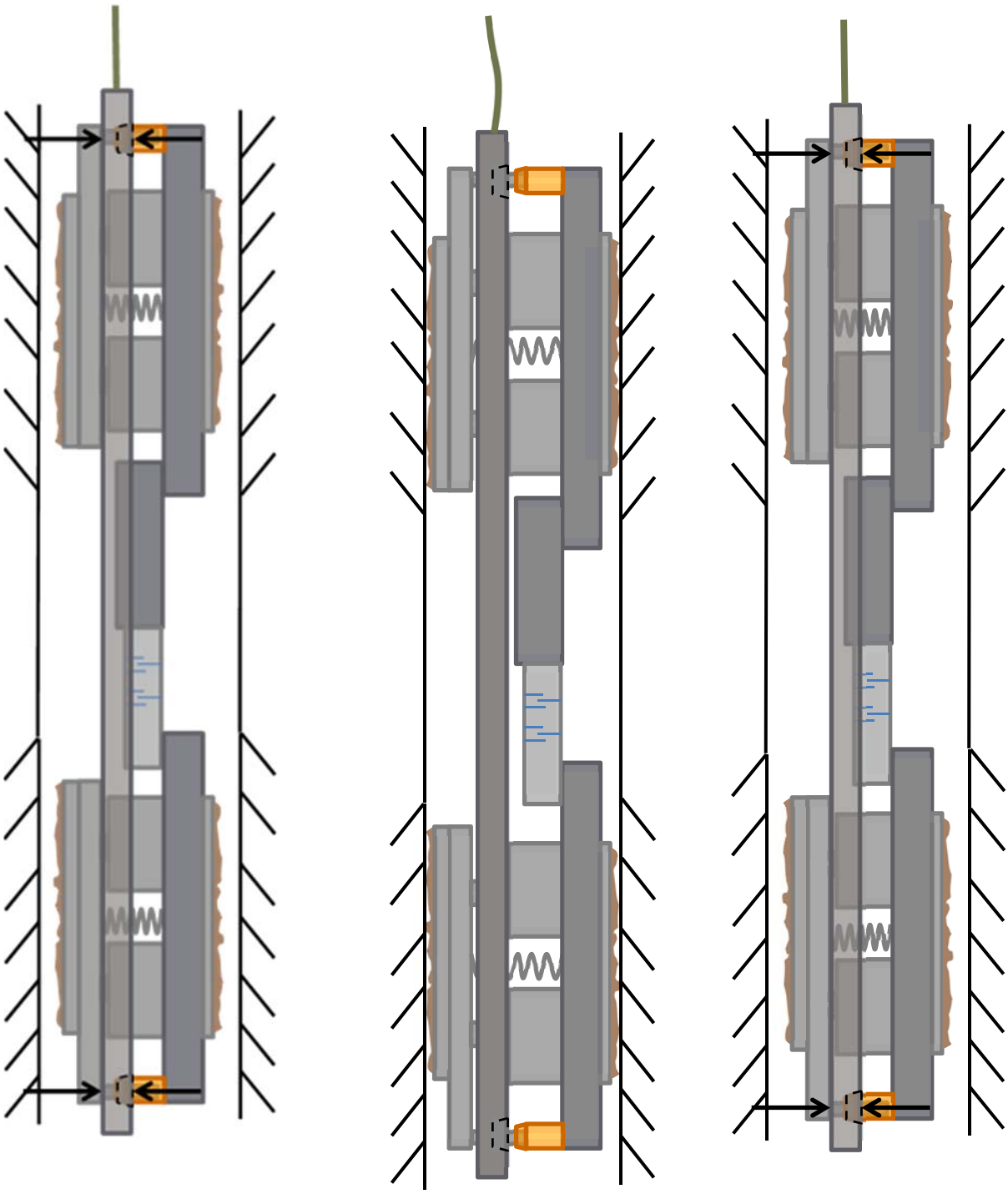

Figure 4.2-29. A conceptual model of the mechanics of the 3DX during deployment. When the anchors of the 3DX are extended the frame detaches from the frame clamping mechanism. When the anchors retract, the frame is positioned so the conical brass piece fits into the conical depression of the frame. During anchor retraction the weight of the 3DX is supported by the frame, and it can be deployed or removed from the borehole.

Transverse Displacement Calibration

The transverse displacement calibration involved determining how the Bragg wavelength from the gauges changes when the top anchor displaces transversely relative to the bottom anchor. A calibration frame was developed that holds the 3DX vertically, securing the top and bottom anchor in place (Figure 4.2-31). Both anchors are extended in aluminum tubes supported in a calibration frame. The top cylinder is held in place by four threaded rods, two on one side and two on the opposing side of the cylinder. The top of the calibration frame contains precision micrometers (1 micron resolution) on one side of the frame. The bottom aluminum tube is secured to a lower calibration frame. Both the upper and lower calibration frames were bolted to a cinderblock wall for rigidity.

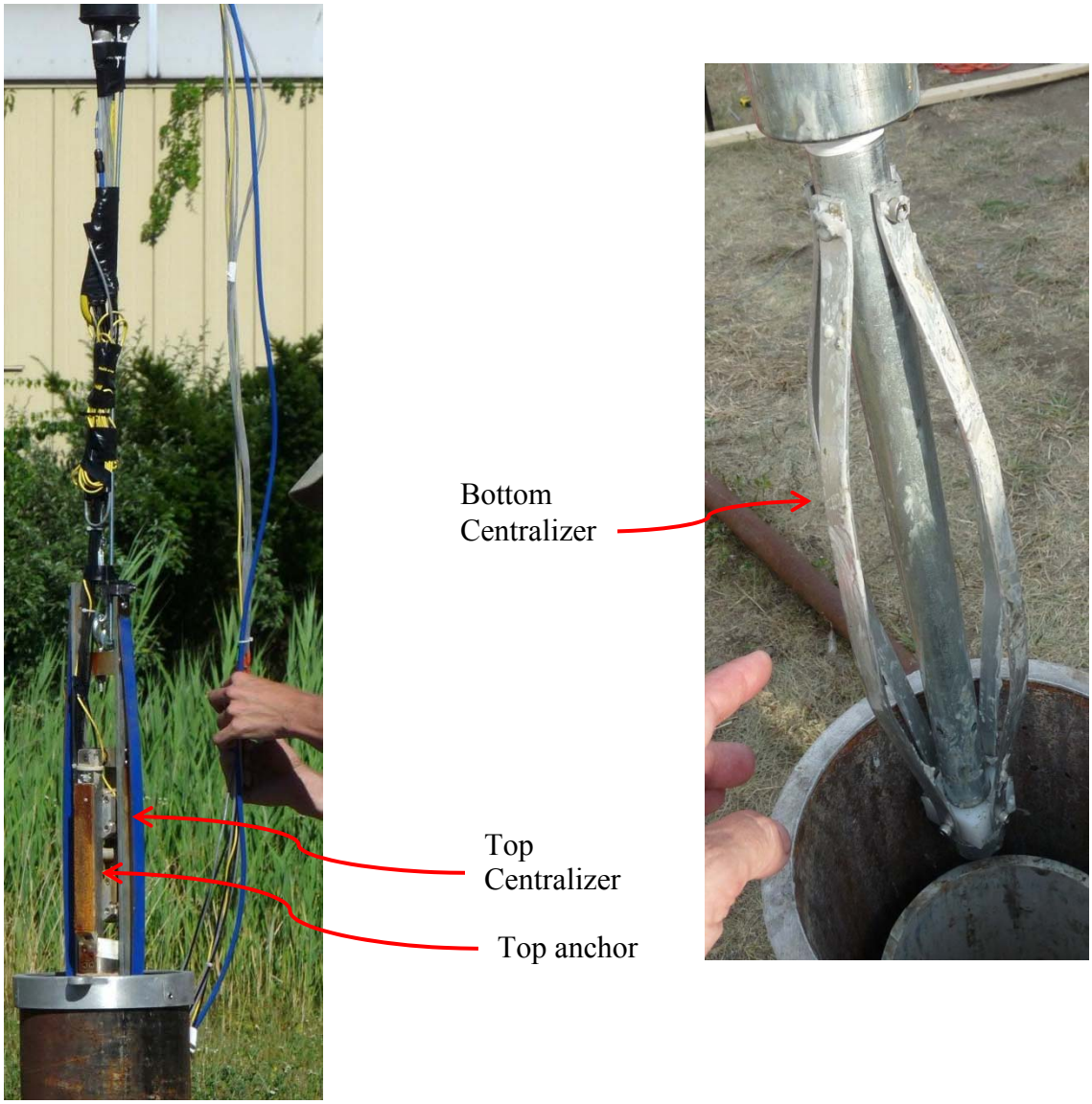

Figure 4.2-30. The right figure is the bottom centralizer, and the left figure is the top centralizer on the 3DX.

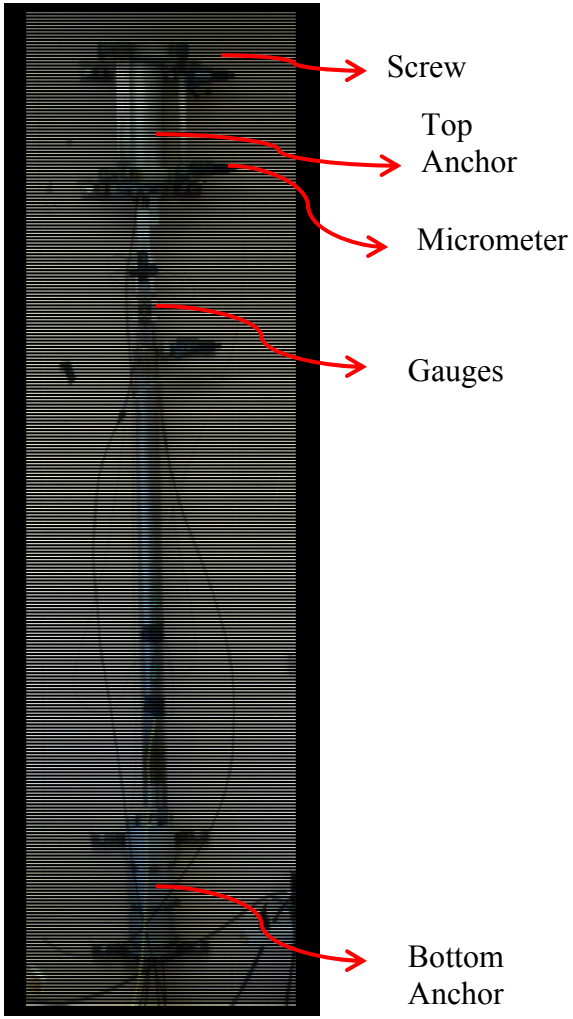

Figure 4.2-31. 3DX in the calibration frame used to transversely displace the top anchor.

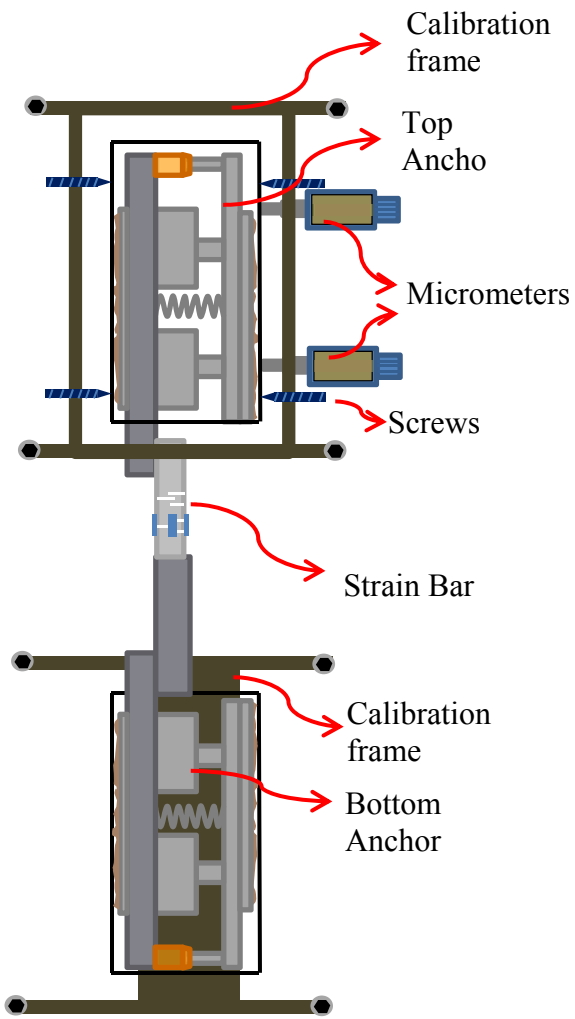

Figure 4.2-32. The 3DX in the calibration frame before the top anchor is transversely displaced by the screws.

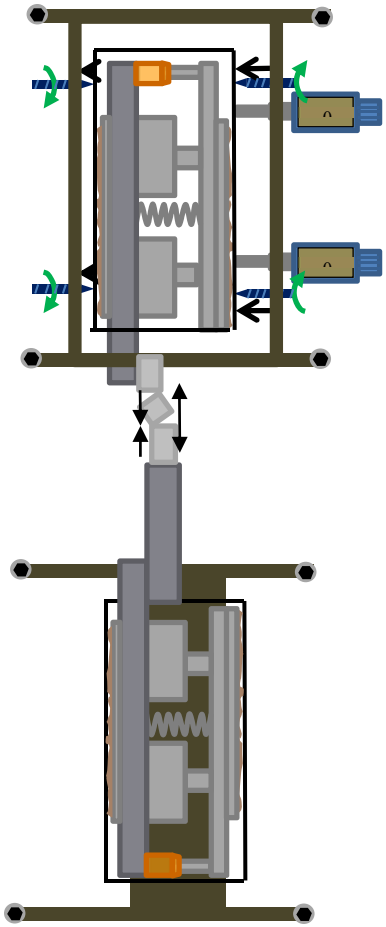

Figure 4.2-33. The 3DX in the calibration frame after the top anchor is transversely displaced by the screws.

The method for calibration is to transversely displace the top anchor by a known amount while measuring the response using the interrogator (Figures 4.2-32 and 4.2-33). Two threaded rods and two micrometers on one side of the cylinder are adjusted to translate the top anchor and prevent it from rotating. The top threaded rod is tightened approximately one quarter turn on one side followed by one quarter turn on the opposing rod. The resulting displacement is measured using the micrometer. The bottom threaded rod is turned approximately one quarter turn to achieve the same displacement. By displacing the bottom rod, the top one is also displaced so it is necessary to measure this and adjust accordingly. This step is repeated until both micrometers indicate the same magnitude of displacement. The displacement and wavelength are then recorded and the process is repeated until gauges approach their measuring threshold.

During the test the two gauges parallel to the direction of motion reacted as expected. One of the gauges compressed while the other extended. The signal from the other two gauges perpendicular to the plane of motion was relatively unchanged, indicating little cross-coupling. The calibration factor is determined from

$$S_t = \frac{\delta_t}{\Delta\lambda_1 - \Delta\lambda_2} \tag{4.2-10}$$

where δ_t is the transverse displacement that occurs for a given change in wavelength $\lambda_1 - \lambda_2$. The results from calibration tests gives S_t = 158 μm/nm +/- 20 μm/nm (Figure 4.2-34), where the uncertainty is the 95% confidence interval.

The transverse displacement can be calculated as a function of the wavelength shift to within a calibration constant, C_r, using the geometry of the strain bar

$$\delta_t = \frac{L_2}{L_1} C_g C_r (\Delta\lambda_1 - \Delta\lambda_2) \tag{4.2-11}$$

where L_2 is the distance between the cuts on the two strain bar 14 cm (5.58 in.), L_1 is the width of the strain bar 2.54 cm (1 in.), C_g is the gauge constant 15.71 μm/nm and is a specification given by Micron Optics, $\Delta\lambda_1$ is the wavelength change of gauge 1, $\Delta\lambda_2$ is the wavelength change of gauge 2. C_r is found by substituting Eq. 4.2-11 into 4.2-10:

$$C_r = \frac{S_t}{C_g}\frac{L_1}{L_2} \tag{4.2-12}$$

The result is that C_r = 2+/- 0.3 using data for S_t in (Figure 4.2-34).

The interpretation is that C_r is the ratio of the measured displacement to the displacement that would occur only due to the flexure of the strain bar. A value of 2 indicates that the observed displacement is 2 times greater than would be expected based on the strain bar alone. The additional displacement is interpreted to result from flexure of the reference rod.

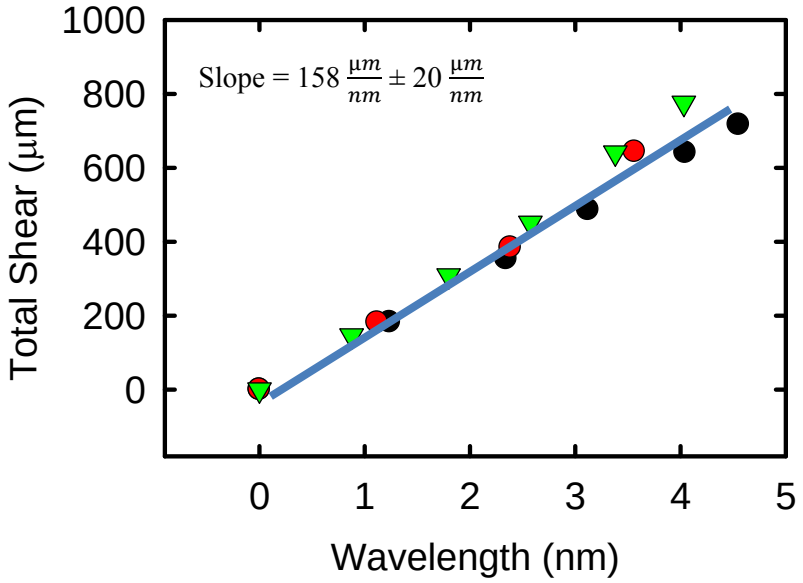

Figure 4.2-34. Transverse displacement measured by the micrometers as a function of the wavelength change ($\lambda_1 - \lambda_2$) for three different tests. The black points is test 1, the red points is test 2, and the green points is test 3.

Axial Displacement Calibration

The axial displacement calibration involved determining how the Bragg wavelength from the gauges changes when the bottom anchor is axially extended relative to the top anchor. The same calibration frame used in the transverse test was used in the calibration test (Figure 4.2-34).

The method for determining the wavelength to axial displacement is to hang weights from the bottom anchor and measure the axial extension with a micrometer while measuring the wavelength change using the interrogator (Figures 4.2-35 and 4.2-36). The bottom anchor is detached from the bottom of the calibration frame and hangs freely. This process is repeated until the strain approaches the measuring limit for the gauges.

The gauges responded similarly during the axial extension test, implying the total axial extension is the average displacement of the gauges. The purpose of the test is to plot the total axial displacement measured by the micrometers and the Bragg wavelength shift from the gauges during the displacement (Figure 4.2-37). The slope of the plot can be used to determine the reference rod constant C_A by considering:

$$Slope = \frac{\delta_a}{\frac{\Delta\lambda_1 + \Delta\lambda_2 + \Delta\lambda_3 + \Delta\lambda_4}{4}} \qquad (4.2\text{-}13)$$

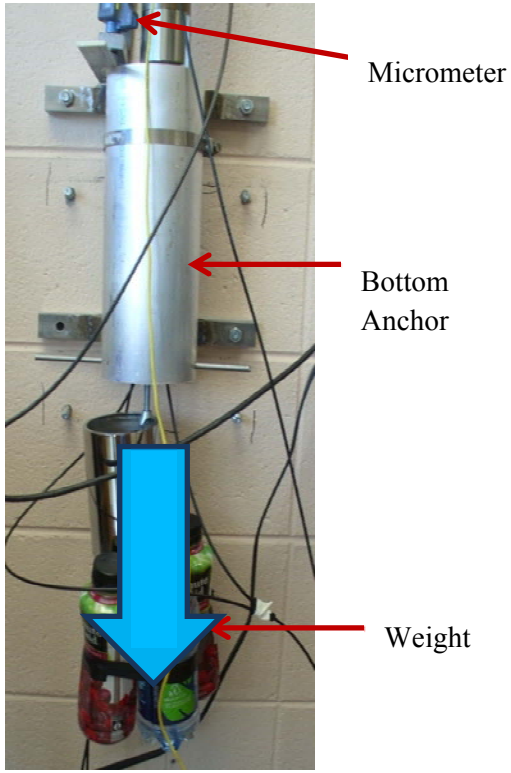

Figure 4.2-35. Picture of the 3DX in the calibration frame with the weights attached. The micrometer at the top of the figure measures the change in displacement.

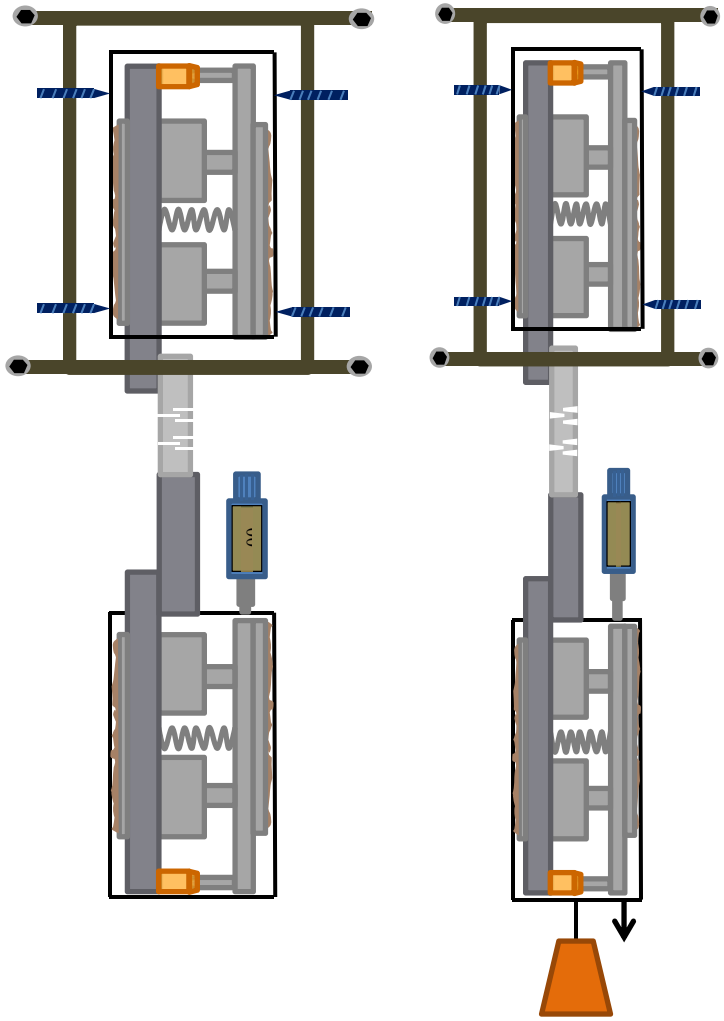

Figure 4.2-36. Idealized picture of the 3DX in the calibration frame during an axial test. The top anchor of the 3DX is secured in the calibration frame and the bottom anchor is left to hang. Weights are attached to the bottom anchor, and the displacement from the weight is measured.

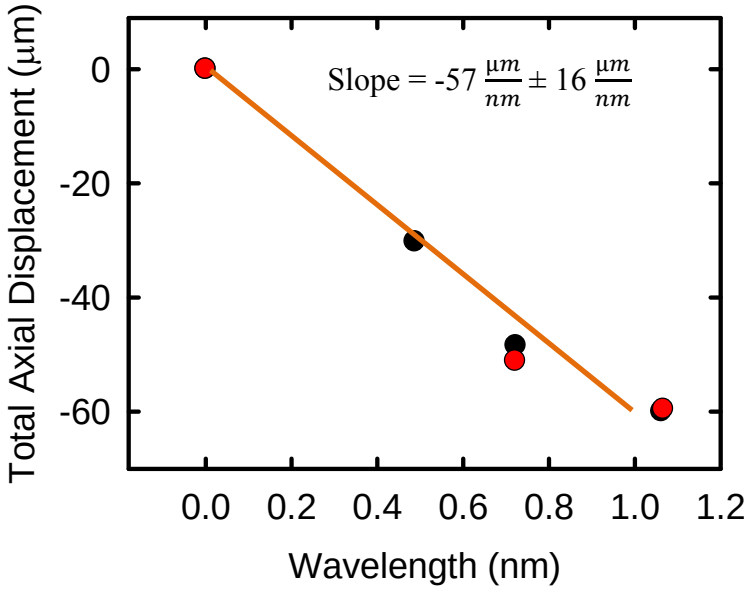

Figure 4.2-37. Axial displacement as a function of wavelength difference.

where δ_a is:

$$\delta_a = C_g C_A \frac{\Delta\lambda_1 + \Delta\lambda_2 + \Delta\lambda_3 + \Delta\lambda_4}{4} \tag{4.2-14}$$

C_A is found by substitution:

$$C_A = \frac{Slope}{C_g} \tag{4.2-15}$$

where C_g = 15.7 μm/nm. The result is $C_A = 3.5$.

Calibration Frame

During the axial displacement test, weights are hung from the bottom anchor which is being held in place by the four screws within the top calibration frame. Approximately 0.66 of the total displacement was from the displacement of the bolts. This was corrected for in the axial calibration test.

There were three parts of the 3DX being measured during the transverse displacement calibration test; the top anchor, the strain bar, and the reference rod. The measured displacement of the top anchor is the total displacement caused by turning the bolts. The strain gauges were measuring the displacement along the strain bar. There is a micrometer located below the strain bar at the top of the reference rod measuring any displacement occurring below the strain bar. When the reference rod displacement is added to the displacement measured along the strain bar, the value does not equal the total displacement measured at the top anchor. For all the transverse displacement calibration tests there is a 15% discrepancy between the total displacement and the added value of the reference rod displacement and strain bar displacement. This indicates that

during the tests 15% of the total displacement is from the top calibration frame moving. It can then further be concluded that the bottom calibration frame is contributing to the total displacement as well. The amount is estimated at approximately 10% ± 10%. This uncertainty will be added to the error analysis.

Combined Error Calculations

The factors used to determine the transverse and axial displacement have error associated with them. In order to determine the displacement error, the error of each individual factor needs to be combined. When two values with errors are added or subtracted, the total error is (Baird 1962)

$$C = A + B \tag{4.2-16}$$

where A has error $\pm E_A$ and B has error $\pm E_B$. The error of C is

$$E_C = \sqrt{E_A{}^2 + E_B{}^2} \tag{4.2-17}$$

When two values with errors are multiplied or divided then the combined error is the relative error. Consider

$$C = AB \tag{4.2-18}$$

The error of C is (Baird 1962)

$$E_C = C\sqrt{\left(\frac{E_A}{A}\right)^2 + \left(\frac{E_B}{B}\right)^2} \tag{4.2-19}$$

Transverse Error

The 3DX was calibrated to determine how the Bragg wavelength of the gauges changed during transverse displacement. The result of the calibration is the reference rod constant (C_r), which is used to determine the displacement when the 3DX is deployed.

$$C_r = S_t \frac{L_1}{L_2} C_g \tag{4.2-20}$$

where L_2 is 14+/- 2.5cm, S_t is the slope from the transverse calibration test. It is 158 ± 20 μm/nm. C_r will have error associated (C_{rerr}) with it from the other terms in Eq. 4.2-18, so

$$C_{rerr} = C_r\sqrt{\left(\frac{S_{terr}}{S_t}\right)^2 + \left(\frac{L_{2err}}{L_2}\right)^2} \tag{4.2-21}$$

It follows that C_{rerr} is ±0.485.

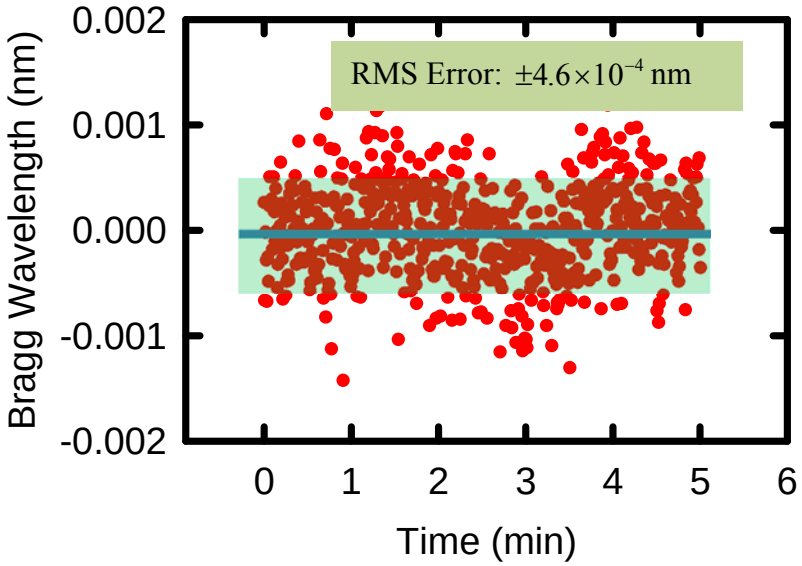

Figure 4.2-38. The residuals used to calculate the 5 min RMS noise for the gauges.

Now that C_{rerr} is known the relative transverse displacement error can be found. Recall that the transverse displacement is:

$$\delta_T = \frac{L_2}{L_1} C_g C_r \left(\Delta\lambda_1 - \Delta\lambda_2\right) \tag{4.2-22}$$

The first step is to find the error from the difference between the Bragg wavelengths. The 5 min RMS error of the Bragg Wavelength from the gauges is $\lambda_{ierr} \pm 4.6\times10^{-4}$ nm (Figure 4.2-38). The actual error from the difference between the Bragg wavelengths of the gauges is:

$$\lambda_{err} = \sqrt{4(\lambda_{ierr})^2} \tag{4.2-23}$$

where λ_{ierr} is the individual bragg wavelength error. The transverse relative error (δ_{Terr}) is

$$\delta_{Terr} = \sqrt{\left(\frac{\lambda_{err}}{\lambda_i}\right)^2 + \left(\frac{C_{rerr}}{C_r}\right)^2 + \left(\frac{L_{2err}}{L_2}\right)^2} \tag{4.2-24}$$

where λ_{err} is the gauge error (0.00182 nm), λ_i is the bragg wavelength from the gauges (1550 nm), C_{rerr}, is the rod constant error (0.485), C_r, is the rod constant (2), L_{2err}, is the error associated with establishing L_2, (2.54 cm), and L_2 is the length between the flexures (14 cm).

Substituting into Eq. 4.2-24 yields a relative transverse displacement error of 0.3. The magnitude of the transverse displacement error is from the error associated with the C_R constant and L_2. They each compose approximately half of the total error, and the gauge error is less than 1% of the total error.

Axial Error

The 3DX was calibrated to determine how the Bragg wavelength of the gauges changed during axial displacement. The result of the calibration is the axial constant (C_A), which is used to determine the displacement when the 3DX is deployed. The equation used to find C_A is:

$$C_A = \frac{S_A}{C_g} \tag{4.2-25}$$

where S_A is the slope from the transverse calibration test. It is 57 ± 16 μm/nm. C_A will have error associated (C_{Aerr}) with it from the other terms in Equation 4.2-13, so this error is found using:

$$C_{Aerr} = C_A \sqrt{\left(\frac{S_{Aerr}}{S_A}\right)^2} \tag{4.2-26}$$

which results in $C_{Aerr} = \pm 0.98$.

Now that C_{Aerr} is known the relative transverse displacement error can be found. Recall that the equation for axial displacement is:

$$\delta_a = C_g C_A \frac{\Delta\lambda_1 + \Delta\lambda_2 + \Delta\lambda_3 + \Delta\lambda_4}{4} \tag{4.2-27}$$

The first step is to find the actual error (λ_{err}) from finding the difference between the Bragg wavelengths. The error from the gauges is the 5 min RMS error of the Bragg wavelength from the gauges. The gauges have an error (λ_{ierr}) of $\pm 4.6 \times 10^{-4}$ nm (Figure 4.2-38). So the axial relative error (δ_{Aerr}) is:

$$\delta_{Aerr} = \delta_A \sqrt{\left(\frac{\lambda_{err}}{\lambda_i}\right)^2 + \left(\frac{C_{Aerr}}{C_A}\right)^2} \tag{4.2-28}$$

where λ_{err} is the actual gauge error (0.00368 nm), λ_i is the bragg wavelength from the gauges (1550 nm), C_{Aerr} is the rod constant error (0.98), C_r is the axial constant (3.5). Substituting these values into Eq. 4.2-28 yields a relative transverse displacement error of 0.28. The magnitude of the transverse displacement error is largely from the error associated with the C_A constant. It is approximately 0.27. The error from the gauges is less than 0.01.

Evaluation of Fiber Optic Strain gauges in Supercritical CO_2

The 3DX could be used to monitor well casing deformation during injection of supercritical CO_2. Monitoring the casing could be a preventative measure taken to avoid damaging the well. It could also be used to further characterize the storage capacity of the formation outside of the well. To evaluate the possibility of using the 3DX during CO_2 injection we conducted a test to measure the effects of a supercritical CO_2 environment on the strain

gauges. It is possible that the supercritical CO_2 could act as a solvent that deteriorates the glue used in the gauge.

During the test a strain gauge was inserted into a pressure vessel and filled with supercritical CO_2 for the duration of one week (Figure 4.2-39). The vessel was pressurized to 200 bars and heated to 50 degrees Celsius.

A bending test was done before and after the gauge was immersed in the supercritical CO_2 (Figure 4.2-40). The bending test involves displacing one end of the strain bar by a known amount while the interrogator is measuring the wavelength change from the gauge. With this information we can compare the sensitivity of the gauges to displacement before and after the test. If the supercritical CO_2 affects the gauge then the displacement as a function of wavelength will be different before and after test. Another quantitative comparison test involved leaving the gauge alone for five minutes while the interrogator collected power level data. This information will be used to determine how the supercritical test affects signal strength. If the heat or CO_2 damages the fiber core then the signal strength will be different for both before and after.

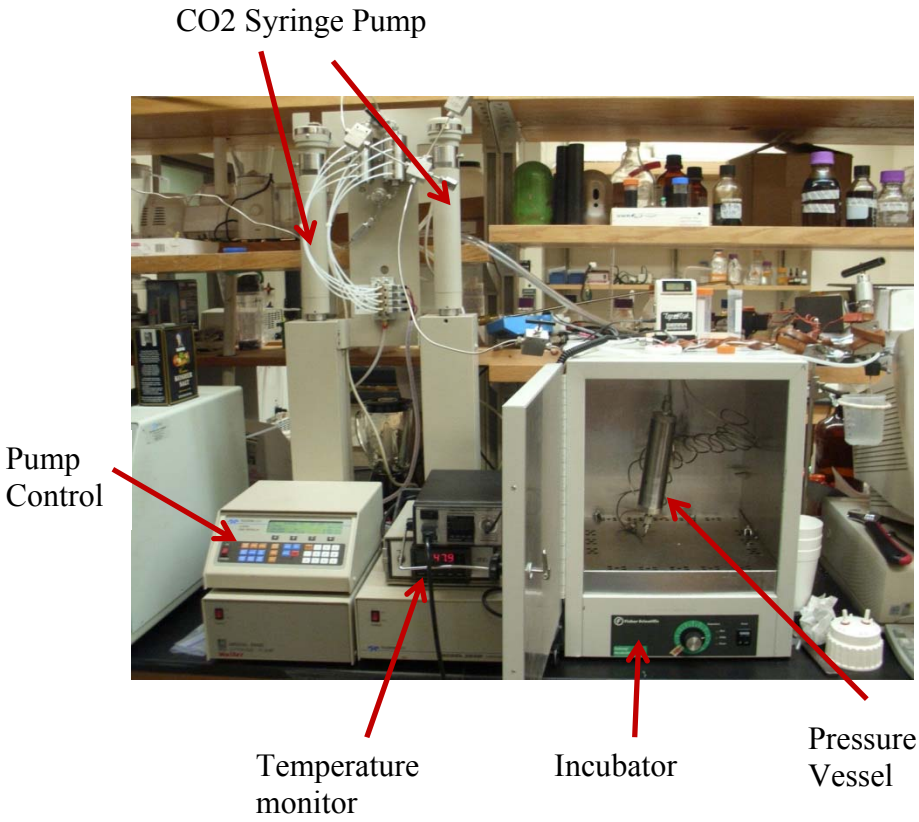

Figure 4.2-39. Apparatus used to test strain gauge in supercritical CO_2, and two syringe pumps used to create and maintain a constant pressure.

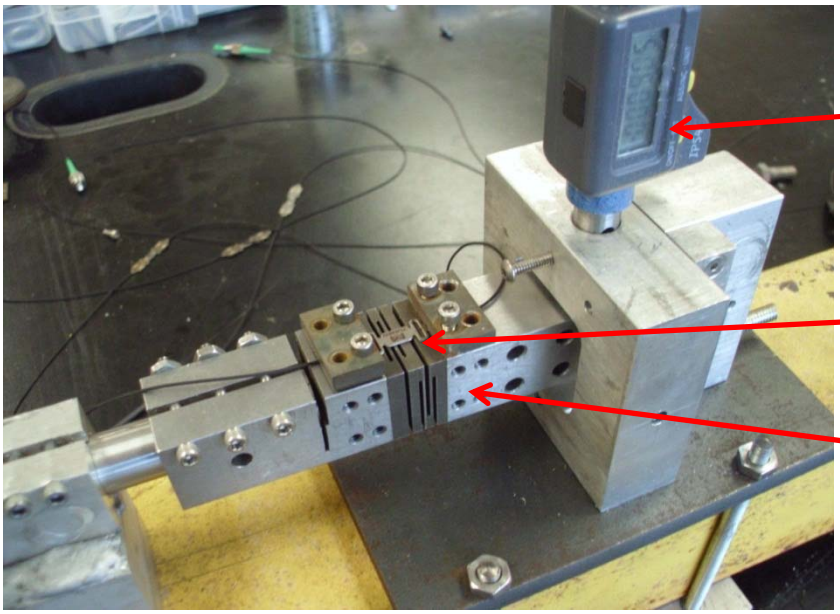

Figure 4.2-40. The transverse displacement test done to compare performance of the gauge before and after being exposed to supercritical CO_2. The micrometer is used to push down on the strain bar. The gauge is secured to the strain bar and extends during the test.

Results

The results of the signal strength test were fit with a line to characterize their variability (Figure 4.2-41). The average value of the signal strength before the supercritical test was -10.98 dBm and the average value of the signal strength after the test was -11.52 dBm. The power units for these sensors are expressed by the ratio of decibels per one milliwatt. One milliwatt equals zero dBm, so if the signal strength decreases below this it becomes negative. The interrogator can detect peaks with a signal strength as low as -40 dBm, so a decrease of 0.54 has no effect on the performance.

The bending test results were fit with a line to determine the slope (Figure 4.2-42). Both before and after tests have the same slope during the test of -0.012 μm/nm. The shift in the plot is due to the induced strain caused by the attachment method used on the strain bar. This does not affect the sensitivity of displacement as a function of wavelength.

Based on the comparison of the signal strength data and the transverse displacement test we conclude that the strain gauges we are using can function properly in a supercritical CO_2 environment.

2 Hz RMS Noise of the Micron Optics sm125

The root mean squared of the noise for the 3DX will give the spread of the axial and transverse displacement around a linear trend line. This section focuses on the RMS for a frequency of 2 Hz. This is important because RMS noise will be different for different frequencies and averaging methods. Averaging decreases the RMS noise according to:

$$R_{avg} = R\frac{1}{\sqrt{n}} \qquad (4.2\text{-}30)$$

where n is the number of points averaged per amount of time (frequency), R is the RMS noise without averaging. The RMS noise is calculated at 2 Hz because the field tests use the Micron Optics sm125, which has a scan frequency of 2 Hz.

The data used to determine the 2 Hz RMS noise is from the 3DX when it was deployed in a borehole at the Clemson well field at a depth of 24.3 meters. At this depth the 3DX was straddling 2 fractures. The device was left to equilibrate for one day. After it equilibrated, the device was left for five days while it collected Bragg wavelength changes from the four gauges at a frequency of 2 Hz. The Bragg wavelength results were then converted to axial and transverse displacement using Eqs. 4.2-6 and 4.2-5 respectively. Five minutes of data was used to characterize the 2 Hz RMS by fitting with a regression line. The linear trend accounts for longer term variability, such as that caused by temperature or deformation in the well bore. Then the residuals are found by:

$$residuals = y_p - y_a \qquad (4.2\text{-}31)$$

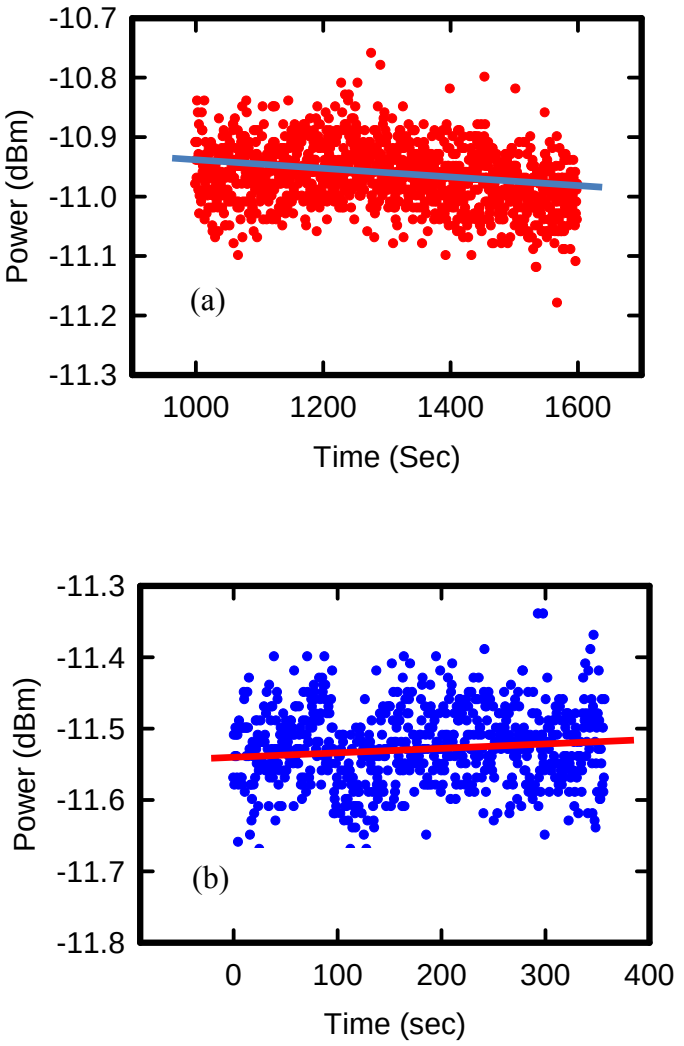

Figure 4.2-41. Power of the signal as a function of time for (a) before exposure to supercritical CO_2 and (b) after exposure.

The fitted regression line and the residuals were found using the software package, TableCurve.

The RMS noise is found using [*Baird*, 1962]:

$$RMSError = \sqrt{\frac{\sum_{i=1}^{n}(residuals_i)^2}{n}} \qquad (4.2\text{-}32)$$

Transverse Displacement

The 3DX can measure transverse displacement in two planes, so the RMS noise of both planes can be calculated and compared. Using the method described above the RMS noise of the transverse displacement for is ±142 nm in one direction and ±146 nm in the other (Figure 4.2-43).

Axial Displacement

Using the method described above the RMS noise of the axial displacement is ±11 nm (Figure 4.2-24).

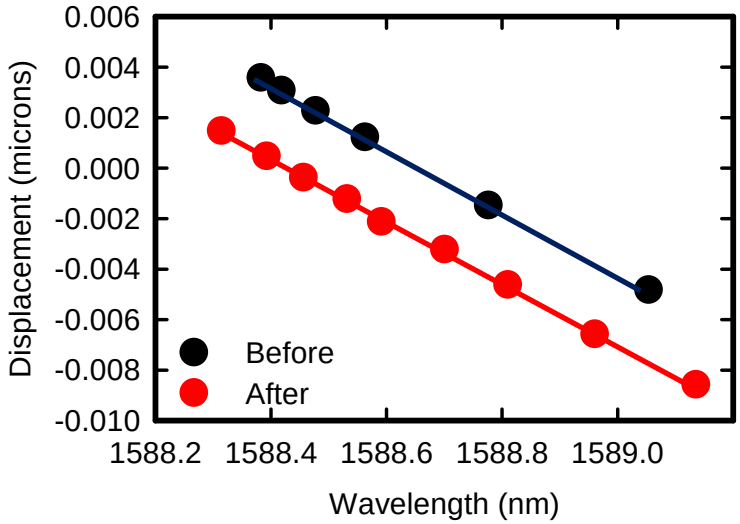

Figure 4.2-42. Displacement as a function of wavelength during a transverse displacement test. The black points are from before exposure to supercritical CO_2 and the red points are from after exposure.

1 KHz RMS noise of Anritsu AR4011A

Evaluating the RMS noise of the Anritsu Interrogator from field measurements, and comparing it to the RMS noise of the Micron Optics sm125 illustrates the resolution improvement from two different scan frequencies. To obtain this data, the 3DX was deployed in a well bore in Japan. The interrogator used to measure the Bragg wavelength of the four gauges attached to the 3DX was the Anritsu AR4011A. The signal used for the analysis had an associated drift to it. The drift may be due to temperature changes, presumably. The signal from the Micron optics interrogator did not have a noticeable drift. This may be due to equilibration times. The 3DX had more time to equilibrate for the signal used for the Micron optics analysis as compared to the Anritsu signal.

The Anritsu Interrogator obtains data at 1 kHz and performs a 1 kHz forward average of the data internally, where each displacement value is the average of the 1,000 forward displacement values (Figure 4.2-45). The 5 min 1 kHz RMS noise for the axial displacement is 7 nm, which is two thirds the noise when using the Micron Optics interrogator (Figure 4.2-45). The 5 min 1 kHz RMS for the transverse displacement is 48 nm, which is one third of the noise when using the Micron Optics interrogator.

Discussion and Summary

The design of the 3DX is based on previous extensometers used at Clemson, but it has been modified to include fiber optic sensors. It includes two anchors separated by a reference rod and two strain bars. The dual anchor separated by a reference rod has been implemented in other extensometers, so we are confident in the performance of these components. When the anchors are secured against the walls of the borehole, the two strain bars can extend, compress, and rotate allowing the anchors to move relative to each other. This motion can be resolved by knowing the compressive and extensive displacement on each side of the strain bar. The strain bar

compression or extension can be determined by attaching a FBG gauges to each of the four sides of the strain bar.

Each gauge reflects a Bragg wavelength and the shift in the Bragg wavelength is proportional to the compression and extension of the strain gauge. The conceptualization of detecting axial displacement is that as the anchors move towards each other axially, the induced displacement is concentrated within the strain bar flexure. The four gauges will compress, so the axial displacement is calculated by taking the average change in wavelength of the four gauges. The conceptualization for measuring transverse displacement is as the anchors displace transversely relative to each other, the strain bar bends. The two gauges facing the direction of transverse displacement react; one compresses and the other extends. The transverse displacement is determined by calculating the difference in the wavelength change of the two gauges.

Calibration

The calibration tests show how the 3DX can measure 3D displacements. The methodology of the tests was to suspend the 3DX vertically, and displace the top anchor relative to the bottom anchor in three dimensions. The gauges are attached to the strain bar, and the displacement of the anchors is measured as a function of the Bragg wavelength. The results of the test suggest that the 3DX can detect axial and transverse displacement. We confirmed that the transverse and axial displacement of the anchors can be measured by coupling a geometrical analysis with

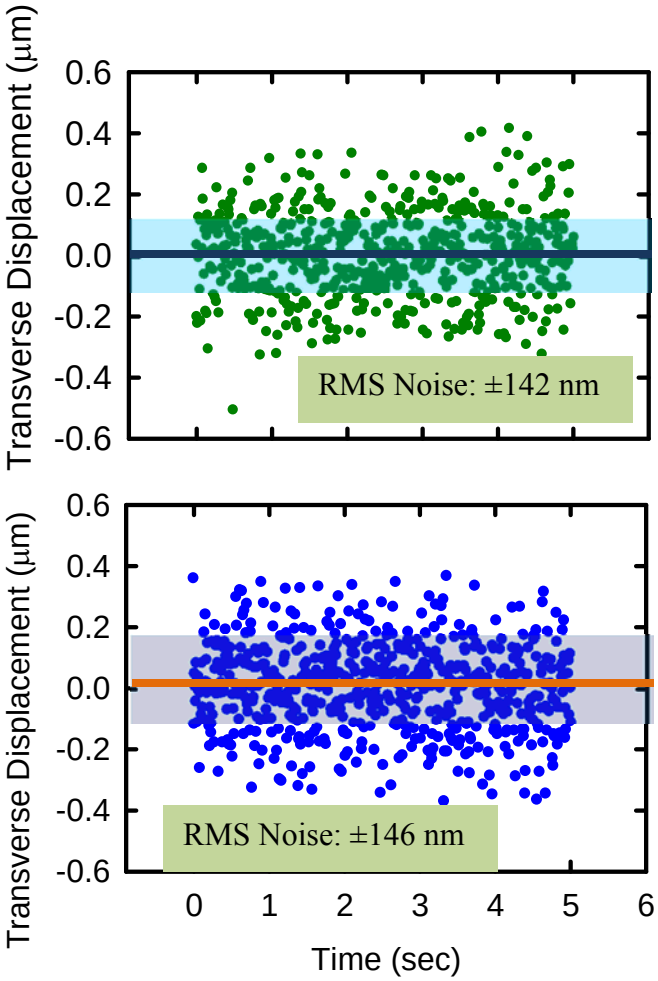

Figure 4.2-43. The residuals used to calculate the 5 min RMS noise for transverse displacement in both planes.

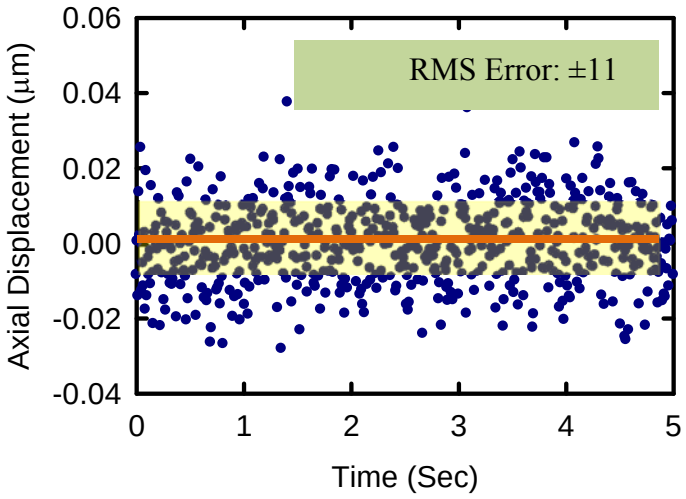

Figure 4.2-44. The residuals used to calculate the 5 min RMS noise for axial displacement.

the gauge measurements. During transverse displacement the two gauges facing the direction motion acted equally but opposite; one compressed and one extended. The strain bar extended during the axial displacement test. This in turn extended all the gauges. The average displacement of all the gauges is the axial displacement.

The compressibility of fractured rock aquifer is approximately 1 micron per meter head axially, and from previous tests 10s of microns transversely. The 2 Hz RMS noise of the 3DX should be at least an order of magnitude less than these signals. For axial displacement the resolution was found to be 31 nm and the transverse resolution was 190 nm. This is within the bounds needed to detect the three dimensional displacements that might occur during a hydromechanical well test.

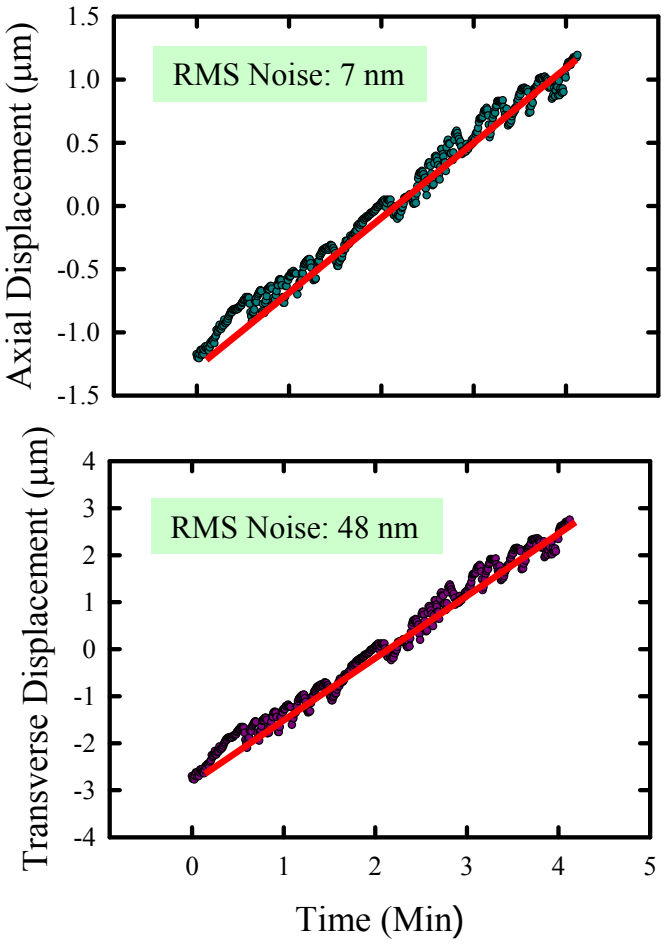

Figure 4.2-45. Displacement as a function of time using the Anritsu AR4011A. Data fit with a line and used to calculate 1KHz 5 min RMS noise of the Anritsu AR4011A.

RMS noise

We found that the RMS noise of the 3DX is within the limits needed to detect 3D displacement during hydromechanical well tests. The RMS noise of the 3DX can be improved by modifications to the device, interrogators, or fiber optic gauges.

The strain gauges are composed of steel carriers that resist displacement. Removing the steel carriers has the possibility to reduce the RMS noise of the 3DX. The drawback of this is that the strain bar would need to be redesigned to protect the gauges during deployment. There would need to be a system that would allow the user to attach the gauges when the 3DX is in the borehole.

The stiffer the reference rod the less it will move during transverse displacement. This can be done by increasing the wall thickness or its total diameter. The resolution improvement from this effect might be offset by an increase in weight, which could increase the chances of damaging the gauges.

The strain bar can be modified by increasing the compliance of the flexure that the gauges attach to, and decreasing the compliance of the second flexure. This will concentrate more of the displacement on the gauges.

The anchors can be modified by using a stiffer spring. The resolution of the 3DX was improved by pressurizing the air cylinders during calibration tests. This occurred because it increased the force on the anchors. The gauges are sensitive to small changes in pressure in the cylinders, so using a stiffer spring is preferred to pressurizing the cylinders.

FIELD TESTING OF 3DX AND 5DX

The 3DX and 5DX instruments were evaluated during tests of shallow (<100 m) wells in Tsukuba, Japan, Clemson, SC, and Trenton, NJ. These tests provided proof-of-concept data on the performance of the instruments and the general viability of the technique under field conditions. The depth of deployment is considerably shallower than that required for CO_2 storage, so this represents only the first step in a field testing process that would result in a technology that could be used during CO_2 storage. The methodology and materials for the tests, and the results from the wells tests and ambient monitoring are outlined below.

Tsukuba Field Test, Japan

A 3DX prototype was was used for initial development and proof of concept Tsukuba, Japan Field Site. This work was funded by a Summer Graduate Fellowship through the National Science Foundation to Glenn Skawski,

The field site is located in an abandoned granite quarry near Tsukuba, Japan at the base of Tskuba Mountain (Figure 4.2-46). The granite is fractured between the surface and 20 meters depth, with decreasing fracture density below this. The water table is approximately 2 meters below the surface. A hydromechanical well test was performed in borehole 3 at a depth of 10.5 meters (Figure 4.2-46). The 3DX was straddling multiple fractures at this location. The borehole is cased down to 3 meters, and the borehole diameter is 95 mm.

Figure 4.2-46. Location of field site in Tsukuba, Japan, at the base of Tsukuba Mountain (bottom right).

Field Tests

The procedure to carry out a hydromechanical well test is to first deploy the 3DX. The device is hung from a tripod and the FBG gauges are secured. The locations of the gauges are then recorded relative to the top of the 3DX. A pressure transducer is attached to the bottom of the frame. At this point the top anchor is retracted and the bottom anchor is expanded. When the gauges are set the bottom anchor is retracted, and it is lowered to a predefined depth. The 3DX is lowered past the desired depth and then pulled back up to prevent offset in the anchors. The air pressure used to retract the anchors is 60 psi. The procedure to set the anchors is to extend the bottom anchor and then extend the top anchor in sequence.

After the 3DX was deployed, water was pumped from the borehole at a varying rate. This rate decreased with time. The water level was measured with water level tape and the pressure transducer. During pumping the interrogator is recording the Bragg wavelength from the active gauges on the 3DX.

A total of five field tests were conducted, with modifications in the equipment and procedures made after each test. An unknown factor was how long the device needed to equilibrate with the borehole surroundings, so the time between deployment and the start of the hydraulic well test varied. The differences in equilibration times were between an hour and approximately half a day. The first two tests had only one active gauge, the next two tests had two active gauges opposite of each other, and the fifth test had all four gauges attached to the strain bar. The fifth test was in a different borehole then the first four tests.

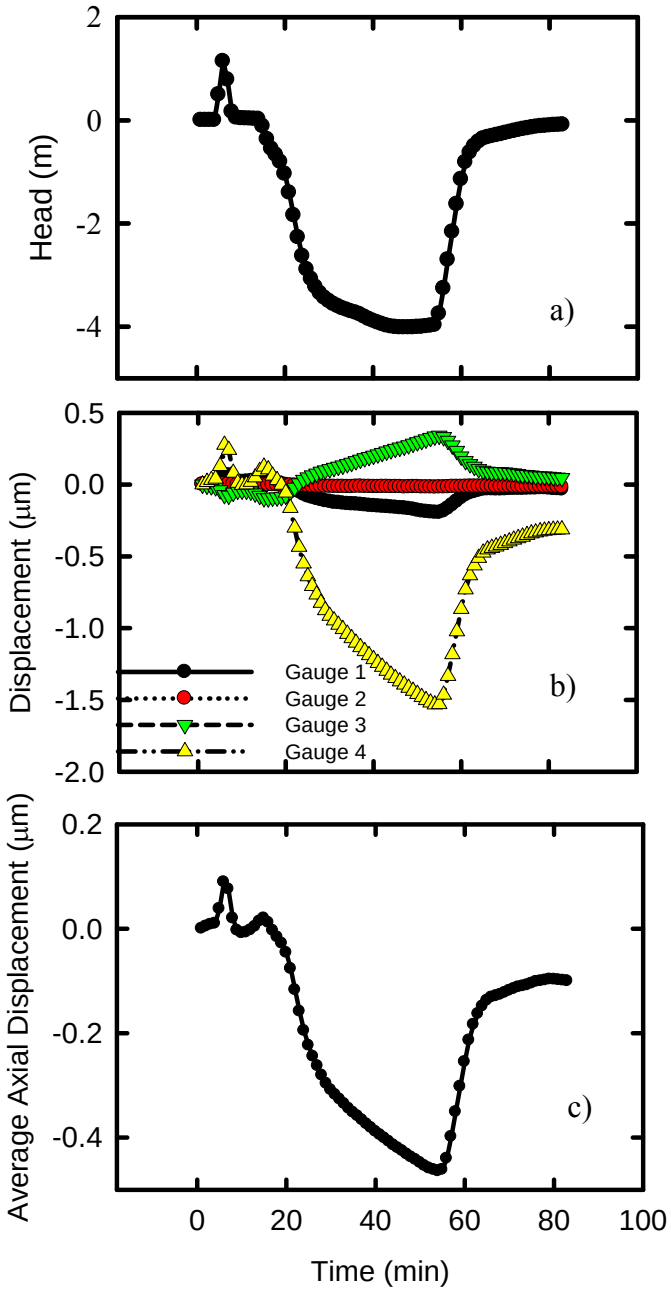

Figure 4.2-47. (a) Pressure head during a well test as a function of time (b) Axial displacement of each individual gauge as a function of time (c) Average axial displacement of the four gauges as a function of time.

Results

The most insightful results occurred during the fifth test. The 3DX was left in the borehole overnight, which allowed it to equilibrate with the surroundings. First a slug was inserted into the borehole, which raised the head by a meter and expanded the fracture by about 0.2 microns (Figure 4.2-48). After this the head was dropped four meters during pumping and 0.8 microns of compression occurred (Figures 4.2-47 and 4.2-48). The experiment ran until the aquifer recovered and the displacement returned to its initial value.

Test 5 showed a compression of 1 micron during a head drop of 5.5 meters (Figure 4.2-48). This was found by averaging the displacement of the four gauges. The transverse displacement was determined using Eq. 4.2-11. This resulted in 12 microns across gauges A3 and A4, and less than 1 micron of transverse displacement occurred across gauges A1 and A2 (Figure 4.2-49).

The displacement data from the fiber optic sensors were averaged to match the measuring rate of the pressure transducer. For instance, the pressure transducer took a measurement every 5 minutes during the hydromechanical well tests at Clemson. The Interrogator was measuring the Bragg wavelength every half second. To match the displacement data with the pressure data a midpoint average was done for every 600 displacement values. The time corresponding to the middle of every 600 displacement value was equal to the time that the pressure was measured every 5 minutes.

Conclusions

The tests at the field site demonstrated proof of concept of measuring 3D deformation in a well during pumping using fiber optic gauges. The experimental data are similar in magnitude and trend to previous findings [*Svenson et al.*, 2007; *Schweisinger*, 2008; *Hisz et al.*, 2012].

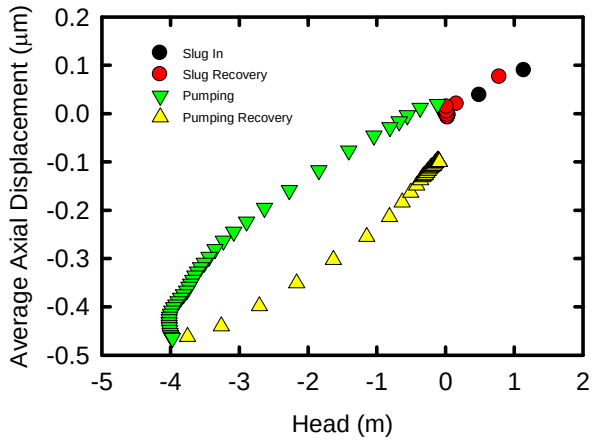

Figure 4.2-48. Average axial displacement during slug and pumping well tests as a function of head.

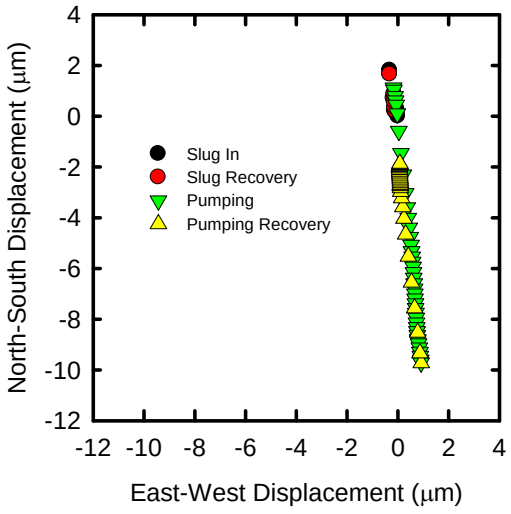

Figure 4.2-49. Transverse displacement in cardinal directions during slug and pumping well tests.

NAWC Field Site, Trenton, NJ

The purpose of the field test was to demonstrate the use of multiple fiber optic extensometers for case deformation monitoring during CO_2 sequestration. This was the first field tests of the 5DX, and the objective was to use it at a site along with the 3DX and a tiltmeter.

The U.S. Naval Air Warfare Center (NAWC) is a 65-acre site in west central New Jersey in the city of West Trenton. It was a jet engine testing facility for military aircraft from the mid-1950's to the late 1990's. Operations at the site caused contamination of ground water by trichloroethylene (TCE) and its degradation products, cis 1,2-dichloroethylene (cis-DCE) and vinyl chloride (VC) (International Technology Corp., 1994). This prompted studies of the hydrogeology of the site starting in 1993. This study was conducted during mid-July, 2012.

The NAWC site is bordered by Mercer County Airport on the north and Parkway Avenue to the south (Figure 4.2-50). A small spring occurs near the southwestern corner of the site, forming the headwaters of the West Branch of Gold Run, which flows within a permeable culvert under Parkway Avenue.

The NAWC site is located along the southern edge of the Newark Basin, a thick sequence of sedimentary rocks and basalt flows of Early Jurassic and Late Triassic age [*Lacombe*, 2000]. The site geology includes the Lockatong and underlying Stockton Formations of late Triassic age (Figure 4.2-50). The Stockton Formation consists of interbedded light reddish-grey sandstone and reddish mudstones, which have been divided into five units based on major changes in lithotype and color. The Lockatong Formation is a laminated to thickly bedded gray, greenish-gray, reddish, and black mudstone [*Lacombe*, 2000].

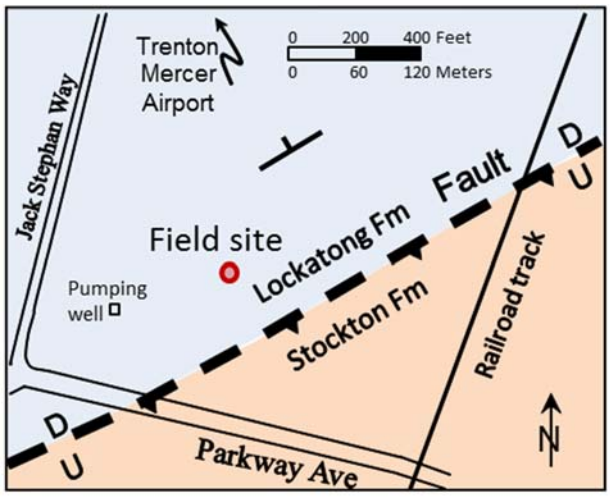

Figure 4.2-50. NAWC site location map relative to Parkway Ave to the south and the Trenton Mercer Airport to the north.

Bedding at the site strikes N70E and dips roughly 15º NW, except near a fault where the rocks have been folded and dips are as steep as 70º. The fault trends parallel to strike of bedding and dips 30º to 50º to the south. Reverse-type displacement of more than 100 m has pushed the Stockton Formation over the Lockatong Formation.

Each formation contains strata that are permeable interbedded with layers that are remarkably tight. The water-bearing zones consist of interconnected bedding-plane partings, whereas the confining units are unfractured, fine-grained or cemented sediments. Bedding plane partings in the Lockatong Formation are generally thinner and less permeable than they are in the Stockton Formation [*Lacombe*, 2000]. Vertical fractures are also present and can contribute to the bulk permeability.

The test was conduct at a cluster of seven wells (Figure 4.2-51). The wells 84-BR to 89-BR are arranged in a hexagonal pattern going clockwise with 83-BR in the center, and 84-BR is the northern most well. The 3DX was in 85-BR, the 5DX was in 86-BR, and the borehole tilt

meter was in 87-BR. These were the wells with the highest specific capacity. The other wells were packed off.

The equipment was mobilized to the site in an equipment trailer. The instruments were packed in cylindrical cases and deployment required unpacking and configuring the FBG gauges on site (Figures 4.2.2-53 and 4.2-54). 3DX was lowered into 85BR to straddle a fracture that was 19.5 meters below the top of the casing (Figure 4.2-51). Approximately 0.6 meters above the 3DX was a packer that was inflated to 240 kPa. There were two pressure transducers; one measuring the pressure below the packer, and another measuring the pressure above the packer in 85-BR. The 5DX was deployed at a depth of 19 m, across what appears to be the same fracture as the one straddled by the 3DX. The borehole tiltmeter was in casing at a depth of 12 m.

There is a pumping center approximately 200 m west used to contain the contaminated ground water.

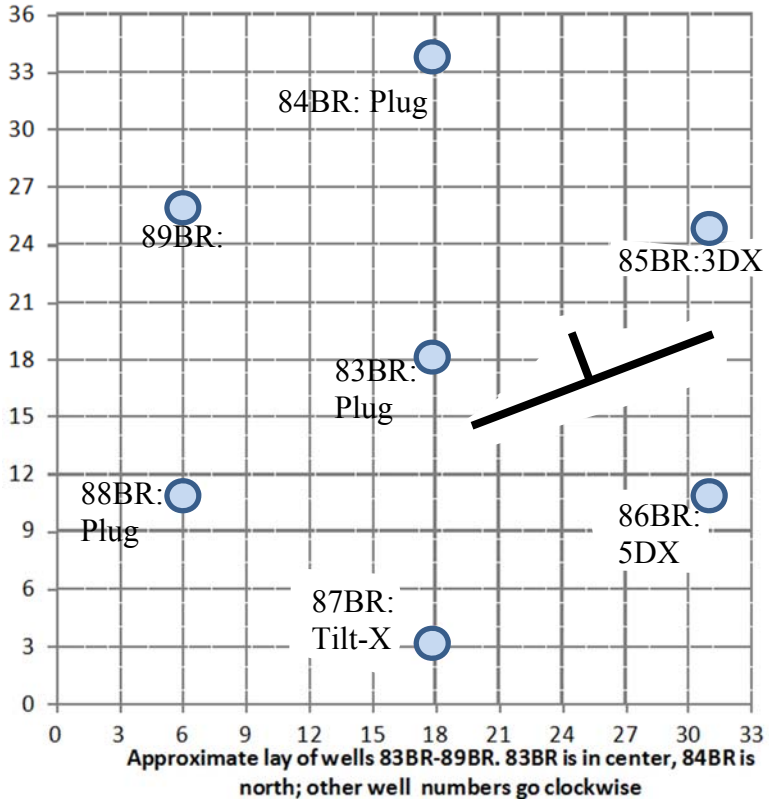

Figure 4.2-51. Map of wells at the NAWC site. Coordinates in ft. Bedding strikes NE and dips to the NW.

Field testing started with a shakedown test that included injecting potable water into 85-BR to confirm the instruments were working properly. This was followed by four pumping tests, which were conducted as follows:

Test 1. The well 86-BR was pumped for approximately 40 minutes at a constant rate of 5 gal/min.

Test 2. The well 86-BR was pumped for 1 hour approximately 12 hours after Test 1. The pumping rate was 5 gal/min.

Test 3. The pumping location was changed to 85-BR. The packer was deflated in the well, and the pumping lasted for approximately one hour at a constant rate of 5 gal/min.

Test 4. This involved turning off well that was pumping at a constant rate several hundred meters away. The well was turned off for 1 hour and the system allowed to recover. The response to recovery was monitored. There is no gauge data after the pump was turned back on for this test because the interrogator was turned off at this point.

The three instruments all generated data and the results were generally consistent with previous observations at other sites. Data were reduced using the equations in the previous section, and in Figure 4.2-52. Descriptions of the tests are outlined below along with observed data.

Test 1: Pumping Test

The first pumping test involved pumping from 86-BR for 41 minutes at a constant rate of 5 gal/min. The head dropped 2 m in the pumping well and 1 m in 85-BR. The average axial displacement was compression during pumping and extension during recovery. The maximum compression of a single gauge on 3DX was approximately 2.5 μm, but the average axial compression was ~1 μm.

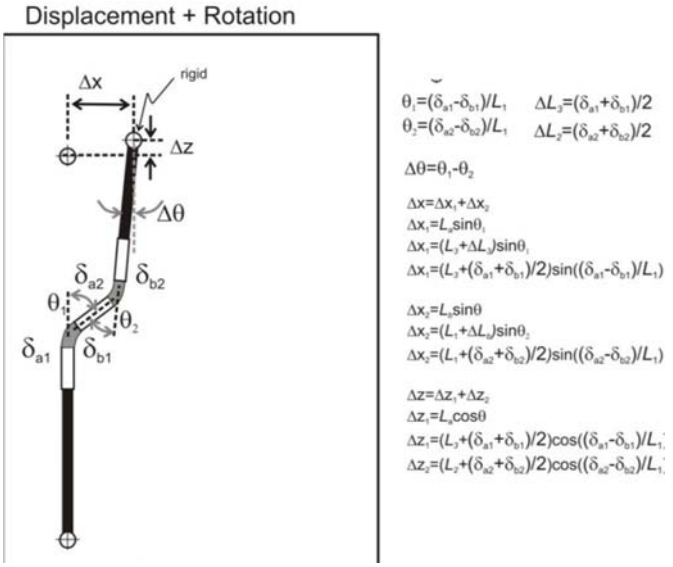

Figure 4.2-52. Geometry and analysis used to evaluate displacements with 5DX.

The response from 5DX, which was located in the pumping well, indicated approximately 8 μm of axial displacement occurred with 2 m of drawdown. The relationship between displacement and drawdown is hysteretic, however, and the late time slope is approximately 8 μm/m. Previous applications have shown that the late time slope is a better indicator of the compliance than the average slope. By comparison, the compliance measured by 3DX was much less, approximately 1 μm/m.

All the strain gauges in 5DX were compressed during pumping and extended during recovery, but two of the gauges in 3DX extended briefly at the beginning of pumping before changing direction. A similar response occurred at the beginning of recovery when compression occurred early and then it changed to extension.

Transverse displacement is calculated from differences in axial displacement among the strain gauges, which indicates bending of the instrument, so the changes in axial displacements in 3DX produce an erratic path that spans approximately 12 μm of transverse displacement (Figure 4.2-54). By contrast, the transverse displacement indicated by 5DX follows a smoother trajectory. It is characterized by displacement to the south during the first few minutes, followed by 15 μm of displacement to the N45E. Transverse displacements during recovery mirrored those from pumping, with an initial displacement to the north followed by 15 μm of movement in the S45W direction.

The 5DX instrument prepared for field testing at the NAWC site.

The 3DX instrument prepared for field testing at the NAWC site.

Borehole tiltmeterat NAWC

Overview of the NAWC test site.

Figure 4.2-53. Field testing at the NAWC site, July 2012.

.

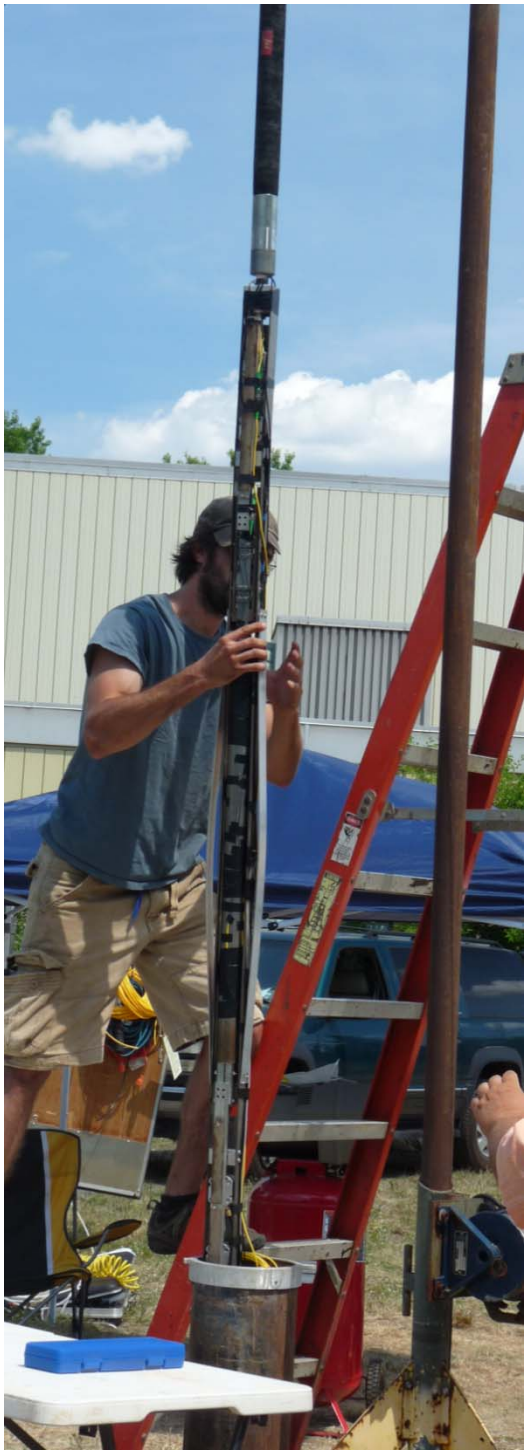

Field deployment of 5DX

Field trailer and set up at NAWC.

Rad-X

Figure 4.2-54. Deployment of instumentation at the NAWC Test Site, NJ. July 2012.

Test 2: Pumping test

The second pumping test involved pumping from 86-BR for one hour at a constant rate of 5gal/min, so it is slightly longer but otherwise similar to the first test.

The general responses from Test 2 are remarkably similar to those from Test 1, confirming the repeatability of the measurements. An exception is the pattern of transverse displacement from 3DX, which is approximately 9 μm to the NW during pumping. This is consistent with the direction from the previous recovery period, but it differs from the direction from the previous pumping.

Data from 5DX closely resembles the response from Test 1.

A borehole tiltmeter was deployed in the casing in 87-BR during this test. It indicated tilting to the east and ESE of several microradians during this test (Figure 4.2-57).

Test 3: Pumping Test

The pumping location was changed to 85-BR for the third pumping test (Test 3). The packer was deflated in the well, and the pumping lasted for one hour at a constant rate of 5gal/min. Test 3 resembles the previous tests except the location of the pump was changed from the well where the 5DX was located to the well where the 3DX was located.

The head dropped 1.3 meters in the pumping well, 85-BR, and approximately 1 m in 86-BR (Figure 4.2-55). All the strain gauges in both instruments compressed during pumping and extended during recovery. The maximum compressions measured by both 3DX and 5DX was similar to the previous tests. The compliance from Test 3 was 1 μm/m from the 3DX and 8 μm/m from 5DX, which also is consistent with other tests.

The plot of displacement as a function of head from 5DX is more nearly linear from Test 3 than it is from Test 1 and Test 2 (Figure 4.2-56). The hysteretic response measured by 5DX during the first two tests changed to a nearly linear response when the pump was moved from the well with the 5DX to an adjacent well. This is consistent with expectations.

The transverse displacement from 5DX roughly doubled in size and swung to the east slightly (to ~N70E) compared to the previous tests.

Test 4: Shut-in test from remote well

Test 4 involved turning off the pump in a dewatering well roughly 100 m from the test site for one hour. This well was in steady use, so turning it off was expected to cause the heads to rise over a broad area.

The observed response was that turning off the pump caused the water level to rise 0.07 meters in 85-BR (Figure 4.2-55). This response is less than 1/10 of that from the other tests. When the pump was turned off all the gauges contracted slightly and then they extended when the pump was turned back on. This is consistent with the expected strains caused by a pressure change, although it is noteworthy that the sign of pressure change with time for this test was opposite that from earlier tests.

The compliance during this test was larger than that during the local pumping tests. It increased from 1 μm/m to 1.6 μm/m with 3DX and from 8 μm/m to 16 μm/m with 5DX.

The transverse displacement indicated by 5DX was approximately 5 μm along a trend N70E. In this case, displacement occurred to NE when the pressure was decreasing and to the SW when it was increasing, which is consistent with all the previous tests.

Discussion and Conclusions

The field test at NAWC demonstrated that the instruments can be mobilized, deployed and successfully provide data describing the deformation of boreholes during injection and pumping tests. All three devices detected strains of reasonable magnitude and direction (Figure 4.2-58). The shut-in test demonstrated sensitivity to deformation from remarkably small changes in pressure.

5DX

This was the only field test conducted with the 5DX during this investigation. The measurement concept was proven using the 3DX at other field areas, but the data from NAWC show the advantage of the 5DX over the 3DX. The instrument includes 2 sets of flexures that can accommodate deformation. 3DX measures one set of flexures and 5DX measures both sets.

Under ideal conditions, the 3DX will give the same results as the 5DX, or other instruments like the Tilt-X. However, this requires that the deformation of the strain bar is symmetric. This would occur when the anchors remain parallel during deformation. This appears to be a reasonable approximation in some cases. In other cases, however, the deformation of the strain bar is not symmetric and one set of flexures bends more than the other set. This causes errors in the transverse displacement calculations of 3DX. 5DX measures both sets of flexures, so it should be able to correctly resolve this scenario.

This may explain the differences between 3DX and 5DX transverse displacements during this test. The results from 5DX are quite repeatable, and consistent among the tests. Data from 3DX are erratic by comparison. These differences may result from the more complete measurements made by the 5DX.

Even though the data from the 5DX was more consistent than that from the 3DX, the magnitude of the data from 5DX was significantly (roughly 8x) greater than that from the 3DX. The results from the 3DX were more consistent with previous tests at NAWC [*Murdoch et al.*, 2009]. It is possible that the interval straddled by the 5DX was particularly compliant, however, additional work on calibration and validation of the instruments is needed to resolve this issue.

CASING DEFORMATION

This test demonstrated the feasibility of obtaining useful displacement data in casing, from the data generated by the borehole tiltmeter. The wells at NAWC were completed as open holes, so the 3DX and 5DX were not deployed in casing because we wanted to measure deformation in the vicinity of the rock where flow was occurring.

FIBER OPTIC GAUGES

The fiber optic strain gauges (FBG gauges) appear to be viable sensors for field measurements. However, data from two sets of gauges appear to be anomalous, and we expect this was a result of loss of gauge sensitivity during deployment. This effect could have occurred by strain applied to the fiber, gauges or to splices in the fiber.

FBG strain gauges, optical fiber, and splices are fragile and are vulnerable during handing. The design of the 5DX includes a registration system intended to restrict movement of the strain bar and protect the gauges during deployment. The deployment of 5DX during the NAWC test involved considerable manipulation of the device because the caliper logs for 86BR indicated a borehole diameter that was larger than the actual diameter. We set up the 5DX based on the caliper log diameter, and this caused the instrument to become stuck in the hole. We were able to remove the instrument and reconfigure it to fit in the borehole, but this required significant manipulation. The registration system protected the gauges from breakage during this manipulation. Large strains of the gauges will break the fiber and this did not occur. Nevertheless, even though the fiber remained intact it appears that the sensitivity of several gauges were reduced during deployment. This was probably an inadvertent consequence of handling.

The design includes redundancy, so we were able to compensate for the anomalous results from the gauges with suspected reduced sensitivity. Nevertheless, these results indicate the need to further harden the instruments before full-scale application in a deep well suitable for CO_2 sequestration.

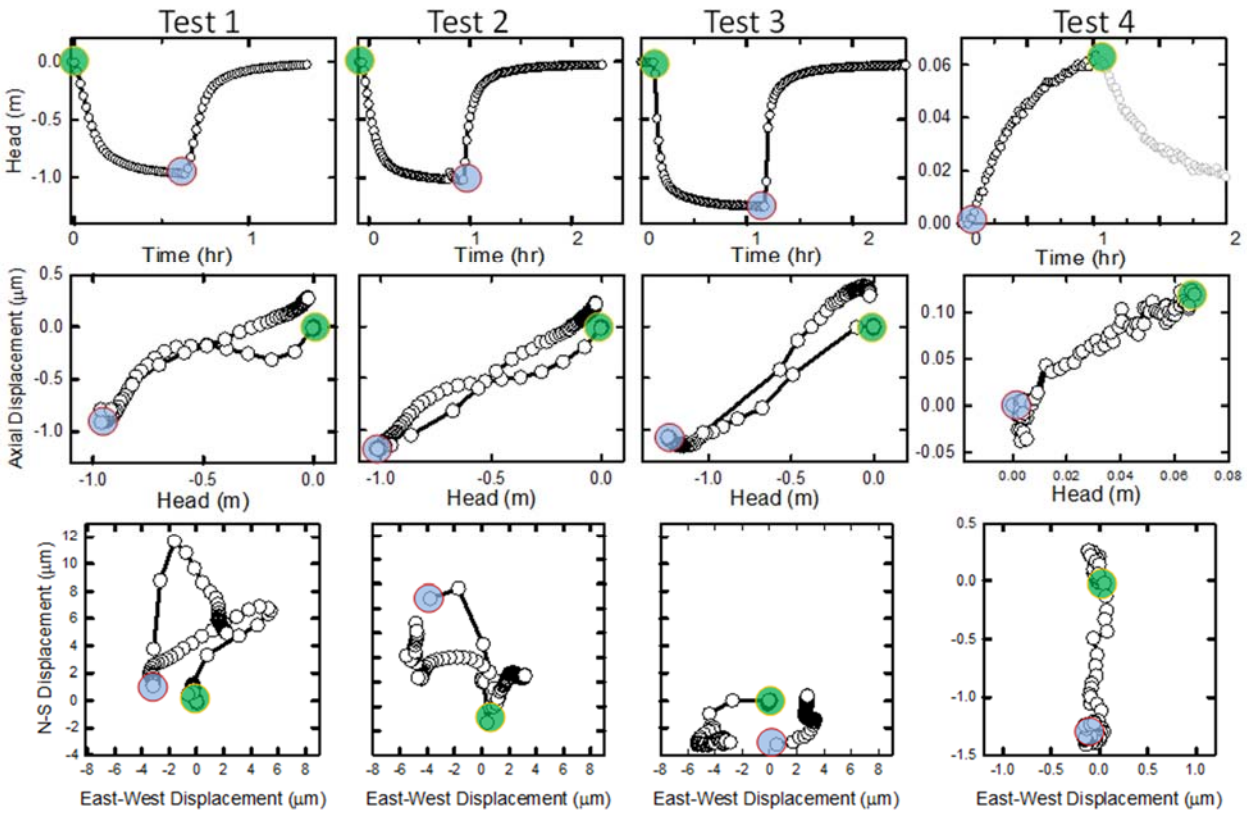

Figure 4.2-55. Results from 3DX in 85-BR during 4 tests at NAWC Test Site, July 2012. Top row is head as a function of time. Middle row is average axial displacement as a function of head. Lower row this is transverse displacement magnitude and direction.

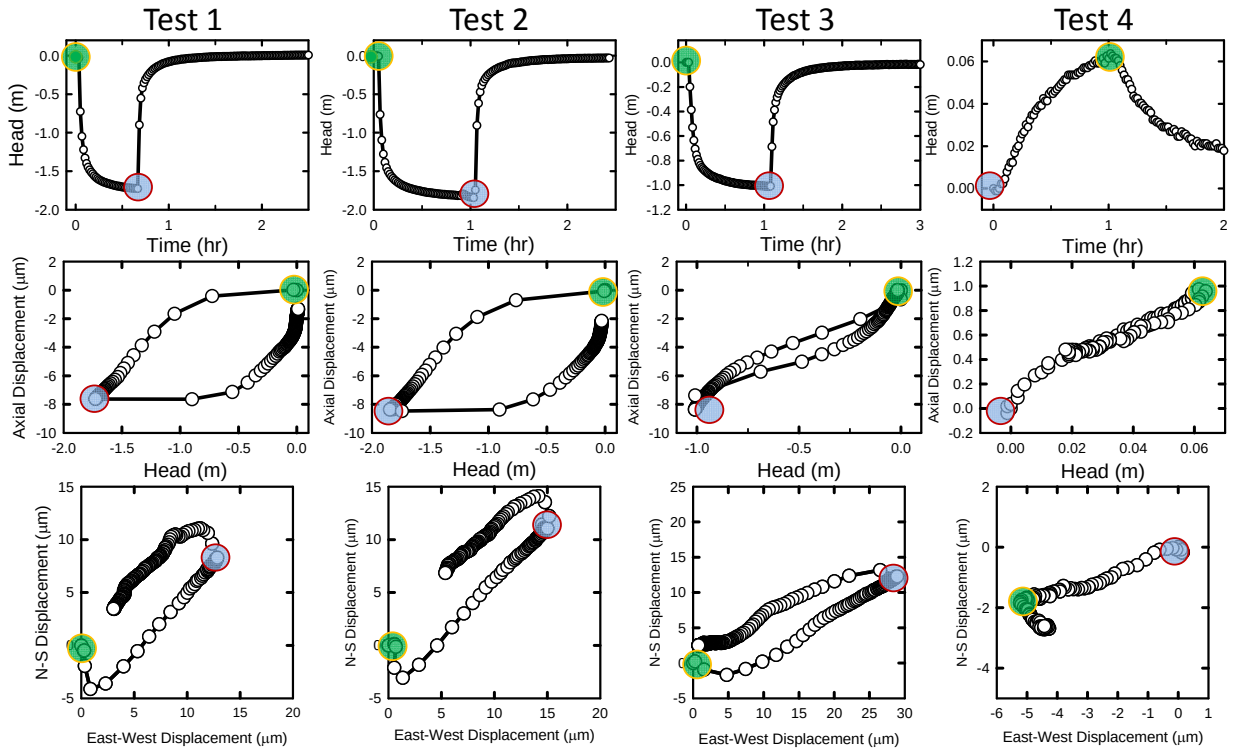

Figure 4.2-56. Results from 5DX in 86-BR during 4 tests at NAWC Test Site, July 2012. Top row is head as a function of time. Middle row is average axial displacement as a function of head. Lower row this is transverse displacement magnitude and direction.

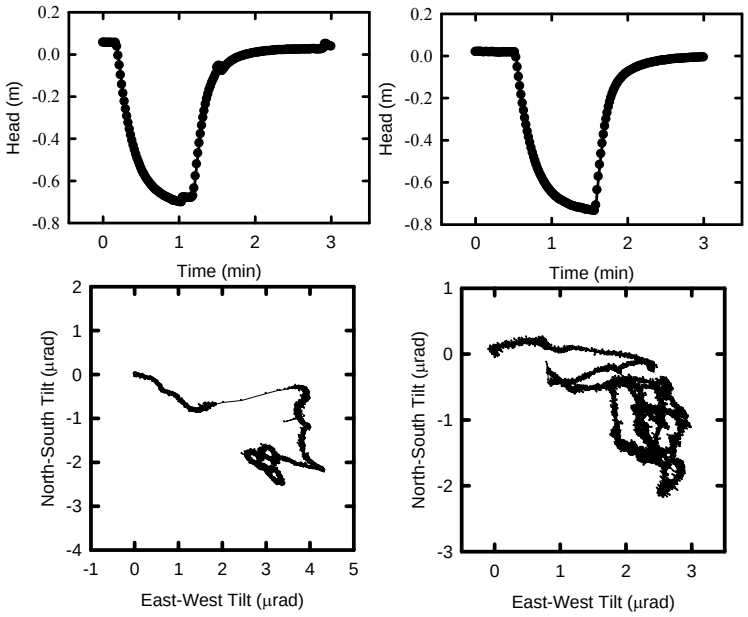

Figure 4.2-57. Pressure head and tilt data from 87-BR during Tests 2 and 3.

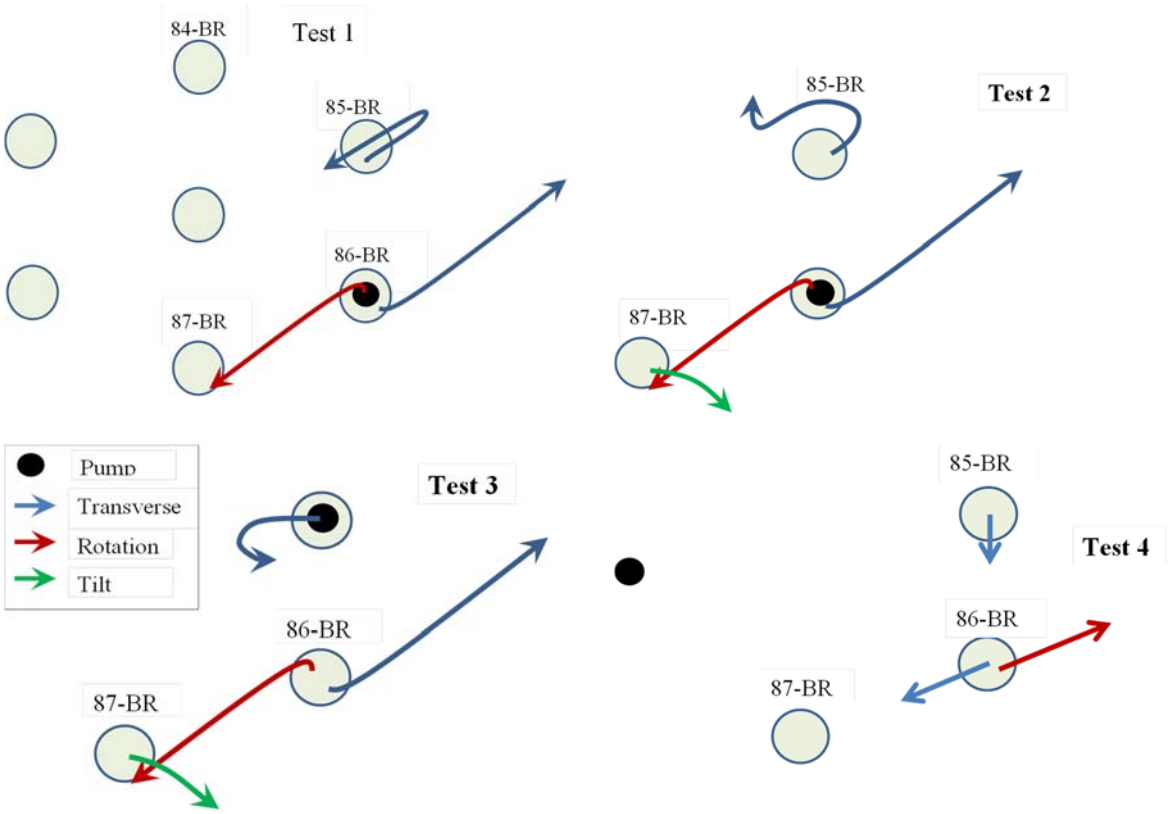

Figure 4.2-58. Summary schematic of the responses from the 3DX in 85-BR, the 5DX in 86-BR and the tiltmeter in 87-BR.

Clemson Field Site, Clemson, SC

Field tests were conducted in two wells located within fracture biotite gneiss (Nelson et al. 1998) at the South Carolina Botanical Garden in Clemson, South Carolina, USA (Figure 4.2-59). Overlying the bedrock is approximately 20 m of saprolite, which saprolite consists of kaolinite, quartz, and iron oxide [*Svenson*, 2006]. The saprolite grades downward through a relatively permeable transition zone into fractured gneiss bedrock.

A borehole survey was done by Svenson (2006) to identify the fractures at Clemson well field (Figure 4.2-60). The distances between fractured zones and single fractures range from a few tenths of a meter to several meters. Most of the fractures occur between 20 meters and 40 meters depth. There are three fracture zones at approximately 25 m, 36 m, and 50 m depth. Tests to determine the hydraulic connection between LAR-4 and LAR-3 were done by Slack (2010). Straddle packers were deployed in the boreholes to separate the zones from the rest of the well during pumping tests. The results determined that the three fractured zones in LAR-3 and LAR-4 are hydraulically connected [*Slack*, 2010].

A study by Slack (2010) sought to identify hydraulically active connections between wellbores at the Clemson well field (Figure 4.2-61). The results can be used to determine the dip of the fractures based on their corresponding depths. The results of the study are that the fracture at 25m in LAR-4 and LAR-3 are connected to each other, but are poorly connected to the other wells. The fracture zones at 36 m and 50 m are intersected by all four wells. The strike of the

fracture zone at 36 m is approximately EW and it dips to the south roughly 20 to 40 degrees. This permeable zone consists of several fractures spaced a few meters apart. The spacing between the wells is 5 m, which results in uncertainty in estimates of dip angle.

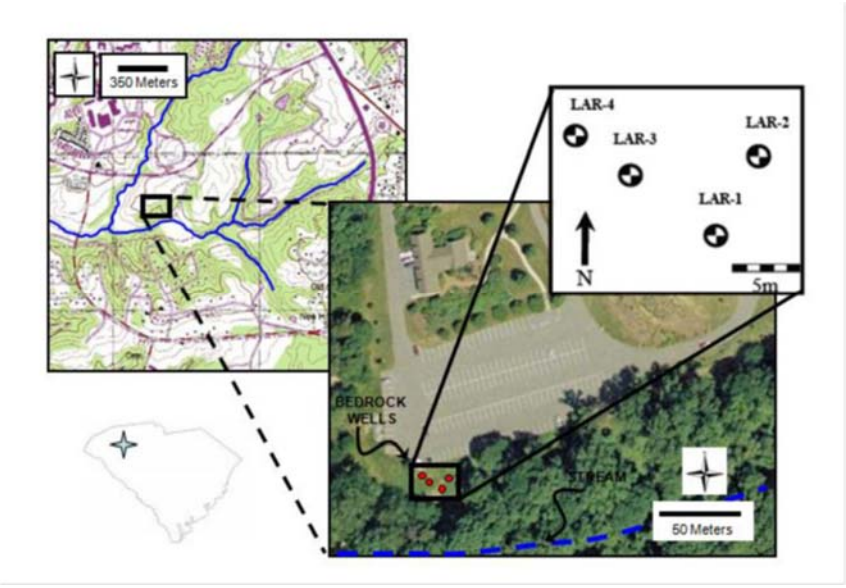

Figure 4.2-59. The location of the wells at the Botanical Gardens in Clemson, South Carolina, USA (Slack, 2010). The pump was located in LAR-3 for all the tests, and the 3DX was deployed in LAR-2 and LAR-4.

Field Tests

Initial testing of the 3DX was in the LAR-2 borehole (Figure 4.2-59). The 3DX was deployed so the center of the reference rod was at a depth of 23.4 meters. There were two fractures between the anchors of the 3DX at this depth. The pumping well is LAR-3, which is located approximately 6 m due west from LAR-2.

The 3DX was deployed in a borehole for a week while displacement, barometric pressure, and pressure were monitored. A series of hydromechanical well tests were be used to stress and cause 3D displacement within the fractures. The hydromechanical well tests involve pumping water from the aquifer while measuring the pressure change and the 3D displacement in the borehole where the 3DX is located.

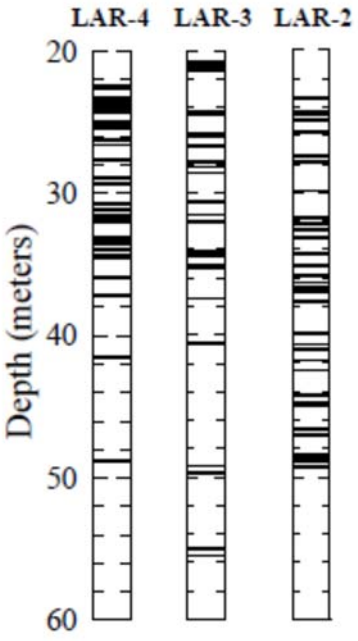

Figure 4.2-60. Profile of boreholes in the lower well field showing the fracture distribution [*Slack*, 2010].

The materials needed to conduct a hydromechanical well test are the 3DX, a pressure transducer, well pump, fiber optic interrogator, computer, and air compressor. The initial steps for carrying out the hydromechanical well at the Clemson site are similar to the tests done in Tsukuba, Japan. The 3DX needs to equilibrate for at least one day preferably two days before testing to allow for equilibrium. A pressure transducer is set in the well above the 3DX to record the head change. A borehole camera is then used to determine the orientation of the 3DX. The camera has a compass attached to it, and the top of the 3DX was sighted with the compass using the camera. Later in the testing program we installed an electronic compass on the instruments, but the camera provided an approximate estimate of orientation during the early tests. The well tests involved pumping water from another well nearby at a constant rate of 7 gal/min for duration of four hours. The

recovery takes approximately eight hours to complete.

Results

The results include data from six hydromechanical well tests performed in two different wells, an ambient monitoring analysis. The data include the pressure change, the axial displacement, and the transverse direction and magnitude. This suite of tests involved the 3DX and the Tilt-X; these tests were conducted prior to the development of the 5DX.

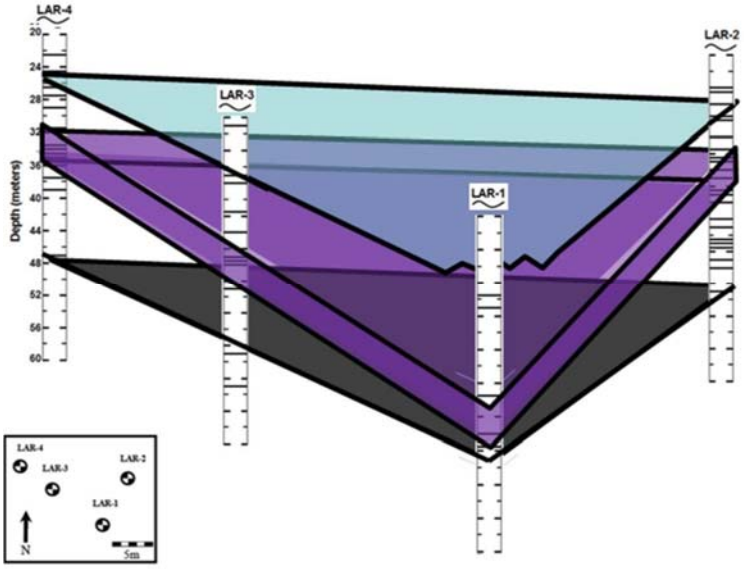

Figure 4.2-61. Interpretation from Slack (2010) of the permeable zones using straddle packer and MLS methods. The colored triangles represent the hydraulically dominant fractures or fracture zones identified at the Clemson University well field.

PUMPING TESTS AT WELL LAR-2

Hydromechanical Well Test 1was done with the 3DX at a depth of 24.3 meters straddling 2 fractures in LAR-2. Hydromechanical Well Test 2 was done with the 3DX at a depth of 24.3 meters straddling 2 fractures in LAR-2. The time between this Test and Test 1 was approximately 24 hours. Hydromechanical Well Test 3 involved retracting the 3DX anchors, raising it by 5 m, and then deploying it back to its original location. The purpose of the test is to evaluate the effects of moving the device. Hydromechanical Well Test 4 was done approximately 48 hours after the device was moved. This test involved removing the 3DX from the borehole, rotating it, and then deploying it at the same location with a different orientation. The 3DX was rotated 135 degrees counter clockwise. Hydromechanical Well Test 5 involved rotating the 3DX by an unknown amount. The orientation was found by comparing the results to the other three tests to determine the orientation.

The drawdown for all the tests is 1.2 meters (Figure 4.2-62). The individual gauges all compressed during pumping and extended during recovery for all the tests (Figure 4.2-62). Individual gauges compressed by different amounts based on the orientation of the device. The average axial displacement of the gauges was ~1.2 microns (Figure 4.2-62). The average axial displacement compressed during pumping and then extended during recovery to approximately its original displacement (Figure 4.2-63). The axial displacement decreased slightly at the end of

pumping. The late-time slope during recovery of the pressure displacement graph is the compliance of the fracture. The compliance of all tests is approximately 1.1 μm/m.

The direction of the transverse displacement is generally the same for all the tests. The 3DX displaces towards the southeast (top anchor displaced relative to bottom anchor) in the first 15 minutes (Figure 4.2-63). The transverse direction switches directions suddenly to the north east for approximately 35 minutes. It then begins a gradual direction change towards the south east for the remainder of pumping (Figure 4.2-63). The transverse displacement during recovery changes signs, and displaces back to its original position during pumping. The sudden changes in the transverse direction correlated to times when the pump was turned on and then off again. The magnitude of the transverse displacement is between 6.4 μm and 11.5 μm for all the tests.

There was a jump in the transverse displacement to the east when the pump was turned on for Test 4. After the jump the transverse displacement is towards the south in the first 15 minutes, and then for approximately 35 minutes the displacement is south east to east, and then to the south east (Figure 4.2-63). This is similar in trend to the other tests. The path of the transverse displacement during recovery is opposite of the one during pumping.

The relative error is used to calculate the total axial and transverse displacement error. The axial displacement error is approximately 27% of the total displacement. The maximum error is approximately 0.9 μm (Figure 4.2-64). The relative error of the transverse displacement for all tests is 30% in both directions, and the maximum error is 1.3 μm (Figure 4.2-65). The relative error for transverse and axial displacement is a fraction of the total displacement measured, so we can assume it is real.

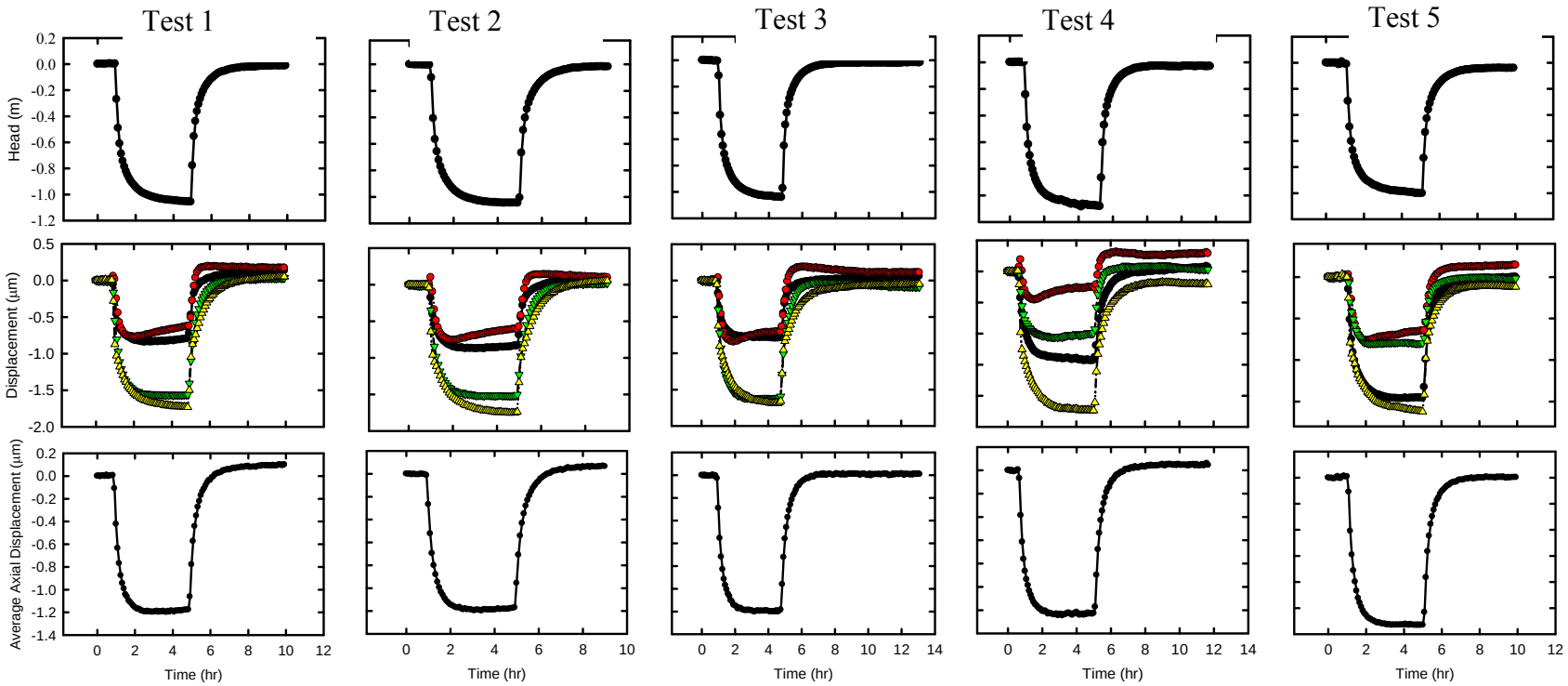

Figure 4.2-62. Top plot is the pressure head during a well test as a function of time for all the tests. The middle graph is the axial displacement of each individual gauge as a function of time for all the tests. The bottom graph is the average axial displacement as a function of time for all the hydromechanical well tests at the Clemson well field.

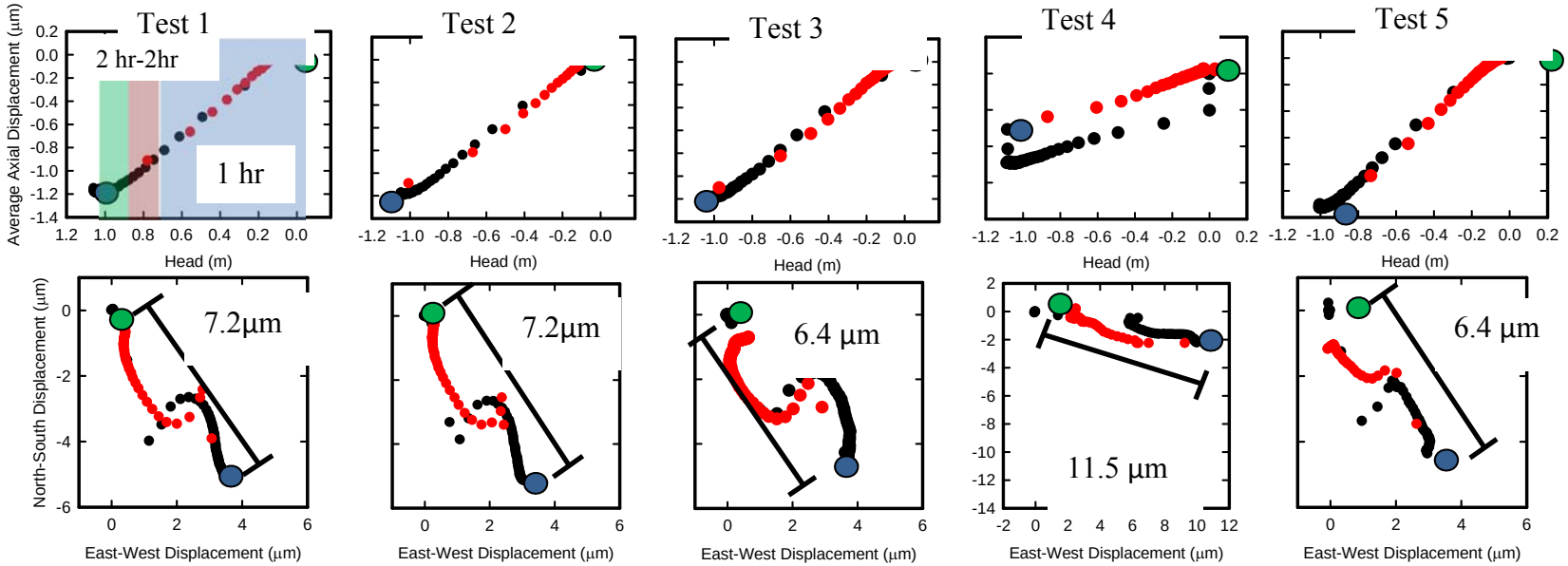

Figure 4.2-63. The top graph is the average axial displacement during a well test plotted as a function of head for all the tests. The bottom plot is the transverse displacement plotted relative to the cardinal directions for all the hydromechanical well tests at the Clemson well field. The green dot is when the pump is turned on; the blue dot is when the pump is turned off. The black points are during pumping and the red points are during recovery.

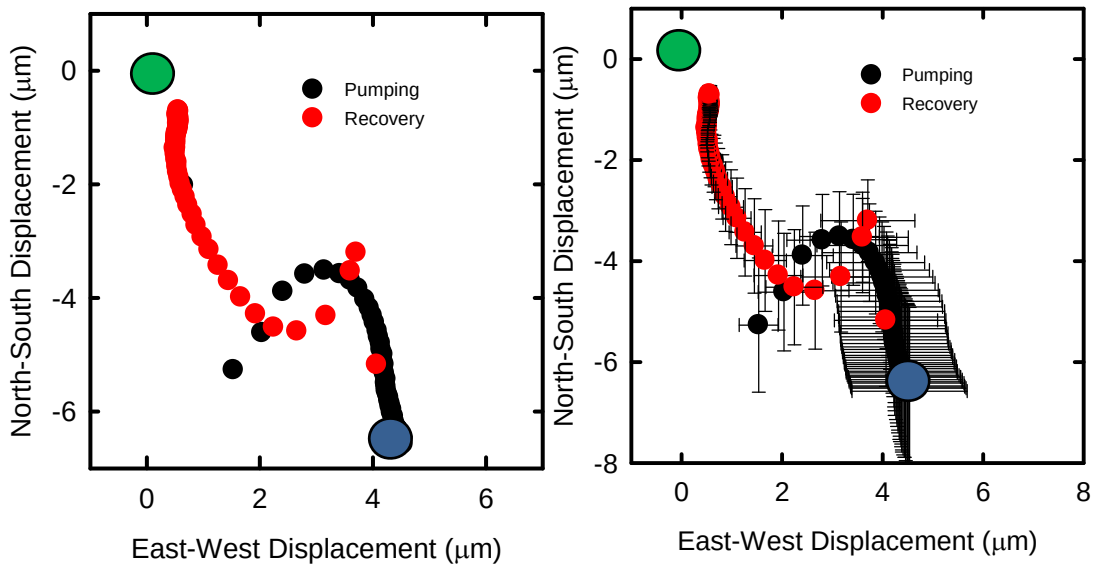

Figure 4.2-64. (a) Transverse displacement relative to the cardinal directions during well test 1. (b) Transverse displacement plotted with error bars. The green points are the start of pumping the blue point is when the pump is turned off.

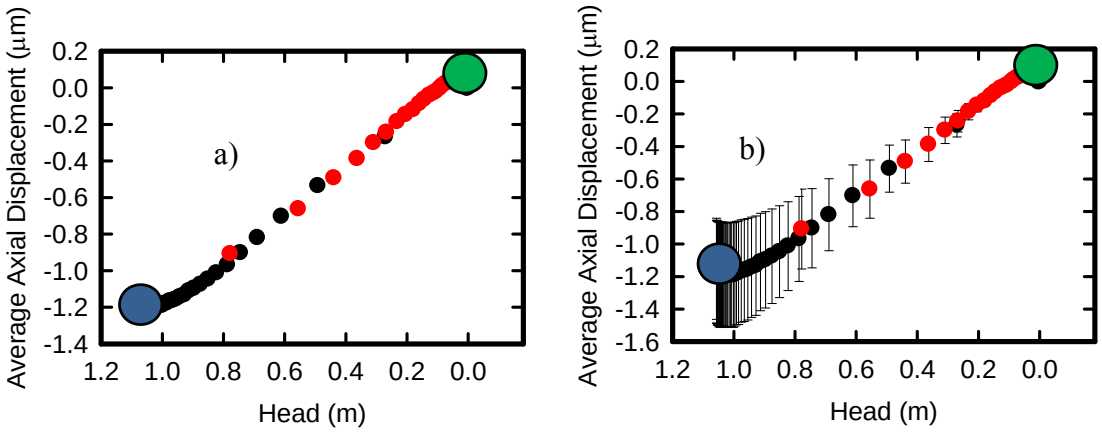

Figure 4.2-65. (a) Axial displacement as a function of pressure during well test 1. (b) Axial displacement plotted with error bars. The green points are the start of pumping the blue point is when the pump is turned off.

PUMPING TESTS AT WELL LAR-4

The 3DX was moved to LAR-4 to a depth of 24 meters where a hydromechanical test was done. The results of this test can be compared to the results of the Tilt-X which is a device that measures axial extension and tilt in a borehole. The Tilt-X has been used extensively in LAR-4, so the direction of tilt in the borehole during hydromechanical well tests is known.

The head dropped approximately 1.6 meters (Figure 4.2-66). The axial displacement was 2 µm. The transverse displacement was approximately 6.3 µm to the west. The compliance of the fracture is approximately 1 µm/m (Figure 4.2-67).

The transverse displacement is to the south initially and then to the southwest for approximately 30 minutes. Displacement then trends to the west-northwest for approximately an hour, and it trends to the southwest for the remainder of pumping it (Figure 4.2-68).

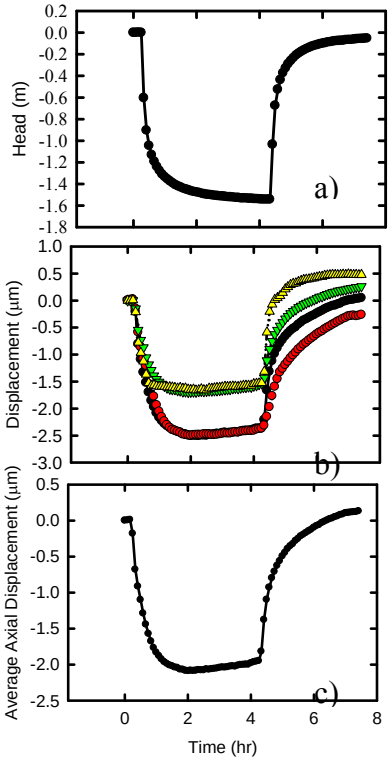

Figure 4.2-66. (a) Pressure head during a well test as a function of time (b) Axial displacement of each individual gauge as a function of time (c) Average axial displacement of the four gauges as a function of time for Test 6.

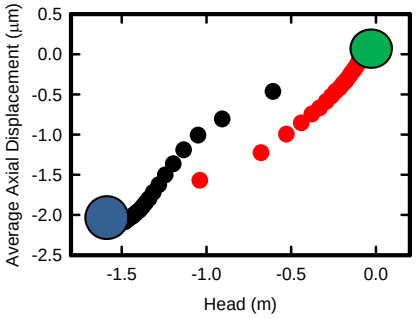

Figure 4.2-67. Average axial displacement during a well test plotted as a function of head during the hydromechanical well test 6.

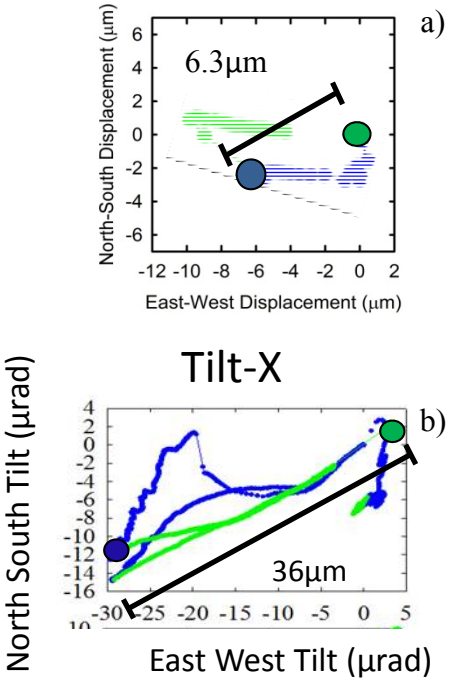

Figure 4.2-68. Transverse displacement plotted relative to the cardinal directions for both the (a) 3DX and (b) Tilt-X from the same depth of 24 meters in LAR-2.

AMBIENT MONITORING AT LAR-2

The 3DX was deployed in LAR-2 at a depth of 24.3 meters for 5 days. This is the same depth used during the previous set of hydromechanical well tests. The barometric pressure and the total pressure in the borehole were monitored. The water level is the difference between total pressure and the barometric pressure. The Tilt-X was measuring the axial displacement and tilt in LAR-4 at the same time. The orientation of the gauges is based on the orientation found during hydromechanical well test 5.

The results of the axial displacement and water level vary with a period of 1 day. In the morning the water level reaches a minimum while the displacement is at a maximum opening, and both signals switch in the afternoon (Figure 4.2-69). The magnitude of the displacement is approximately 0.05 microns. The transverse displacement is also diurnal. The displacement occurs over a 6 hour period in the middle of the day. The rest of the time the transverse displacement is increases steadily on a long-term trend of approximately 0.01 micron/day.

The transverse displacement is approximately 1.75 microns in the north and south direction and submicron in the east and west direction (Figure 4.2-70). There is a long-term transverse displacement signal trending downward and diurnal transverse displacement signal that occurs in response to the water level change. When the fracture is closing, the top anchor of the 3DX tilts to the north and to the south when the fracture is opening (Figure 4.2-70).

The 3DX and the Tilt-X have a similar response to the diurnal water level change (Figure 4.2-71). They both indicate axial extension when the water level drops and compression when the water level rises. There is also a long-term trend in the Tilt-X signal, where the axial displacement increases with time. The magnitudes of the 3DX and Tilt-X signals are similar.

The transverse displacement is approximately 2 microns in the north and south direction and submicron in the east and west direction (Figure 4.2-71). There is a long-term transverse displacement signal trending downward and diurnal transverse displacement signal that occurs in response to the water level change. When the fracture is closing, the top anchor of the 3DX tilts to the north, and when it is opening the tilts is to the south (Figures 4.2-69 and 4.2-70).

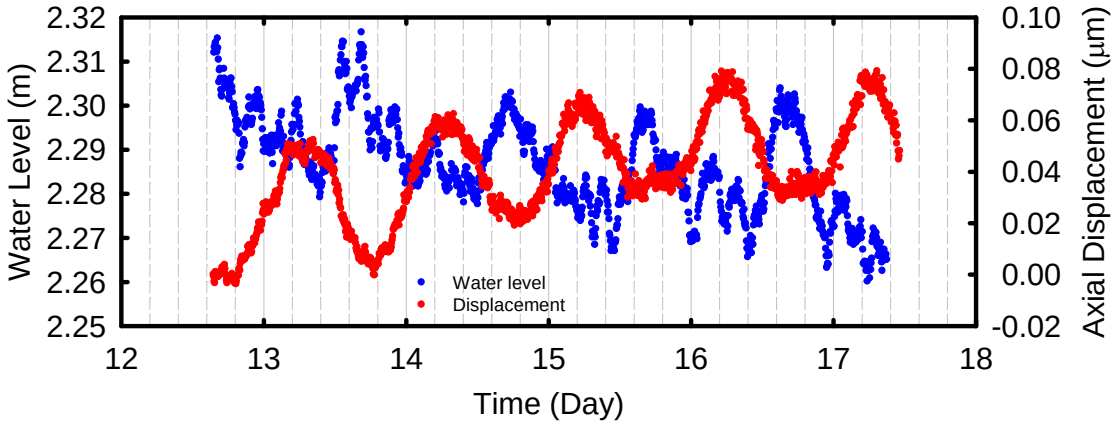

Figure 4.2-69. The average axial displacement and the ambient water level as functions of time during ambient conditions.

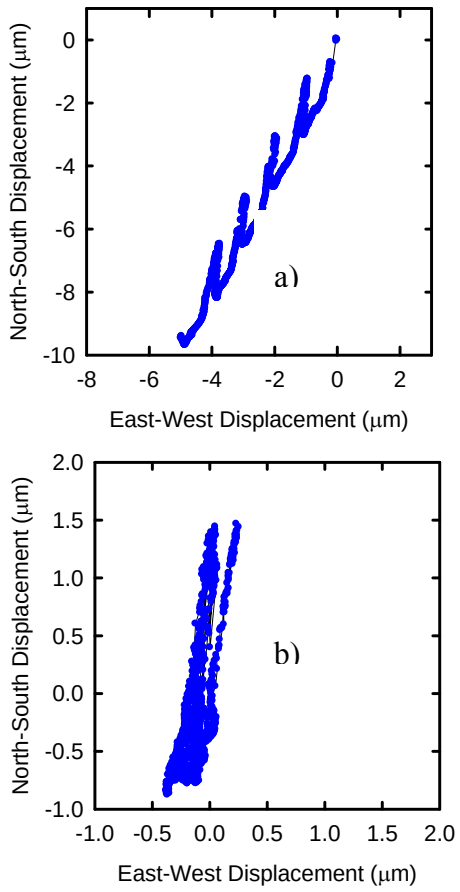

Figure 4.2-70. (a) The transverse direction of the 3DX during ambient conditions. (b) The transverse direction with the SW trend taken out during ambient monitoring.

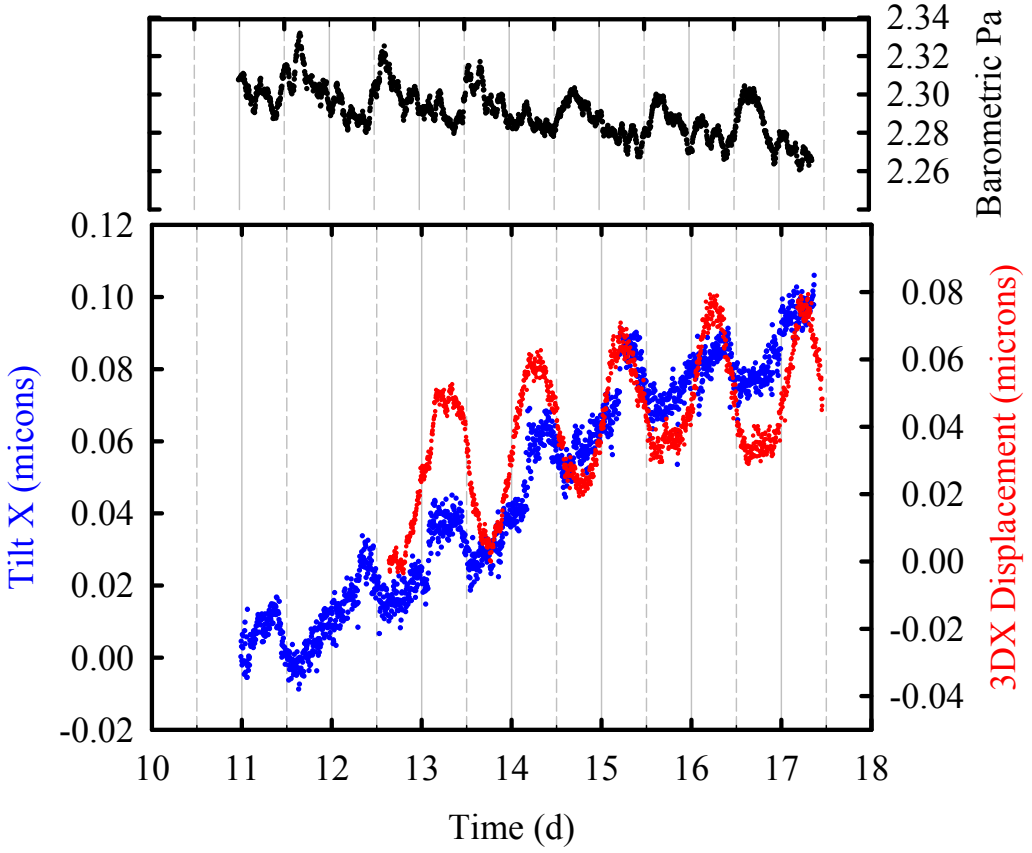

Figure 4.2-71. (a) Water level as a function of time. (b) Axial displacement measured by the Tilt-X and the 3DX deployed in neighboring wells as a function of time during ambient conditions.

TEMPERATURE EFFECTS

A test was done when displacements were measured while the anchors of the 3DX were retracted. LAR-1 was pumped for approximately one hour with the 3DX in LAR-2. The resolution of the temperature monitoring device is ±0.001 ºC. The temperature was at a consistent temperature of 18.711 ºC for the duration of the test. There was a brief temperature change to 18.616 ºC that occurred for approximately 5 minutes during the test, and then was back to 18.711 ºC for the remainder of the test. The displacement of the 3DX during this time did not indicate that there would be signals caused by temperature

Discussion

The five hydromechanical well tests from LAR-2 were used to evaluate the repeatability of the 3DX when it is deployed at the same depth. The axial displacement trend for all five tests was similar. The maximum axial displacement as a function of pressure was 1.2 µm for all the tests with a drop in head of approximately 1.2 meter (Figure 4.2-72). The axial displacement decreased during pumping and increased during recovery for all the hydromechanical well tests. The late time slope of the axial displacement as a function of pressure is 1 µm/m for all the tests. The shape of the axial displacement as a function of pressure for most of the tests is the axial displacement is less during pumping then at the same head during recovery. This creates a hysteretic shape in the graphs. The general transverse displacement trend is similar for all five tests (Figures 4.2-72 and 4.2-73). The transverse direction for all the tests was generally to the south east initially, then to the east, finally to the southeast for the remainder of pumping. The magnitude of the transverse displacement in the east and west direction during pumping is between 3 and 11 µm. The magnitude of the transverse displacement in the north south direction during pumping is 3 and 5 µm. The transverse displacement graph shows that the 3DX returns to its initial location during recovery.

The results from Test 4 are slightly different than the other tests. There were large jumps after the pump was turned on and again when it was turned off during Test 4. This could be due to pumping in the area, or a slip in the formation. The transverse displacement during Well Test 4 is similar to the other three well tests in that it follows a similar trend, but it is more eastward trending. For this test the transverse displacement is to the south when the pump is turned on, then to the east, and then to the south east for the rest of pumping. The fifth well test which had an unknown orientation had the same transverse displacement trend as tests 1 through 3, which is how its orientation was determined.

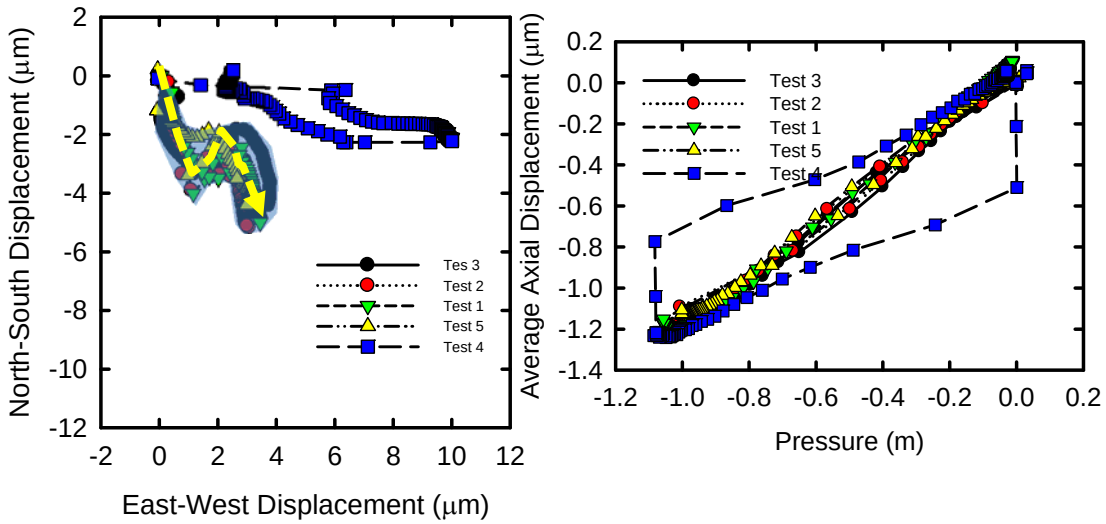

Figure 4.2-72. (a) Transverse displacement all 5 tests in LAR-2 (b) Axial displacement as a function of pressure graphs for all 5 tests in LAR-2.

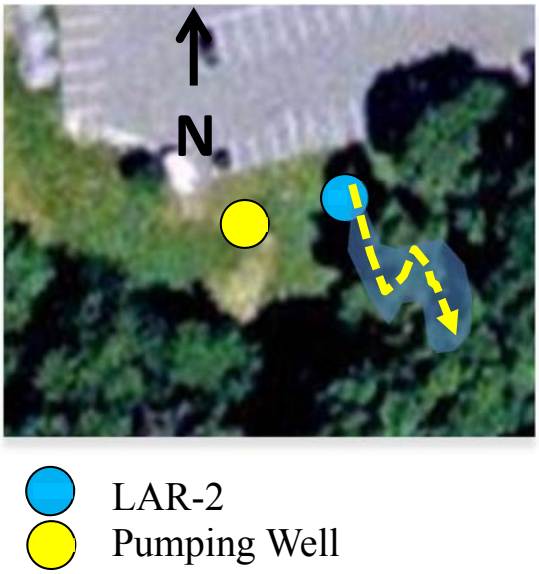

Figure 4.2-73. The general transverse displacement direction for five hydromechanical well tests.

3D DISPLACEMENT DURING AMBIENT MONITORING

The 3D displacements during ambient conditions are a result of the diurnal fluctuations in water level. When the water level drops the fracture opens and when the water level rises the fracture closes. This occurs because an increase in barometric pressure causes water in the well to be displaced into the fracture. This causes the fracture to open, just as injection using a pump or slug opens the fractures.

The transverse displacement direction of the 3DX during ambient monitoring is to the north when the fracture is closing and to the south when the fracture is opening. It appears that

the transverse displacement direction follows the southward dip direction of the fracture zone at approximately 35 m. When a dipping fracture closes, rock on the hanging wall of the fracture will transversely displace up dip relative to the lower boundary (Figures 4.2-74 and 4.2-75). This is a similar effect seen by Burbey et al. (2012), where they characterized the dip direction of a fracture based on the tilt direction. This explains the transverse displacement observed by both the 3DX and the Tilt-X — displacement occurred in the up-dip direction to the north when the fracture was closing and in the down-dip direction when the fracture was opening (Figure 4.2-70).

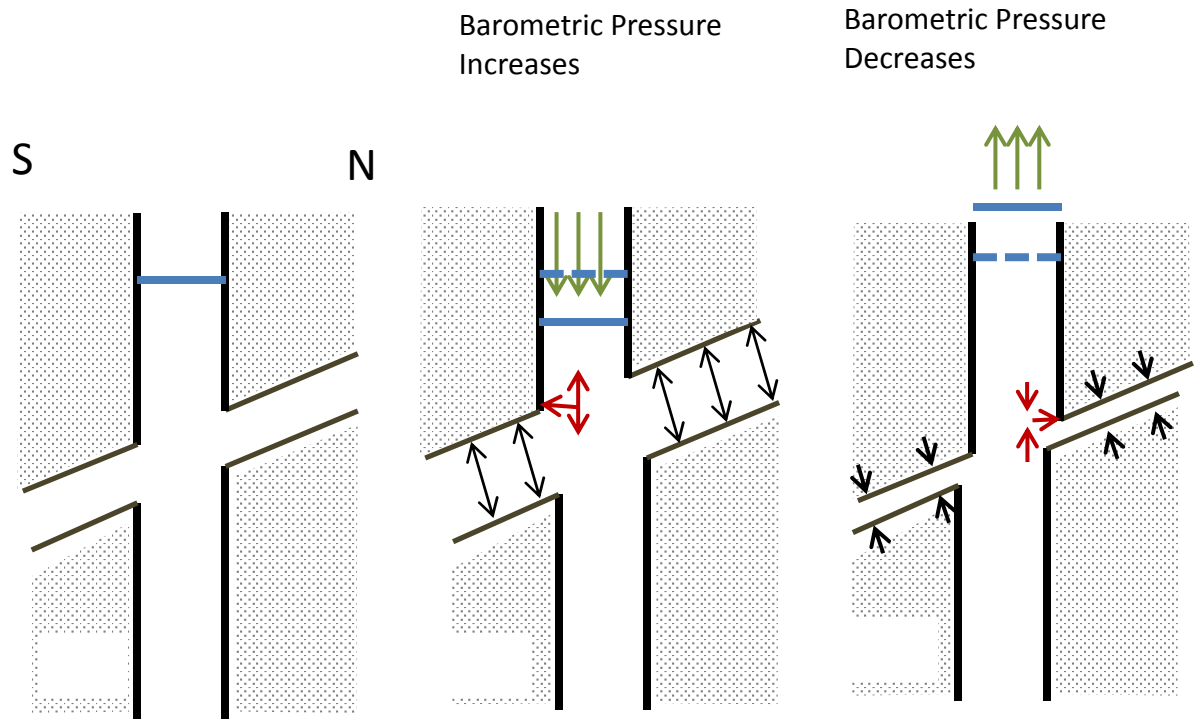

Figure 4.2-74. (a) Conceptualization of fracture intersecting a borehole. (b) When barometric pressure increases fracture opens and transversely displaces down dip. (c) When barometric pressure decreases fracture closes and transversely displaces up dip.

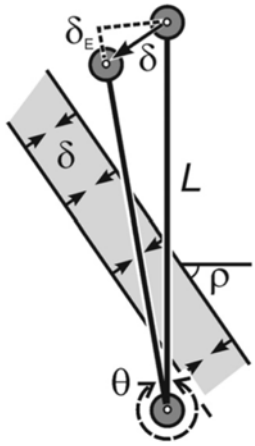

Figure 4.2-75. Displacements during closing of a dipping fracture showing tilt, θ, displacement measured by the extensometer, δ_E, and the normal displacement of the fracture, δ. Dip of the fracture is ρ. L is gauge length [*Burbey et al.*, 2012].

AXIAL DISPLACEMENT DURING HYDROMECHANICAL WELL TESTS

The results from previous hydromechanical well tests indicate that the axial displacement as a function of pressure is a hysteretic function [*Svenson et al.*, 2008; *Schweisinger and Murdoch*, 2011; *Burbey et al.*, 2012]. This means that the axial displacement is larger after the pump is turned off compared to when the pump is on for the same head level. The reason for this is when the pump is first turned on the pressure wave is spread over a small area. The fracture is responding elastically to these local pressure changes by deforming within the vicinity of the drop in pressure [*Murdoch and Germanovich*, 2006]. When the pump is turned off the induced pressure change has spread out, affecting a larger area. Due to the differences in the sizes of the pressure fronts when the pump is turned on and off, there is more leverage to cause the fracture to deform. This in turn causes the axial displacement to be larger during recovery compared to during pumping, resulting in hysteresis in plots of displacement as a function of hydraulic head during well tests.

Data from the 3DX and 5DX are consistent with results from Tilt-X and earlier measurements with extensometers. All of them indicate that compression typically occurs during pumping and extension occurs during recovery. Hysteresis is better developed in pumping wells than in monitoring wells. Anomalous responses occur locally or briefly, and appear to result from local heterogeneities.

The compliances measured by 3DX and Tilt-X are similar. Both of them indicate values of approximately 1 mm/m for the shallowest fractures at the Clemson Well Field. It appears to be feasible to determine compliance values from measurements of axial displacement during ambient conditions.

TRANSVERSE DISPLACEMENTS AND TILT

The results from LAR-2 are from the 3DX at a depth of 24.3 meters, and the results from LAR-4 are from the Tilt-X at a depth of 22 meters (Figure 4.2-76). These two zones were identified by Slack (2010) as being hydraulically connected, and dipping to the south. The pumping well is between both boreholes. The transverse displacement observed in both

boreholes is in opposite directions during the beginning of pumping, and by the end of pumping is in the same direction. The fracture in LAR-4, measured by the Tilt-X, tilts towards the south west, west, and finally towards the south. The fracture in LAR-2, measured by the 3DX, transversely displaces southeast, east/northeast, and finally towards the southeast.

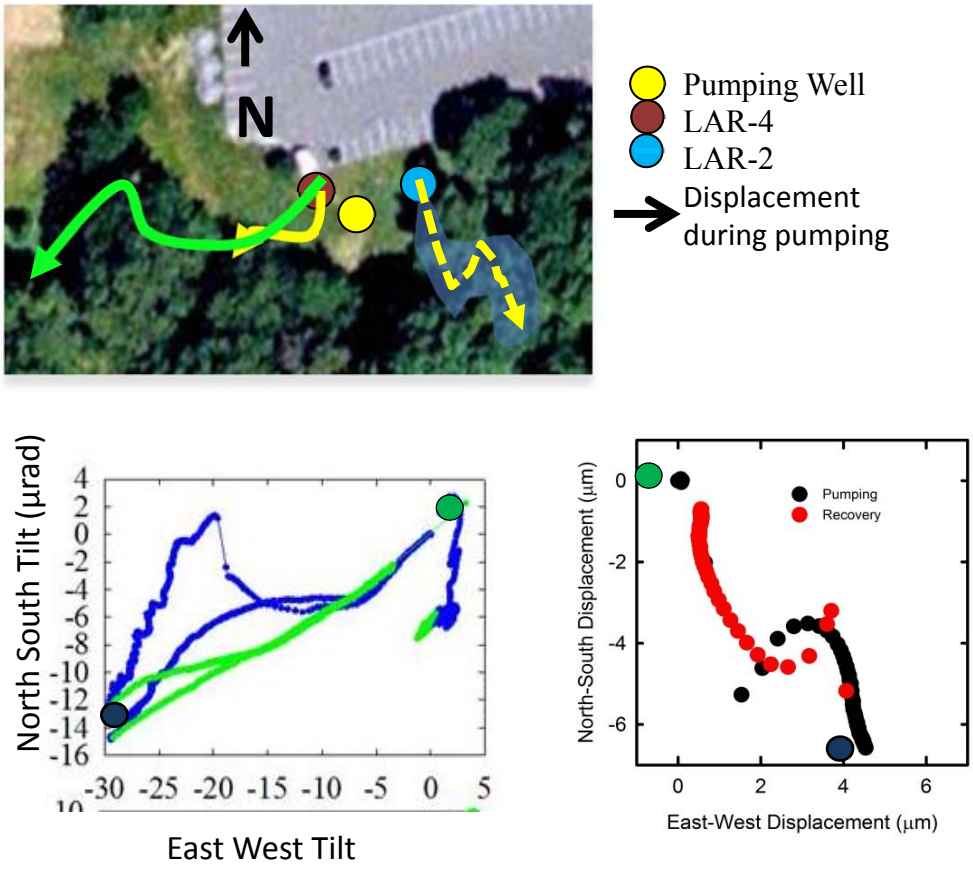

Figure 4.2-76. Transverse displacements from well testing at 24.3 m in LAR-2 and 22 meters in LAR-4. The green dot is the beginning of pumping. The blue dot is the beginning of recovery.

The results are surprising because under ideal conditions tilting is expected to occur on a radial path from the monitoring point to the pumping well. Analytical models of pumping in a homogeneous aquifer suggest that the tilt in porous media will be in the same direction a radial line through the pumping well [*Kumpel*, 1989; *Lehmann*, 2001; *Wang and Kumpel*, 2003; *Burbey and Helm*, 1999]. In contrast, instead of being parallel to a radial line from the pumping well, the tilt and transverse displacements are at high angles to the radial line.

A possibility for the observed tilt/transverse direction could be explained by the dip of the conductive fractures. An analytical analysis done by Hisz et al. (2012) evaluated the tilt field that would occur at 24 meters around a pumping well with a dipping fracture at 35 meters embedded in a uniform tight porous matrix (Figure 4.2-77). The results are that the tilt at 24 meters radiates from a point approximately 5 m up-dip from the well. The analytical results are similar to the results obtained in the field (Figure 4.2-78).

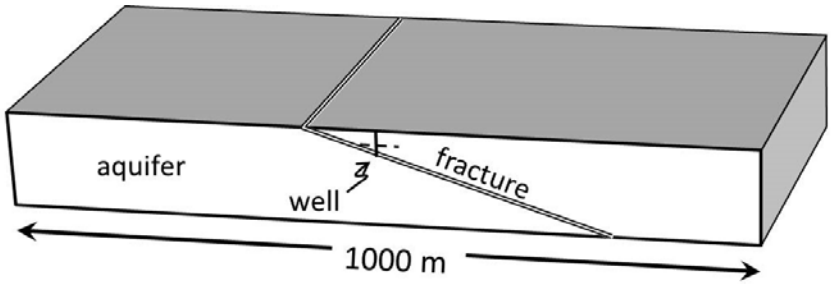

Parameter	aquifer	fracture
Young's Modulus, *E*	10^9 Pa	$0.5x10^9$ Pa
Poisson's ratio, μ	0.25	0.25
Permeability, *k*	10^{-15} m^2	10^{-11} m^2
Biot-Willis coef, α	0.7	0.7
Biot Modulus, *M*	$3x10^9$ Pa	$1.5x10^9$ Pa

Figure 4.2.3-77. Geometry and parameters used in Hisz et al. (2012) analysis of a dipping fracture embedded in a homogeneous aquifer.

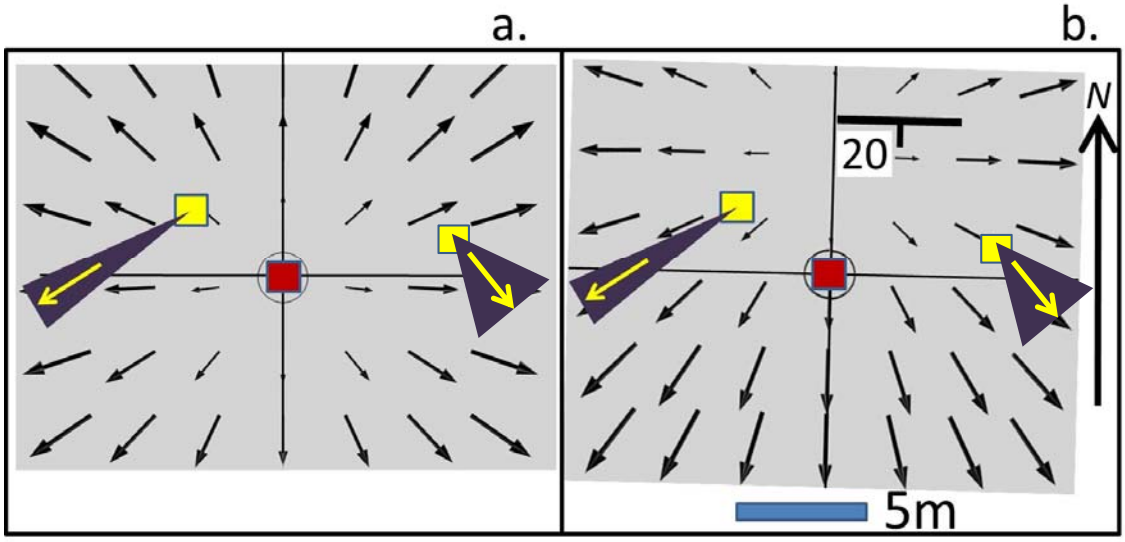

Figure 4.2-78. Tilt vectors (arrows) predicted at a depth of 25 m in the vicinity of the pumping well (red square). Observed azimuth of tilts (purple wedge and yellow arrow) at monitoring well (yellow square). (a) flat lying fracture. (b) fracture oriented as shown with strike and dip symbol (Modified graph from Hisz et al., 2012).

The transverse displacement for both LAR-2 and LAR-4 has a sinusoidal shape that is not fully explained by a single dipping fracture analysis. The transverse displacement analysis for a dipping fracture indicates that the 3DX would tilt linearly during the pumping test. The transverse displacement we observe is to the southeast 15 minutes into pumping then it changes displaces to the northeast for 30 minutes until it gradually moves towards the southeast for the remainder of pumping. This change in orientation of tilting appears to result from

heterogeneities. Numerical inversion methods would potentially be a useful approach to interpret these heterogeneities.

CONCLUSIONS OF 3DX AND 5DX

The 3DX and 5DX are instruments for measuring 3D displacements in wells using multiple fiber Bragg strain gauges. The FBGs are not affected by electronic interference so multiple devices can be used in or near the well, or a pump can also be used in the same well. Nor are the gauges affected by supercritical CO_2.

The instruments were calibrated in the lab and the 5-minute RMS noise for axial displacement is 30 nm, and for transverse displacement 5-min RMS noise is 180 nm. The noise level of the axial displacement during deployment under ambient conditions is somewhat smaller than this, in the range of 10 nm. This corresponds to a strain of approximately 10^{-8}.

The 3DX was used at 3 sites during this investigation and it gives results that were expected based on our experience. In a few cases, data from the 3DX could be validated by comparing to results using another instrument, the Tilt-X.

The 5DX monitors two sets of flexures instead of the one set monitored by the 3DX. This allows the 5DX to measure an additional degree of freedom (rotation), or the additional measurements can be used to further constrain axial and transverse displacements. The results from tests using both 3DX and 5DX in adjacent wells at NAWC indicate that the signals are generally similar, although the magnitude of displacements from the 5DX were 4 to 8 times greater than those from the 3DX. The two instruments measured different fractures, so it is possible that the differences in displacements reflect differences the compliances of the fractures.

The major limitation of the 3DX and 5DX is the durability of the FBG strain gauges. Several gauges gave anomalous signals during the NAWC test and time limitations precluded their replacement during the test. A registration system was developed for the 5DX to secure the gauges during deployment, and this appears promising but the gauges are still quite vulnerable. Additional work will be needed to harden the instrument in order to avoid damaging the FBG gauges in future deployments.

An objective of the research was to evaluate the feasibility of using FBGs in the 3DX or 5DX for applications during CO_2 sequestration. This includes aquifer characterization in deep formations, and well casing monitoring during CO_2 injection. The results indicate that it should be feasible to create a portable instrument that can measure axial strains in the range of 10^{-7} or less. Additional work to further hardened and field test the instruments would be needed prior to deployment at depths typical of CO_2 storage.

GROUTED BOREHOLE STRAINMETERS

Borehole strainmeters that are grouted in place are the most stable and have the highest resolution of methods for measuring strain at depth. It would be feasible to use a grouted borehole strainmeter for applications associated with CO_2 storage, although these instruments have been developed to measure strains associated with tectonic processes. This section includes descriptions of two instruments, the Gladwin Borehole Strainmeter, and the Borehole Optical Fiber Strainmeter (BOFS).

Several grouted borehole strainmeters have been described that are not presented here. The Sacks-Evertson dilatometer [*Sacks et al.*, 1971] was developed in the late 1960s and 1970s

and then used for several decades in a variety of applications related to understanding natural earth processes. This device characterizes strain by measuring the fluid exchange with one or several oil-filled chambers that are grouted into a borehole. Ishii and coworkers (2001, 2002, 2015) developed an instrument to measure multicomponent strain using an system similar to one by Gladwin outlined below. The Ishii strainmeters have been widely used in Japan.

4.2.4 GLADWIN BOREHOLE STRAINMETER

The Gladwin Borehole Strainmeter (GTSM) is a permanently installed, grout-in system that was developed in the late 1970s and early 1980s by Michael T. Gladwin at the University of Queensland, Australia [*Gladwin*, 1984]. Its design aim was to make very high precision measurements of tectonic strains in the formation in which it was emplaced [*Langbein et al.*, 1999]. Perhaps its most notable application is measuring so-called episodic slip and tremor events associated with aseismic displacements along tectonic faults [*Gladwin*, 1994]. There are currently 80 GTSMs deployed as a part of the Plate Boundary Observatory, or PBO (http://pbo.unavco.org), and dozens of others are used around the world for regional studies.

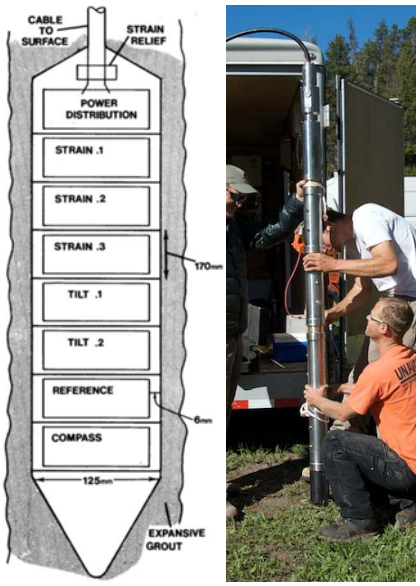

Figure 4.2-79. Schematic of the GTSM down-hole instrument package taken from Gladwin, 1984 (left) as well as a picture of the device prior to installation (right).

The down-hole instrument package consists of a gyroscopic compass, two pendulum tiltmeters, and four extensometers (Figure 4.2-79), where the fourth is intended as a reference to correct for drift common to all four gauges. The extensometers measure the diameter of the borehole at three azimuths separated by 120º using capacitive displacement transducers (Figure 4.2-79). These function by measuring the capacitance between the two conductive plates, which follow the relationship:

$$C = \frac{\varepsilon_0 K A}{d} \qquad (4.2\text{-}33)$$

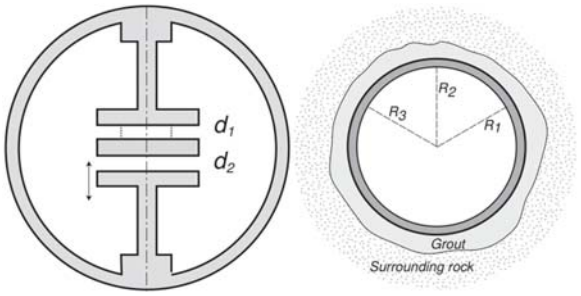

Figure 4.2-79. Schematic showing a top-down view of a single capacitive strain gauge (left) and the three gauges separated by 120º and emplaced in grout (right).

where ε_0 is the permittivity of free space, K is the dielectric constant of the material between the plates, A is the surface area of the plates, and d is the gap between the plates. These transducers are capable of measuring displacements as small as several picometers over its 10 cm base length. This short gauge length implies a stability of better than 1 part in 10^{10} per year given that tectonic strains are on the order of several parts per billion per year.

The high resolution and stability of the GTSM strain gauges are the result of several factors. First, each gauge consists of a fixed plate and one that is allowed to move with changes in the borehole diameter. These two

capacitive plates to operate as two inputs to a bridge circuit such as the one shown in Figure 4.2-80. This forms a differential system that allows for very high amplification since all common mode noise is eliminated. The fourth, redundant gauge can be used to correct for other common mode problems such as inductive noise in the cable. This gauge can also be used as a fourth radial strain measurement, resulting in an over-determined system where a problematic or faulty gauge can be omitted from the strain tensor calculation.

The principle advantages of the GTSM are its compact design and that it is permanently installed down-hole. Its overall diameter is 100 mm (just under 4") and 2.2 m long and is deployed from 100 m to 250 m depth in a 150 mm (6") diameter hole. Expansive grout is used to both couple the instrument to the surrounding formation and ensures that it operates under a state of compression. This deep, fully grouted, closed-hole deployment is clearly the most optimal configuration for maximizing instrument stability.

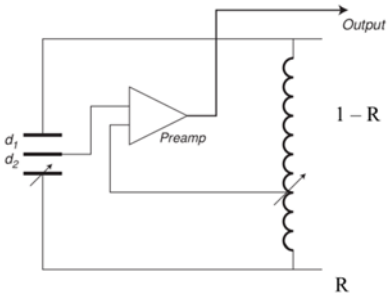

Figure 4.2-80. The electronic bridge circuit used to make very high-resolution measurements of the sensor plate gaps.

The GTSM has several distinct disadvantages. Chief among these is its approximately $150,000 cost, which does not include the requisite expensive, large-diameter borehole. The installation is permanent, and this cost can be difficult to justify for some applications. In-situ calibration of the instrument can be challenging. While the instrument is designed to have an isotropic response with a package that matches the stiffness of the formation, the manufacturer's suggested calibration leads to estimates of the strain field that differ significantly from the predicted tides [*Roeloffs,* 2010; *Hodgkinson et al.*, 2013] and what is observed from seismic wavefield gradiometry [*Grant*, 2010]. These differences will be quantified in Section 4.2.5.

Performance

Figure 4.2-81 shows the power spectra computed from approximately 1 year of data recorded by the PBO strainmeter B084 located in Southern California. The inset plot shows both the tided and detided spectra roughly between 1 and 2 cycles per day (CPD). The GTSM has a noise level of ~140 dB in this intertidal band between 1 and 2 CPD, indicating very good stability and an almost 40-50 dB signal-to-noise for the tides. There is some residual energy at 1 CPD that can also be seen in Figure 4.2-81 in the next section.

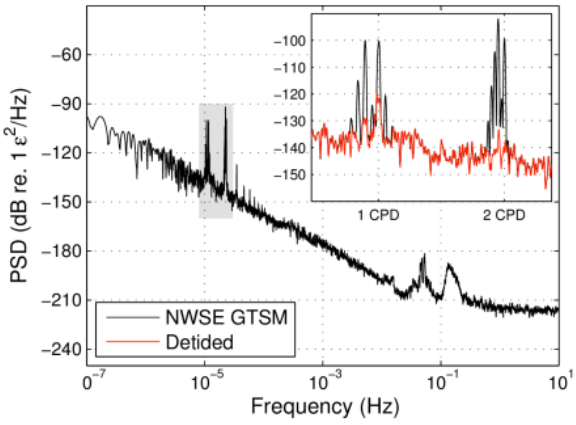

Figure 4.2-81. Power spectrum estimate from the GTSM B084 located at the Piñon Flat Observatory in Southern California. For conversion, displacement of -220 dB = 10^{-12} m.

Several issues can be observed in the higher frequencies. First is the noise below 10^{-1} Hz, which is unfortunately common to many GTSMs in the PBO network [*Barbour and Agnew*, 2011], and is believed to be residual power supply noise in the capacitance bridge circuit. Just above this is the microseism peak centered between 0.15 to 0.2 Hz. The spectrum levels off above this indicating that the

instrument noise floor has been reached at about -220 dB.

This corresponds to a displacement of roughly 1×10^{-12} m at 1 Hz, which is a strain of approximately 10^{-11}. This is the limit of the capacitor gauge technology.

4.2.5 BOFS

The Borehole Optical Fiber Strainmeter (BOFS) is a long baseline vertical strainmeter system that has been in operation at the Piñon Flat Geophysical Observatory (PFO) in Southern California since early 2012. It consists of three redundant 250-m-long optical fibers that each function as one arm of a Michelson interferometer system very similar to the one described in Section 4.1.4. BOFS was developed to test the efficacy of using inexpensive optical fibers to measure geophysical strain signals. The principle advantage of optical fibers is that they allow for very precise displacement measurements to be made over long distances along paths that do not have to be straight. The desire to use a 250 m long baseline is that it relaxes the 1 part in 10^{10} per year stability required by the GTSM to make long period tectonic measurements by a factor of 2,500. While it is deployed in a 150 mm (6") diameter borehole, the vertical components could easily be installed in a much smaller (and therefore much less expensive), 50 mm (2") hole. What follows is a brief summary of the design of BOFS, and a more detailed account can be found in DeWolf (2014).

BOFS is a completely passive device, consisting of an upper borehole package (herein referred to as a "sonde"), a lower sonde, and the fiber cables stretched between them. Figure 4.2-82 shows a schematic of the deployed system. The upper sonde is clamped inside of the borehole 4 m below the surface to limit its exposure to surface temperature changes as well as to thermal stresses in the surface material. This is connected to the lower sonde grouted in place 250 m farther down hole by two optical fiber cables. (One cable contains two of the three redundant strainmeters, and the other just one). Each fiber cable was tensioned to an initial strain of ~0.15% and the upper sonde clamp set once the lower sonde was secured in competent grout such that both positive and negative strains are measured.

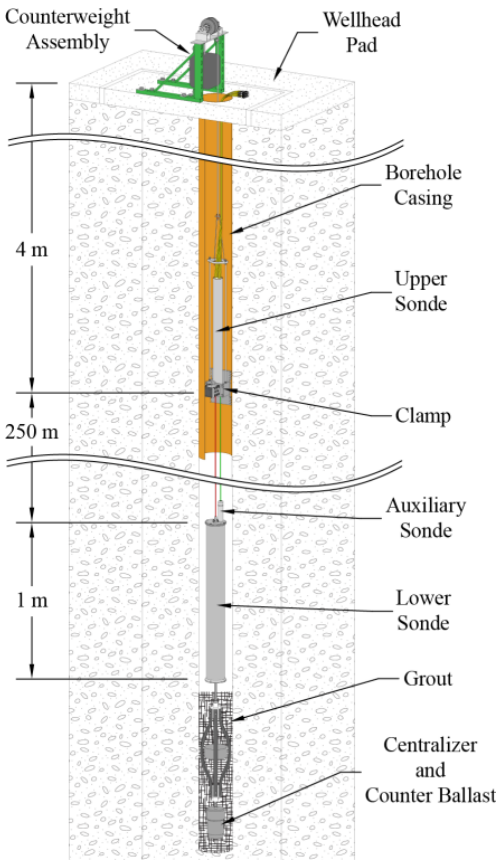

Figure 4.2-82. Schematic of the deployed BOFS system.

Figure 4.2-83 shows the opto-mechanical layout of the upper sonde. This contains the 3×3 fiber couplers and reflective "Faraday" mirrors used in each of the three vertical strainmeters. A total of 12 optical fibers are used to interrogate the system from a vault approximately 25 m from the borehole. The two fiber cables penetrate the upper sonde using a pair of feed-throughs that simultaneously form seals between the fiber cables and the upper sonde as well as secure the individual optical fibers in place to form the upper

termination point of the strainmeter. This upper sonde is a completely sealed unit with no serviceable components.

The lower sonde is shown in Figure 4.2-84, which is a 10 cm diameter stainless steel pressure case that also forms the lower termination point of two of the vertical strainmeters. (The optical fiber for the third vertical strainmeter makes a loop in the auxiliary sonde and terminates back in the upper sonde, thereby forming a redundant sensor that is twice as long as the other two.) A thin aluminum sleeve wrapped with 80 m of optical fiber is epoxied into the interior of the lower sonde pressure case to form an areal strainmeter. Unfortunately, an error during deployment left it uncoupled to the borehole wall and therefore no results are available. The lower sonde is also completely sealed and unserviceable since it is intended to be permanently deployed.

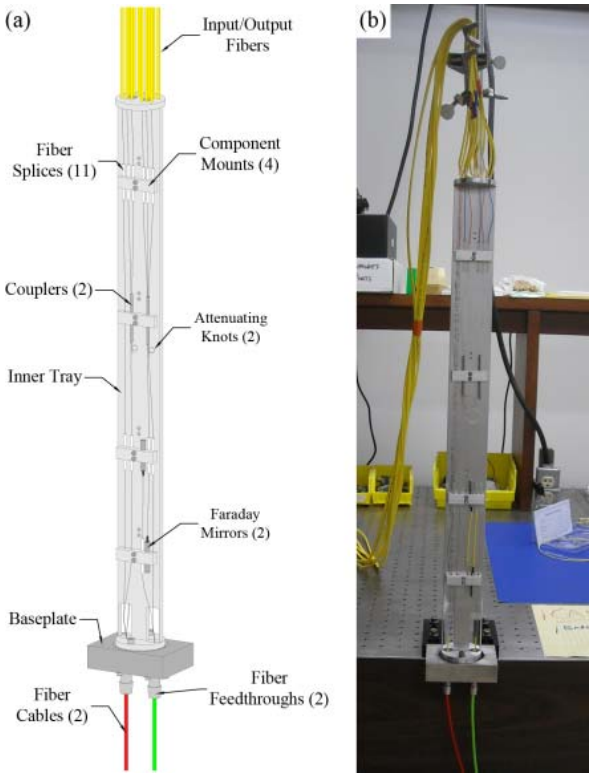

Figure 4.2-83. Opto-mechanical schematic of the BOFS upper sonde (a) along with a photograph of the same (b).

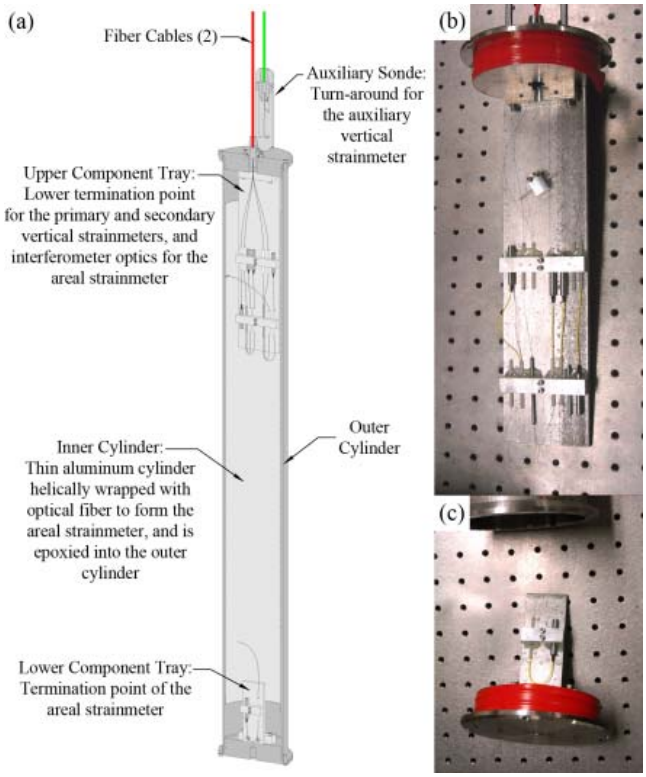

Figure 4.2-84. BOFS lower sonde schematic (a). Pictures of the upper and lower optical component trays (b and c, respectively).

Performance

BOFS has been collecting geophysically meaningful data since several months following its deployment in December 2011. Several tensioning and surface loading tests have been conducted to verify the calibration factor C that can be expressed in the closed-form algebraic relationship:

$$C = \frac{4\pi\mu}{\lambda} L \qquad (4.2\text{-}34)$$

where μ is the strain-optic coefficient of the glass fiber, λ is the laser wavelength, and L is the length of the instrument. It is essential to note that there are no other measurements of vertical strain at PFO that can be used to directly compare to BOFS. However, the vertical strain ϵ_z can be inferred from the areal strain at the surface assuming a traction-free half-space using the relationship:

$$\epsilon_z = \frac{-\nu}{1-\nu}\epsilon_A \qquad (4.2\text{-}35)$$

where $\epsilon_A = \epsilon_1 + \epsilon_2$ are two orthogonal horizontal strains. (Note that for a Poisson solid $\nu = 0.25$, and the vertical strain is -1/3 of the areal strain.) This relationship is used throughout these analyses to compare the vertical strain from BOFS to the areal strain observed by a pair of orthogonal, 730 m base length laser strainmeters (LSM areal) as well as the areal strain from the GTSM B084, both located at PFO.

Figure 4.2-85 shows a 50-day recording of BOFS along with that of the inferred vertical strain from the LSM and GTSM. Both the raw and detided time series are presented. While all three records clearly show the tides, the GTSM has a noticeable and unexplained 1 cycle per day residual signal. BOFS also has a similarly sized ~2 nϵ residual that is much higher frequency that is believed to be due to fluid exchange in the open borehole. Perhaps more revealing are the power spectra shown in Figure 4.2-86, which shows that at the very longest periods (~10^{-6} Hz) the spectral level of BOFS is about 16 dB higher than from either the LSM, and is generally 20 dB higher on BOFS between 1 and 2 CPD (the intertidal band). While there is excellent agreement for the largest amplitude tides, the signal-to-noise levels are clearly lower for BOFS. In general, the spectral levels on BOFS are about 20 dB higher than that of the LSM until approximately 0.1 Hz, where the 0.5 Hz Nyquist frequency of the LSM obscures further comparison.

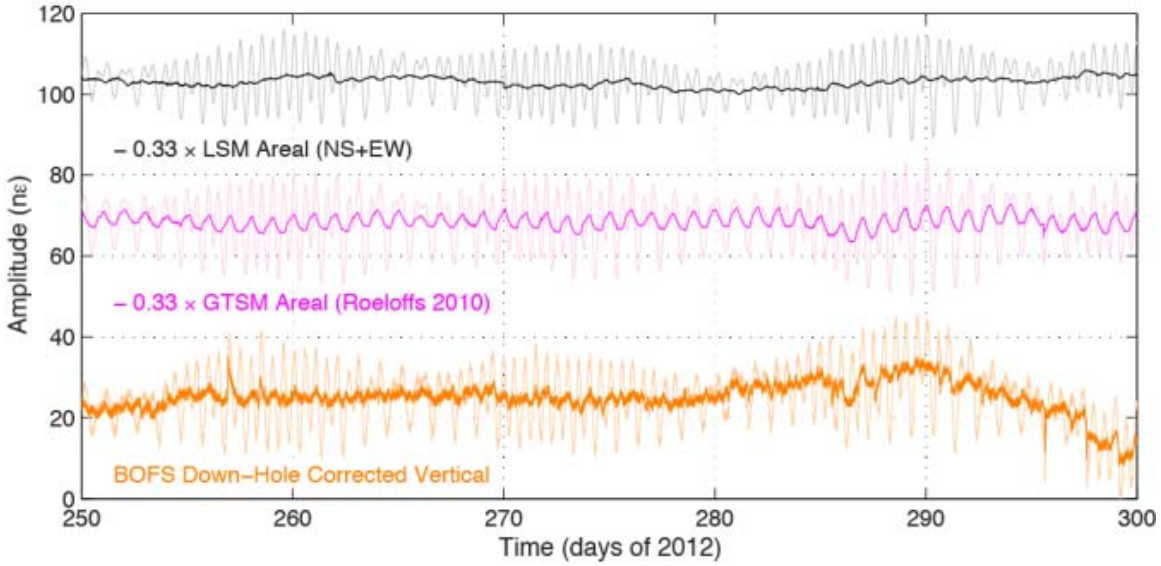

Figure 4.2-85. 50-day time series of BOFS along with the inferred vertical strain recorded by the LSM and GTSM.

The spectrum of the difference series (BOFS PV minus SV in Figure 4.2-86) is one measure of the intrinsic capabilities of this optical fiber strainmeter. While the lack of data makes comparisons below about 10^{-6} Hz difficult, this measurement of the instrument "self-noise" is more than 25 dB lower than the LSM above 10^{-4} Hz. The inset plot also shows a 10 to 12 dB peak in the difference spectral level at 1 CPD that is due to some unknown effect, such as thermally induced tractions between the two fibers.

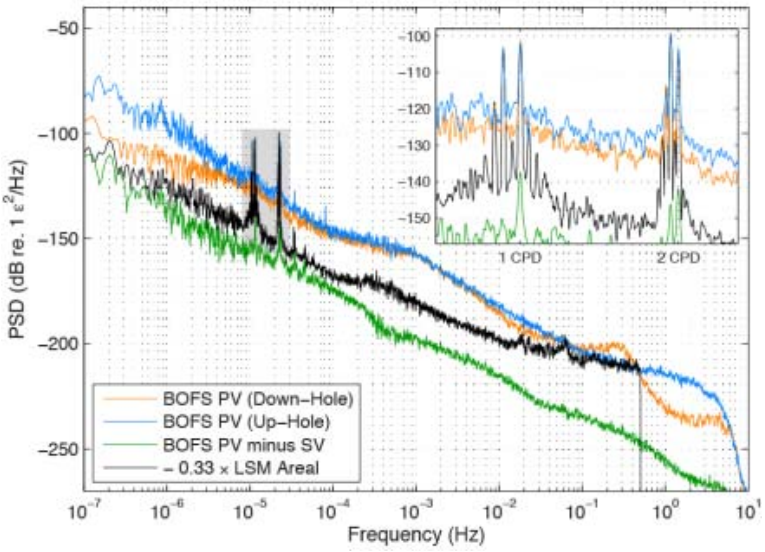

Figure 4.2-86: Power spectra from BOFS compared to the -1/3 times the LSM areal strain record.

Earth tides are one way to estimate Poisson's ratio from the vertical and areal strain records and to compare signal-to-noise levels. The O1 (25.8 hour period) and M2 (12.4 hour period) tidal constituents are excellent candidates since their periods are sufficiently far from 24 and 12 hours to not be contaminated by temperature and barometric pressure effects. Table 4.2-2 shows the Poisson's ratio computed using Eq. 4.2-35 using both the O1 and M2 tidal amplitudes as determined by least-squares. While the BOFS/LSM results agree with previous results of approximately 0.25 [*Wyatt, et al.*, 1983], the "GTSM (M)" results do not. This is believed to be the result of the manufacturer's calibration (labeled as "(M)") not being representative of the true coupling between the formation and the instrument. Results from two other calibration matrices are also presented in Table 4.2-2 from the literature: Roeloffs (2010) denoted by "(R)" and Hodgkinson et al. (2013) as "(H)." These results agree much more closely with the expected value of ~0.25.

Long-period surface waves produced by teleseismic events are another way to compute Poisson's ratio. Figure 4.2-87 shows an example of four surface wave fits from a magnitude 7.3 earthquake located off the east coast of Honshu, Japan on December 7th, 2012. Ensemble results are shown in Table 4.2-3 for the vertical strain to areal strain amplitude ratio converted to Poisson's ratio using Eq. 4.2-35. The LSM/BOFS results are in very good agreement with a Poisson solid with an ensemble standard deviation of just under 5%, whereas the estimate is also higher than expected for the GTSM (M) and slightly lower for GTSM (R) and GTSM (H).

Table 4.2-2. Inferred Poisson's ratio results using the BOFS primary vertical and areal strain amplitudes of the best-fit M2 and O1 tidal constituents.

Areal	M2 Poisson's Ratio	M2 Phase (º)	O1 Poisson's Ratio	O1 Phase (º)
LSM	0.2682 ± 0.0002	177.86 ± 0.07	0.2853 ± 0.0005	175.8 ± 0.2
GTSM (M)	0.3873 ± 0.0003	182.88 ± 0.08	0.3909 ± 0.0007	180.2 ± 0.9
GTSM (R)	0.2341 ± 0.0002	180.48 ± 0.08	0.2608 ± 0.0006	180.3 ± 0.9
GTSM (H)	0.2454 ± 0.0003	182.14 ± 0.08	0.2528 ± 0.0005	178.0 ± 0.9

Table 4.2-3. Ensemble averages for the Poisson's ratio using 36 earthquakes.

Areal	Poisson's Ratio
LSM	0.254 ± 0.012
GTSM (M)	0.349 ± 0.024
GTSM (R)	0.212 ± 0.023
GTSM (H)	0.215 ± 0.005

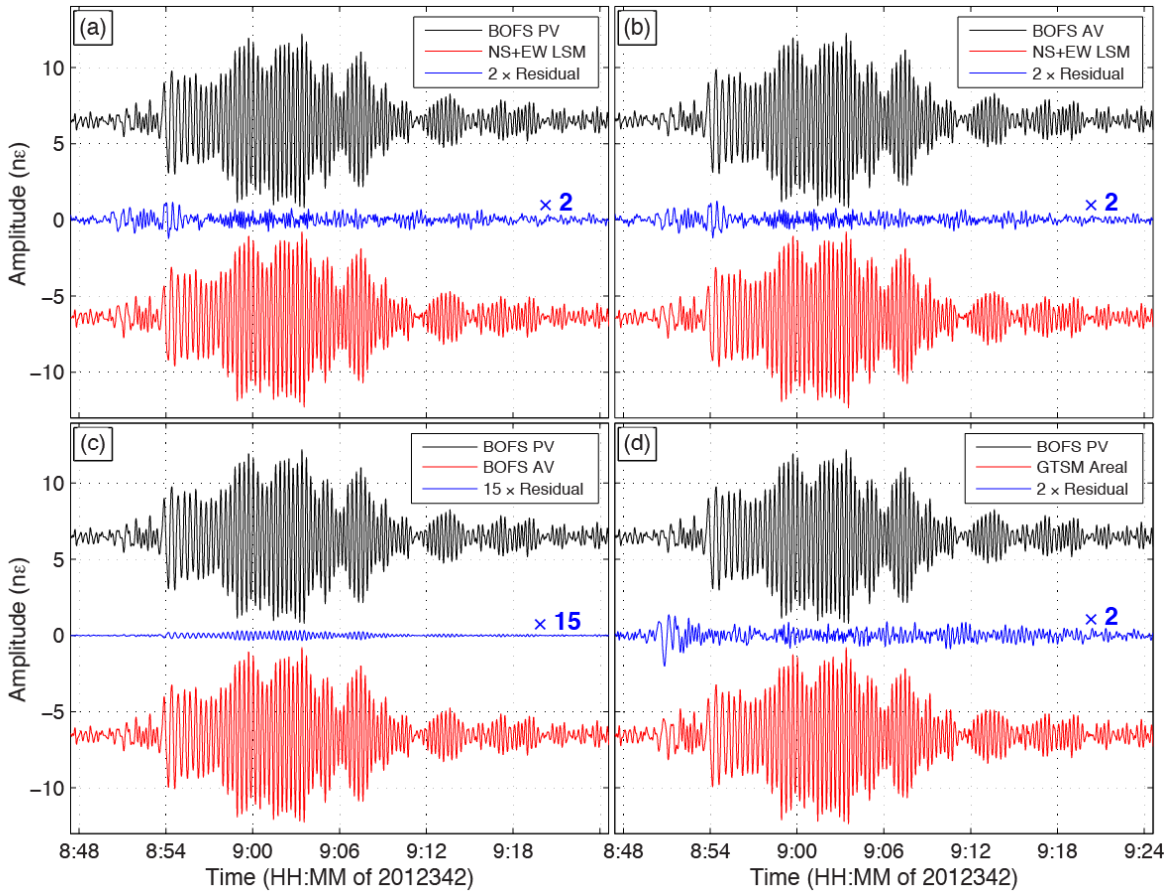

Figure 4.2-87. Surface wave fits from a teleseismic earthquake used to compare BOFS to the LSM and GTSM. (a) Fit of the LSM areal to the BOFS primary vertical (PV). (b) Fit of the LSM areal to the BOFS auxiliary vertical (AV). (c) Comparison between the BOFS PV and AV. (d) Fit between the BOFS PV and the GTSM. Note that the residual time series have been scaled up by a factor of 2 except for the PV/AV, which has been scaled by 15.

4.3 SUMMARY OF CHAPTER FINDINGS

Three classes of in situ instruments have been evaluated for measuring deformation of wellbores associated with pressure changes in aquifers or reservoirs. The classes trade logistics of deployment and well use, for resolution in strain magnitude, and spatial resolution in the distribution of strain that can be measured. As previously stated, different classes of instruments are more suitable for different applications.

Annular strain sensors (characterize 1000 nε) provide the most flexible logistics because they are mounted on the outside of casing so the wellbore is open and use of the wellbore is unaffected. Moreover, the sensors are isolated by casing and cement from the harsh conditions inside the wellbore.

The WIRE system developed by Baker Hughes is currently the only commercially available system for making this measurement, to our knowledge. WIRE is currently designed to be deployed on the outside of casing, so deployment must be done during well completion. The deployment process is relatively straightforward, but the use of this system currently requires deployment on a new well—a capability to retrofit existing wells is currently unavailable.

The WIRE system uses FBGs configured using a proprietary interferometric interrogator system. The strain resolution of each sensor appears to be in the range of 10^{-7} to 10^{-6}, which is the lowest resolution of the systems we evaluated. Strain signals of ~1 με (1,000 nε) could likely be characterized with the system in its current form. Even though this is lower resolution than other systems, it is feasible to deploy hundreds of sensors along a borehole using WIRE, and this is by far the highest spatial resolution of the systems we considered here. Moreover, the system is design to measure multiple degrees of freedom, so both axial and bending strains can be measured.

The WIRE system is particularly well suited to monitoring complicated strain patterns in casing under conditions where strains are particularly large. Strains during brief well tests may be too small to be resolved, but it seems highly likely that strains during CO_2 storage operations could be resolved by this technique. The WIRE system appears to be well suited to monitoring for large strains in injection casings that could lead to problems with wellbore integrity.

Portable strain instruments (characterize 10s nε), including extensometers, tiltmeters and strainmeters, are temporarily anchored to the inside of a wellbore. The instruments are several meters long and occupy a significant fraction of the cross-section of the wellbore. This will affect the logistics of well operation, but injection operations could likely continue during deployment. Water wells can be pumped or used for injected while these instruments are in place, for example. The instrument could be removed when testing was completed, or for maintenance. This would reduce the cost and improve the reliability compared to instruments that are grouted in place. The instruments could be deployed in existing wells, which would reduce costs and increase versatility compared to instruments that must be installed during completion.

The portable instruments can measure smaller deformations than the embedded annular sensors, with axial and tilt strain resolutions in the range of 10^{-9} to 10^{-8}. Strains signals of 10s of nε or nrad could be characterized by these instruments. This improved resolution in the magnitude of strain comes at the expense of the spatial resolution because portable strain instruments are designed to only measure one location at a time.

Electromagnetic and fiber sensors are available that have characteristics suitable for use in portable strain instruments. DVRTs, eddy current sensors, fiber Bragg gratings, fiber interferometers, electrolytic tilt sensors and pendulum sensors all appear suitable for some downhole applications, and they each have constraints on deployment that must be considered in the design of a downhole instrument.

Portable strain instruments appear to be suited to applications in injection wells during short-term testing. This would include injection tests to characterize the formation prior to full scale operations, for example. These types of instruments also appear to be suited to applications in monitoring wells in the vicinity of the injection interval where strains are expected to be greater than approximately 10^{-8}.

Grouted Strainmeters (characterize < 1 nε) are the most sensitive strain meters available, but they are also have the most logistical constraints. They can resolve strains on the order of 10^{-11}, so strain signals of less than 1 nε could likely be characterized with these instruments.

They are designed to be grouted in place, so the bottom of the bore cannot be used for injection or monitoring. The completion can include a well screen for access to the formation and fluid pressure monitoring above the grouted instrument, however. As a result, it seems feasible to include a grouted strainmeter in the bottom of wells that are used to monitor fluid pressure or water composition in a CO_2 storage project. Grouting in place increases costs because instruments must be dedicated to a particular location, and maintenance is difficult.

Grouted strainmeters are the most cumbersome and expensive to deploy, but they can provide multiple components of the highest resolution strain data. This is the most likely instrument to be able to detect strains associated with injection, so it would have applications at larger lateral distances, or further above the injection formation than the portable instruments.

Application The three classes of instruments that are currently available have their own application niche, and a full complement of monitoring could include all of them. The WIRE system is the best suited to monitoring deformation of the injection well itself, although it currently requires installation during completion of the well. Portable strainmeters are best suited to preliminary testing of the injection well, and to applications in monitoring wells in the vicinity of the injection well. Grouted strainmeters are best suited to deployment further away from the injection well where strains will be small.

An opportunity to advance the application is to combine the strengths of the different classes of instruments. For example, it could be feasible to increase the resolution of the portable instruments so they rival that of grouted strainmeters. Alternatively, it could be feasible to reduce the cost and complexity of the grouted strainmeters so they could be included as a routine component of monitoring wells.

4.4 REFERENCES

Agnew, D.C., 1986. Strainmeters and tiltmeters. Rev. Geophys., 24(3): 579-624.

Agnew, D.C., and F.K. Wyatt 2003. Long-base laser strainmeters: a review, SIO Technical Report: *http://repositories.cdlib.org/sio/techreport/2/*, Scripps Institution of Oceanography.

Agnew, D.C., 2007. Before PBO: an overview of continuous strain and tilt measurements in the United States. Journal of the Geodetic Society of Japan, 53: 157-182.

Barbour, A. J., Agnew, D. C., 2011. Noise Levels on Plate Boundary Observatory Borehole Strainmeters in Southern California. *Bulletin of the Seismological Society of America*, 101(5):2453-2466.

Beavan, J., and R. Bilham, 1977. Thermally induced errors in fluid tube tiltmeters. Journal of Geophysical Research, 82(36): 5699-5704.

Burbey, T. J., Hisz, D., Murdoch, L. C., and Zhang, M., 2011. Quantifying fractured crystalline-rock properties using well tests, earth tides and barometric effects. Journal of Hydrology, Volumes 414-415, pp. 317-328.

Butler, J.J., W. Jin, G.A. Mohammed, and E.C. Reboulet, 2011. New insights from well responses to fluctuations in barometric pressure. Groundwater, 49(4): 525-533.

Butter, C. D., Hocker, G. B., 1978. Fiber optics strain gauge. *Applied Optics*, 17(18):2867-2869.

Cappa, F., Guglielmi, Y., Fénart, P., Merrien-Soukatchoff, V., Thoraval, A., 2005,"Hydromechanical Interactions in a Fractured Carbonate Reservoir Inferred from Hydraulic and Mechanical Measurements," International Journal of Rock Mechanics & Mining Sciences, Vol. 42, pp. 287-306.

Cappa, F., Guglielmi, Y., Gaffet, S., Lancon, H., Lamarque, I., 2006. "Use of in situ Fiber Optic Sensors to Characterize Highly Heterogeneous Elastic Displacement Fields in Fractured Rocks," International Journal of Rock Mechanics & Mining Sciences, Vol. 43, No. 4, pp. 647-654.

Cappa, F., Y. Guglielmi, J. Rutqvist, C.-F. Tsang, and A. Thoraval , 2006. Hydromechanical modeling of pulse tests that measure fluid pressure and fracture normal displacement at the Coaraze Laboratory site, France, Int. J. Rock Mech. Min. Sci., 43, 1062 – 1082.

Cappa, F., Y. Guglielmi, and J. Virieux, 2007. Stress and fluid transfer in a fault zone due to overpressures in the seismogenic crust, Geophys. Res. Lett., 34, L05301, doi:10.1029/2006GL028980.

Castillo, D., Hunter, S., Harben, P., Wright, C., Conant, R., and Davis, E., 1997. Deep hydraulic fracture imaging: Recent advances in tiltmeter technologies. *Int. J. Rock Mech. & Min. Sci.* 34:3-4, Paper No. 047.

Cleveland, T.G., Bravo, R., and Rogers, J.R., 1992. Storage coefficients and vertical hydrualic conductivities in aquitards usings extensometer and hydrograph data. Groundwater, 30(5): 701-708.

Clark, W.E., 1967. Computing the barometric efficiency of a well. American Society of Civil Engineers, Journal of the Hydraulic Division, Proceedings 93(HY4): 93-98.

Davis, S.N., F.L. Peterson, A.D. Halderman, 1969. Measurement of small surface displacements induced by fluid flow. Water Resources Research v. 5 n. 1, 129-138.

Davis , P.M., 1983. Surface deformation associated with a dipping hydrofracture. Journal of Geophysical Research, 88(B7), pp.5826-5834.

Davis, E., Wright, C., Demetrius, S., Choi, J., Craley, G., 2000. Precise tiltmeter subsidence monitoring enhances reservoir management. SPE62577, SPE AAPG Western regional Meeting, Long Beach, CA, June 19–23.

Detournay, E. and A. H.-D. Cheng, 1993. *Fundamentals of poroelasticity*, Chapter 5, Comprehensive Rock Engrg. (J. Hudson, ed.), Vol. II, Pergamon Press, 113-169.

DeWolf, S., 2014. *Optical Fiber Sensors for Infrasonic Wind Noise Reduction and Earth Strain Measurement*, University of California San Deigo Ph.D. Thesis, 215 p. http://roger.ucsd.edu/record=b8191107~S9

Domenico, P.A. and F.W. Schwartz. 1998. *Physical and Chemical Hydrogeology*. 2nd ed. John Wiley, New York.

Du, J., Brissenden, S.J., McGillivray, P., Bourne, S., Hofstra, P., Davis, E.J., Roadarmel, W.H., Wolhart, S.L., and Wright, C.A., 2005. Mapping fluid flow in a reservoir using tiltmeter-based surface-deformation measurements. SPE 96897, SPE Annual Technical Conference and Exhibition, Dallas, TX, October 9-12.

Dusseault, M.B., Bilak, R.A., and L. Rothenburg, 1993. Inversion of surface displacements to monitor in situ processes. Int. J. Rock Mech. Min. Sci. & Geomech. Abstr., 30(7): 1219-1222.

Eagle Alloys Corporation, 2012. “Invar 36 Alloys, Technical Data”, http://www.eaglealloys.com/c-7-invarsuper-invar.html.

Evans , K.F., Holzhausen, G.R., and Wood, M.D., 1982. The geometry of a large-scale nitrogen gas hydraulic fracture formed in Devonian shales: An example of fracture mapping using tiltmeters. Soc. Pet. Eng. J., 22, 755-763.

Evans, K. and G. Holzhausen, 1983. On the development of shallow hydraulic fractures as viewed through the surface deformation field: Part 2 – Case histories. Journal of Petroleum Technology, 35(2): 411-420.

Fabian, M., 2004. Near surface tilt and pore pressure changes induced by pumping in multi-layered poroelastic half-spaces, number 229 in Berichte ausdem Fachbereich Geowissenschaften, ISSN: 0931-0800, Universität Bremen. Doctoral thesis, Rheinische Friedrich-Wilhelms-Universität Bonn

Fabian, M., and H.-J. Kumpel, 2003. Poroelasticity: observations of anomalous near surface tilt induced by ground water pumping. Journal of Hydrology, 281(3):187-205.S

Ferrari, P., and D. Mariloli, 2008. IEEE 1588-based synchronization system for a displacement sensor network. IEEE Transactions on Instrumentation and Measurement, 57(2): 254-260.

Feipel, V., Berghe, M.V.; Rooze, M.A., 2003. No effects of cervical spine motion on cranial dura mater strain. Clinical Biomechanics, 18(5): 389-392.

Furbish, D.J., 1991. The response of water level in a well to a time series of atmospheric loading under confined conditions. Water Resources Research, 27(4): 557-568.

Gale, J., 1975, A numerical, field and laboratory study of flow in rocks with deformable fractures: PhD Dissertation, University of California, Berkely.

Gladwin, M. T., 1984. High-precision multicomponent borehole deformation monitoring. *Review of Scientific Instruments*, 55:2011-2016.

Gladwin, M. T., Breckenridge, K. S., Gwyther, R. L. and Hart, R., 1994. Measurements of the Strain Field Associated with Episodic creep events at San Juan Bautista, California. *J. Geophys. Res.* 99(B3):4559-4565.

Grant, E. G., 2010. *Gladwin Tensor Strainmeter Calibration using Seismic Data: Instrument Calibration Methods and Wave Gradiometry Applications*. Ph.D. Thesis, University of Memphis.

Guglielmi, Y., Cappa, F., and D. Amitrano, 2008. High-definition analysis of fluid-induced seismicity related to the mesoscale hydromechanical properties of a fault zone. Geophysical Res. Let., 35: 6 pp.

Guglielmi, Y., F. Cappa, J. Rutqvist, S.Y. Wang. 2009. Hydromechanical imaging of fractured porous rock properties and coupled processes. AGU Fall Meeting abstract.

Haneberg, W.C., and R.L. Friesen, 1995. Tilts, strains, and ground-water levels near an earth fissure in the Mimbres Basin, New Mexico. GSA Bulletin, 107(3): 316-326.

Hesler, G., Zheng, Z., and Meyer, L., 1990, In-situ fracture stiffness determination; Rock Mechanics contributions and challenges: Hustrulid and Johnson, eds., Balkema, Totterdam, p. 405-411.

Hocker, G. B., 1979. Fiber optic acoustic sensors with composite structure: an analysis. *Applied Optics*, 18(21):3679-3683.

Hocker, G. B., 1979. Fiber-optic sensing of pressure and temperature. *Applied Optics*, 18(9):1445-1448.

Hodgkinson, K., Langbein, J., Henderson, B., Mencin, D., Borsa, A., 2013. Tidal calibration of plate boundary observatory borehole strainmeters. *Journal of Geophysical Research: Solid Earth*, 118(1):447–458.

Holzhausen, G.R., Card, C.C. Raisbeck, J.M., and Dobecki, T.L., 1985. Hydrualic fracture growth during steam stimulation in a single-well test, SPE 13619, California Regional Meeting, SPE, Bakersfield, March 27-29.

Hunter, S.L., 2002. Self adjusting inclinometer. US Patent 6,349,477.

Ishii, H., Jentzsch, G., Graupner, S., Nakao, S., Ramatschi, M. and Weise, A., 2001. Observatory Nokogiriyama / Japan: Comparison of different tiltmeters. Proc. 14th International Symposium on Earth Tides, Special Issue of the Journal of the Geodetic Soc. of Japan, 47/1, 155 – 160.

Ishii H, Yamauchi T, Matsumoto S, Hirata Y, Nakao S (2002) Development of multi-component borehole instrument for earthquake prediction study: some observed example of precursory and co-seismic phenomena relating to earthquake swarms and application of the instrument for rock mechanics. Seismogenic Process Monitoring, Balkema, The Netherlands, pp 365–377.

Ishii, H. and Y. Asai 2015. Development of a borehole stress meter for studying earthquake predictions and rock mechanics, and stress seismograms of the 2011Tohoku earthquake (M 9.0). Earth, Planets and Space (2015) 67:26. DOI 10.1186/s40623-015-0197-z

Jacob, C.E., 1940. On the flow of water in an elastic artesian aquifer. Eos Trans., AGU, 21, 574-586.

Jacob, T., Chery, J., Boudin, F., and R. Bayer, 2010. Monitoring deformation from hydrologic processes in a karst aquifer using long-based tiltmeters. Water Resources Research, 46(W09542).

Jahr, T., Letz, H., and Jentzsch, G., 2006. Monitoring fluid induced deformation of the earth's crust: a large scale experiment at the KTB location/Germany. Journal of Geodynamics, 41: 190-197.

Karasaki, K., B. Freifeld, C. Cohen, K. Grossenbacher, P. Cook, and D. Vasco. 2000. A multidisciplinary fractured rock characterization study at Raymond field site, Raymond, CA. Journal of Hydrology, 236(1-2): 17-34.

Klein, F.W., 1984. Eruption forecasting at Kilauea Volcano, Hawaii. Journal of Geophysical Research, 89(B5): 3059-3073.

Kohl, M.L., and J. Levine 1995. Measurement and interpretation of tidal tilts in a small array. Journal of Geophysical Research, 100, B3, pp: 3929-3941.

Kumpel, H.-J., P. Varga, K. Lehmann, and G. Mentes, 1996. Ground tilt induced by pumping – preliminary results from the Nagycenk test site, Hungary. Acta Geodaetica et Geophysica Hungarica, 31:67-78.

Langbein, J., Gwyther R. L., Hart, R. H. G., Gladwin, M. T., 1999. Slip-rate increase at Parkfield in 1993 detected by high-precision EDM and borehole tensor strainmeters. *Geophys. Res. Lett.* 26(16):2529-2532.

Lecampion, B., R. Jeffrey, and E. Detournay, 2005. Resolving the geometry of hydraulic fractures from tilt measurements. Pure appl. Geophys, 162: 2433-2452.

Levine, J., Meertens, C., and R. Busby, 1989. Tilt observations using borehole tiltmeters 1. Analysis of tidal and secular tilt. Journal of Geophysical Research, 94(No. B1): 574-586.

Li, Z. et al., 2003. A neural network approach to correcting nonlinearity in optical interferometers. *Meas. Sci. Technol.* 14(3):376-381.

Lofgren, B.E., 1961. Measurement of compaction of aquifer systems in areas of land subsidence. In: Geological Survey Research 1961. U.S. Geological Survey Professional Paper, pp. B49-B52.

Lofgren, B.E. 1969. Field measurment of aquifer-system compaction, San Joaquin Valley, California, USA. Land Subsidence, 1. Internation Association of Scientific Hydrology, 13 pp.

Longuevergne, L., N. Florsch, F. Boudin, L. Oudin, and C. Camerlynck 2009. Tilt and strain deformation induced by hydrologically active natural fractures: Application to the tiltmeters installed in Sainte-Croix-aux-Mines observatory (France), Geophys. J. Int., 178(2): 667-677.

Martin, C. D., Davison, C. C., and Kozack, E. T., 1990. Characterizing normal stiffness and hydraulic conductivity of a major shear zone in granite, A. A. Balkema, Rotterdam, pp. 549-556.

Meertens, C., Levine, J., and R. Busby, 1989. Tilt observations using borehole tiltmeters 2. Analysis of data from Yellowstone National Park. Journal of Geophysical Research, 94(B1): 587-601.

Melchior, P., 1964, Earth tides *in* Research in Geophysics, v. 2, edited by H. Odishaw, Cambridge, Massachusetts, Massachusetts Institute of Technology Press, pp. 183-193.

Murdoch, L.C., and Germanovich, L. N., 2006. Analysis of a deformable fracture in permeable material. International Journal for Numerical and Analytical Methods in Geomechanics, Vol. 30, pp. 529-561.

Murdoch, L.C., D.B. Hisz, J.F. Ebenhack, D.E. Fowler, C. R. Tiedeman, L. N. Germanovich. 2009. Analysis of Hydromechanical Well Tests in Fractured Sedimentary Rock at the NAWC Site, New Jersey. Asheville 2009, the 43rd US Rock Mechanics Symposium and 4th U.S.-Canada Rock Mechanics Symposium, held in Asheville, NC June 28th – July 1, 2009, 8 p.

Myer, L. R., 1991, "Hydromechanical and Seismic Properties of Fractures", *Proceedings of the Congress of the International Society for Rock Mechanics*, Aachen, Germany, Wittke, Ed., Balkema, Rotterdam, Vol. 7, pp. 397-404.

Nelson, A. E., Horton, J. W., and Clarke, J. W., 1998, Geologic map of the Greenville 1° x 2° quadrangle, Georgia, South Carolina, and North Carolina: U.S. Geological Survey Map I-2175, scale 1:250,000.

Pierson, J.G., 1999. The Art of Practical and Precise Strain Based Measurement. Pierson & Associates LLC, Rockaway, NJ.

Pollard, D.D., and Holzhausen, G.R., 1979. On the mechanical interaction between a fluid-filled fracture and the earth's surface. Tectonophysics, 53, 27-57.

Pope, J.P., and T.J. Burbey, 2004. Multiple-Aquifer characterization from single borehole extensometer records. Ground Water 42 (1), pp.45-58.

Pozar, T., Mozina, J., 2011. Enhanced ellipse fitting in a two-detector homodyne quadrature laser interferometer. *Meas. Sci. Technol.* 22:085301.

Rasmussen, T.C., and Crawford, L.A., 1997, Identifying and removing barometric pressure effects in confined and unconfined aquifers: Ground Water, 35(3), p. 502–511.

Riley, F.S., 1961. Analysis of borehole extensometer data from central California. Land Subsidence. IASH-Unesco, International Assocation of Scientific Hydrology.

Riley, F. S., 1969, Analysis of borehole extensometer data from central California, in Tison, L. J., ed., Land subsidence, v. 2: International Association of Scientific Hydrology Publication 89, p. 423-431.

Roeloffs, E., 2010. Tidal calibration of Plate Boundary Observatory borehole strainmeters: Roles of vertical and shear coupling. *Journal of Geophysical Research*, 115:B06405.

Sacks IS, Suyehiro S, Evertson DW, Yamagishi Y (1971) Sacks-Evertson strain meter, its installation in Japan and some preliminary information concerning strain steps. Papers Meteoro Geophys 22:195–208

Schweisinger, T., Murdoch, L.C., and C.O. Huey Jr.. 2007. Design of a removable borehole extensometer. Geotechnical Testing Journal 30 (3):

Schweisinger, T., Svenson, E.J., Murdoch, L.C.,.2009. Introduction to hydromechanical well tests in fractured rock aquifers. Groundwater, 47(1):69-79.

Schweisinger, T., Svenson, E.J., Murdoch, L.C.,.2011. Hydromechanical behavior during constant-rate pumping tests in fractured gneiss. Hydrogeology Journal, 19(5), p. 963-980. DOI: 10.1007/s10040-011-0728-z.

Sheem, S. K., 1980. Fiber-optic gyroscope with [3×3] directional coupler. *Applied Physics Letters*, 37(10):869–871.

Sirkis, J. S., Mathews, C. T., 1993. Experimental investigation of phase-strain-temperature modelfor structurally embedded interferometric fiber-optic sensors. Experimental Mechanics, 33(1):26-31.

Sleeman, R., H.W. Haak, M.S. Bos, J.J.A. van Gend, 2000. Tidal tilt observations in the Netherlands using shallow borehole tiltmeters. Physics and Chemistry of the Earth (A), 25: 415-420.

Spane, F. A., 2002. Considering barometric pressure in ground-water flow investigations. Water Resources Research 38 (6), 1078, doi:10.1029/2001WR000701.

Svenson, E., 2006. Methods for Measuring and Analyzing Transient Head and Aperture Changes During Air-Slug Tests in Fractured Bedrock, Master's Thesis, Clemson University.

Svenson, E.J., Schweisinger, T., Murdoch, L.C., 2008. Field evaluation of the hydromechanical behavior of flat-lying fractures during slug tests. Journal of Hydrology 359, 30-45.

Theis, C. V., 1935. The relation between the lowering of the piezometric surface and the rate and duration of discharge of a well using ground-water storage. Transactions, American Geophysical Union, Vol. 16, pp. 519-524.

Thompson, P. M. and E.T.Kozak .1991. "In situ measurement of coupled hydraulic pressure/fracture dilation in stiff crystalline." Field Measurements in Geotechnics, Balkema, Rotterdam, 23-31.

Urlaub, M., and Fabian, M., 2011. Poroelasticity: finite element modelling of anomalous tilt and pore pressure caused by pumping in a sedimentary half space with fault. Journal of Geodynamics. Vol. 51, pp. 219-232.

Vali, V., Shorthill, R. Fiber ring interferometer. Applied Optics 15:1099-1100, 1976.

van der Kamp, G., and J. E. Gale, 1983. Theory of earth tide and barometric effects in porous formations with compressible grains, Water Resour. Res., 19(2), 538-544.

van der Kamp, G., and Schmidt, R., 1997, Monitoring of total soil moisture on a scale of hectares using groundwater piezometers: Geophysical Research Letters, v. 24, no. 6, p. 719–722.

Vasco, D.W., Karaski, K., and Myer, L., 1998. Monitoring of fluid injection and soil consolidation using surface tilt measurements, Journal of Geotechnical and Geoenvironmental Engineering, 1124(1): 29-37.

Vasco, D.W., and Karasaki, K., 2001. A coupled inversion of pressure and surface displacement. Water Resour. Res., 37(12), 3071-3089.

Vasco, D.W., K. Karasaki, and C. Doughty, 2000. Using surface deformation to image reservoir dynamics. Geophysics, 65(1): 132-147.

Vasco, D.W., Karasaki, K., Nakagome, O., 2002. Monitoring reservoir production using surface deformation at the Hijiori test site and the Okuaizu geothermal field, Japan. Geothermics 31, 303–342.

Wang, H., 2000. *Theory of Linear Poroelasticity: with Applications to Geomechanics and Hydrogeology*. 287 pp., Princeton University Press, Princeton, N.J.

Wang, R. and H.-J. Kumpel, 2003. Poroelasticity: efficient modeling of strongly coupled, slow deformation processes in a multilayered halfspace. Geophysics, 68(2): 705-717.

Warpinski, N.R., Branagan, P.T., Engler, B.P., Wilmer, R., and S.L. Wolhart, 1997. Evaluation of a downhole tiltmeter array for monitoring hydraulic fractures. Int. J. Rock Mech. & Min. Sci. 34:3-4, paper No. 329.

Weise, A., Jentzsch, G., Kiviniemi, A., and Karriainen, J., 1999. Comparison of long-period tilt measurements: results from the two clinometric stations Metsahovi and Lohja, Findland. Geodynamics, 27(2): 237-257.

Weeks, E.P., 1979. Barometric fluctuations in wells tapping deep unconfined aquifer, Water Resources Research 15(5): 1167-1176.

Wyatt, F. K., and J. Berger, 1980. Investigation of tilt measurements using shallow borehole tiltmeters. Journal of Geophysical Research, 85(No. B8): 4351-4362.

Wyatt, F. K., Cabaniss, G., and D.C. Agnew, 1982. A comparison of tiltmeters at tidal frequencies. Geophysical Research Letters, 9(7): 743-746.

Wyatt, F. K., Agnew, D. C., Linde, A. T., Sacks, I. S., 1983. Borehole strainmeter studies at Piñon Flat Observatory. *Year Book Carnegie Institute of Washington*, 82:533–538.

Wyatt, F. K., 1989. Displacement of surface monuments: vertical motion. Journal of Geophysical Research, 94 (No. B2): 1655-1664.

Zumberge, M. A., Wyatt, F. K., Yu, D. X., Hanada, H., 1988. Optical fibers for measurement of earth strain. Applied Optics, 27(19):4131-4138.

Zumberge, M. A., Berger, J., Dzieciuch, M. A., Parker, R. L., 2004. Resolving Quadrature Fringes in Real Time. *Applied Optics*, 43(4):771-775.

CHAPTER FIVE
SUMMARY AND CONCLUSIONS

CONTENTS

CHAPTER FIVE
SUMMARY AND CONCLUSIONS

This project consists of coordinated investigations into the feasibility of measuring and analyzing subsurface deformation of wellbores to improve CO_2 storage. The investigation includes contributions related to the simulation of deformation during injection, the interpretation of deformation measurements using inversion, and the instrumentation needed to measure deformation.

5.1 DEFORMATION DURING INJECTION

We conducted a series of theoretical analyses using analytical and numerical models that solved problems in poroelasticity related to injection of fluid into wells. We found that readily available computer codes (ABAQUS and COMSOL) can solve problems related to deformation in the vicinity of injection wells using finite element methods. We tested these codes in a variety of relevant example problems, and we developed a poroelastic benchmark model intended to be used by other investigators interested in validating other codes. The run times for fully coupled finite element codes can be time consuming and may be prohibitive for some inverse methods. To address this constraint, we developed two analytical asymptotic solutions that can be used to calculate deformation very quickly.

The magnitude and pattern of deformation were calculated using an idealized simulation that was based on properties typical of CO_2 storage operations. The analysis assumed an injection pressure of 1 MPa, which resulted in an injection rate of approximately 100 gpm, and the injection lasted for 100 days. This is a lower pressure and shorter duration than full scale operations, but it may be a higher pressure and longer than an injection test conducted for formation evaluation.

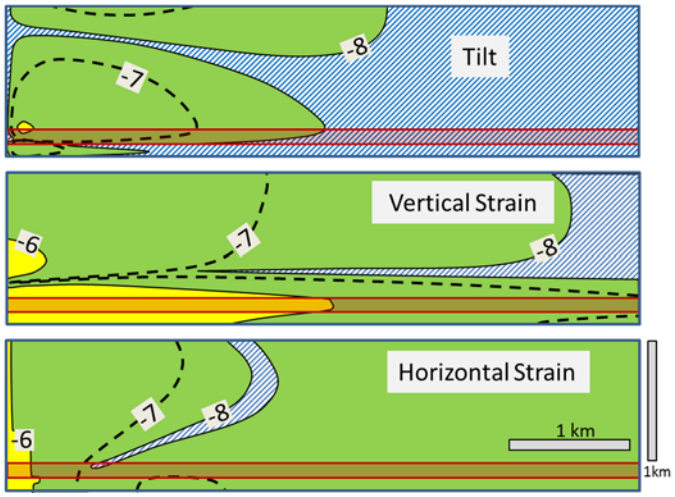

Figure 5.1-1. Summary strain magnitudes (as log of absolute value) in cross section after injecting for 100 days at 1MPa according to baseline example. Colors show three categories (yellow: $\varepsilon > 10^{-6}$; green: $10^{-8} < \varepsilon < 10^{-6}$; hatched: $\varepsilon < 10^{-8}$). Aquifer/reservoir as red. Well on the lower left.

The results indicate that the axial strain will be tensile and approximately 10 με adjacent to the pressurized interval. It will decrease and change sign upward with axial compression of several με in the casing adjacent to the confining unit. Radial displacements of several microns are largely due to pressurizing the wellbore, but smaller changes in radial displacements occur with time as the formation pressure changes.

The pattern of strain in the casing is sensitive to the pressure in the annular space and in the confining unit. It may be feasible to estimate changes in pressure on the outside of solid casing by measuring casing deformation, and this could be used to characterize well bore integrity or the permeability of confining units.

Strain rates of 10^{-12} 1/s or greater are expected in the vicinity of the wellbore early in the injection. The strain rate will decrease with time to 10^{-13} 1/s or less in the first 100 days of injection. Strain rates of 10^{-13} 1/s occur in the confining unit and they also decrease with time.

The magnitude of strain at the well and in the formation increases roughly in proportion to the injection pressure (the results above are for 1 MPa)

The magnitude of the strain rate at the well and in the formation increases roughly in proportion to the injection rate (the results above are for approximately 100 gpm).

Formation properties will affect the magnitude of expected deformation, but the overall effect is generally less than a factor of two when using ranges of properties associated with a particular type of reservoir.

The distributions of strain components in the formation create varied patterns that evolve with time. An example of three components of the strain tensor after injecting for 100 days is summarized in Figure 1.6-1. The strain patterns depend on the magnitude and distribution of formation properties, so they are sensitive to heterogeneities in the aquifer and overlying confining unit. Patterns of horizontal and vertical strains, as well as displacement gradients (tilts) occur in the overlying confining unit in response to pressure changes in the underlying reservoir. The patterns result from both a.) radially outward and upward displacement of the reservoir, and b.) upward bending of the ground surface.

The strains predicted to occur in the vicinity of an injection well are in the range of available instrumentation. Strain in excess of 1 με ($>10^{-6}$) will likely occur in the vicinity of the injection well, according to the analysis. Strains of this magnitude can be measured by common strain gauges, and a system called WIRE, which consists of many strain gauges on a fiber optic cable, is available for downhole deployment along wellbores. Strains in excess of 10^{-8} can be measured by portable extensometers and tiltmeters, according to tests conducted in shallow aquifers. Vertical and horizontal strains and tilts of this magnitude occur within a few km of the injection well within 100 days of injection (Figure 1.6-1), according to the simulations. It appears that the strains that are expected to occur in the vicinity of injection wells are within the resolution of instruments that could be temporarily anchored in monitoring wells. Horizontal and vertical strains greater than 10^{-10} can be resolved by instruments that are grouted into boreholes. Strains of these low magnitudes occur up to many km from injection wells, although distinguishing these small strains from background noise may be challenging.

5.2 PARAMETER ESTIMATION

We evaluated the potential of using geomechanical data collected during injection operations as a constraint on reservoir model parameters. A major enabling contribution of this work was, therefore, the development of advanced optimization algorithms that leverage high performance computing to calibrate reservoir parameters. The approach developed here integrates several different sampling and optimization schemes (genetic algorithms, MCMC, naïve Monte Carlo, and Voronoi polygons) to balance algorithmic speed versus the evaluation of parameter uncertainty and tradeoffs in the data. This method was then used to study the ability of different types of data to constrain reservoir parameters and evaluate how this translates to predictions of long-term operational behavior. The key outcomes of the research are summarized in the three sections below that relate directly to the three goals outlined in the original project proposal. The

rest of this report, however, is structured in a format that provides a clearer explanation of the results given substantial overlaps between the sections.

Parameter Uncertainty and Uniqueness We demonstrated that different combinations of geomechanical measurements such as pressure, tilt and strain can be used to estimate poroelastic parameter values and their uncertainties. Notably, the most accurate parameter estimates with the lowest uncertainties are obtained when pressure data are used in conjunction with measurements sensitive to all three components of reservoir strain. We have also investigated how measurement location impacts our ability to estimate parameters and found that measurements within cap rock theoretically provide sufficient information for calibrating the model parameters, thus suggesting that field studies may not require penetration of the target formation, thus reducing risk.

Prediction Sensitivity Evaluating the sensitivity of predictions to uncertainty and error in model estimates was considered within the scope of this work. Using Monte Carlo simulations, we were able to produce forecasts of reservoir performance for different data constraint cases, i.e., where parameter uncertainty depended on the type of data used in the optimization. We found that the degree of uncertainty in the forecasts scaled with the degree of uncertainty in the parameter estimates. A second type of study we performed evaluated the effect of model errors on predictions, i.e., the case where a model does not capture key information about the underlying reservoir system, such as a preferential flow path through a fracture or along the borehole. We found that in these scenarios, significant errors in parameter estimates could occur, but model predictions were well outside reasonable uncertainties in the data thus providing a mechanism to identify and correct these model errors when geomechanical data are used as a constraint.

Large-scale Optimization We investigated stochastic and deterministic optimization methods, and evaluated their viability for large-scale optimization of poroelastic forward models. We have observed that while some deterministic methods, e.g., gradient descent, converge quickly in ideal circumstances, they perform poorly in the presence of non-unique problems or non-convex error structures. By integrating these methods with stochastic techniques like genetic algorithms, Markov chain Monte Carlo, and naïve Monte Carlo with a novel sampling technique based on Voronoi polygons, we have developed a new hybrid algorithm that balances fast convergence with an improved exploration of the parameter space. As these stochastic methods require many simulation runs in order to perform adequately, we have used high-performance computing methods to distribute simulation runs over many computational nodes on a cluster computer. To support the analysis of these data, we implemented a statistical method for combining non-unique pieces of information into superior parameter estimates.

5.3 INSTRUMENTATION

Three classes of in situ instruments were evaluated for measuring deformation of wellbores associated with pressure changes in aquifers or reservoirs. The classes trade logistics of deployment and well use, for resolution in strain magnitude, and spatial resolution in the distribution of strain that can be measured. This results in causes the different classes of instruments to be suitable for different applications.

Annular strain sensors ($\varepsilon > 10^{-6}$) provide the most flexible logistics because they are mounted on the outside of casing so the wellbore is open and use of the wellbore is unaffected. Moreover, the sensors are isolated by casing and cement from the harsh conditions inside the wellbore.

The WIRE system developed by Baker Hughes is currently the only available system for making this measurement, to our knowledge. WIRE is currently designed to be deployed on the outside of casing, so deployment must be done during well completion. The deployment process is relatively straightforward, but the use of this system currently requires deployment on a new well—a capability to retrofit existing wells is currently unavailable.

The WIRE system uses FBGs configured using a proprietary interferometric interrogator system. The strain resolution of each sensor appears to be in the range of 10^{-7} to 10^{-6}, which is the lowest resolution of the systems we evaluated. Strain signals of ~1 με (1000 nε) could likely be characterized with the system in its current form. Even though this is lower resolution than other system, it is feasible to deploy hundreds of sensors along a borehole using WIRE, and this is by far the highest spatial resolution of the systems we considered here. Moreover, the system is design to measure multiple degrees of freedom, so both axial and bending strains can be measured.

The WIRE system is particularly well suited to monitoring complicated strain patterns in casing under conditions where strains are particularly large. Strains during brief well tests may be too small to be resolved, but it seems highly likely that strains during CO_2 storage operations could be resolved by this technique. The WIRE system appears to be well suited to monitoring for large strains in injection casings that could lead to problems with wellbore integrity.

Portable strain instruments ($\boldsymbol{\varepsilon > 10^{-8}}$), including extensometers, tiltmeters and strainmeters, are temporarily anchored to the inside of a wellbore. The instruments are several meters long and occupy a significant fraction of the cross-section of the wellbore. This will affect the logistics of well operation, but injection operations could likely continue during deployment. Water wells can be pumped or used for injected while these instruments are in place, for example. The instrument could be removed when testing was completed, or for maintenance. This would reduce the cost and improve the reliability compared to instruments that are grouted in place. The instruments could be deployed in existing wells, which would reduce costs and increase versatility compared to instruments that must be installed during completion.

The portable instruments can measure smaller deformations than the embedded annular sensors, with axial and tilt strain resolutions in the range of 10^{-9} to 10^{-8}. Strains signals of 10s of $n\epsilon$ or nrad could be characterized by these instruments. This improved resolution in the magnitude of strain comes at the expense of the spatial resolution because portable strain instruments are designed to only measure one location at a time.

Electromagnetic and fiber sensors are available that have characteristics suitable for use in portable strain instruments. DVRTs, eddy current sensors, fiber Bragg gratings, fiber interferometers, electrolytic tilt sensors and pendulum sensors all appear suitable for some downhole applications, and they each have constraints on deployment that must be considered in the design of a downhole instrument.

Portable strain instruments appear to be suited to applications in injection wells during short-term testing. This would include injection tests to characterize the formation prior to full scale operations, for example. These types of instruments also appear to be suited to applications in monitoring wells in the vicinity of the injection interval where strains are expected to be greater than approximately 10^{-8}.

Grouted Strainmeters $\varepsilon > 10^{-10}$) are the most sensitive strain meters available, but they are also have the most logistical constraints. They can resolve strains on the order of 10^{-11}, so strain signals of less than 1 nε could likely be characterized with these instruments.

They are designed to be grouted in place, so the bottom of the bore cannot be used for injection or monitoring. The completion can include a well screen for access to the formation and fluid pressure monitoring above the grouted instrument, however. As a result, it seems feasible to include a grouted strainmeter in the bottom of wells that are used to monitor fluid pressure or water composition in a CO_2 storage project. Grouting in place increases costs because instruments must be dedicated to a particular location, and maintenance is difficult.

Grouted strainmeters are the most cumbersome and expensive to deploy, but they can provide multiple components of the highest resolution strain data. This is the most likely instrument to be able to detect strains associated with injection, so it would have applications a larger lateral distances, or further above the injection formation than the portable instruments.

Application The three classes of instruments that are currently available have their own application niche, and a full complement of monitoring could include all of them. The WIRE system is the best suited to monitoring deformation of the injection well itself, although it currently requires installation during completion of the well. Portable strainmeters are best suited to preliminary testing of the injection well, and to applications in monitoring wells in the vicinity of the injection well. Grouted strainmeters are best suited to deployment further away from the injection well where strains will be small.

5.4 RECOMMENDATIONS

It appears to be feasible to measure and interpret in-situ deformation during CO_2 injection, according to our evaluation. Existing instrumentation and methods should be sufficient to provide benefits to the CO_2 storage program, such as improving the ability to estimate storage capacity, and several emerging methods or refinements of existing methods appear poised to reduce costs.

Improve resolution of portable strainmeter

Cost will be an important factor affecting the viability of a strain monitoring program, and we recommend further investigations that are designed to reduce costs. Two opportunities appear viable to reduce costs of instrumentation. One is to improve the resolution of portable strainmeters so the necessary data can be obtained without requiring the expense of a dedicated instrument that is grouted into that location. This would require improvements in the displacement transducers employed by the portable strainmeters to increase their resolution to the nanostrain level, and a rigorous evaluation of the anchoring methods and other elements of the mechanical design that can affect drift.

Reduce the cost of grout-in strainmeter

Another strategy that should be evaluated is the use of low cost sensors that are grouted into a borehole. One reason why grout-in borehole strainmeters (e.g., Gladwin Tensor Borehole Strainmeter (GTSM), Sacks-Evertson (Carnegie) Strainmeter) are expensive is because they use specialized, custom fabricated sensors. These specialized sensors were required when the currently available borehole strainmeters were developed in the 1970s and 1980s because commercially available sensors that could detect very small strains were unavailable at that time. However, the capability of commercially available sensors (like eddy current sensors) has

improved in recent decades and current models appear to have sufficient resolution. We recommend that the cost and performance of grout-in borehole strainmeters using commercially available sensors be evaluated.

Optical fiber interferometers

Optical interferometry offers the ability to measure small strains, and systems that use optical fibers have the potential to measure strains without downhole electronics. The WIRE technology makes use of optical fibers to measure strains at many locations along a well casing, and it appears to be a good approach for characterizing deformation of the injection borehole. The WIRE system appears to offer the ability to understand deformation processes at the injection well that could lead to wellbore integrity problems. We recommend that optical fiber strain sensing be evaluated further as a method for characterizing and monitoring the integrity of wellbores used for CO_2 storage.

Optical fiber interferometers also have the potential to provide strain measurements with a resolution that rivals that used in grout-in borehole strainmeters. However, optical fiber interferometers require no downhole electronics, so they are immune to failure from lightning strikes or other processes that could incapacitate the electronics in instruments like the GTSM. This is particularly important with grout-in strainmeters where problems with unrecoverable electronics would effectively end the useful life of the instrument. The low attenuation of light in an optical fiber allows for measurements to be made over long baselines or multiple paths along a short baseline (e.g., many redundant measurements of the radial strain along the axis of the borehole) to average out the effects of local inhomogeneities known to significantly impact the performance of the GTSM.

The use of optical interferometers in a grout-in strainmeter would require the development of a design that could be constructed and operated at low cost. The BOFS system has demonstrated the feasibility of using optical fiber interferometers to measure strain in a borehole. This approach could lead to a low-cost design since the passive downhole components are very inexpensive (a few hundreds of dollars), and the up-hole interrogation system (laser, fringe detection and counting system, etc.) can be easily moved from one sensor deployment to the next. We recommend that optical fiber interferometers be evaluated as strain sensors in boreholes.

Strain components and sensor location

The original intent of this project was to utilize strains measured along the injection borehole, but we soon realized that strain measured at monitoring wells could also be important. Moreover, it became clear that the entire strain tensor had information related to the injection process, so there could be significant value in measuring multiple components of strain. This is important because drilling is a significant component of the cost of deploying in situ sensors, so measuring multiple components of strain at a single location makes good use of this cost. We recommend that future applications measure multiple components of strain to make the best use of the cost of drilling.

Strains caused by injection will be greatest in the vicinity of the well screen, but the strain field will quickly expand to include the overlying confining unit. Strain measurements in both the injection formation and in the overlying confining unit can be interpreted to better understand formation properties or pressure distribution, according to our results. We recommend that future applications consider deploying sensors over a range locations provided by available monitoring

wells. Furthermore, we recommend that shallow settings be considered to reduce costs of deploying sensors that require new boreholes to be created.

Stochastic Optimization

The work performed in this project provides a strong initial basis for supporting the value of the hybrid stochastic optimization. The complexity of the reservoir heterogeneity considered in our tests was, however, somewhat limited as we focused on relatively idealized two-dimensional scenarios. We recommend that future work should evaluate the algorithm for scenarios where reservoirs exhibit spatial variations of parameters within the reservoirs (e.g., three dimensional models with preferential flow paths like channel structures). Furthermore, the algorithms should be applied to data obtained from real field tests. The complexities of data noise and model errors that occur in these settings can significantly challenge inversion schemes and are thus the ultimate test of any technique.

One specific limitation of the optimization algorithm that we have developed in this project is a critical dependence on the serial processing of data. This can lead to performance issues if there is a slowdown in any step of the algorithm, i.e., the algorithm can only proceed as fast as the slowest model. To overcome this challenge, we recommend modifying the algorithm to obtain a more flexible architecture that allows for each step to run independently. This would remove the dependence on the slowest model (i.e., chains utilizing fast simulation methods would not have to wait for those with slower simulations to continue the optimization). Such an approach would also allow for more flexibility in changing algorithms or adding data to the optimization on the fly, which would be an advantage for data synthesis in long-term operational settings.

Our multi-objective optimization methodology could be used to integrate various types of instruments to better evaluate and monitor a carbon storage site. We would recommend equipping a carbon injection site with a wide range of instrument types (pressure, tilt and strain meters, geodetic instruments, InSAR, seismic, ground penetrating radar, magnetotelluric, etc.), and using our optimizations to integrate the optimization of these datasets.

The distributed approach to model calibration and hierarchical data fitting that was developed for use in evaluating and monitoring carbon storage projects, should also be useful in characterizing oil, natural gas and geothermal reservoirs. Our code uses a modular design that allows the forward models to be easily replaced by others representing entirely different physical processes. Therefore, in future work the methodology developed for this project could be readily adapted for use in a wide range of scientific problems involving parameter estimation and imaging. These might include medical imaging, meteorology, and geophysical methods such as electrical resistivity and ground penetrating radar.

Field Test

The project described in the previous chapters and summarized in this one has provided encouraging preliminary results, and we recommend that the next step in the evaluation process be a field test of the proposed method under controlled conditions. The primary goal of the field test should be to measure and interpret in-situ deformation using sensor systems that could lead to cost-effective deployment. This would include the refinement of instrumentation, as recommended above, along with the application of inversion methods as outlined in Chapter Three. We also recommend that the field test include the deployment of an existing grout-in borehole strainmeter, such as a GTSM. This type of instrument will provide a baseline set of deformation

measurements that will serve to validate the results from the new instruments. Moreover, the use of a GTSM would provide a baseline dataset that could be used for proof-of-concept demonstration in the event that the signals were too small to be resolved by the new instruments.

The field test would ideally involve the measurement of deformation in the vicinity of a CO_2 injection well. The logistics involved with CO_2 injection may add a significant logistical burden, so we recommend that analogs to CO_2 injection also be considered. The reasoning is that injecting fluids other than CO_2, like water, will cause effects that resemble the deformation during CO_2 storage. Water flooding could be considered as a suitable analog, for example.